University of South Carolina
Scholar Commons

Theses and Dissertations

Spring 2022

Well–Defined Donor–Acceptor Materials

Gabrielle A. Leith

Follow this and additional works at: https://scholarcommons.sc.edu/etd

 Part of the Chemistry Commons

Recommended Citation
Leith, G. A.(2022). *Well–Defined Donor–Acceptor Materials.* (Doctoral dissertation). Retrieved from https://scholarcommons.sc.edu/etd/6748

This Open Access Dissertation is brought to you by Scholar Commons. It has been accepted for inclusion in Theses and Dissertations by an authorized administrator of Scholar Commons. For more information, please contact digres@mailbox.sc.edu.

WELL–DEFINED DONOR–ACCEPTOR MATERIALS

by

Gabrielle A. Leith

Bachelor of Arts
Hanover College, 2017

Submitted in Partial Fulfillment of the Requirements

For the Degree of Doctor of Philosophy in

Chemistry

College of Arts and Sciences

University of South Carolina

2022

Accepted by:

Natalia B. Shustova, Major Professor

Linda S. Shimizu, Committee Member

Hans-Conrad zur Loye, Committee Member

Melissa A. Moss, Committee Member

Tracey L. Weldon, Interim Vice Provost and Dean of the Graduate School

© Copyright by Gabrielle A. Leith, 2022

All Rights Reserved.

DEDICATION

My dissertation and voyage throughout graduate school is dedicated to my family. My parents, Jill Yeary and Lester Leith, challenged me since I was a little girl to be the best I could be and to push my boundaries to grow. I'm especially grateful to my mother who always provided a listening ear when I needed to complain and consoled me when I had bad days or when I doubted myself. I will be forever grateful for your unwavering support. I'm blessed to have parents who sacrificed so much to provide me with the best life and education that set me up for success in my future endeavors. My older sister, Courtney, who always answered the phone when I needed someone and provided me with the support I needed to get through the hard days. To my grandparents, Laurie Spegal and Dennis Morin, who always asked what I was up to in school and enveloped me in hugs and love when I went home to Indiana. I do not know how I could have made it through graduate school without the support and kindness of my family. I am also so blessed to have met my fiancé, Cody Small, during this challenging time who not only encouraged me daily but went the extra mile to do anything he could to make my days easier and happier. Over the past five years, I was able to make lifelong friendships and cannot imagine this time without the laughs, chats, and coffee breaks with my outstanding, supportive friends.

ACKNOWLEDGMENTS

Before anything else, I would like to thank my major advisor, Dr. Natalia Shustova for her steadfast guidance, daily mentorship, and constant friendship through my time at the University of South Carolina. On a daily basis, she challenged me and urged me to step beyond my comfort zone, and above all else, she truly cared about my development as a scientist and as a human-being. The words “thank you” cannot convey the feelings that I have. I am so appreciative of all of the lessons and opportunities that you provided to me, and I know that we will always remain close and in touch. I would also like to thank my committee members: Dr. Shimizu, Dr. zur Loye, and Dr. Moss. You were always there to guide me, challenge me, and provide support throughout my journey.

Thank you to my incredible co-workers who I’ve had the pleasure of working with, including those who have left USC and those who are still here. Dr. Allison Rice was my mentor during my first year and that mentorship evolved into a beautiful friendship that I am thankful for every day. I cannot imagine completing this unbelievable time without you by my side. Mr. Brandon Yarbrough taught me synthetic techniques that were crucial to my projects as well as provided scientific fun facts, laughter, and true kindness. To Corey Martin who began this journey with me, provided constant daily companionship, scientific advice, and was my other half in G+C. Thank you to Kyoungchul Park, Dr. Preecha Kittikhunnatham, Grace Thaggard, Gina Wilson, Matthew Ariwoola, and Buddhima Maldeni as well for your support and help during my time. You all have made this time a wonderful experience and I am thankful to call you all lifelong friends.

ABSTRACT

The modularity of multivariant scaffolds such as covalent–organic frameworks (COFs) provides an unprecedented level of control in the alignment of donor (D) and acceptor (A) units, a demand that is driven by the production of optoelectronic, photonic, and spintronic devices. The foray into novel motifs bearing D-A ensembles in frameworks has been applied towards material property modulation for device performance enhancement. This dissertation presents an emerging trend in the development of D-A interfaces by highlighting recent advances probing D-A interactions in porous crystalline matrices and co-crystals, with a focus on energy transfer (ET) and charge transfer (CT) processes in pre-designed pathways. The work presented within the following five chapters is focused on the design, synthesis, and characterization of corannulene- and fullerene-containing materials. Overall, this work comprises a burgeoning field in which D-A materials are not only synthetic triumphs but are also valuable contributions to the revolution of the technological sector.

TABLE OF CONTENTS

Dedication iii

Acknowledgments iv

Abstract v

List of Tables vii

List of Figures ix

List of Schemes xix

Chapter 1: Graphitic Supramolecular Architecture's Based On Corannulene, Fullerene, And Beyond 1

Chapter 2: "Broken-Hearted" Carbon Bowl Via Electron Shuttle Reaction: Energetics And Electron Coupling 42

Chapter 3: Stack the Bowls: Tailoring the Electronic Structure of Corannulene Integrated Crystalline Materials 112

Chapter 4: A Dual Threat: Redox-Activity and Electronic Structures of Well-Defined Donor-Acceptor Fulleretic Covalent-Organic Materials 176

References 240

Appendix A: Permission to Reprint 245

LIST OF TABLES

Table 2.1 X-ray structure refinement data for **1,** pyr·TCNQ, $C_{19}H_{16}$, $C_{21}H_{20}$, and $C_{19}H_{12}$ 75

Table 2.2 Electronic and zero-point vibrational energies (ZPE), and the total enthalpy at standard temperature and pressure (298 K, 1 atm) 79

Table 2.3 Strain energy (E_s) and released energy (E') for several polycyclic aromatic hydrocarbons (PAHs). Released energy was calculated using the B3LYP/6-31+G* level of theory.....80

Table 2.4 Strain energy (E_s) and average released energy (E'_{avg}) for several extended carbon π-bowls. 81

Table 2.5 Electron couplings estimated by the direct coupling method for TCNQ/$C_{20}H_{10}$ "stack" with different mutual orientations and TCNQ/P-$C_{20}H_{14}$ "stack" 84

Table 2.6 The bowl depth, bowl-inversion barrier ($E^{\dagger}$), and the maximum and average distance between rim carbons (d(C_{rim}-C_{rim})) for an isolated corannulene molecule computed at B3LYP/ 6-31+G* level of the electronic structure theory. 85

Table 3.1 X-ray structure refinement data for BPTA 140

Table 3.2 Analysis of the ground state electron transfer within the two-state direct coupling method (ES method is HF/6-31+G*). 146

Table 3.3 The ratios of the charge transfer rates and diffusion constants for different geometrical arrangements.....149

Table 3.4 The lowest excitation energies: method LRC-wPBEh/ 6-31+G*/EMPIRICAL- GRIMME3 (dispersion correction) in eV.....151

Table 4.1 X-ray structure refinement data for $C_{22}H_{15}N_5 \cdot (C_6H_6)_{0.5}$. 207

Table 4.2 The Marcus model parameters estimated the direct coupling and energy gap methods.....216

Table 4.3 The lowest optical transition for the COF-fragment,
TCNQ[**COF**]-fragment and 2 stacked COF-fragments calculated
at different theory levels 217

LIST OF FIGURES

Figure 1.1 Molecular structures of corannulene and fullerene 3

Figure 1.2 Corannulene-based oligomer.....5

Figure 1.3 Corannulene-containing nanodots 7

Figure 1.4 Polymer containing corannulene and fullerene 9

Figure 1.5 Fullerene-containing polymer shape transformation by applying an external stimulus (e.g., heat) 11

Figure 1.6 Molecular structures of tetrakiscalix[5]arene, dumbbell-shaped fullerene, and the main-chain fullerene polymer 12

Figure 1.7 MOF/fullerene composite.....17

Figure 1.8 Endohedral fullerene/MOF composite 20

Figure 1.9 Macrocycle/fullerene composite 23

Figure 1.10 Dipyrrolylbenzodiazepine derivatives and fullerene composite.....25

Figure 2.1 Mechanistic pathway to transform corannulene to P-$C_{20}H_{14}$ 48

Figure 2.2 (a) (*left*) Developed route for the preparation of P-$C_{20}H_{14}$ and (*right*) a part of the single-crystal X-ray structure of **1** showing an alternating column of TCNQ and P-$C_{20}H_{14}$. (b) molecular orbitals of TCNQ/P-$C_{20}H_{14}$ in **1**: HOMO-2 and LUMO, related to electron excitation (transition) from P-$C_{20}H_{14}$ to TCNQ, respectively. I Optical transition strength for TCNQ/P-$C_{20}H_{14}$ and TCNQ/$C_{20}H_{10}$.....50

Figure 2.3 (*top left*) Single-crystal X-ray structure of P-$C_{20}H_{14}$. (*bottom left*) Optical transition strengths computed at the ground state optimal geometry for P-$C_{20}H_{14}$ in THF and at the second excited singlet state optimal geometry for P-$C_{20}H_{14}$ in THF. (*right*) Energies and isosurfaces of the HONTO and LUNTO of P-$C_{20}H_{14}$ in the ground and the second singlet excited states. 52

Figure 2.4 (a) (*left top*) Single-crystal X-ray structure of **X**. (*left bottom*) Optical transition strengths computed at the ground state optimal geometry for **X** in THF and at the second singlet excited state optimal geometry for **X** in THF. (*right*) Energies and isosurfaces of the HONTO and LUNTO of **X** in the ground and the second singlet excited states.....53

Figure 2.5 Crystal structure of **1** 88

Figure 2.6 Packing of **1** along the *c*-axis.....89

Figure 2.7 Mass spectrum of **1**.....89

Figure 2.8 Mass spectrum of (corannulene)$_2$·TCNQ 90

Figure 2.9 Normalized emission spectra of **1** and corannulene ($C_{20}H_{10}$) collected on corresponding single crystals.....90

Figure 2.10 Normalized diffuse reflectance spectra of $C_{20}H_{10}$, TCNQ, and **1**.....91

Figure 2.11 Optical transition strengths for the components of (*a*) P-$C_{20}H_{14}$, (*b*) TCNQ, (*c*) $C_{20}H_{10}$, (*d*) TCNQ/P-$C_{20}H_{14}$, (*e*) TCNQ/$C_{20}H_{10}$.....92

Figure 2.12 Optical transition strengths and the corresponding electron couplings for TCNQ/$C_{20}H_{10}$ "stack" with different mutual orientations: (*a*) TCNQ/$C_{20}H_{10}$/TCNQ, (*b*) $C_{20}H_{10}$/ TCNQ, and I TCNQ/$C_{20}H_{10}$.....93

Figure 2.13 Schematic representation of the technique for calculating the electronic component of released energy (*E′*) during planarization of $C_{20}H_{14}$.....94

Figure 2.14 Released energy (*E′*) estimated for the cleavage of various C=C bond in: (*a*) cyclopenta[*bc*]corannulene, (*b*) dicyclopenta[*bc,ef*] corannulene, I tricyclopenta[*bc,ef,kl*]corannulene, (*d*) tetracyclopenta[*bc,ef,hi,kl*]corannulene, and (*e*) half-buckminsterfullerene 94

Figure 2.15 Optimized geometries of three $C_{20}H_{12}$ isomers 95

Figure 2.16 Optimized geometries of three $C_{20}H_{12}^{-\bullet}$ isomers.....95

Figure 2.17 Optimized geometries and molecular electrostatic potential (MEP) maps of $C_{20}H_{11}^{\bullet}$, $C_{20}H_{12}$, and $C_{20}H_{13}^{\bullet}$.....95

Figure 2.18 Estimation of the electronic component of $E_{C–C}$ in $RCH_2–CH_2R$ with R belonging to a pyrene core.....96

Figure 2.19 Estimation of the electronic component of $E_{C–C}$ and released energy in $C_{20}H_{12}$ and $C_{24}H_{14}$. 96

Figure 2.20 Released energy (E') estimated for the cleavage of various C=C bond in: phenanthrene, anthracene, pyrene, coronene, and corannulene.....97

Figure 2.21 Crystal structure of $C_{16}H_{10}·C_{12}H_4N_4$ (pyr·TCNQ) 97

Figure 2.22 ^{1}H NMR and ^{13}C NMR spectra of 1,6,7-trimethylfluoranthene.....98

Figure 2.23 ^{1}H NMR and ^{13}C NMR spectra of 7-ethyl-1,6,10-trimethylfluoranthene.....99

Figure 2.24 ^{1}H NMR and ^{13}C NMR spectra of 5-methylbenzo-[*ghi*]fluoranthene.....100

Figure 2.25 ^{1}H NMR and ^{13}C NMR spectra of 5-ethyl-6-methylbenzo[*ghi*]-fluoranthene.....101

Figure 2.26 Crystal structure of 1,6,7-trimethylfluoranthene 102

Figure 2.27 Crystal structure of 7-ethyl-1,6,10-trimethylfluoranthene 102

Figure 2.28 Crystal structure of 5-methylbenzo[*ghi*]fluoranthene 103

Figure 2.29 Optimized structure of 5-ethyl-6-methylbenzo-[*ghi*]fluoranthene.....103

Figure 2.30 Normalized emission spectra of **X** and **X′** collected on corresponding single crystals.....103

Figure 2.31 (*top*) Normalized absorbance spectrum of 5-methylbenzo [*ghi*]fluoranthene in THF. (*bottom*) Optical transition strengths computed at the ground state, first excited singlet state, second excited singlet state optimal geometry for 5-methylbenzo [*ghi*]fluoranthene in THF.....104

Figure 2.32 (*top*) Normalized absorbance spectrum of 5-ethyl-6-methylbenzo[*ghi*]fluoranthene in THF. (*bottom*) Optical transition strengths computed at the ground state, first excited singlet state, second excited singlet state optimal geometry for 5-ethyl-6-methylbenzo[*ghi*]-fluoranthene in THF 105

Figure 2.33 (*top*) Normalized absorbance spectrum of P-$C_{20}H_{14}$ in THF. (*bottom*) Optical transition strengths computed at the ground state, first excited singlet state, second excited singlet state optimal geometry for P-$C_{20}H_{14}$ in THF.....106

Figure 2.34 Estimation of the electronic component of $E_{C–C}$ in RCH_2 –CH_2R with R belonging to a benzo[*ghi*]fluoranthene core.....106

Figure 3.1 (*top*) Synthesis of **1≡(50%)** including the reaction conditions utilized for azide-alkyne cycloaddition reaction in the solid state. Blue color highlights the moieties participating in CuAAC reaction on molecular species. (*bottom*) Building blocks utilized in a stepwise approach for the development of the CuAAC synthetic conditions applicable for the COF.....117

Figure 3.2 (*left*) FTIR spectra of **1≡(50%)** (black) and πB-$C_{20}H_9N_3$ [**1≡(50%)**]. Gray areas show H–C≡C and C≡C stretches, present in **1≡(50%)** and absent in πB-$C_{20}H_9N_3$[**1≡(50%)**]. (*right*) ^{13}C CP-MAS NMR spectra of **1≡(50%)**, a control experiment with **1≡(50%)**, and πB-$C_{20}H_9N_3$[**1≡(50%)**] 119

Figure 3.3 (a) Normalized diffuse reflectance spectra of πB-$C_{20}H_{10}$@ **1-Ome**, **1-Ome**, πB-$C_{20}H_9N_3$[**1≡(50%)**], and πB-$C_{20}H_{10}$ with corresponding conductivity values. (b) XPS data for the valence band region for πB-$C_{20}H_{10}$@**1-Ome**, **1-Ome**, πB-$C_{20}H_9N_3$ [**1≡(50%)**], and πB-$C_{20}H_{10}$. I Fluorescent decays of πB-$C_{20}H_{10}$ @**1-Ome**, πB-$C_{20}H_9N_3$[**1≡(50%)**], and **1-Ome**. (d) Photographs of **1-Ome**, πB-$C_{20}H_{10}$, and πB-$C_{20}H_{10}$@**1-Ome**. The table shows the amplitude-weighted average lifetimes for **1-Ome**, πB-$C_{20}H_{10}$@ **1-Ome**, and PAHs@**1-OMe**.....122

Figure 3.4 (*top*) Interlayer distance in **1-Ome**. (*bottom*) Selected LUMOs, associated with the ground CT for the three πB-$C_{20}H_{10}$ units in "stack" and "pinwheel" orientations The theory level is LRC-wPBEh/6-31G*.....124

Figure 3.5 ^{1}H NMR and ^{13}C NMR spectra of TAPB in DMSO-d_6 153

Figure 3.6 FTIR spectrum of TAPB. 154

Figure 3.7 ^{1}H NMR spectrum of DMTA in DMSO-d_6.....154

Figure 3.8 ^{13}C NMR spectrum of DMTA in DMSO-d_6.....155

Figure 3.9 ^{1}H NMR spectrum of BPTA in DMSO-d_6. 155

Figure 3.10 ^{13}C NMR spectrum of BPTA in DMSO-d_6 156

Figure 3.11 FTIR spectrum of DMTA.....156

Figure 3.12 FTIR spectrum of BPTA 157

Figure 3.13 Crystal structure of BPTA and packing.....157

Figure 3.14 ^{1}H NMR spectrum of (1*E*,1'*E*)-1,1'-(2,5-dimethoxy-1,4-phenylene)bis(*N*-phenylmethanimine), $C_{22}H_{20}O_2N_2$ 158

Figure 3.15 ^{1}H NMR spectrum of (1*E*,1'*E*)-1,1'-(2,5-bis(prop-2-yn-1-yloxy)-1,4-phenylene)bis(*N*-phenylmethanimine).....158

Figure 3.16 PXRD patterns of **1-Ome**: simulated and experimental.....159

Figure 3.17 FTIR spectrum of **1-Ome**.....159

Figure 3.18 Thermogravimetric analysis plot of **1-Ome**.....160

Figure 3.19 N_2 adsorption isotherm of **1-Ome**.....160

Figure 3.20 PXRD patterns of **1≡(50%)**: simulated and experimental 161

Figure 3.21 Thermogravimetric analysis plot of **1≡(50%)**.....161

Figure 3.22 N_2 adsorption isotherm of **1≡(50%)**.....162

Figure 3.23 FTIR spectrum of **1≡(34%)** 162

Figure 3.24 ^{1}H NMR spectrum of 2,5-bis((1-(2-hydroxyethyl)-1*H*-1,2,3-triazol-4-yl)methoxy)terephthalaldehyde.....163

Figure 3.25 FTIR spectra of BPTA and 2,5-bis((1-(2-hydroxyethyl)-1*H*-1,2,3-triazol-4 yl)methoxy)terephthalaldehyde 163

Figure 3.26 FTIR spectra of **1≡(34%)** and 2-azidoethanol[**1≡(34%)**].....164

Figure 3.27 FTIR spectra of **1≡(34%)** and bis(2-azidoethyl) malonate[**1≡(34%)**.....164

Figure 3.28 FTIR spectra of **1≡(50%)** and dimethyl 5-azidoisophthalate[**1≡(50%)**] 165

Figure 3.29 FTIR spectra of **1≡(50%)** and 1-azidopyrene[**1≡(50%)**] 165

Figure 3.30 PXRD pattern of πB-$C_{20}H_9N_3$[**1≡(50%)**] 166

Figure 3.31 N_2 adsorption isotherm of πB-$C_{20}H_9N_3$[**1≡(50%)**] 166

Figure 3.32 FTIR spectra of **1≡(50%)** and a control experiment involving **1≡(50%)** 167

Figure 3.33 ^{1}H NMR spectrum of digested πB-$C_{20}H_{10}$@**1-OMe** 167

Figure 3.34 PXRD pattern of πB-$C_{20}H_{10}$@**1-OMe**. 168

Figure 3.35 N_2 adsorption isotherm of πB-$C_{20}H_{10}$@**1-OMe** 168

Figure 3.36 Molecular arrangements of πB-$C_{20}H_{10}$ 169

Figure 3.37 Dependence of coupling constants from the distance between πB-$C_{20}H_{10}$ units in the "stack" arrangement 169

Figure 3.38 Selected LUMOs, associated with the ground state electron transport, for the three-unit πB-$C_{20}H_{10}$ 170

Figure 3.39 (a) XPS data for the valence band region for πB-$C_{20}H_{10}$ and πB-$C_{20}H_9N_3$[**1≡(50%)**]. (b) Simulated density of states for the valence band for the "stack" and "pinwheel" orientation of four πB-$C_{20}H_{10}$ units 170

Figure 3.40 Decomposition of the lowest excited singlet state for the 4-unit geometry. 171

Figure 3.41 X-ray photoelectron spectroscopy data for the C(1s) region for: πB-$C_{20}H_{10}$@**1-OMe**, **1-Ome**, πB-$C_{20}H_9N_3$[**1≡(50%)**], and πB-$C_{20}H_{10}$ 171

Figure 4.1 (*top*) Development of reaction conditions utilizing molecular TCNQ moieties for the [2+2] cycloaddition reaction, followed by ring opening of a strained cyclobutene intermediate. (*middle*) The 1,3-cycloaddition and [2+2] cycloaddition reactions, followed by ring opening of a strained cyclobutene intermediate in the case of the latter, for integration of fullerene and TCNQ moieties, respectively. (*bottom*) Integration of a fluorescent tag using Sonogashira cross-coupling reaction 180

Figure 4.2 (a) FTIR spectra of **1≡(34%)** and NEM-C_{60}[**1≡(34%)**]. (b) ^{13}C CP-MAS NMR spectra of **1≡(34%)**, a control experiment with **1≡(34%)**, and NEM-C_{60}[**1≡(34%)**]. I Fluorescent decays of **1≡(34%)**, NEM-C_{60}[**1≡(34%)**] and TCNQ[**1≡ (50%)**]. (d) XPS data for the valence band region for **1≡(34%)**, C_{60}, and NEM-C_{60}[**1≡ (34%)**] 182

Figure 4.3 (a) FTIR spectra of **1≡(34%)** and TCNQ[**1≡(50%)**]. (b) ^{13}C CP-MAS NMR spectra of **1≡(34%)** and TCNQ[**1≡(50%)**]. I Normalized diffuse reflectance spectra of **1≡(34%)**, C_{60}, NEM-C_{60}[**1≡(34%)**], TCNQ, and TCNQ[**1≡(50%)**]. (d) Photographs of **1≡(x%)**, NEM-C_{60}[**1≡ (34%)**], and TCNQ[**1≡(50%)**]. (e) The optical transition strength calculated for the COF-fragment and TCNQ**[COF]**-fragment and the corresponding electron transfer rates. (f) Schematic representation of the frontier orbitals for the truncated molecular model comprised of the TCNQ**[COF]**-fragment.....186

Figure 4.4 ^{1}H NMR spectrum of 2-azidoethanol in DMSO-d_6 and ^{13}C NMR spectrum of 2-azidoethanol in $CDCl_3$ 218

Figure 4.5 ^{1}H NMR and ^{13}C NMR spectra of NEM in $CDCl_3$ 219

Figure 4.6 FTIR spectrum of 2-azidoethanol.....219

Figure 4.7 FTIR spectrum of NEM.....220

Figure 4.8 FTIR spectrum of NEM-C_{60}. 220

Figure 4.9 FTIR spectra of **1≡(34%)** and 2-azidoethanol[**1≡(34%)**].....221

Figure 4.10 PXRD pattern of **1≡(34%)** and simulated pattern.....221

Figure 4.11 WAXS pattern of **1≡(34%)**. 222

Figure 4.12 WAXS pattern of NEM-C_{60}[**1≡(34%)**].....222

Figure 4.13 Thermogravimetric analysis plot of **1≡(34%)**.....223

Figure 4.14 FTIR spectra of **1≡(34%)** and a control experiment involving **1≡(34%)** 223

Figure 4.15 X-ray crystal structure of $C_{22}H_{15}N_5$.....224

Figure 4.16 ^{1}H NMR (*top*) and ^{13}C NMR (*bottom*) spectra of 2-(4-(4,4-dicyano-2-(4-(dimethylamino)phenyl)butylidene)cyclohexa-2,5-dien-1-ylidene)malononitrile in CD_2Cl_2 225

Figure 4.17 . ^{1}H NMR (*top*) and ^{13}C NMR (*bottom*) spectra of 4-(□etraanion-2-ylethynyl)-*N,N*-dimethylaniline in $CDCl_3$ 226

Figure 4.18 N_2 adsorption isotherm of **1≡(34%)**. 227

Figure 4.19 N_2 adsorption isotherm of NEM-C_{60}[**1≡(34%)**] 227

Figure 4.20 N_2 adsorption isotherm of TCNQ[**1≡(50%)**] 228

Figure 4.21 Cyclic voltammogram of C_{60} with 0.1 M tetrabutylammonium hexafluorophosphate and 0.5 mM analyte in DMF with a scan rate of 0.1 V 228

Figure 4.22 Cyclic voltammogram of TCNQ with 0.1 M tetrabutylammonium hexafluorophosphate and 0.5 mM analyte in ACN with a scan rate of 0.1 V 229

Figure 4.23 Cyclic voltammogram of NEM-C_{60} with 0.1 M tetrabutylammonium hexafluorophosphate and 0.5 mM analyte in DMF with a scan rate of 0.1 V 229

Figure 4.24 Cyclic voltammogram of NEM-C_{60}[**1≡(34%)**] with 0.1 M tetrabutylammonium hexafluorophosphate in DMF with a scan rate of 0.1 V 230

Figure 4.25 Normalized emission spectra of 2-bromoanthracene and anthracene[**1≡(50%)**] (λ_{ex}= 365 nm) in the solid state 230

Figure 4.26 Normalized diffuse reflectance and emission spectra of 6-bromo-3-cyano-4-methylcoumarin, and normalized emission spectrum of 4-methyl-2-oxo-2*H*-chromene-3-carbonitrile[**1≡(50%)**] (λ_{ex}= 365 nm) 231

Figure 4.27 Normalized diffuse reflectance and emission spectra of 2-bromoanthracene@TCNQ[**1≡(50%)**], and normalized diffuse reflectance and emission spectra of anthracene[**1≡(50%)**] 231

Figure 4.28 Normalized diffuse reflectance and emission spectra of 6-methyl-3-cyano-4-methylcoumarin@TCNQ[**1≡(50%)**] and normalized diffuse reflectance and emission spectra of 4-methyl-2-oxo-2*H*-chromene-3-carbonitrile[**1≡(50%)**] (λ_{ex}= 365 nm) 232

Figure 4.29 Normalized emission spectrum of anthracene[**1≡(50%)**] (λ_{ex}= 365 nm) in the solid state 232

Figure 4.30 Normalized emission spectra of [**1≡(50%)**], TCNQ[**1≡(50%)]**, and NEM-C_{60}[**1≡(34%)**] (λ_{ex}= 365 nm) in the solid state.....233

Figure 4.31 PXRD patterns of: 4-methyl-2-oxo-2*H*-chromene-3-carbonitrile[**1≡(50%)**], anthracene[**1≡(50%)**], 2-bromoanthracene@TCNQ[**1≡(50%)**], 6-methyl-3-cyano-4-methylcoumarin@TCNQ[**1≡(50%)**], and TCNQ[**1≡(50%)**].....233

Figure 4.32 FTIR spectra of [**1≡(50%)**] and anthracene[**1≡(50%)**] 234

Figure 4.33 FTIR spectra of [**1≡(50%)**] and 4-methyl-2-oxo-2*H*-chromene-3-carbonitrile [**1≡(50%)**] 234

Figure 4.34 FTIR spectra of 2-bromoanthracene@TCNQ[**1≡(50%)**] 235

Figure 4.35 ^{1}H NMR spectrum of digested SP@[**1≡(0%)**].....235

Figure 4.36 Photoisomerization of the spiropyran derivatives 236

Figure 4.37 Tauc plots for C_{60}, **1≡(34%)**, and NEM-C_{60}[**1≡(34%)**] 236

Figure 4.38 Tauc plots for TCNQ, **1≡(34%)**, and TCNQ[**1≡(50%)**].....236

Figure 4.39 Geometries a-e are considered truncated models for the COF theoretical modeling.....237

Figure 4.40 Two models for TCNQ bonding within the COF: (*top left*) TCNQ in every layer and (*top right*) TCNQ in every second layer. 238

Figure 4.41 Optical transition strengths for TCNQ, COF-fragment, and TCNQ[**COF**]-fragment.....239

Figure 4.42 (*top left*) HOMO and (*top right*) LUMO orbitals for the TCNQ[**COF**]-fragment. (*bottom*) LUMO orbital for 2 stacked COF-fragments 239

LIST OF SCHEMES

Scheme 2.1 (*top*) A schematic representation of π-bowl (corannulene) opening through a solid-state route. Single-crystal X-ray structure of corannulene (*left*) and X-ray structure of 5,6-dimethyl-benzo[*ghi*] fluoranthene (P-$C_{20}H_{14}$) ("open" corannulene, *right*). (*bottom*) Strain energy (E_s, purple) and released energy (E', red) as a function of PAH (*left to right*) phenanthrene, anthracene, pyrene, coronene, and corannulene 44

Scheme 2.2 Synthesis of 5-methylbenzo[*ghi*]fluoranthene 56

Scheme 2.3 Synthesis of 5-ethyl-6-methylbenzo[*ghi*]fluoranthene.....60

Scheme 2.4 E_s (purple) and E' (red) as a function of carbon π-bowls for the PAHs: corannulene, cyclopenta[*bc*]corannulene, dicyclopenta-[*bc*,*ef*]corannulene, tricyclopenta[*bc*,*ef*,*kl*] corannulene, tetracyclopenta-[*bc*,*ef*,*hi*,*kl*]corannulene, and half-buckminsterfullerene 81

Scheme 3.1 (*left*) Schematic representation of πB organization inside the crystalline framework through 1,3-cyloaddition. (*right*) Delocalization of πB molecular orbitals associated with ground state charge transport 115

Scheme 3.2 Synthesis of 1,3,5-tri-(4-aminophenyl) benzene 126

Scheme 3.3 Synthesis of 2,5-dimethoxyterephthalaldehyde and 2,5-bis(2-propynyloxy) terephthalaldehyde 127

Scheme 3.4 Synthesis of (1*E*,1'*E*)-1,1'-(2,5-dimethoxy-1,4-phenylene)bis(*N*-phenylmethanimine), $C_{22}H_{20}O_2N_2$ 129

Scheme 3.5 Synthesis of (1*E*,1'*E*)-1,1'-(2,5-bis(prop-2-yn-1-yloxy)-1,4-phenylene)bis(*N*-phenylmethanimine), $C_{26}H_{20}O_2N_2$ 130

Scheme 3.6 Synthesis of πB-$C_{20}H_9N_3$ 132

Scheme 3.7 Synthesis of 2,5-bis((1-(2-hydroxyethyl)-1*H*-1,2,3-triazol-4-yl)methoxy)terephthalaldehyde, $C_{18}H_{20}O_6N_6$.....133

Scheme 3.8 Synthesis of 2-azidoethanol[**1≡(34%)**].....134

Scheme 3.9 Synthesis of bis(2-azidoethyl) malonate[**1≡(34%)**].....134

Scheme 3.10 Synthesis of dimethyl 5-azidoisophthalate[**1≡(50%)**].....135

Scheme 3.11 Synthesis of 1-azidopyrene[**1≡(50%)**].....136

Scheme 3.12 Synthesis of πB-$C_{20}H_9N_3$[**1≡(50%)**].....136

Scheme 4.1 (*left*) Donor-acceptor alignment inside of a porous well-defined organic framework resulting in conductivity enhancement. (*right*) The cyclic voltammetry curve of crystalline porous material with embedded electron-accepting moieties TCNQ[**1≡(34%)**].....178

Scheme 4.2 Synthesis of **NEM-C_{60}**.....191

Scheme 4.3 Synthesis of TCNQ[**1≡(x%)**], where *x* = 34, 50, and 100.....197

Scheme 4.4 Atomic definition for the TCNQ-[**COF**] fragment.....213

CHAPTER 1

GRAPHITIC SUPRAMOLECULAR ARCHITECTURE'S BASED ON CORANNULENE, FULLERENE, AND BEYOND

Leith, G. A. and Shustova, N. B. *Chem. Comm*. **2021**, *57*, 10125–10138.

INTRODUCTION

Over the past five years, there has been an influx of interest in expanding the realm of carbon-rich chemistry, with a focus on corannulene ($C_{20}H_{10}$, buckybowls) and fullerene (C_{60}, buckyballs) in particular (Figure 1.1).[1–16] Significant advancements in the preparation of fullerene and corannulene (the smallest subunit of fullerene that retains its curvature) have been made since the advent of these new forms of carbon in 1985 and 1966, respectively.[17–21] Due to these synthetic improvements, the translation from their preparation in the laboratory to practical real-world applications became plausible. The curved structures of buckybowls and buckyballs endow the carbon architectures with interesting physicochemical, electrochemical, and electronic properties.[22–26] Due to the low-lying lowest unoccupied molecular orbital (LUMO) and unique curved surface, fullerenes and their derivatives have been used as electron-accepting units in a variety of applications ranging from supercapacitors and electrodes to drug delivery systems. [27–30] For instance, fullerene, C_{60}, can reversibly accept and stabilize up to six electrons on its surface, forming a stable hexaanion,[31,32] and therefore, could significantly affect the material electronic properties by promoting efficient charge and energy transfer (CT and ET, respectively).[31,32] However, one of the challenges in fullerene chemistry is that the synthesis of buckyballs and their derivatives relies on high performance liquid chromatography (HPLC) purification. At the same time, corannulene, $C_{20}H_{10}$, can be prepared in a traditional laboratory setting on a kilogram scale, without the involvement of labor-intensive chromatographic purification.[21] Similar to fullerene, corannulene can reversibly accept and stabilize up to four electrons on its surface, forming a stable

tetraanion. The $C_{20}H_{10}$ molecule also possesses a significant dipole moment (2.1 D), while exhibiting tunable photophysical properties as a function of π-bowl derivatization. [23,33–35]

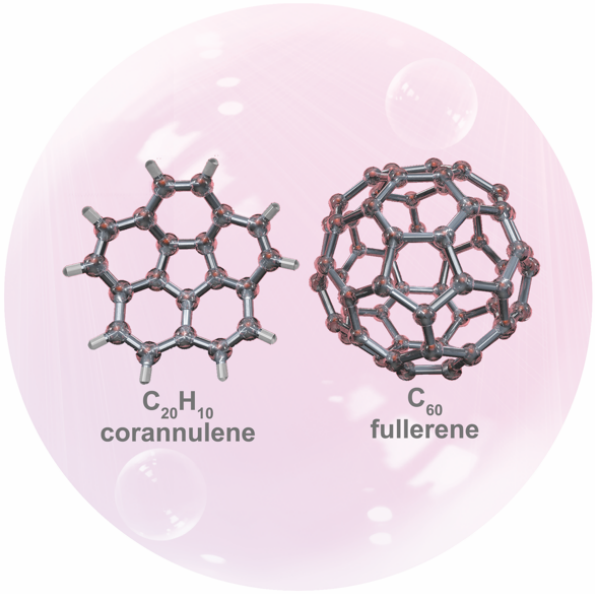

Figure 1.1 Molecular structures of (*left*) corannulene, $C_{20}H_{10}$, and (*right*) fullerene, C_{60}.

Overall, exploration of fulleretic assemblies has resulted in the discovery of larger buckybowl molecules,[36] design of nanographene-like materials,[5,17,36–41] and the formation of a carbon-based nanocone[42]. In addition to synthetic efforts, computational modelling has also predicted the formation of unique classes of innovative carbon structures,[43–45] provided strategies for enhancing nonlinear optical responses, and outlined routes for efficient intermolecular CT in carbon-based materials.[46,47] Due to a plethora of studies in the field of graphitic materials,[8,22,23,48,49] this Feature Article aims to shed light on the expansion of corannulene- and fullerene-based supramolecular motifs and extended architectures solely over the past five years. The main goal of this Feature Article is not to provide an all-inclusive review of fulleretic materials, but rather to highlight the most prominent trends and latest significant advances in the field.

This section will cover several advances in the field of corannulene- and fullerene-containing oligomers and polymers during the last five years. Notably, this section does not detail all discoveries in the corannulene- and fullerene-containing oligomer and polymer field, but instead brings attention to fundamental structural discoveries and harnessing the unique properties of fullerene- and corannulene-based materials.

In 2017, a family of discrete π-conjugated oligomers, containing corannulene I and thiophene (T) units connected with each other through an acetylene linkage, was reported by Stuparu and co-workers (Figure 1.2).[57] The properties of the prepared oligomers, C_1T_1, C_2T_1, C_3T_2, and C_4T_3, were probed as a function of the oligomer length. As a result, a significant bathochromic shift in the oligomer absorption profile, upon increasing the chain length, was detected. For example, one of the main absorption bands in the spectrum of C_1T_1 possessed λ_{max} at 370 nm, while in the absorption spectrum of C_3T_2, λ_{max} was shifted to 450 nm.[57] The density functional theory (DFT) calculations corroborated the experimental results by demonstrating a decrease in the highest occupied molecular orbital (HOMO)-LUMO gap upon increasing the oligomer length. In addition, corannulene-containing oligomers with longer chains (e.g., C_3T_2) possessed a relatively high quantum yield of 40% (C_3T_2) in solution, a large two-photon absorption cross-section of 600 GM, and two-photon-excited bright luminescence, providing an avenue for further investigations of these materials for nonlinear optics applications.

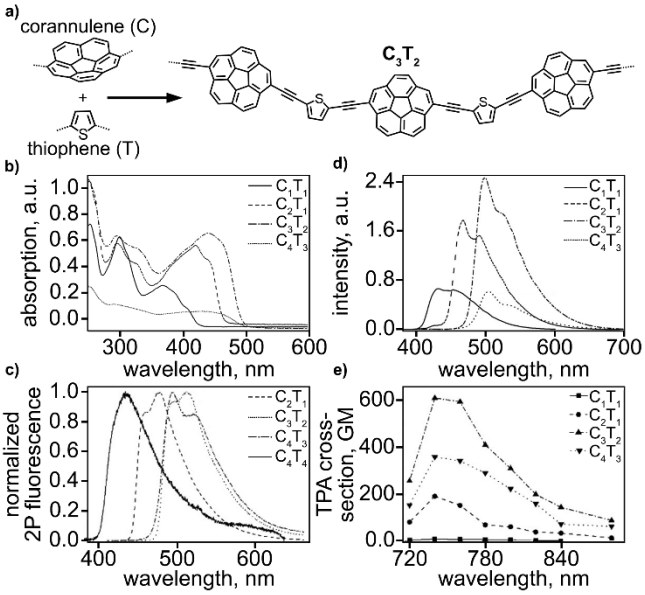

Figure. 1.2 (a) Schematic representation of C_3T_2 synthesis. (b) UV-vis absorption spectra of oligomers in chloroform (4×10^{-4} M). © Two-photon excited emission of oligomers in chloroform (4×10^{-4} M). (d) Emission spectra of oligomers in chloroform (4×10^{-4} M, λ_{ex} = 370 nm). (e) Two-photon action spectra of oligomers in chloroform.

The first examples of amorphous corannulene-based polymers were designed by the Smaldone group.[9] These materials were prepared through Sonogashira copolymerization of tetrabromocorannulene with monomers containing terminal alkyne groups such as 1,4-diethynylbenzene, 1,3,5-trisethynylbenzene, or tetra(4-ethynylphenyl)methane.[9] To probe the effect of π-bowl curvature on the possibility of gas adsorption, the authors examined the prepared corannulene-based materials for carbon dioxide uptake. The highest gas uptake measured for these polymers was found to be 57 $cm^3\ g^{-1}$ (11.7 wt%) at 273 K (and 900 mmHg), that is comparable (and even surpassed) the uptake of CO_2 observed by several porous organic materials such as COF-5 (7.4 wt%)[58], COF-103 (7.6 wt%)[58], or BLP-1H (7.4 wt%)[59].

In a similar vein, Stuparu and co-workers synthesized an amorphous polymer from a corannulene-based oxa-norbornadiene monomer using ring-opening metathesis polymerization.[60] This polymer possessed an average pore size of 1.4 nm and a surface area of 49 m^2 g^{-1}. The prepared polymer also displayed a high specific capacitance value of 134 F g^{-1} at 0.5 A g^{-1} (1.0 V voltage window) measured in a three-electrode cell configuration. In the asymmetric supercapacitor, the prepared corannulene-based material was utilized as the positive electrode, while activated carbon was employed as the negative electrode. This corannulene-based supercapacitor displayed good cyclability with 90% capacitance retention after 10,000 cycles. Overall, this work was one of the first studies that outlined the previously proposed potential[3,9,27,28,61] of using corannulene-based polymers as electrochemical storage components. In line with these studies, it is important to mention Petrukhina's pioneering work focusing on tetrareduced corannulene bowls, $C_{20}H_{10}^{4-}$, with intercalated alkali metals.[62–65] In these studies, corannulene tetraanions were shown to self-assemble with multiple alkali metal cations into unique sandwich-type aggregates.[63] For instance, these investigations revealed the formation of triple-decker sandwiches containing high nuclearity $(Li_3M_3)^{6+}$ (M = K, Rb, and Cs) species between two tetrareduced corannulene decks.[63] Notably, two interior lithium ions within the $(Li_3M_3)^{6+}$ sandwiches could be replaced with larger alkali metals, resulting in $(LiM_5)^{6+}$ (M = K and Rb) motifs. However, the central lithium ion, trapped within the sandwich, stayed intact during the transmetallation procedure. Overall, these results could be used as a foundation for further understanding the lithium storage processes in carbonaceous materials.

Corannulene- and fullerene-containing nanomaterials have also been studied as potential candidates for biomedical applications.[30,66–68] For instance, a strategy developed by Tang and co-workers in 2018 led to the fabrication of corannulene-based aggregation-induced-emission (AIE) "dots" (Cor-AIE dots) for cancer phototheranostics (Figure 1.3).[67] These corannulene-containing dots were constructed from 4-(2,2-bis(4-(diphenylamino)phenyl)-1-(4-methoxyphenyl)vinyl)-1-methylpyridinium hexafluorophosphate (TPP-

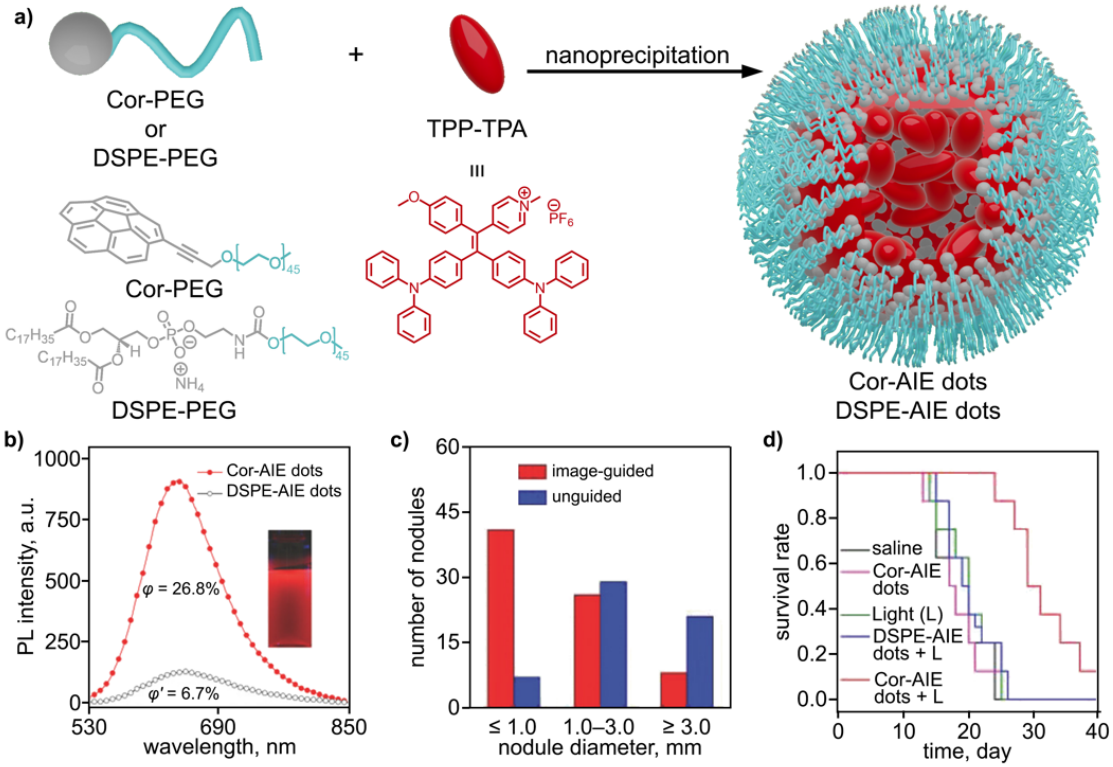

Figure 1.3 (a) Schematic representation of the synthetic procedure used for Cor-AIE and DSPE-AIE dots. (b) Photoluminescence lifetime spectra collected for Cor-AIE and DSPE-AIE dots (λ_{ex} = 500 nm). Inset shows a photo of fluorescent Cor-AIE dots under λ_{ex} = 365 nm. (c) Histogram of nodule diameters extracted from unguided and Cor-AIE-guided groups. (d) The curve of mice survival rates after different treatments using "saline," "Cor-AIE dots," "light (L)," "DSPE-AIE dots + L," and "Cor-AIE dots + L." "L" indicates exposure under a white light (0.4 W cm^{-2}) for 10 minutes.

TPA) and corannulene-decorated polyethylene glycol (Cor-PEG). For accurately comparing the properties, analogous DSPE-AIE dots (without the inclusion of corannulene

moieties) were constructed from the same linker, TPP-TPA, and 1,2-distearoyl-*sn*-glycero-3-phosphoethanolamine-*N*-[methoxy(polyethylene glycol)-2000] (DSPE-PEG). The following assessment of the two materials revealed that the Cor-AIE dots possessed a 4-fold greater fluorescence quantum yield and a 5.4-fold enhanced production of reactive oxygen species, in contrast to the DSPE-AIE dots. The authors hypothesized that the observed enhanced properties could be attributed to the presence of corannulene moieties in the dots. The corannulene molecules provided intraparticle rigidity and restricted intramolecular rotation of the TPP-TPA fragments, thus suppressing nonradiative decay pathways.[67] To demonstrate that the prepared fluorescent Cor-AIE material could be utilized for image-guided cancer surgery, mice with cancerous tissue were injected with the Cor-AIE dots. During *in vivo* NIR fluorescence studies, utilized for identification of the cancerous tissue during surgery, the Cor-AIE dots exhibited a very strong fluorescent response. After the Cor-AIE dot-guided surgery, 70% of the treated mice survived, while a 0% survival rate was reported for non-Cor-AIE-guided surgery. Thus, these results demonstrate the advantages and perspectives of employing fluorescent corannulene-based dots for *in vivo* NIR fluorescence image-guided surgery.

In 2021, Stuparu and co-workers investigated the formation of a biomedically relevant micellar structure possessing a corannulene-based fullerene-loaded core and a PEG shell (Figure 1.4).[66] In these materials, the core is made up of a host polymer, containing corannulene moieties, that assembled with fullerenes due to the favorable interactions between concave and convex aromatic surfaces. As shown in Figure 1.4, the host polymer block backbone has several corannulene moieties attached, allowing for

structural accommodation of fullerenes of different sizes, such as C_{60} and C_{70}, in the micellar core. Of fullerene, followed by polymer assembly and cross-linking to "lock in"

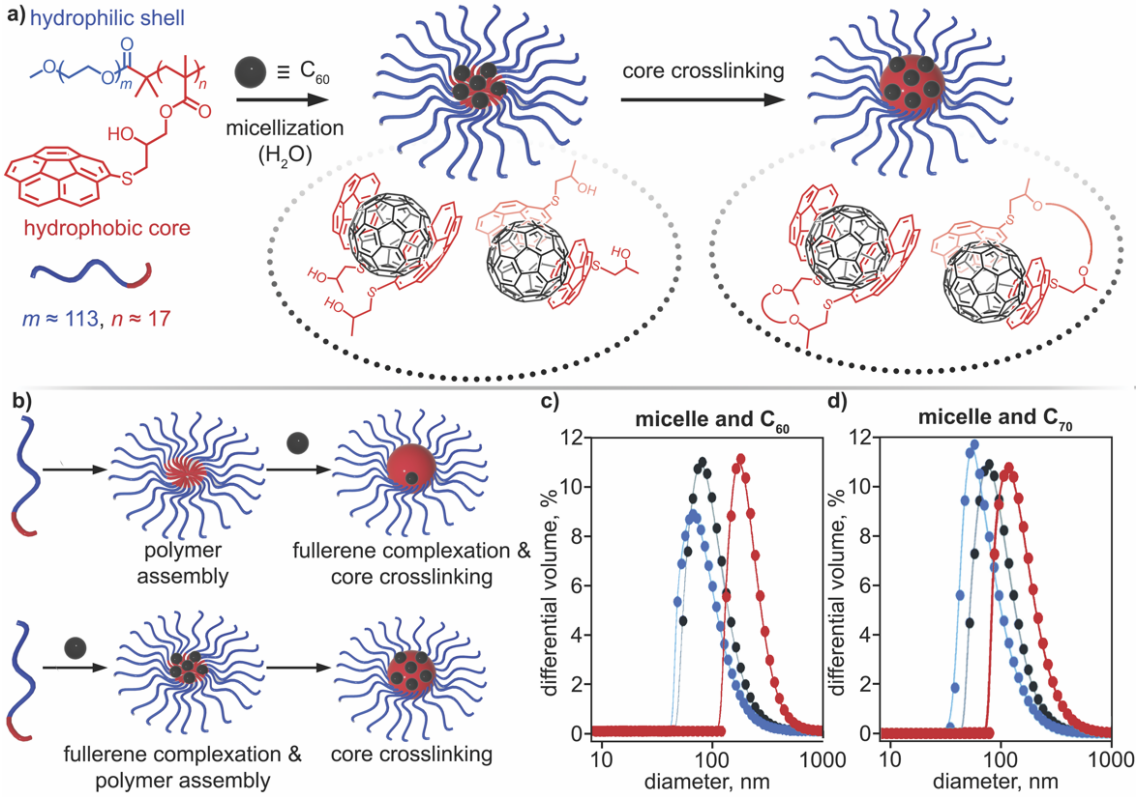

Figure 1.4 (a) Chemical structure of host polymer with corannulenes and its assembly with fullerene through ball-and-socket interactions resulting in formation of micellar nanoparticles. (b) Two approaches for encapsulating fullerene into the host polymer micelle. (c) Dynamic light scattering (DLS) data for block copolymer micelles and C_{60} before cross-linking in water (black) and after cross-linking in water (blue) and after cross-linking in DMF (red). (d) DLS data for block copolymer micelles and C_{70} before cross-linking in water (black) and after cross-linking in water (blue) and after cross-linking in DMF (red).

The fullerene molecules, resulting in core-crosslinked nanoparticles (Figure 1.4). This approach led to approximately 8 wt% of fullerene loading into the nanoparticles. Dynamic light scattering (DLS) studies were conducted to evaluate the micellar size and stability of the prepared nanoparticles. After cross-linking of the core, the micellar size was determined to be about 30 nm, and the prepared nanoparticles exhibited chemical stability at two measured pHs of 2.5 and 7.4.[66] Further investigations of "concave-convex"

corannulene and fullerene assemblies could help to build a foundation for preparation of stable bionanomaterials for the detection and mediation of chronic or acute diseases.

Haino and co-workers recently explored a supramolecular approach for merging fullerene and polymer areas.[69,70] In 2020, they created shape-transformable polymers based on calix[5]arenes, a macrocyclic molecule with a large cavity, that could bind fullerene-terminated polymethyl methacrylate (PMMA) via calixarene-fullerene complexation (Figure 1.5).[69] The fullerene-terminated PMMA facilitated the formation of three unique shapes through assembling the macrocyclic host (linear ditopic, **2**, or branched tritopic, **3**) with fullerene-terminated PMMA in solution. Upon combining, the fullerene-terminated PMMA to either the linear ditopic or the branched tritopic calix[5]arene hosts, emission from the host was efficiently quenched. The authors hypothesized that the observed quenching occurred due to fullerene integration that is in line with previous literature reports.[71] The complexation of calixarene and fullerene was verified by size-exclusion chromatography and diffusion-ordered NMR spectroscopy.[69] To summarize, these results provided evidence that employing a supramolecular approach to shape-transformable polymers can allow for access to three distinct polymer shapes, and offers the foundation for fabricating stimuli-responsive fullerene-based materials.

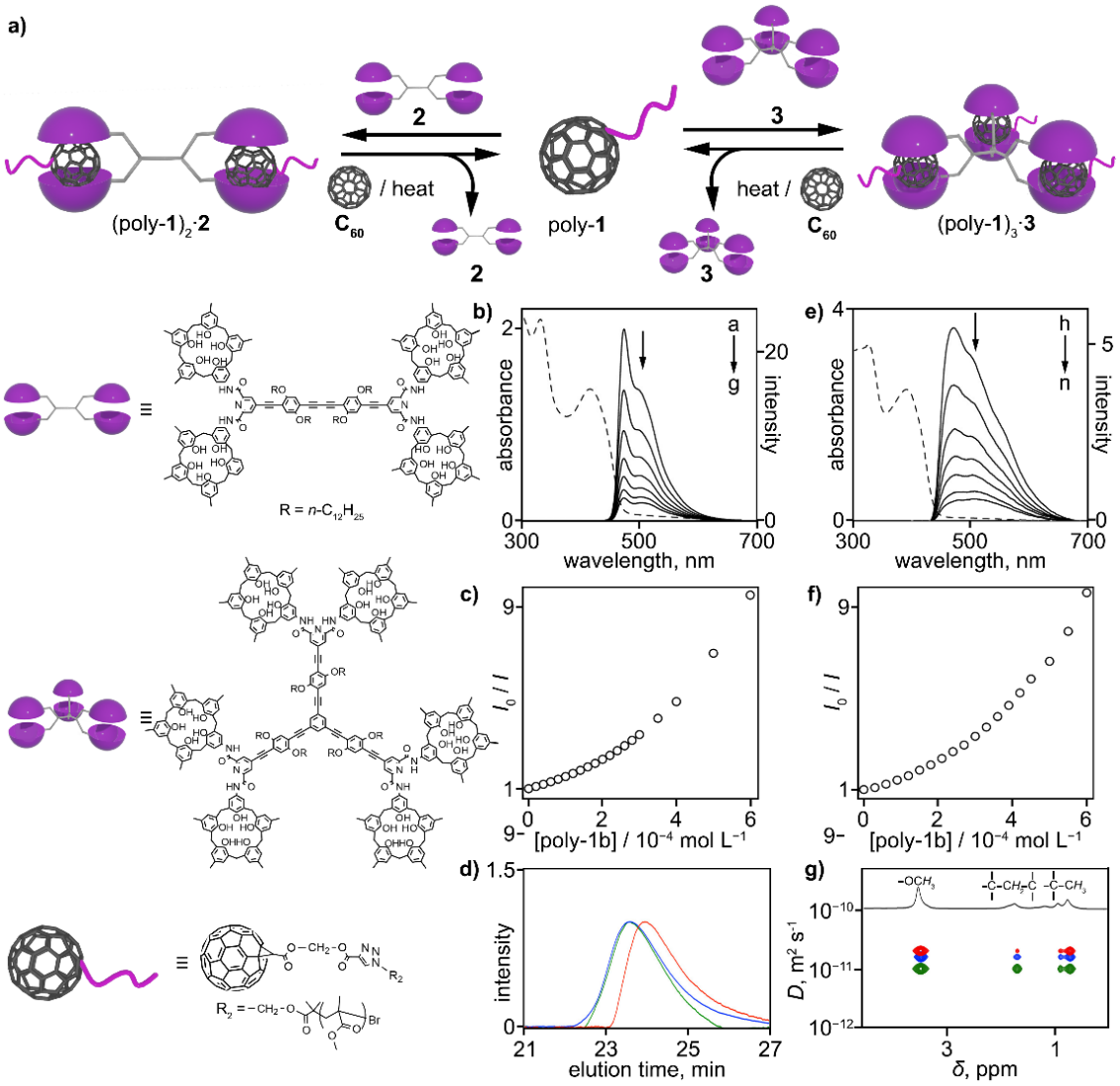

Figure 1.5 (a) Schematic representation of polymer shape transformation by applying an external stimulus (e.g., heat). Changes in the fluorescence spectra of (b) **2** (1.0×10^{-4} mol L^{-1}, λ_{ex} = 420 nm) and (e) **3** (2.0×10^{-5} mol L^{-1}, λ_{ex} = 400 nm) upon the addition of poly-**1b**. The dashed line indicates the absorption spectrum of (b) **2** or (e) **3** (2.0×10^{-5} mol L^{-1}). Stern-Volmer plots for (c) **2** and (f) **3** in the presence of poly-**1c**. (d) Size-exclusion chromatogram of poly-**1b** (red line), a 1:2 mixture of poly-**1b** and **2** (blue line), and a 1:3 mixture of poly-**1b** and **3** (green line) in toluene. (g) Diffusion coefficients (D) of poly-**1b**, as inferred from diffusion-ordered NMR measurements in chloroform-*d*. The red, blue, and green lines denote the spectra obtained from poly-**1b**, a 2:1 mixture of poly-**1b** and **2**, and a 3:1 mixture of poly-**1b** and **3**, respectively.

In a follow-up study, the same group endeavored to create a main-chain fullerene-based polymer.[70] The authors achieved this through a helically-organized-fullerene array

made by polymerizing a chiral ditopic tetrakiscalix[5]arene host with a dumbbell-shaped fullerene (Figure 1.6). The association between the chiral hosts and the fullerene led to a

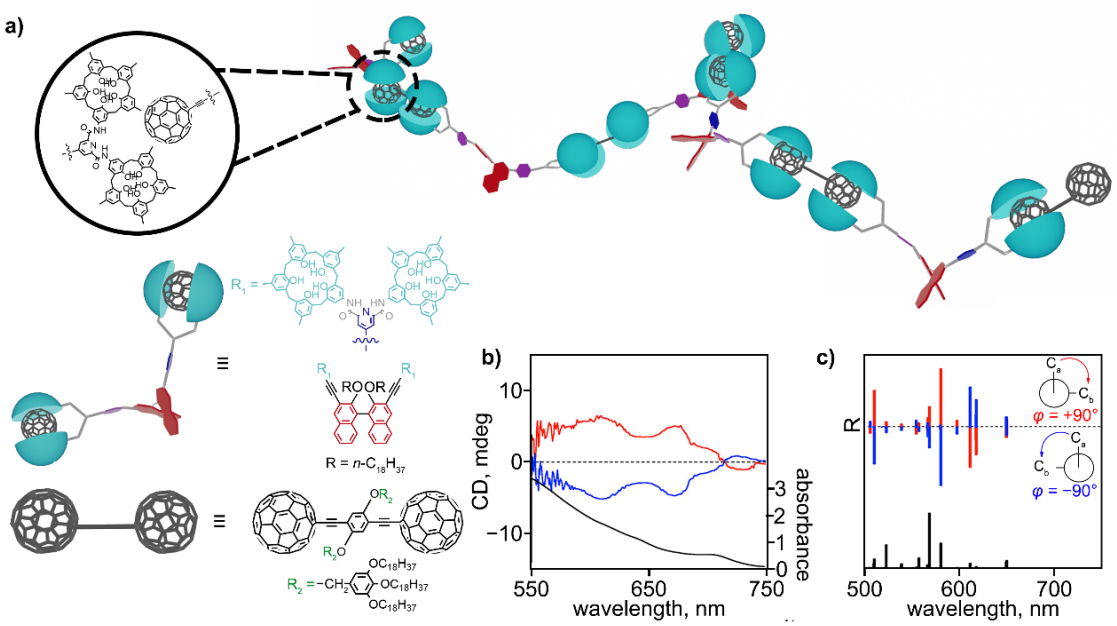

Figure 1.6 (a) Molecular structures of tetrakiscalix[5]arene (teal), dumbbell-shaped fullerene (black), and the main-chain fullerene polymer. (b) Circular dichroism (CD) spectra of 1:1 mixture of (red) *R*-tetrakiscalix[5]arene (1.0×10^{-2} mol L^{-1}) and dumbbell-shaped fullerene (1.0×10^{-2} mol L^{-1}) and (blue) (*S*)-tetrakiscalix[5]arene (1.0×10^{-2} mol L^{-1}) and dumbbell-shaped fullerene (1.0×10^{-2} mol L^{-1}) at 278 K. The black line denotes the UV-vis absorption spectrum of a 1:1 mixture of ©-tetrakiscalix[5]arene (1.0×10^{-2} mol L^{-1}) and dumbbell-shaped fullerene (1.0×10^{-2} mol L^{-1}) at 278 K. (b) Calculated CD and UV-vis absorption spectra of a model compound with a dihedral angle (φ)of ±90°.

Sizable supramolecular polymer with a degree of polymerization exceeding 32. The prepared material was investigated by circular dichroism spectroscopy, and these studies demonstrated that the major transitions from 650 to 500 nm were associated with π–π* fullerene derivative transitions. This successful design of the fullerene-containing polymer could be just the tip of the iceberg for the formation of new functional polymeric materials.

The presented papers in the section of fullerene- and corannulene-based materials only provides a general overview on the progress made in the past five years in this community. Thus, several reports have harnessed the advantages of flexible polymer

materials for manipulating and restricting fullerene molecules, whether that is within the polymer chain itself or with the assistance of a host. The applications of these materials are far-reaching, promoting advances in biomedical, gas adsorption, and stimuli-responsive material research areas.

Merging the properties of buckybowl and buckyball molecules with extended crystalline organic scaffolds such as covalent-organic frameworks (COFs) is an area that has only recently started to be explored. Several studies have demonstrated that two-dimensional (2D) COFs can be used as templates for controlling the structural arrangement of fulleretic guest molecules including corannulene and fullerenes, C_{60} or C_{70}.[72–75] For instance, Bein and co-authors designed the first COF-based fullerene-containing UV-to-NIR-responsive photodetector.[76] For that, [6,6]-phenyl C_{71} butyric acid methyl ester ($PC_{71}BM$) was spincoated onto a layer of COF that was deposited on a MoO_x surface of indium tin oxide-coated glass substrate. The resulting interdigitated heterojunction acted as the active layer in a voltage-switchable photodetector. At 0 mV bias, the photodetector displayed sensitivity toward blue and red light, while it did not exhibit any sensitivity toward green and NIR light. However, an increase in the reverse bias led to a decrease in the relative and absolute intensities in the blue and red spectral regions, and an increase in the green and NIR regions. Thus, nearly complete inversion of spectral sensitivity was achieved, providing a pathway forward for applications of these materials in the information technology or spectral imaging sectors.

The electronic properties of buckybowl- and buckyball-integrated COFs were probed by Shustova and co-workers over the last four years.[77,78] In 2018, the Shustova research group designed the first example of a donor-acceptor (D-A) COF in which the

buckybowl was integrated through (i) coordinative immobilization using a copper-catalyzed azide-alkyne cycloaddition (CuAAC) and (ii) non-coordinative encapsulation.[77] The selected parent COF possesses a pore aperture of 33 Å, that was sufficient for integration of bulky corannulene derivatives (with a diameter of ~6.6 Å). According to time-resolved and steady-state spectroscopic studies, CT between corannulene units and the COF matrix was detected.[77] Changes in the electronic profile of the prepared corannulene-containing COFs were surveyed by estimating the optical band gaps and performing bulk conductivity measurements. A decrease in the optical band gaps from 2.24 eV (the parent COF) to ~1.94 eV (for corannulene-integrated COFs) was reported, that was in line with the results from the conductivity measurements. Indeed, four-orders-of-magnitude and seven-orders-of-magnitude conductivity enhancement were observed for the COF that contained corannulene guest molecules and the framework with coordinatively-incorporated corannulene moieties, respectively. CT rate as a function of mutual corannulene orientation was evaluated through application of the Marcus theory. Within this model, the authors reported that a shift from noncolumnar organization (e.g., as a guest) to a 1D stack of corannulene molecules (e.g., covalently tethered to the COF) could result in a *ca.* 42-fold increase in conductivity. In a follow-up report, Shustova and co-workers targeted incorporation of a bulkier fulleretic molecule, fullerene C_{60}, inside the same COF matrix.[78] In a similar way to the previous synthesis of corannulene-containing COF, they covalently tethered the bulky fullerene building block to the decorated COF walls, allowing for promotion of D-A alignment. Due to this favorable interaction between donor (parent COF) and acceptor (fullerene moiety), a six-orders-of-magnitude conductivity enhancement in the fullerene-integrated COF versus the parent COF was

detected. Due to the integration of redox-active building blocks, C_{60} derivatives, the authors were able to perform electrochemical studies. Their investigations demonstrated an unrevealed potential for the utilization of fullerene-containing COFs for the development of electroactive multidimensional crystalline materials.

The field of fulleretic COFs remains in its infancy with a plethora of investigations yet to take place. Although the work discussed in this section has laid a solid foundation for future efforts to build upon, the current reports are primarily dominated by acquiring fundamental knowledge and pursuing electronic property investigations. Currently, there is a wealth of knowledge to be uncovered regarding fulleretic COFs that will hopefully be revealed within the next decade. Historically, fullerene-containing materials, such as fullerene-based metal-organic frameworks (MOFs), are the more explored class of materials in comparison with their corannulene analogs, and especially over the past five years, the fulleretic MOF community has blossomed.[79–83] Rational synthetic design and innovative approaches have led to the development of controllable, tunable hierarchical structures, that were previously inaccessible.[23,71,81,83,84]

As mentioned before, fullerenes possess an arsenal of unique characteristics including their curved surface and excellent electron-accepting properties. In this regard, incorporation of electron-accepting fullerene into traditionally insulating matrices, such as MOFs, can allow for tailoring and enhancing their electronic properties. For instance, Espallargas and co-workers targeted fullerene encapsulation into the MUV-2 framework consisting of a $[Fe_3(\mu_3\text{-}O)(COO)_6]$ secondary building unit connected by $TTFTB^{4-}$ ligands (H_4TTFTB = 4,4',4'',4'''-([2,2'-bi(1,3-dithiolylidene)]-4,4',5,5'-tetrayl)tetrabenzoic acid.[85] Specifically, the H_4TTFTB linkers were chosen due to the tetrathiafulvalene (TTF)

core, a well-known electron donor. The appearance of a broad band from 450–800 nm in the absorption profile supported the possibility of intermolecular CT between C_{60} and TTF units, that was also corroborated by theoretical calculations. The experimental optical band gap was estimated to be 1.4 eV for C_{60}@MUV-2, and electrical conductivity measurements revealed a two-orders-of-magnitude enhancement (4.7×10^{-9} S cm^{-1}) compared to MUV-2 itself (3.7×10^{-11} S cm^{-1}).

Huang and co-workers probed simultaneous MOF growth and C_{60} encapsulation inside UiO-67 (UiO = University of Oslo), followed by coordination of palladium nanoparticles to C_{60}, through metal-π-interactions, for catalytic applications.[86] The prepared hybrid fullerene-containing MOF was then employed for tandem hydrogenation. In particular, the synthesis of secondary arylamines was chosen as a model reaction that required three steps: (1) nitroarene hydrogenation, (2) reductive amination of aldehydes, and (3) selective hydrogenation, resulting in the formation of secondary arylamines. Comparison of the catalytic activity of the prepared hybrid with a previously reported MOF-supported Pd catalyst[86] demonstrated that the former catalyst required shorter reaction times and milder synthetic conditions.

Carbon-rich molecules are typically hydrophobic, and thus their incorporation into a porous matrix may affect the materials behavior in aqueous environments. Falcaro and co-workers employed this strategy to improve the stability of γ-cyclodextrin MOFs (γ-CD-MOFs) utilized for drug delivery applications (Figure 1.7).[87] Typically, γ-CD-MOFs disintegrate instantly upon interaction with an aqueous environment due to an externally hydrophilic structure. However, the internal cavity of the MOF is hydrophobic, allowing for the incorporation of hydrophobic guest molecules such as fullerenes. Immobilization

of C_{60} within the MOF cavities led to improvement of the hydrophobic material properties and increased the overall MOFs water-resistance. Indeed, immersion of C_{60}@γ-CD-MOF in water revealed that the MOF was stable in an aqueous environment for up to 24 hours. This fact is remarkable considering that crystals of the unmodified γ-CD-MOF were immersed in water and completely degraded within a few seconds. To probe C_{60}@γ-CD-MOF as a drug delivery vehicle, an anticancer drug, doxorubicin (DOX), was loaded into the composite. Kinetics studies demonstrated a 49.2%, 78.5%, and 92.2% release of DOX molecules in a buffer solution after 3, 6, and 18 hours, respectively (Figure 1.7).

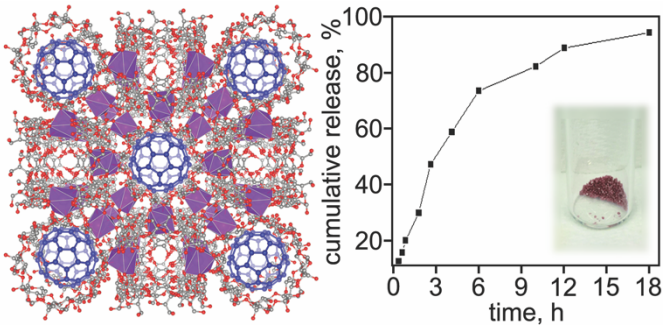

Figure 1.7 (*left*) Schematic representation of the γ-CD-MOF/C_{60} composite. The purple polyhedra and gray and red spheres correspond to potassium, carbon, and oxygen atoms, respectively. Hydrogen atoms are omitted for clarity. Blue spheres represent C_{60} molecules. (*right*) Release profile of DOX@γ-CD-MOF/C_{60} at 37 °C.

During the past several decades, porphyrin-containing MOFs have attracted significant interest for fullerene encapsulation applications.[82,89–90] In the last five years, several research groups continued studying frameworks constructed from photoactive porphyrin building blocks and integrated fullerene molecules, targeting applications in the field of organic photovoltaics.[82,88,91] In 2016, the first example of a metal-organic fullerene-containing framework was reported, in which control over the mutual orientation of both donor and fullerene-based acceptor was achieved through coordination of fullerene-linkers to the metal.[71] To ensure mutual orientation of donor and acceptor molecules, a crucial

aspect for active layer morphology formation, the authors prepared electron-donating layers of Zn_2(ZnTCPP) (H_4TCPP = 5,10,15,20-tetrakis(4-carboxyphenyl)-porphyrin) and then installed the electron-accepting fullerene-based pillars, BPCF (BPCF = bis(□etraani-4-ylmethyl)-3'H-cyclopropa-[1,2](C_{60}-I_h)[5,6]fullerene-3',3'-dicarboxylate), forming the D-A Zn_2(ZnTCPP)$(BPCF)_{0.23}(DEF)_{0.77}$ framework (DEF = *N,N*-diethylformamide). DFT calculations were employed to gain a deeper understanding regarding the structural and electronic properties of Zn_2(ZnTCPP)$(BPCF)_{0.23}(DEF)_{0.77}$. Theoretical modeling demonstrated that the bands near the Fermi level had a small dispersion that was indicative of the frontier orbitals localized nature. The HOMO and LUMO orbitals in the Γ-point were found to be localized on ZnTCPP and BPCF, respectively. The photophysical behavior of the prepared fullerene-containing framework was significantly affected by the presence of fullerenes inside the MOF matrix. For instance, photoluminescence, originating from the Zn_2(ZnTCPP) layers, was nearly completely quenched upon fullerene integration. Time-resolved photoluminescence studies also demonstrated a significant decrease in the material lifetime values due to the installation of fullerene-based linkers. The estimated ET efficiency between porphyrin units and fullerene moieties was determined to be 49.5%, with a corresponding rate constant of 9.18×10^8 s^{-1}.[71]

In addition to empty buckyballs, encapsulation of endohedral metallofullerenes (containing metal or metal clusters inside the carbon cage) is of great interest due to their unique structures, magnetic behavior, and responsivity to a confined environment, i.e., displaying dramatically distinctive spin dynamics as a result of a confined space.[79,80,92] For instance, recent studies reported that incorporation of Gd@C_{82} into MOF-177 ($Zn_4O(BTB)_2$; H_3BTB = 1,3,5-benzenetribenzoic acid) led to pronounced magnetic

behavior (Figure 1.8).[79] In a 5–300 K temperature range, the magnetization-field strength (*M*–*H*) curve of Gd@C_{82}⊂MOF-177 indicated a paramagnetic pattern within the magnetic field near 0 tesla. Remarkably, the inverse magnetic susceptibility versus temperature (χ^{-1}–*T*) plot of Gd@C_{82}⊂MOF-177 revealed a transition from paramagnetic to antiferromagnetic behavior at T = 135 K. Although this work presented a new and unique magnetic host-guest system, developing magnetic extended architectures based on endohedral metallofullerenes is an area that is ripe with opportunity.

An example of a porous crystalline framework built from redox-active corannulene-based ligands, with the buckybowl derivatives covalently linked to zinc cations, was reported in 2016.[84] Coordinative immobilization of the corannulene linker allowed for maintenance of the bowl shape, in comparison with other literature reports demonstrating corannulene flattening owing to host-guest interactions.[93,94] The electrochemical studies revealed that the corannulene-based MOF had less negative reduction potentials, with values of ΔE_p(I) = −1.42 V and ΔE_p(II) = −1.69 V compared to pristine corannulene, ΔE_p(I) = −1.87 V and ΔE_p(II) = −2.41 V.[84] In the following year,

Shustova and co-workers designed the first D-A corannulene-integrated MOF with efficient ligand-to-ligand ET.[81] The D-A alignment was achieved through the synthesis of the Zn_2(ZnTCPP) scaffold, followed by corannulene-based pillar installation. As expected,

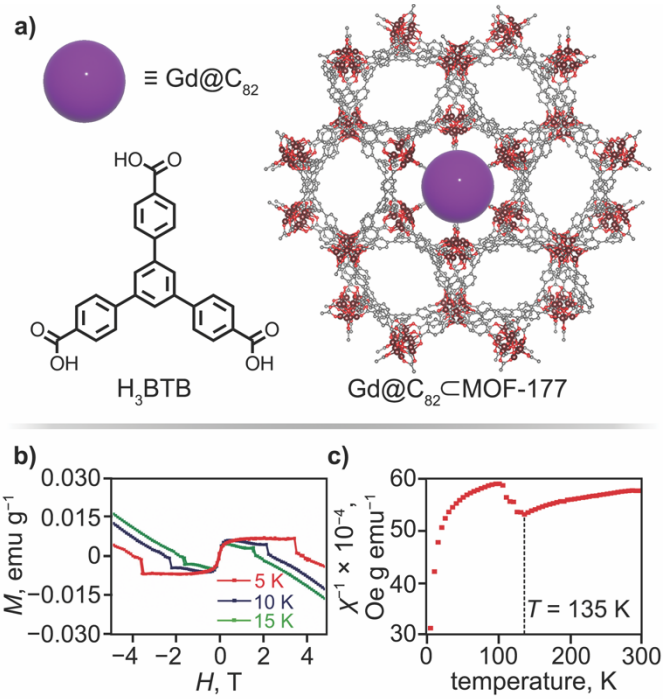

Figure 1.8 (a) Single-crystal X-ray structure of MOF-177. The brown, gray, and red spheres correspond to zinc, carbon, and oxygen atoms, respectively. Hydrogen atoms are omitted for clarity. Purple sphere represents Gd@C_{82}. (b) *M*–*H* curve of Gd@C_{82}⊂MOF-177 measured at 5, 10 and 15 K. I χ^{-1}–*T* curve of Gd@C_{82}⊂MOF-177 measured between 5 and 300 K with an applied field of 0.1 T.

based on the calculated spectral overlap function, incorporation of corannulene within the matrix led to nearly complete disappearance of the Zn_2(ZnTCPP) emission, that was indicative of efficient ET. Indeed, the ET efficiency was estimated to be 85% with an ET rate of 1.01×10^{-9} s^{-1}. This study was the first report describing the photophysics of any corannulene-based compounds in the solid state, and also presented the possibility to strategically engineer D-A corannulene-containing materials.

A recent study pursued preparation of a corannulene-containing MOF with integrated Pd nanoparticles for utilization in heterogeneous catalysis.[95] The support was

constructed from ZIF-67 (ZIF = zeolitic imidazolate framework), containing corannulene as a guest, followed by electrochemical deposition of Pd nanoparticles on the framework surface. The resulting material demonstrated long-term stability under continuous CV cycles (up to 350) that were performed in a 1.0 M KOH solution containing 1.0 M methanol. Moreover, this composite possessed a large electrochemical surface area of 114.6 $m^2 g^{-1}$ with a high electrocatalytic activity of 90.2 mA cm^{-2}.

In the past five years, studies in the field of corannulene- and fullerene-based discrete supramolecular structures focused on initially gaining fundamental understanding of material properties, followed by considering their potential applications. [35,94,96–100] The field of discrete supramolecular motifs containing fullerene and corannulene has been cultivated over the years; therefore, the selected works in this section only provides a glimpse of the progress made over the last five years. Reviews focusing on the integration of fullerenes in D-A arrays can be found elsewhere.[101–103] For example, a recently-reported corannulene-based coordination cage possessed a unique supramolecular helical structure existing as four stereoisomers; formation of the structure was attributed to bowl-to-bowl inversion.[104] The inherent chirality of the corannulene ligand, due to its concave shape,[105] could potentially be harnessed for chiral molecular recognition. Another unique corannulene-containing structure was reported by Jiang and co-workers, who prepared a self-assembled carcerand-like corannulene-based cage.[96] Due to the possibility of concave-convex interactions, the prepared cage served as a host for quantitative encapsulation of both C_{60} and C_{70}, and the prepared fullerene@cage possessed a relatively high thermal stability of 130 °C for 3 days. Due to temperature-dependent binding preference for C_{60} over C_{70} (C_{60} displaced C_{70} nearly quantitatively at 130 °C for 48 hours), this cage could

also be used for purification and separation of C_{60} from C_{70} that originated from fullerene soot. The authors demonstrated the recyclability (up to five cycles) of the organic ligand (1,3,5,7,9-pentakis(3-pyridylethynyl)corannulene), used for the synthesis of the empty cage, after fullerene separation (necessary for regeneration of the Pd-based cage). Using a similar concept of fullerene separation (C_{60} from higher-order fullerenes, C_{2n} where $n \geq 35$), Gong and co-workers developed a macrocycle, CDMB-8 (CDMB-8 = cyclo[8](1,3-(4,6-dimethyl)benzene); Figure 1.9).[106] The as-synthesized CDMB-8 macrocycle, possessing C_s symmetry, did not behave as an efficient fullerene receptor in the as-synthesized form. However, heating the macrocycle under anaerobic conditions at 300 °C for one hour resulted in an hourglass-like transformation, leading to symmetry changes from C_s to D_{4d} Figure 1.9). In contrast to the as-synthesized material, the macrocycle (D_{4d}) obtained after heating could form complexes with both fullerenes, C_{60} and C_{70}, and more importantly, could separate C_{60} from C_{70}. To demonstrate the feasibility of the separation procedure, a mixture of CDMB-8, C_{60}, and C_{70} was dissolved in tetrachloroethane and allowed to precipitate over 48 hours. The precipitate revealed a C_{60}/C_{70} molar ratio of 9:91, according to HPLC analysis. Recrystallization of the precipitate led to an enhanced molar ratio for C_{60}/C_{70} of <1:99 with a molar yield of C_{70} of 43%. A similar experiment was performed for separation of C_{60} from a mixture of higher fullerenes, C_{2n} where $n \geq 35$, resulting in a purity of C_{60} above 99% and a 35% mass yield.[106] These results demonstrate an alternative pathway for separation and purification of C_{60} and higher fullerenes in comparison with the traditional HPLC approach.

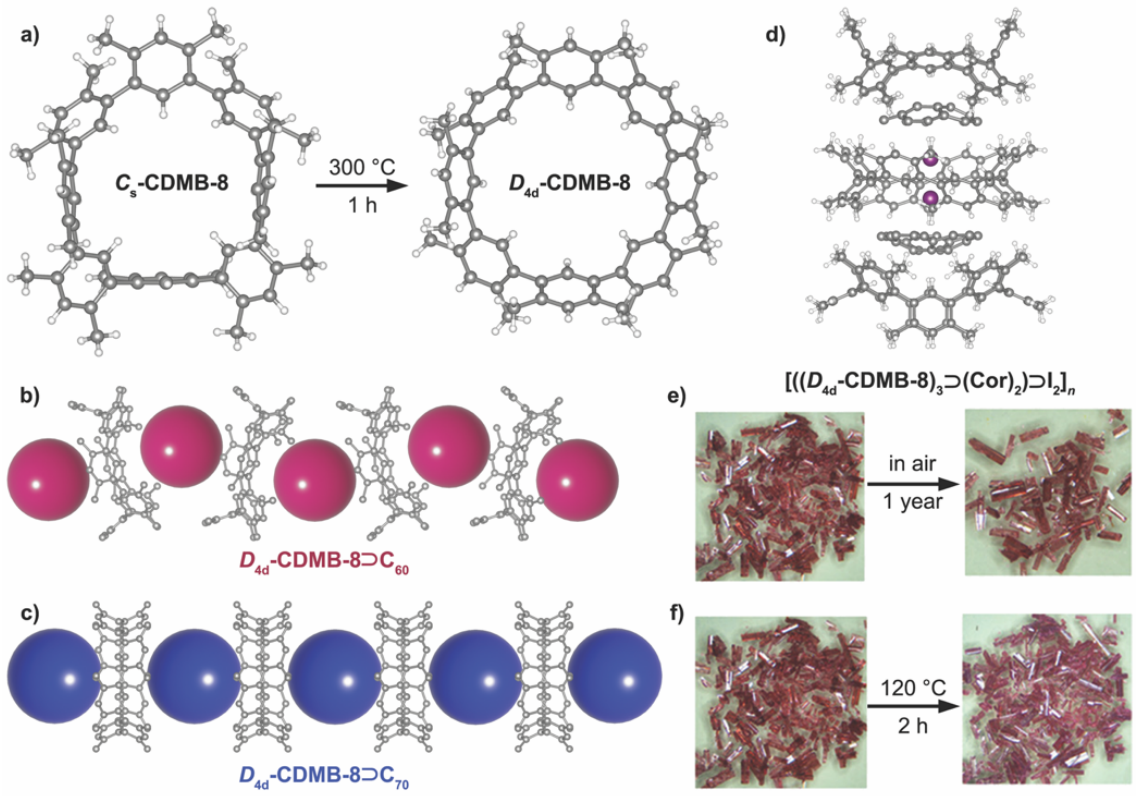

Figure 1.9 (a) Single-crystal X-ray structure of C_s-CDMB-8 and D_{4d}-CDMB-8. The gray and white spheres correspond to carbon and hydrogen atoms, respectively. (b) Single-crystal X-ray structure showing interactions between D_{4d}-CDMB-8⊃C_{60}. The gray spheres correspond to carbon. Hydrogen atoms are omitted for clarity. The pink spheres correspond to C_{60} molecules. (c) Single-crystal X-ray structure showing interactions between D_{4d}-CDMB-8⊃C_{70}. The gray spheres correspond to carbon atoms. Hydrogen atoms are omitted for clarity. The blue spheres correspond to C_{70} molecules. Reproduced from Ref. 106 with permission from the Royal Society of Chemistry. (d) Single-crystal X-ray structure of the iodine-containing capsule, (D_{4d}-CDMB-8)$_3$⊃(Cor)$_2$⊃I$_2$. The purple, gray, and white spheres correspond to iodine, carbon, and hydrogen atoms, respectively. (e) Photographs of single crystals of (D_{4d}-CDMB-8)$_3$⊃(Cor)$_2$⊃I$_2$ as prepared and after exposure to air for 1 year at room temperature. (f) Photographs of single crystals of (D_{4d}-CDMB-8)$_3$⊃(Cor)$_2$⊃I$_2$ as prepared and after heating at 120 °C for 2 hours.

In a follow-up study, Gong and co-workers utilized the same CDMB-8 to probe the formation of a capsule-like ensemble with corannulene, and its utilization for capturing volatile guest molecules.[98] As shown in Figure 1.9, a stack of alternating macrocycle (3 units) and corannulene molecules (2 units) efficiently trapped an iodine molecule, forming a supramolecular assembly, [(CDMB-8)$_3$⊃(Cor)$_2$)⊃I$_2$]$_n$. Further examination of the I$_2$@complex properties revealed that iodine sublimation from the confined environment of

the supramolecular structure was hindered, even at 145 °C. Furthermore, the I_2@complex crystals were stable in air for one year, and the same crystals maintained their integrity even upon heating at 120 °C for two hours (Figure 1.9).[98] Thus, the corannulene-containing supramolecular assembly could efficiently trap a guest molecule and exhibited unique thermostability without releasing highly-volatile species.

Along with these studies, a 2019 report highlighted the versatility of a chiral and flexible decapyrrylcorannulene host that could entrap and align a significant number of different fullerenes (e.g., 15 different cages were tackled) that resulted in the crystallographic resolution of various molecular structures of previously unknown fullerene cages.[99] The concave corannulene core was decorated with electron-rich pyrryl moieties to mimic molecular "hands" for cradling a number of buckyballs in a (+)hand-ball-hand(-) mode (each pair of chiral molecules is indicated by (+) and (-)). This design is similar to the well-known "buckycatcher" host[107–109] that provided evidence of concave-convex π-π interactions.[107] In addition, these molecular tweezers can also assist in reducing crystallographic disorder, allowing for the precise identification of novel fullerene structures through single-crystal X-ray diffraction.[100,110–112] Furthermore, decapyrrylcorannulene could host nearly all of the currently known types of fullerenes including exohedral, endohedral, dimeric, fulleroid, pentagon-fused, and heteroderivatized structures, and participated in the assembly of 2D layered structures.[99]

In a similar vein to the decapyrrylcorannulene host, Maeda and co-workers synthesized curved π-electronic molecules, dipyrrolylbenzodiazepine derivatives, that could assemble with C_{60} (Figure 1.10).[113] Specifically, dipyrrolylbenzodiazepines were synthesized as seven-membered heterocycle-based dipyrrolyl derivatives that co-assembled with C_{60}, resulting in the formation of a D-A system. Crystallographic packing revealed that dipyrrolylbenzodiazepines formed a hydrogen-bonding 1D chain structure with bonding between the pyrrole NH group and the diazepine nitrogen atom (Figure 1.10), resulting in an unusual complex in which C_{60} was surrounded by a ring made from the

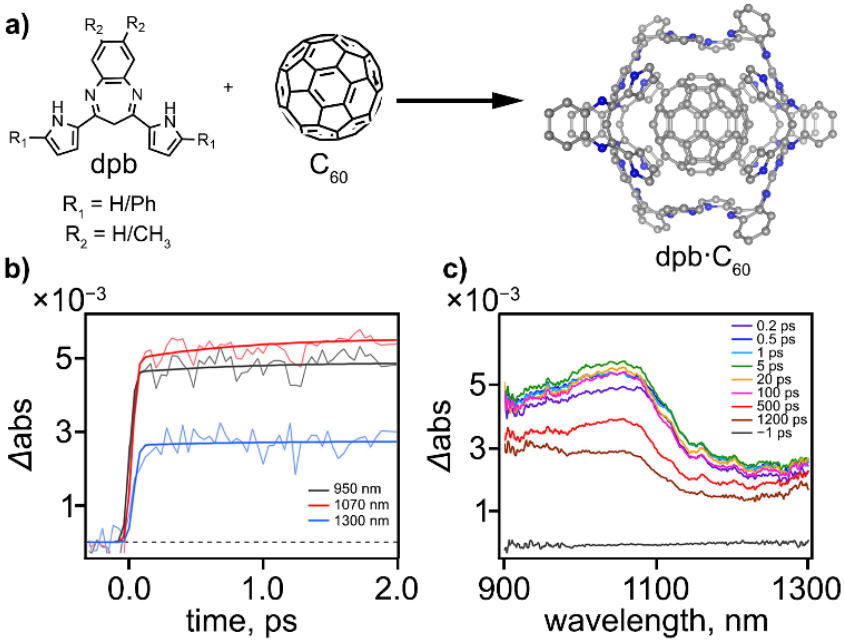

Figure 1.10 Molecular structures of dipyrrolylbenzodiazepine derivatives and fullerene forming donor-acceptor (D-A) structures. Single-crystal X-ray structure of the D-A cocrystals. The gray and blue spheres correspond to carbon and nitrogen atoms, respectively. (b) Transient absorption decay profiles of the material in the ranges from −0.3 to 2 ps excited at 400 nm and monitored at 950 (black), 1070 (red), and 1300 nm (blue). © Subpicosecond to nanosecond transient absorption spectra of a single crystal excited at 400 nm with delay time spanning from −1 to 1200 ps.

Assembled dipyrrolylbenzodiazepines. The same group probed the possibility of electron transfer in their D-A cocrystals by utilizing transient absorption (TA) spectroscopy in the

near-infrared light region. Excitation of the donor (dipyrrolylbenzodiazepine) was performed by utilizing a 400 nm excitation wavelength, resulting in the appearance of a broad absorption band near 1070 nm. The authors attributed this band to the formation of a C_{60} radical anion. The estimated electron transfer in this system occurred in less than the tens of femtosecond range, that is notably faster than that observed in other donor-C_{60} systems in which the typical reported electron transfer occurred within hundreds of femtoseconds or picoseconds.[114,115] Based on experimental evidence and time-dependent density functional theory (TD-DFT) calculations, the authors hypothesized that the observed ultrafast electron transfer occurred due to the close proximity of the donor and acceptor arising from the curved geometry of the donor. Notably, the TA measurements also suggested that the photogenerated carriers could be transported over several D-A units along the *c*-axis, portending the potential of the crystals as 1D photoconductive materials.

Another example of investigating CT interactions in a fullerene-based supramolecular cocrystal was performed by Kim and co-workers in 2020.[116] They utilized a shape-persistent zinc-metalated porphyrin box (Zn-PB) and C_{60}/C_{70} to construct the porphyrin/fullerene cocrystals. This was the first example of fullerene tetramers that were prepared and in close proximity to one another. Notably, the fullerene tetramers were surrounded by six Zn-PBs forming D-A domains. The C_{60} tetramers and Zn-PBs close packing arrangement (with a distance of 3.1 Å between Zn and C_{60}) promoted CT. Spectroscopic investigations revealed the formation of charge-separated states with long lifetimes in the excited state and a remarkably high photoconductivity compared to that of crystalline Zn-PB (a 10-fold enhancement in transient photoconductivity was observed for

Zn-PB/4C_{60} that had a value of 3.1×10^{-5} cm^2 v^{-1} s^{-1}). Similarly, a 3-fold enhancement in transient photoconductivity was observed for Zn-PB/4C_{70}.[116]

In a similar vein, Beuerle and co-workers utilized a trigonal-bipyramidal covalent organic cage as a host for complexation of C_{60} and C_{70}.[117] In contrast to the previous reports focused on the electronic properties of D-A dyads, the authors endeavored to utilize the cage as a template to functionalize C_{60}. Based on UV-vis titration experiments, 1:1 complexes of cage⊃C_{60} and cage⊃C_{70} had binding constants of $(6.3 \pm 0.4) \times 10^5$ and $(5.3 \pm 0.4) \times 10^5$ M^{-1}, respectively. According to crystallographic analysis, only four *trans*-trisadducts formed due to matching the trigonal planar arrangement of the cage windows, allowing for selective exohedral functionalization of C_{60}. The authors performed a Prato reaction for C_{60}-integrated inside the cage and formed a symmetry-matched trisadduct of C_{60}, that typically only forms in trace amounts without the presence of a cage. These findings present another route to realize regioselectivity in a Prato reaction that is intrinsically nonselective, paving the way for the application of covalent-organic cages as templating agents for functionalizing complex π-systems.

Several noteworthy structures containing corannulene were also formed in the past five years and analyzed crystallographically. The Nitschke group probed the reaction of *sym*-pentakis(4-aminothiophenyl)corannulene with different organic linkers (e.g., 2-formyl-6-methylpyridine and 2-formyl-1,10-phenanthroline) and metals (e.g., copper, cobalt, and zinc).[118] Their efforts led to the formation of two unique structures: the first was an S_{10} symmetric five-fold interlocked [2]catenane, while the second cage possessed D_5 symmetry.[118] According to DFT calculations, the driving force for the formation of the [2]catenane interlocked structure was aromatic stacking interactions. Notably, another

driving force highlighted in a recent report,[35] that could play a crucial role in the discovery of novel corannulene-based derivatives and could promote extraordinary structural transformation, is strain energy.[35] The Shustova group recently described an unprecedented C=C bond cleavage of pristine corannulene in a one-pot solid-state reaction, forming a planar corannulene analog, $C_{20}H_{14}$.[35] The reported approach could open an avenue for preparation of highly complex structures that are not accessible through conventional routes, and therefore, could advance applications in the areas of field-effect transistors, light-emitting diodes, or conductive electrodes.

The field of supramolecular cages and macrocycles has grown leaps and bounds over the past five years. Innovative approaches fusing molecular dynamics simulations with 2D NMR spectroscopy, as portrayed, for instance, by Ribas and co-workers, has led to a greater understanding of the nuances directing encapsulation.[119] Similarly, the advantages of utilizing a confined space, e.g., a cage or macrocycle, to restrict curved molecules has led to rapid energy and charge transfer as well as synthetic feats that were previously challenging.[98,117,118]

As highlighted in this report, interest in the design and preparation of fulleretic materials is unrelenting. Several extraordinary structures containing corannulene and fullerene building units have recently been created. Moreover, tailoring the properties of MOFs and COFs, a rapidly growing research field, through integration of buckybowls and buckyballs has been put in motion.[71,78,81,84] Despite very few reports that currently exist in the area of fulleretic frameworks, D-A alignment facilitated through coordinative immobilization of curved molecules as linkers within a rigid matrix, or through non-coordinative inclusion of buckybowls(ball) as guests inside the pores, could significantly

affect the photophysics and electronic properties of the resulting materials.[71,78,81,84] Furthermore, extensive studies of corannulene and alkali metal interactions performed by Petrukhina's research team provided an intriguing guiding hand for merging the intrinsically high surface area of COFs or MOFs with the high reversible alkali metal capacity inherent to corannulene and its derivatives.[62–65] Currently, literature reports in this direction are primarily dominated by supramolecular discrete structures, that could be used to provide valuable insight and design principles for extended structure engineering.

Fullerene, and especially its derivatives such as PCBM, have been extensively explored in the field of organic photovoltaics over the last few decades, while the corannulene family has not received much attention for applications in this direction.[120–125] However, the first attempts in this avenue demonstrated that corannulene derivatives (a naphthalimide-annulated corannulene) could be used as an electron acceptor, and in combination with an electron-donating polymer (PCE-10), resulted in a power conversion efficiency (PCE) of 2.1%.[126]

Another recent trend for improving the performance of photovoltaics is the addition of curved molecules for enhancement of the materials hydrophobicity (e.g., the perovskite layer).[122] For instance, one study reported the incorporation of corannulene-pentakis-(triethyleneglycol-monomethyl ether)-sulfone (Cor-TEG), containing a hydrophobic corannulene core and hydrophilic side chains, for increasing the moisture resistivity of a perovskite solar cell device.[122] This strategic design resulted in a noteworthy PCE of 17%, that only changed slightly (15.4%) after 65 days under inert conditions or under a humid environment (14.8%).[122] One rationale for the observed high PCE was attributed to the

enhanced charge carrier mobility due to the electron-withdrawing nature of the corannulene derivative.

The first steps in the arena of corannulene-based biomaterials were only recently taken and already demonstrated corannulene's potential for applications in image-guided surgery for the successful removal of cancerous tissue.

To summarize, the field of fulleretic architectures has achieved extraordinary feats over the past five years in a number of areas mentioned above, including recent discoveries in the rapidly growing fields of metal- and covalent-organic frameworks. The possibility of merging the advantages of hierarchical crystalline structures (COFs and MOFs) with buckybowls(balls) possessing unique electronic properties, dipole moments, spin dynamics (for endohedral metallofullerenes), and 3D curved surfaces, could portend the discovery of novel applications that are thus far unrealized.

REFERENCES

(1) R. K. Radha Krishnan, B. J. Reeves, S. H. Strauss, O. V. Boltalina and B. Lüssem, *Org. Electron.* **2020**, *86*, 105898.

(2) C. Dubceac, Y. Sevryugina, I. V. Kuvychko, O. V. Boltalina, S. H. Strauss and M. A. Petrukhina, *Cryst. Growth Des.* **2018**, *18*, 307–311.

(3) M. Gaboardi, F. Pratt, C. Milanese, J. Taylor, J. Siegel and F. Fernandez-Alonso, *Carbon N. Y.* **2019**, *155*, 432–437.

(4) X. Tian, L. M. Roch, N. Vanthuyne, J. Xu, K. K. Baldridge and J. S. Siegel, *Org. Lett.* **2019**, *21*, 3510–3513.

(5) C. Bruno, E. Ussano, G. Barucca, D. Vanossi, G. Valenti, E. A. Jackson, A. Goldoni, L. Litti, S. Fermani, L. Pasquali, M. Meneghetti, C. Fontanesi, L. T. Scott, F. Paolucci and M. Marcaccio, *Chem. Sci.* **2021**, *12*, 8048–8057.

(6) A. Y. Rogachev, Y. Zhu, Z. Zhou, S. Liu, Z. Wei and M. A. Petrukhina, *Org. Chem. Front.* **2020**, *7*, 3591–3598.

(7) Z. Zhou, Z. Wei, Y. Tokimaru, S. Ito, K. Nozaki and M. A. Petrukhina, *Angew. Chem. Int. Ed.* **2019**, *58*, 12107–12111.

(8) E. Nestoros and M. C. Stuparu, *Chem. Commun.* **2018**, *54*, 6503–6519.

(9) A. A. K. Karunathilake, C. M. Thompson, S. Perananthan, J. P. Ferraris and R. A. Smaldone, *Chem. Commun.* **2016**, *52*, 12881–12884.

(10) H. T. Mitchell, M. K. Smith, N. D. Blelloch, D. W. Van Citters and K. A. Mirica, *Chem. Mater.* **2017**, *29*, 2788–2793.

(11) Y. Wang, X. Chen, Q. G. Zhai, J. Guo and P. Feng, *J. Power Sources* **2019**, *434*, 126678.

(12) I. I. Stoikov, D. S. Ibragimova, N. V. Shestakova, D. B. Krivolapov, I. A. Litvinov, I. S. Antipin, A. I. Konovalov and I. Zharov, *Supramol. Chem.* **2009**, *21*, 564–571.

(13) Y. Zhang, Y. Zhu, D. Lan, S. H. Pun, Z. Zhou, Z. Wei, Y. Wang, H. K. Lee, C. Lin, J. Wang, M. A. Petrukhina, Q. Li and Q. Miao, *J. Am. Chem. Soc.* **2021**, *143*, 5231–5238.

(14) J. E. Huang, D. J. Guo, Y. G. Yao and H. L. Li, *J. Electroanal. Chem.* **2005**, *577*, 93–97.

(15) J. L. Shott, M. B. Freeman, N. A. Saleh, D. S. Jones, D. W. Paley and C. Bejger, *Inorg. Chem.* **2017**, *56*, 10984–10990.

(16) X. Tian, J. Xu, K. K. Baldridge and J. S. Siegel, *Angew. Chem. Int. Ed.* **2020**, *59*, 1460–1464.

(17) G. Báti, D. Csókás, T. Yong, S. M. Tam, R. R. S. Shi, R. D. Webster, I. Pápai, F. García and M. C. Stuparu, *Angew. Chem. Int. Ed.* **2020**, *59*, 21620–21626.

(18) W.-B. Zhang, J. He, X. Dong, C.-L. Wang, H. Li, F. Teng, X. Li, C. Wesdemiotis, R. P. Quirk and S. Z. D. Cheng, *Polymer* **2011**, *52*, 4221–4226.

(19) J. P. Barham, S. Tanaka, E. Koyama, N. Ohneda, T. Okamoto, H. Odajima, J.-I. Sugiyama and Y. Norikane, *J. Org. Chem.* **2018**, *83*, 4348–4354.

(20) H. Keypour, M. Noroozi and A. Rashidi, *J. Nanostructure Chem.* **2013**, *3*, 45–53.

(21) A. M. Butterfield, B. Gilomen and J. S. Siegel, *Org. Process Res. Dev.* **2012**, *16*, 664–676.

(22) R. Chen, R.-Q. Lu, P.-C. Shi and X.-Y. Cao, *Chinese Chem. Lett.* **2016**, *27*, 1175–1183.

(23) A. M. Rice, E. A. Dolgopolova and N. B. Shustova, *Chem. Mater.* **2017**, *29*, 7054–7061.

(24) J. Yadav, *Res. Rev. J. Phys.* **2017**, *6*, 1–6.

(25) Z. Biglari and H. Rezaei, *Comput. Theor. Chem.* **2020**, *1190*, 113002.

(26) R. Macovez, *Front. Mater.* **2018**, *4*, 46.

(27) B. A. Ali, A. H. Biby and N. K. Allam, *ChemElectroChem* **2020**, *7*, 1672–1678.

(28) A. J. Khan, M. Hanif, M. S. Javed, S. Hussain and Z. Liu, *J. Mater. Sci. Mater. Electron.* **2019**, *30*, 8568–8576.

(29) H. Kazemzadeh and M. Mozafari, *Drug Discov. Today* **2019**, *24*, 898–905.

(30) M. Kumar and K. Raza, *Pharm. Nanotechnol.* **2017**, *5*, 169–179.

(31) W. E. Billups and M. A. Ciufolini, *Buckminsterfullerenes* VCH, New York, **1993**.

(32) Y.-T. Wu and J. S. Siegel, *Chem. Rev.*, **2006**, *106*, 4843–4867.

(33) G. Valenti, C. Bruno, S. Rapino, A. Fiorani, E. A. Jackson, L. T. Scott, F. Paolucci and M. Marcaccio, *J. Phys. Chem. C* **2010**, *114*, 19467–19472.

(34) J. Mack, P. Vogel, D. Jones, N. Kaval and A. Sutton, *Org. Biomol. Chem.* **2007**, *5*, 2448–2452.

(35) G. A. Leith, A. M. Rice, B. J. Yarbrough, P. Kittikhunnatham, A. Mathur, N. A. Morris, M. J. Francis, A. A. Berseneva, P. Dhull, R. D. Adams, M. V. Bobo, A. A. Vannucci, M. D. Smith, S. Garashchuk and N. B. Shustova, *Chem. Sci.* **2021**, *12*, 6600–6606.

(36) Q. S. Stöckl, T. C. Wu, A. Mairena, Y. T. Wu and K. H. Ernst, *Faraday Discuss.* **2017**, *204*, 429–437.

(37) Q. Xu, C. Wang, D. Zheng, J. He, Y. Wang, X. Chen and H. Jiang, *J. Org. Chem.* **2021**, *86*, 13990–13996.

(38) Q. Xu, C. Wang, J. He, X. Li, Y. Wang, X. Chen, D. Sun and H. Jiang, *Org. Chem. Front.* **2021**, *8*, 2970–2976.

(39) H. A. Lin, K. Kato, Y. Segawa, L. T. Scott and K. Itami, *Chem. Sci.* **2019**, *10*, 2326–2330.

(40) J. M. Fernández-García, P. J. Evans, S. Medina Rivero, I. Fernández, D. García-Fresnadillo, J. Perles, J. Casado and N. Martín, *J. Am. Chem. Soc.* **2018**, *140*, 17188–17196.

(41) T. Wang, J. Lawrence, N. Sumi, R. Robles, J. Castro-Esteban, D. Rey, M. S. G. Mohammed, A. Berdonces-Layunta, N. Lorente, D. Pérez, D. Peña, M. Corso and D. G. de Oteyza, *Phys. Chem. Chem. Phys.* **2021**, *23*, 10845–10851.

(42) K. Shoyama and F. Würthner, *J. Am. Chem. Soc.* **2019**, *141*, 13008–13012.

(43) M. Qasemnazhand, F. Khoeini and F. Marsusi, *Sci. Rep.* **2021**, *11*, 2511.

(44) M. Y. Li, Y. X. Zhao, Y. B. Han, K. Yuan, S. Nagase, M. Ehara and X. Zhao, *ACS Appl. Nano Mater.* **2020**, *3*, 547–554.

(45) A. R. Khamatgalimov and V. I. Kovalenko, *Int. J. Mol. Sci.* **2021**, *22*, 3760.

(46) Y. D. Song and Q. T. Wang, *J. Mol. Model.* **2021**, *27*, 1–11.

(47) L. Wang, Y. L. Liu, S. H. Chen, D. He, Q. J. Li and M. S. Wang, *Phys. Chem. Chem. Phys.* **2021**, *23*, 405–414.

(48) E. M. Muzammil, D. Halilovic and M. C. Stuparu, *Commun. Chem.* **2019**, *2*, 58.

(49) V. Barát and M. C. Stuparu, *Chem. Asian J.* **2021**, *16*, 20–29.

(50) X. Li, F. Kang and M. Inagaki, *Small* **2016**, *12*, 3206–3223.

(51) M. C. Stuparu, *Acc. Chem. Res.* **2021**, *54*, 2858–2870.

(52) D. Lu, R. Tao and Z. Wang, *Front. Chem. Sci. Eng.* **2019**, *13*, 310–323.

(53) X. Q. Hou, Y. T. Sun, L. Liu, S. T. Wang, R. L. Geng and X. F. Shao, *Chinese Chem. Lett.* **2016**, *27*, 1166–1174.

(54) D. R. Jones, P. Bachawala and J. Mack, *Top. Curr. Chem.* **2014**, *348*, 37–52.

(55) C. B. Larsen and N. T. Lucas, *ChemInform* **2012**, *2*, 49–55.

(56) M. A. Petrukhina and L. T. Scott, *Dalt. Trans.* **2005**, 2969–2975.

(57) J. Li, A. Terec, W. Yue, H. Joshi, Y. Lu, H. Sun and M. C. Stuparu, *J. Am. Chem. Soc.* **2017**, *139*, 3089–3094.

(58) H. Furukawa and O. M. Yaghi, *J. Am. Chem. Soc.* **2009**, *131*, 8875–8883.

(59) K. T. Jackson, M. G. Rabbani, T. E. Reich and H. M. El-Kaderi, *Polym. Chem.* **2011**, *2*, 2775–2777.

(60) A. Mishra, M. Ulaganathan, E. Edison, P. Borah, A. Mishra, S. Sreejith, S. Madhavi and M. C. Stuparu, *ACS Macro Lett.* **2017**, *6*, 1212–1216.

(61) C. Bruno, R. Benassi, A. Passalacqua, F. Paolucci, C. Fontanesi, M. Marcaccio, E. A. Jackson and L. T. Scott, *J. Phys. Chem. B* **2009**, *113*, 1954–1962.

(62) A. V. Zabula, A. S. Filatov, S. N. Spisak, A. Y. Rogachev and M. A. Petrukhina, *Science* **2011**, *333*, 1008–1011.

(63) S. N. Spisak, Z. Wei and M. A. Petrukhina, *Dalt. Trans.* **2017**, *46*, 5625–5630.

(64) A. V. Zabula, S. N. Spisak, A. S. Filatov, A. Y. Rogachev and M. A. Petrukhina, *Acc. Chem. Res.* **2018**, *51*, 1541–1549.

(65) M. A. Petrukhina, *Dalt. Trans.* **2019**, *48*, 5125–5130.

(66) T. Eom, V. Barát, A. Khan and M. C. Stuparu, *Chem. Sci.* **2021**, *12*, 4949–4957.

(67) X. Gu, X. Zhang, H. Ma, S. Jia, P. Zhang, Y. Zhao, Q. Liu, J. Wang, X. Zheng, J. W. Y. Lam, D. Ding and B. Z. Tang, *Adv. Mater.* **2018**, *30*, 1801065.

(68) W. Lin, J. Gong, W. Ye, X. Huang and J. Chen, *Zeitschrift fur Anorg. Und Allg. Chemie* **2020**, *646*, 1900–1903.

(69) T. Hirao, K. Fukuta and T. Haino, *Macromolecules* **2020**, *53*, 3563–3570.

(70) T. Hirao, Y. Iwabe, N. Fujii and T. Haino, *J. Am. Chem. Soc.* **2021**, *143*, 4339–4345.

(71) D. E. Williams, E. A. Dolgopolova, D. C. Godfrey, E. D. Ermolaeva, P. J. Pellechia, A. B. Greytak, M. D. Smith, S. M. Avdoshenko, A. A. Popov and N. B. Shustova, *Angew. Chem. Int. Ed.* **2016**, *55*, 9070–9074.

(72) D. Cui, M. Ebrahimi, F. Rosei and J. M. Macleod, *J. Am. Chem. Soc.* **2017**, *139*, 16732–16740.

(73) D. Cui, J. M. MacLeod and F. Rosei, *Small* **2019**, *15*, 1903294.

(74) J. Plas, O. Ivasenko, N. Martsinovich, M. Lackinger and S. De Feyter, *Chem. Commun.* **2016**, *52*, 68–71.

(75) D. Cui, M. Ebrahimi, J. M. Macleod and F. Rosei, *Nano Lett.* **2018**, *18*, 7570–7575.

(76) D. Bessinger, L. Ascherl, F. Auras and T. Bein, *J. Am. Chem. Soc.* **2017**, *139*, 12035–12042.

(77) A. M. Rice, E. A. Dolgopolova, B. J. Yarbrough, G. A. Leith, C. R. Martin, K. S. Stephenson, R. A. Heugh, A. J. Brandt, D. A. Chen, S. G. Karakalos, M. D. Smith, K. B. Hatzell, P. J. Pellechia, S. Garashchuk and N. B. Shustova, *Angew. Chem. Int. Ed.* **2018**, *57*, 11310–11315.

(78) G. A. Leith, A. M. Rice, B. J. Yarbrough, A. A. Berseneva, R. T. Ly, C. N. Buck, D. Chusov, A. J. Brandt, D. A. Chen, B. W. Lamm, M. Stefik, K. S. Stephenson, M. D. Smith, A. K. Vannucci, P. J. Pellechia, S. Garashchuk and N. B. Shustova, *Angew. Chem. Int. Ed.* **2020**, *59*, 6000–6006.

(79) Y. Feng, X. Wang, P. Dong, J. Li, J. Huang, L. Cao, T. Wang and C. Wang, *Fullerenes, Nanotub. Carbon Nanostructures* **2020**, *28*, 353–360.

(80) H. Meng, C. Zhao, Y. Li, M. Nie, C. Wang and T. Wang, *Nanoscale* **2018**, *10*, 3291–3298.

(81) A. M. Rice, W. B. Fellows, E. A. Dolgopolova, A. B. Greytak, A. K. Vannucci, M. D. Smith, S. G. Karakalos, J. A. Krause, S. M. Avdoshenko, A. A. Popov and N. B. Shustova, *Angew. Chem. Int. Ed.* **2017**, *56*, 4525–4529.

(82) X. Liu, M. Kozlowska, T. Okkali, D. Wagner, T. Higashino, G. Brenner-Weiß, S. M. Marschner, Z. Fu, Q. Zhang, H. Imahori, S. Bräse, W. Wenzel, C. Wöll and L. Heinke, *Angew. Chem. Int. Ed.* **2019**, *58*, 9590–9595.

(83) V. Martinez, B. Karadeniz, N. Biliškov, I. Lončarić, S. Muratović, D. Žilić, S. M. Avdoshenko, M. Roslova, A. A. Popov and K. Užarević, *Chem. Mater.*,**2020**, *32*, 10628–10640.

(84) W. B. Fellows, A. M. Rice, D. E. Williams, E. A. Dolgopolova, A. K. Vannucci, P. J. Pellechia, M. D. Smith, J. A. Krause and N. B. Shustova, *Angew. Chem. Int. Ed.* **2016**, *55*, 2195–2199.

(85) M. Souto, J. Calbo, S. Mañas-Valero, A. Walsh, G. M. Espallargas and C. J. Beltrán, *Beilstein J. Nanotechnol* **2019**, *10*, 1883–1893.

(86) D. Y. Zheng, X. M. Zhou, S. Mutyala and X. C. Huang, *Chem. Eur. J.* **2018**, *24*, 19141–19145.

(87) H. Li, M. R. Hill, R. Huang, C. Doblin, S. Lim, A. J. Hill, R. Babarao and P. Falcaro, *Chem. Commun.* **2016**, *52*, 5973–5976.

(88) C. Liu, C. Wang, H. Wang, T. Wang and J. Jiang, *Eur. J. Inorg. Chem.* **2019**, *2019*, 4815–4819.

(89) M. A. Gordillo, D. K. Panda and S. Saha, *ACS Appl. Mater. Interfaces* **2019**, *11*, 3196–3206.

(90) T. Ohmura, A. Usuki, Y. Mukae, H. Motegi, S. Kajiya, M. Yamamoto, S. Senda, T. Matsumoto and K. Tatsumi, *Chem. Asian J.* **2016**, *11*, 700–704.

(91) N. Huang, K. Wang, H. Drake, P. Cai, J. Pang, J. Li, S. Che, L. Huang, Q. Wang and H. C. Zhou, *J. Am. Chem. Soc.* **2018**, *140*, 6383–6390.

(92) J. Cao, Y. Feng, S. Zhou, X. Sun, T. Wang, C. Wang and H. Li, *Dalt. Trans.* **2016**, *45*, 11272–11276.

(93) M. Juríček, N. L. Strutt, J. C. Barnes, A. M. Butterfield, E. J. Dale, K. K. Baldridge, J. F. Stoddart and J. S. Siegel, *Nat. Chem.* **2014**, *6*, 222–228.

(94) B. M. Schmidt, T. Osuga, T. Sawada, M. Hoshino and M. Fujita, *Angew. Chem. Int. Ed.* **2016**, *55*, 1561–1564.

(95) H. Khuntia, K. S. Bhavani, T. Anusha, T. Trinadh, M. C. Stuparu and P. K. Brahman, *Colloids Surfaces A Physicochem. Eng. Asp.* **2021**, *615*, 126237.

(96) W. Sun, Y. Wang, L. Ma, L. Zheng, W. Fang, X. Chen and H. Jiang, *J. Org. Chem.* **2018**, *83*, 14667–14675.

(97) T. Tsutsui, L. Catti, K. Yoza and M. Yoshizawa, *Chem. Sci.* **2020**, *11*, 8145–8150.

(98) Y.-D. Yang, X.-L. Chen, J. L. Sessler and H.-Y. Gong, *J. Am. Chem. Soc.* **2021**, *143*, 2315–2324.

(99) Y.-Y. Xu, H.-R. Tian, S.-H. Li, Z.-C. Chen, Y.-R. Yao, S.-S. Wang, X. Zhang, Z.-Z. Zhu, S.-L. Deng, Q. Zhang, S. Yang, S.-Y. Xie, R.-B. Huang and L.-S. Zheng, *Nat. Commun.* **2019**, *10*, 485.

(100) R. Q. Lu, S. Wu, Y. H. Bao, L. L. Yang, H. Qu, M. Saha, X. Y. Wang, Y. Z. Zhuo, B. Xu, J. Pei, H. Zhang, W. Weng and X. Y. Cao, *Chem. Asian J.*, **2018**, *13*, 2934–2938.

(101) M. Madhu, R. Ramakrishnan, V. Vijay and M. Hariharan, *Chem. Rev.* **2021**, *121*, 8234−8284.

(102) A. Kraft and F. Beuerle, *Tetrahedron Lett.* **2016**, *57*, 4651–4663.

(103) S. Das and M. Presselt, *J. Mater. Chem. C* **2019**, *7*, 6194–6216.

(104) F. Huang, L. Ma, Y. Che, H. Jiang, X. Chen and Y. Wang, *J. Org. Chem.* **2018**, *83*, 733–739.

(105) A. Szumna, *Chem. Soc. Rev.* **2010**, *39*, 4274–4285.

(106) Y.-D. Yang and H.-Y. Gong, *Chem. Commun.* **2019**, *55*, 3701–3704.

(107) A. Sygula, F. R. Fronczek, R. Sygula, P. W. Rabideau and M. M. Olmstead, *J. Am. Chem. Soc.* **2007**, *129*, 3842–3843.

(108) A. V. Zabula, Y. V. Sevryugina, S. N. Spisak, L. Kobryn, R. Sygula, A. Sygula and M. A. Petrukhina, *Chem. Commun.* **2014**, *50*, 2657–2659.

(109) P. A. Denis and F. Iribarne, *Int. J. Quantum Chem.* **2015**, *115*, 1668–1672.

(110) D. C. Yang, M. Li and C. F. Chen, *Chem. Commun.* **2017**, *53*, 9336–9339.

(111) M. Takeda, S. Hiroto, H. Yokoi, S. Lee, D. Kim and H. Shinokubo, *J. Am. Chem. Soc.* **2018**, *140*, 6336–6342.

(112) Y. Shoji, T. Kajitani, F. Ishiwari, Q. Ding, H. Sato, H. Anetai, T. Akutagawa, H. Sakurai and T. Fukushima, *Chem. Sci.* **2017**, *8*, 8405–8410.

(113) Y. Haketa, M. Miyasue, Y. Kobayashi, R. Sato, Y. Shigeta, N. Yasuda, N. Tamai and H. Maeda, *J. Am. Chem. Soc.* **2020**, *142*, 16420–16428.

(114) G. J. Moore, M. Causa', J. F. Martinez Hardigree, S. Karuthedath, I. Ramirez, A. Jungbluth, F. Laquai, M. Riede and N. Banerji, *J. Phys. Chem. Lett.* **2020**, *11*, 5610–5617.

(115) Y. Wu, Y. Zhen, Z. Wang and H. Fu, *J. Phys. Chem. A* **2013**, *117*, 1712–1720.

(116) X. Yu, B. Wang, Y. Kim, J. Park, S. Ghosh, B. Dhara, R. D. Mukhopadhyay, J. Koo, I. Kim, S. Kim, I. C. Hwang, S. Seki, D. M. Guldi, M. H. Baik and K. Kim, *J. Am. Chem. Soc.* **2020**, *142*, 12596–12601.

(117) V. Leonhardt, S. Fimmel, A. M. Krause and F. Beuerle, *Chem. Sci.* **2020**, *11*, 8409–8415.

(118) T. K. Ronson, Y. Wang, K. Baldridge, J. S. Siegel and J. R. Nitschke, *J. Am. Chem. Soc.* **2020**, *142*, 10267–10272.

(119) C. Garciá-Simón, C. Colomban, Y. A. Çetin, A. Gimeno, M. Pujals, E. Ubasart, C. Fuertes-Espinosa, K. Asad, N. Chronakis, M. Costas, J. Jiménez-Barbero, F. Feixas and X. Ribas, *J. Am. Chem. Soc.* **2020**, *142*, 16051–16063.

(120) F. Zhang, W. Shi, J. Luo, N. Pellet, C. Yi, X. Li, X. Zhao, T. J. S. Dennis, X. Li, S. Wang, Y. Xiao, S. M. Zakeeruddin, D. Bi and M. Grätzel, *Adv. Mater.* **2017**, *29*, 1606806.

(121) R. Q. Lu, Y. Q. Zheng, Y. N. Zhou, X. Y. Yan, T. Lei, K. Shi, Y. Zhou, J. Pei, L. Zoppi, K. K. Baldridge, J. S. Siegel and X. Y. Cao, *J. Mater. Chem. A* **2014**, *2*, 20515–20519.

(122) B. T. Muhammad, V. Barát, T. M. Koh, X. Wu, A. Surendran, N. Yantara, A. Bruno, A. C. Grimsdale, M. C. Stuparu and W. L. Leong, *Chem. Commun.* **2020**, *56*, 11997–12000.

(123) S. Collavini and J. L. Delgado, *Sustain. Energy Fuels*, **2018**, *2*, 2480–2493.

(124) T. Umeyama and H. Imahori, *Acc. Chem. Res.* **2019**, *52*, 2046–2055.

(125) N. Y. Doumon, M. V. Dryzhov, F. V. Houard, V. M. Le Corre, A. Rahimi Chatri, P. Christodoulis and L. J. A. Koster, *ACS Appl. Mater. Interfaces* **2019**, *11*, 8310–8318.

(126) R. Renner, B. Mahlmeister, M. Stolte and F. Würthner, *Org. Mater.* **2020**, *2*, 229–234.

CHAPTER 2

"BROKEN-HEARTED" CARBON BOWL VIA ELECTRON SHUTTLE REACTION: ENERGETICS AND ELECTRON COUPLING

Leith, G. A.; Rice, A. M.; Yarbrough, B. J.; Kittikhunnatham, P.; Mathur, A.; Morris, N. A.; Francis, M. J.; Berseneva, A. A.; Dhull, P.; Adams, R. D.; Bobo, M. V.; Vannucci, A. A.; Smith, M. D.; Garashchuk, S. and Shustova, N. B. *Chem. Sci.* **2021**, *12*, 6600–6606.

Unzipping nanotubes,[127–131] nanosheets,[132,133] buckyballs,[134–137] or annulenes[138–142] is driven by the renewed interest in fundamental understanding and practical access to novel structural transformations[143,144] leading to materials with unique optical and electronic profiles. For instance, cutting and unravelling of nanotubes resulted in nanoribbons having electronic properties that can be varied as a function of their width, and therefore, applied in a variety of electronic devices including field effect transistors, light emitting diodes, and transparent conductive electrodes.[145,146] In addition, hydrogenation of graphene nanoribbons led to enhanced photoluminescent properties that could pave the way for the development of optically active graphene nanoribbon-based devices.[147] However, promotion of selective C=C bond cleavage in graphitic materials is challenging,[148–150] and although there have been examples of structural changes due to periphery modifications of buckybowls (π-bowls),[151–154] ring expansion[148], or opening of the strained π-bowl,[155,156] these accounts are overall very limited. Pursuing the route of C–C bond activation in curved π-bowl-containing systems is advantageous as this could lead to addressing challenges such as selective sphere opening for preparation of endohedral fullerenes, shortening carbon nanotubes (CNTs), guest integration within the CNT body, as well as access to a class of materials that has not been prepared through "wet-chemistry conventional" routes. One strategy to facilitate C–C bond activation is to employ, for instance, strain energy as a variable, release of which could energetically promote such transformations. Indeed, as presented in this report, release of strain energy can be the driving force for planarization of the naturally curved buckybowl surface (e.g., $C_{20}H_{10}$, corannulene), since there is no

direct route to cleave a C=C bond, except through uncontrollable flash vacuum pyrolysis[148,153,155] or addition of a directing group (and a catalyst).[158]

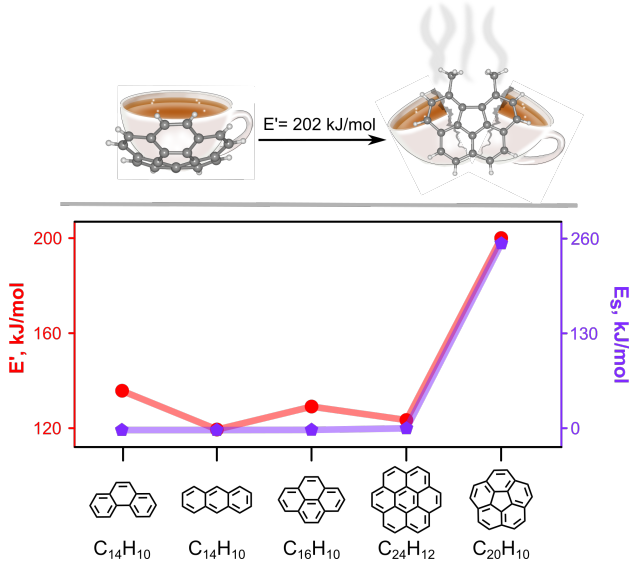

Scheme 2.1 (*top*) A schematic representation of π-bowl (corannulene) opening through a solid-state route. Single-crystal X-ray structure of corannulene (*left*) and X-ray structure of 5,6-dimethyl-benzo[*ghi*]fluoranthene (P-$C_{20}H_{14}$) ("open" corannulene, *right*). (*bottom*) Strain energy (E_s, purple)[157] and released energy (E', red) as a function of PAH (*left to right*) phenanthrene, anthracene, pyrene, coronene, and corannulene.

Although there are numerous reports of catalytic hydrocracking of planar polycyclic aromatic hydrocarbons (PAHs) i.e., increasing the ratio of hydrogen-to-carbon,[159–162] there are very few accounts on C–C bond cleavage following the hydrogenation step.[163] The literature precedent for C–C bond scission primarily relies on the assistance of transition metal catalysts, high hydrogen pressure, elevated temperatures, or a combination of all three parameters.[164–170] Therefore, unexpected C–C bond cleavage (discovered from photophysical studies of alignment of electron donor (corannulene) and acceptor (7,7,8,8-tetracyanoquinodimethane, TCNQ) in the solid state) reported herein led us to probe mechanistic pathways to determine the feasibility for π-bowl planarization and factors that could affect such a transformation including strain energy (E_s) and

released energy (*E*', Scheme 2.1). The electron coupling and charge transfer (CT) rates between "open" corannulene (or parent corannulene) and TCNQ were evaluated by applying the Marcus theory. In addition to the solid-state reaction, we also offer "more conventional" solution-based nine-step synthetic routes for the preparation of novel "open" corannulene analogs. In the reported findings, we also discuss the electronic structure and photophysical profiles of the synthesized "open" analogs through estimation of their energies and isosurfaces of the frontier natural transition orbitals (HONTO and LUNTO).

The reductive C=C bond cleavage and consecutive corannulene planarization to form 5,6-dimethyl-benzo[*ghi*]fluoranthene (planar corannulene analog (P-$C_{20}H_{14}$), Scheme 2.1) was achieved through a one-pot solid-state reaction, in which corannulene (15 mg, 0.060 mmol), TCNQ (an electron shuttle; 14 mg, 0.068 mmol), and zinc powder (a reducing agent; 50 mg, 0.76 mmol) were ground. After that, the reaction mixture was placed in a glass tube, a drop of hydrochloric acid (proton source) was added, and the glass tube was flame-sealed under dynamic vacuum (4 $\times$ 10^{-5} mbar). Heating the reaction mixture at 200 °C for six days resulted in the formation of dark brown needles suitable for single-crystal X-ray diffraction analysis (Scheme 2.1). As shown in Scheme 2.1, such treatment resulted in planarization of the corannulene bowl through partial hydrogenation and formation of P-$C_{20}H_{14}$. X-ray crystallographic studies of ($C_{20}H_{10}$)·(P-$C_{20}H_{14}$)·(TCNQ) (**1**) co-crystals revealed that the packing consists of alternating columns of TCNQ and P-$C_{20}H_{14}$ along the *c*-axis direction (Figure 2.5 and 2.6). Furthermore, neither mass spectrometry nor spectroscopic studies identified the presence of any other partially hydrogenated products (Figure 2.6 and 2.7).

To gain insight into a plausible mechanism of such π-bowl opening during the one-pot solid-state synthesis (Scheme 2.1), we initially tested the hypothesis of whether *all* components of the reaction mixture were essential to perform the solid-state C=C bond cleavage. Our results illustrated that the absence of one of the components of the reaction mixture resulted in either no transformation or formation of (corannulene)$_2$·(TCNQ) co-crystals, previously reported in the literature (CCDC 1037414)[171] and also detected in our studies (Figure 2.7). Utilization of a different redox mediator rather than TCNQ (e.g., methyl viologen) did not lead to corannulene opening despite previous reports in which TCNQ and methyl viologen have both been used as electron shuttles in various biological applications.[172–175] Variation of synthetic conditions, for instance, replacement of the zinc powder with sodium dithionite[176] as a reducing agent did not lead to hydrogenated products (see ESI for more details).

Utilization of more conventional solution-based routes through heating the same reagents ($C_{20}H_{10}$/TCNQ/Zn/HCl) in a series of organic solvents was also attempted. We varied the reaction media starting with the solvents possessing low boiling points (e.g., dichloromethane or methanol), transitioning to dichloromethane/water or methanol/water mixtures, and finally attempting heating in the higher boiling glycerol (b.p. = 290 °C) or ethylene glycol (b.p. = 197 °C) to more closely match the reaction temperature (200 °C) of the solid-state synthesis. In all reactions, no evidence of P-$C_{20}H_{14}$ was detected according to the ^{1}H nuclear magnetic resonance (NMR) spectroscopic or mass spectrometry analysis. Notably, the reported hydrogenation reactions of corannulene typically occurred under relatively harsh conditions (e.g., electron bombardment, alkylithium reagents, or alkali metals), and

even despite them, reactions typically led to hydrogenation of one or two rim C=C bonds without carbon–carbon bond cleavage.[177–183] Since the developed conditions ($C_{20}H_{10}$/TCNQ/Zn/HCl) required the presence of zinc, we also probed the Clemmensen reduction that uses zinc amalgam and concentrated hydrochloric acid.[184] Mass spectrometry and ^{1}H NMR spectroscopy studies of reaction products detected the presence of only pristine corannulene and did not detect any traces of corannulene hydrogenation. As a logical progression, we surveyed an electrochemical method suitable for arene reductive transformations,[185] but proved unsuccessful. Finally, attempts to electrochemically cleave the C=C bond by bulk electrolysis were performed in anhydrous *N*,*N*-dimethylformamide or acetonitrile for up to two days, but were also not successful. In line with these studies, we probed the reaction conditions previously utilized for the ring-opening of other nonplanar structures such as *o*-carborane.[186–188] For that, we used a triosmium carbonyl complex, $Os_3(CO)_{10}(NCMe)_2$; however, no ring-opening of corannulene was observed, while successful *o*-carborane opening occurred at 150 °C in a nonane reflux.[188]

Further experimental investigations were pursued to rule out aromaticity stabilization as a main factor by performing reactions with significantly less strained PAHs including pyrene (0.0 kJ/mol)[157] or phenanthrene (0.0 kJ/mol)[189] under experimental conditions similar to those used for the reaction with highly-strained

corannulene (101 kJ/mol[157]; see ESI for more details). As a result, no bond cleavage was detected in any of these systems, and formation of only PAH·TCNQ complexes

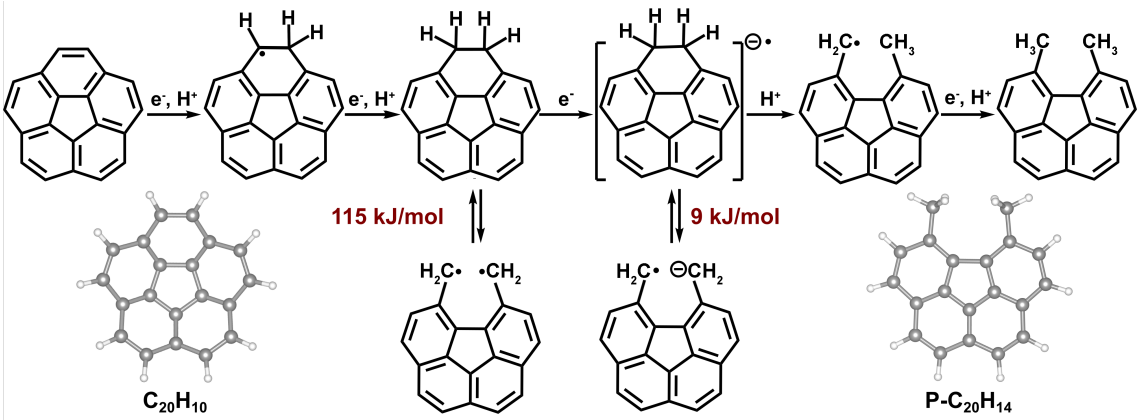

intermediate	$C_{20}H_{12}$	$C_{20}H_{12}^{\bullet-}$	$C_{20}H_{13}^{\bullet}$
bowl depth, Å	0.811	0.798	0.000
$d(C_{rim}–C_{rim})_{max}$, Å	1.587	1.610	3.439
$E_{C–C}$, kJ/mol	115	9	-
E', kJ/mol	163	169	6

Figure 2.1 Mechanistic pathway to transform corannulene to P-$C_{20}H_{14}$. Calculations based on B3LYP/6-31+G* level of theory.

Was observed (e.g., phenanthrene·TCNQ complex (similar to the structure reported in the literature[190]) or pyrene·TCNQ, Figure 2.20). Thus, these experimental evidence points out that one of the driving forces for the observed solid-state reaction could potentially be a release of energy through buckybowl planarization (Figure 2.1). To prove this hypothesis, we estimated released energy, *E*', for PAHs and carbon π-bowls as shown in Scheme 2.1. For instance, *E*' for corannulene was calculated to be 202.0 kJ/mol. In contrast, *E*' calculated for the PAHs in Scheme 2.1 was found to be less than 135.7 kJ/mol (Table 2.3). Therefore, corannulene opening is much more energetically favorable in comparison with the PAHs shown in Scheme 2.1. Similar statement is also valid for a family of extended π-bowls for which estimated *E*' was even higher than that of corannulene (Scheme 2.4).

The estimated enthalpy of the reaction (eqn (2)),

$C_{20}H_{10} + 2\ H_2 = C_{20}H_{14}$ (2)

was found to be −179.5 kJ/mol (–239 and 59.5 kJ/mol for only the electronic and the ZPE-corrected electronic energies, respectively, using density functional theory (DFT, Table 2.2, see the ESI for more details)). Thus, a combination of two parameters, strain energy (E_s) and released energy (E'), highlights the unique nature of buckybowls in comparison with the considered PAHs (Scheme 2.1).

As a next step, we took a closer look at a possible mechanism for π-bowl hydrogenation and C–C bond cleavage. On the basis of our theoretical calculations, experimental results, and literature reports, we hypothesize that the transformation of $C_{20}H_{10}$ to planar P-$C_{20}H_{14}$ occurs in a series of reactions that is first initiated by a sequence of electron and proton transfers in which hydrochloric acid acts as the proton source (Figure 2.1). Moreover, probing the strength of the C–C bond revealed a significantly weaker bond (115 kJ/mol for $C_{20}H_{12}$ and 9 kJ/mol for $C_{20}H_{12}^{-\bullet}$, Figure 2.1) than a typical C–C bond in RCH_2–CH_2R systems, allowing for bond cleavage to occur.[192] For instance, if R is a substituent on a pyrene or coronene core then the electronic energy of the C–C bond would be approximately 350 kJ/mol (Figure 2.17) and 302 kJ/mol, respectively (Figure 2.18).

Comprehensive analysis of photophysical data for the obtained crystals of **1** revealed properties that are uncharacteristic of the individual components i.e., corannulene and TCNQ themselves. Based on photoluminescence and epifluorescence microscopy studies, the obtained crystals of **1** exhibited red emission (λ_{max} = 705 nm, λ_{ex} = 365 nm) in contrast to their constituents ((TCNQ) = undetectable emission and λ_{max} (corannulene) = 490 nm, λ_{ex} = 365 nm, Figure 2.8). Furthermore, in contrast to diffuse reflectance (DR) profiles of pristine corannulene

and TCNQ (Figure 2.9), the appearance of a new red-shifted band (550 nm) in the DR profile of **1** was detected. Based on our theoretical calculations using time-dependent density functional theory (TDDFT), the new band (550 nm) is characteristic of CT complex formation (see the ESI for more

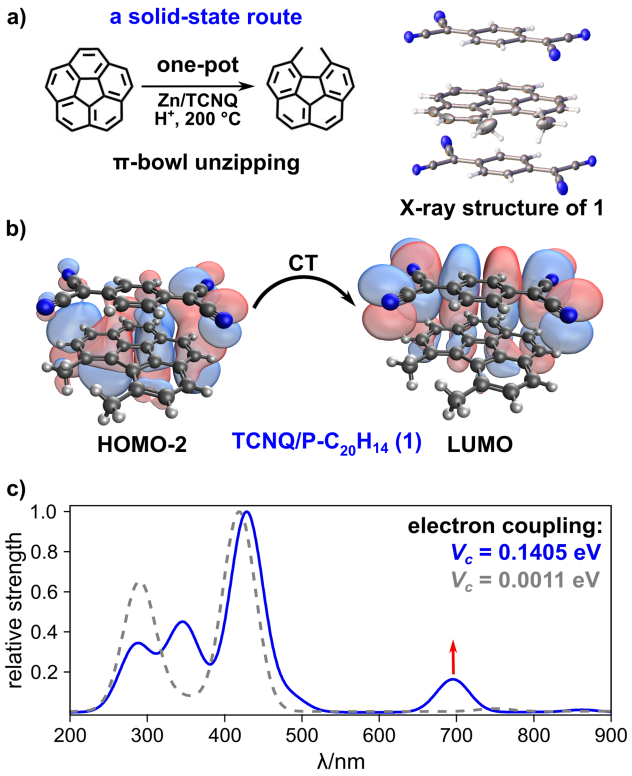

Figure 2.2 (a) (*left*) Developed route for the preparation of P-$C_{20}H_{14}$ and (*right*) a part of the single-crystal X-ray structure of **1** showing an alternating column of TCNQ and P-$C_{20}H_{14}$. (b) molecular orbitals of TCNQ/P-$C_{20}H_{14}$ in **1**: HOMO-2 and LUMO, related to electron excitation (transition) from P-$C_{20}H_{14}$ to TCNQ, respectively. I Optical transition strength for TCNQ/P-$C_{20}H_{14}$ (blue) and TCNQ/$C_{20}H_{10}$ (gray) calculated using TDDFT/RPA based on the B3LYP-D3/6-311+G** level of theory.

Details) that is in line with the previous reports on PAHs and TCNQ co-crystals.[150] In particular, according to our studies using the B3LYP-D3/6-311+G** level of

theory (Figure 2.2), both a bathochromic shift and new band appearance could be attributed to CT[192,193] between the HOMO-2 and LUMO of TCNQ/P-$C_{20}H_{14}$ "stack" (Figure 2.2). To further shed light on the experimental changes of the emission profile, we examined optical excitations of isolated corannulene, P-$C_{20}H_{14}$, TCNQ, and the relevant dimers through the TDDFT calculations based on the B3LYP-D3/6-311+G** method. The considered TCNQ/P-$C_{20}H_{14}$ "stack" is the only species with excitation energies of appreciable strength around 690 nm (1.8 eV; Figure 2.10), which is in agreement with the experimentally observed red emission at λ_{max} = 705 nm (Figure 2.8). The lowest excitations for TCNQ, π-bowl, and P-$C_{20}H_{14}$ are 413, 288, and 344 nm (3.0, 4.3, and 3.6 eV), respectively (Figure 2.10).

To further probe the idea that CT is more effective in an exclusively planar TCNQ/P-$C_{20}H_{14}$ "stack" rather than in a TCNQ/$C_{20}H_{10}$ "stack", that encounters steric hindrance from the curved surface of the π-bowl,[171] we employed the Marcus theory[194] to compare the electron coupling (that is proportional to CT rate) between TCNQ/$C_{20}H_{10}$ and TCNQ/P-$C_{20}H_{14}$ using eqn (1).

$$k = 2\pi/\hbar \cdot |V_c|^2/\sqrt{(4\pi\lambda k_B \mathrm{T})} \cdot \exp\left(-\frac{(\lambda+\Delta G^0)^2}{4\lambda k_B \mathrm{T}}\right) \sim |V_c|^2 \qquad (1)$$

where k = charge transfer rate, V_c = electron coupling, λ = reorganization energy of the system, and ΔG^o = energy difference between the initial and final states (see the ESI for more details). According to the Marcus theory model, TCNQ/P-$C_{20}H_{14}$ could result in ca. 128-fold increase in electron coupling compared to TCNQ/$C_{20}H_{10}$ (Figure 2.11 and Table 2.5, see the ESI for more details). Since electron coupling is related to the electron transfer rate, we can surmise that there is likely an increased electron transfer rate as well.[192] The charge on the TCNQ molecules was evaluated by applying the Kistenmacher relationship

(i.e., correlation between TCNQ intramolecular bond distances and charge on TCNQ)[195] using the crystallographic data of **1** and (corannulene)$_2$·TCNQ co-crystals.[171] In the case of **1**, the charge on TCNQ was estimated to be –0.84 and for (corannulene)$_2$·TCNQ co-crystals was found to be –0.20, suggesting more effective CT can occur in **1** between "open" corannulene (P-$C_{20}H_{14}$) and TCNQ. We calculated electronic transitions corresponding to

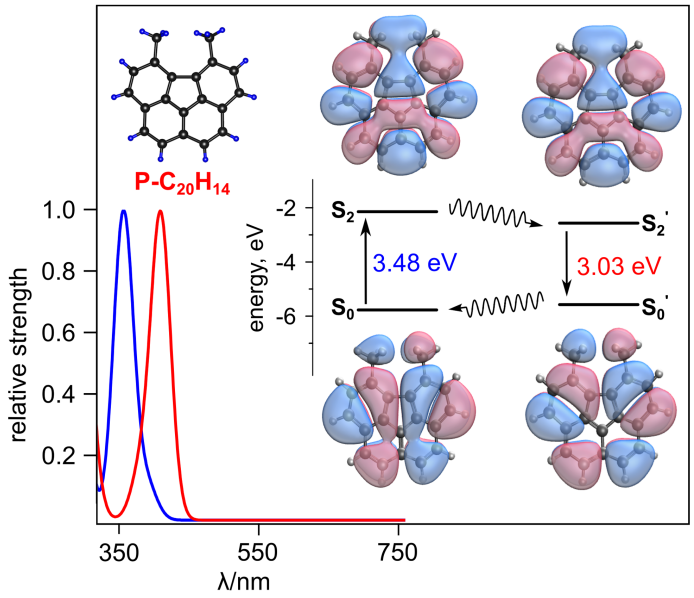

Figure 2.3 (*top left*) Single-crystal X-ray structure of P-$C_{20}H_{14}$. (*bottom left*) Optical transition strengths computed at the ground state optimal geometry for P-$C_{20}H_{14}$ in THF (blue) and at the second excited singlet state optimal geometry for P-$C_{20}H_{14}$ in THF (red). (*right*) Energies and isosurfaces of the HONTO and LUNTO of P-$C_{20}H_{14}$ in the ground and the second singlet excited states. S_0 and S_2 are the ground and excited states for P-$C_{20}H_{14}$ of the ground state. S_0 and S_2' are the ground and excited state intermediates for the minimum energy geometry of the second excited singlet state. The black solid and wavy arrows indicate absorption ($S_0 \rightarrow S_2$) or emission ($S_2' \rightarrow S_0'$) and vibrational relaxation ($S_2 \rightarrow S_2'$ and $S_2' \rightarrow S_2$), respectively. The theory level is TDDFT/RPA based on the B3LYP-D3/6-31+G* method.

The ground state, first and second excited singlet states of P-$C_{20}H_{14}$ in THF (Figure 2.3 and 2.32). Delocalization of excited energy levels in P-$C_{20}H_{14}$ was slightly enhanced,

leading to optical transitions of the first and second excited states with values of 399 and 409 nm, respectively (Figure 2.32).

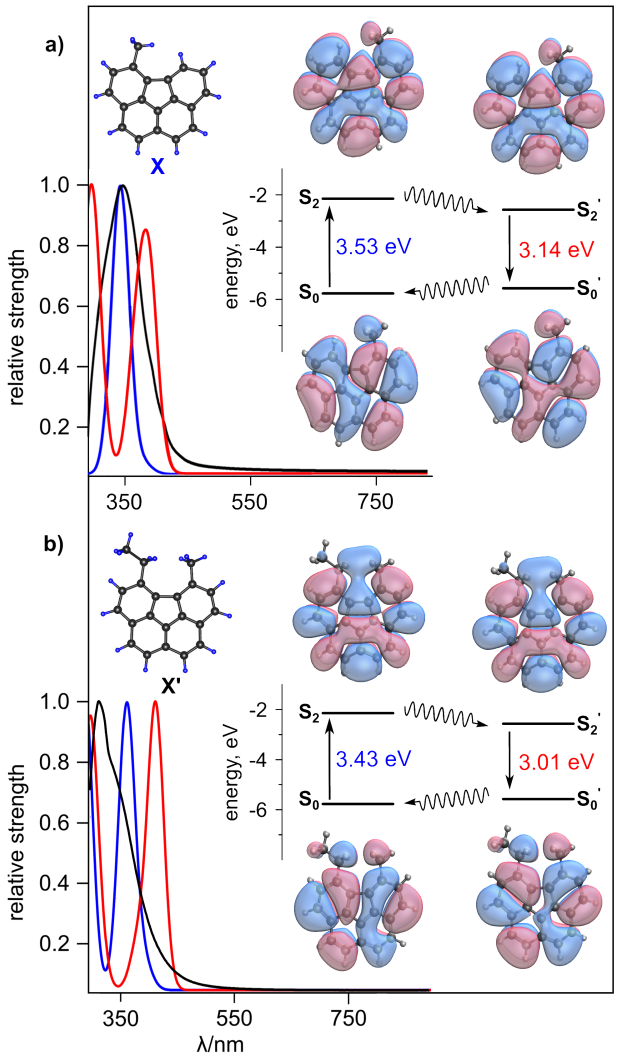

Figure 2.4 (a) Single-crystal X-ray structure of **X**. Optical transition strengths computed at the ground state optimal geometry for **X** in THF (blue) and at the second singlet excited state optimal geometry for **X** in THF (red). (*right*) Energies and isosurfaces of the HONTO and LUNTO of **X** in the ground and the second singlet excited states. (b) Geometrically optimized structure of **X'**.Optical transition strengths computed for **X'** in THF (blue) and at the second singlet excited state optimal geometry for **X'** in THF (red). (*right*) Energies and isosurfaces of HONTO and LUNTO of **X'** in the ground and the second singlet excited states. The theory level is TDDFT/RPA based on the B3LYP-D3/6-31+G* method.

As an alternative scalable approach to access a family of "open" corannulene-containing derivatives, we report a solution-phase route.[196] Despite a number of required steps (Schemes 2.2 and 2.3), in comparison with the one-step solid-state synthesis, the "solution" approach has some advantages since it does not rely on selection of the specific substrate/electron shuttle/reducing agent system and also provides a scalable route for synthesis of a library of new planar corannulene-type analogs. The synthetic details of preparation of 5-methylbenzo[*ghi*]fluoranthene ($C_{19}H_{12}$, **X**, Figure 2.4a) and 5-ethyl-6-methylbenzo[*ghi*]fluoranthene ($C_{21}H_{16}$, **X'**, Figure 2.4b) using this approach are provided in ESI. Sublimation of **X** (Scheme 2.2) allowed for the formation of single crystals of **X** suitable for X-ray diffraction (Figure 2.27). The structure of **X'** was confirmed using ^{1}H and ^{13}C NMR spectroscopy and mass spectrometry (Figure 2.24). As in the case of solid-state "open" P-$C_{20}H_{14}$, both **X** and **X'** structures possess a planar geometry (Figure 2.27 and 2.28). The emission studies of the prepared **X** and **X'** compounds revealed a red-shifted emission (λ_{max} = 548 nm and 573 nm, λ_{ex} = 365 nm, respectively, Figure 2.29) in contrast to pristine corannulene (λ_{max} = 490 nm, λ_{ex} = 365 nm, Figure 2.8). The emission maxima of **X** and **X'** in THF was found to be 479 nm and 502 nm, respectively, (λ_{ex} = 365 nm) and is hypsochromically shifted compared to the solid-state 548- and 573-nm-centered emission, respectively, (λ_{ex} = 365 nm, Figure 2.4a, 2.4b, 2.30, and 2.31). In a similar vein to TDDFT calculations of P-$C_{20}H_{14}$, we determined the optical transitions corresponding to the ground state, first and second excited singlet states of **X** and **X'** (Figure 2.30 and 2.31). While the electronic transition of the first excited singlet state for both **X** and **X'** did not differ from the

optical transitions corresponding to the ground state (351 nm for **X** and 361 nm for **X'**), optical transitions for the second excited singlet states were determined to be 395 nm and 412 nm for **X** and **X'**, respectively. Electronic transitions corresponding to the second excited singlet state can be associated with the emission profiles similar to the experimental data (see the ESI for more details).

To summarize, we report the first example of a unique one-step C=C bond cleavage in the traditionally very robust π-bowl occurring via an electron shuttle reaction. Such ring opening is unprecedented in the literature and has not been observed for pristine π-bowls (e.g., corannulene) to date (with the exception of uncontrollable brute force vacuum pyrolysis[148]). PAH hydrogenation has been previously observed under harsh experimental conditions (e.g., high hydrogen pressure or extreme temperatures above 1000 °C)[164–170], therefore the formation of P-$C_{20}H_{14}$ in a one-pot synthesis under relatively mild conditions is an unexpected and remarkable result. Through employment of Marcus theory, optical and crystallographic analysis, we estimated the electron coupling between "open" corannulene and a strong electron acceptor, TCNQ. A solution-phase route was employed for preparation of two novel "open" corannulene-based derivatives with the corresponding spectroscopic analysis of their properties experimentally and theoretically. Furthermore, through a combination of theoretical modeling with experimental results, mechanistic studies were undertaken to shed light on possible factors (such as strain energy) that could act as a driving force for the observed π-bowl opening. Our studies highlight the possibility to implement novel synthetic routes for π-bowl transformations, that are drastically different from the conventional approaches toward derivation of traditional PAHs. Thus, the presented

solid-state, solution, and theoretical methodology are the first steps toward understanding possible avenues to prepare barely accessible structures by "unlocking" the corannulene core and application of the latter for molecular electronic development.

EXPERIMENTAL

Compounds **I**–**V** were prepared according to a modified literature procedure.[1,2]

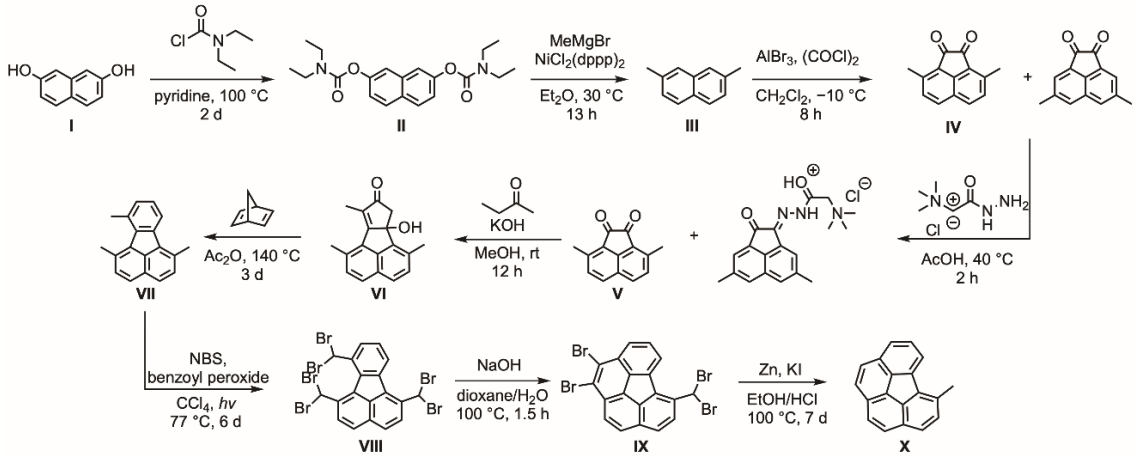

Scheme 2.2. Synthesis of 5-methylbenzo[*ghi*]fluoranthene (**X**).

The products (**X** and **X′**) and several precursors were characterized by ^{1}H and ^{13}C NMR spectroscopy and mass spectrometry (Figure 2.21–2.24). For the synthesis of the "open" corannulene analogs, instead of 3-pentanone utilized for traditional corannulene preparation,1 we used 2-butanone (route 1, step 5, Scheme 2.2) and 3-hexanone (route 2, step 5, Scheme 2.3). We were able to isolate and characterize the products: 1,6,7-trimethylfluoranthene (**VII**, Scheme 2.2, Figure 2.21) and 7-ethyl-1,6,10-trimethylfluoranthene (**VII'**, Scheme 2.3, Figure 2.22) by single-crystal X-ray diffraction in addition to spectroscopic analysis. The lack of a methyl group (Scheme 2.2 and Figure 2.23) and additional ethyl group (Scheme 2.3 and Figure 2.24) on the fluoranthene core, in

comparison with the corannulene synthesis, allowed us to close only one side of the ring, resulting in formation of 5-methylbenzo[*ghi*]fluoranthene ($C_{19}H_{12}$, **X**) and 5-ethyl-6-methylbenzo[*ghi*]fluoranthene ($C_{21}H_{16}$, **X'**), respectively. Sublimation of the produced yellow powder (**X**, Scheme 2.2) in a sealed ampule at 200 °C allowed for the formation of single-crystals of **X** suitable for X-ray diffraction (Figure 2.27). The structure of **X'** was confirmed based on ^{1}H and ^{13}C NMR spectroscopy and mass spectrometry analysis (Figure 2.28). As in the case of solid-state "open" P-$C_{20}H_{14}$, both **X** and **X'** structures possess a planar geometry (Figure 2.27 and 2.28).

7-dihydro-8*H*-cyclopenta[*a*]acenaphthylene-8-one ($C_{18}H_{16}O_2$ (VI), Scheme 2.2).

Potassium hydroxide (0.35 g, 6.2 mmol) was dissolved in dry methanol (0.64 mL, 16 mmol) in a 5-mL Schlenk flask purged with nitrogen. Then, methyl ethyl ketone (0.22 mL, 2.5 mmol) and 3,8-dimethylacenaphthylene-1,2-dione (**V**, 54 mg, 0.26 mmol) were added to the flask under a nitrogen flow. The resulting mixture was stirred at room temperature for 12 hours and then the mixture was diluted with equal volume of water. The desired compound was extracted from the aqueous layer using dichloromethane (3 × 10 mL). The combined organic layers were neutralized with hydrochloric acid (1 mL, 3 M), washed with water (3 × 10 mL), and dried using magnesium sulfate. Dichloromethane was removed under reduced pressure, resulting in a brown oil (0.042 g), which was used without further purification.

1,6,7-trimethylfluoranthene ($C_{19}H_{16}$ (VII), Scheme 2.2).

Norbornadiene (0.18 mL, 1.8 mmol), 7-dihydro-8*H*-cyclopenta[*a*]□etraanion□ene-8-one (**VI**, 54 mg, 0.26 mmol), and acetic anhydride (2.2 mL, 23 mmol) were added in a 5-mL round bottom flask. The reaction mixture was heated at 140 °C for three days, cooled down to room temperature, and then a solution of sodium hydroxide (2.2 mL, 10 wt%) was added to quench the excess of acetic anhydride. The desired compound was extracted from the aqueous layer with dichloromethane (3 × 10 mL). The combined organic layers were washed with water (3 × 10 mL), dried using magnesium sulfate, and then dichloromethane was removed under reduced pressure. The resulting product was purified by column chromatography using cyclohexane to give 1,6,7-trimethylfluoranthene (**VII**, 35 mg, 68%) as a yellow solid. Single crystals of **VII** were obtained by slow evaporation of a saturated cyclohexane solution at room temperature. The detailed description for the crystallographic data collection and refinement details are given in Table 2.1. ^{1}H NMR ($CDCl_3$, 300 MHz): δ = 7.89 (1H, d, J = 7.5), 7.71–7.67 (2H, m), 7.38–7.28 (3H, m), 7.17 (1H, d, J = 7.6), 2.99 (3H, s), 2.90 (3H, s) and 2.89 (3H, s). ^{13}C NMR ($CDCl_3$, 101 MHz) δ = 141.08, 141.07, 139.01, 135.40, 133.39, 133.12, 132.98, 132.91, 132.89, 132.43, 130.74, 130.65, 127.04, 126.68, 126.11, 121.37, 25.64, 25.50, and 20.98 ppm (Figure 2.21). HRMS (EI, m/z) calculated for $C_{19}H_{16}$ $[M+H]^+$ 244.1303, found 244.1306.

1,6,7-tris(dibromomethyl)fluoranthene ($C_{19}H_{10}Br_6$ (VIII), Scheme S1).

Benzoyl peroxide (8.1 mg, 0.033 mmol), 1,6,7-trimethylfluoranthene (**VII**, 0.86 g, 3.5 mmol), *N*-bromosuccinimide (5.9 g, 33 mmol), and carbon tetrachloride (69 mL, 0.71

mol) were added in a 100-mL Schlenk flask purged with nitrogen. The reaction mixture was heated at 77 °C while irradiated with a 300 W lamp for six days. The solvent was removed under reduced pressure, and the obtained powder (1.4 g, 54%) was used without further purification.

1,2-dibromo-6-(bromomethyl)benzo[*ghi*]fluoranthene ($C_{19}H_8Br_4$ (IX), Scheme S1).

Sodium hydroxide pellets (24 mg, 0.59 mmol), 1,6,7-tris(dibromomethyl)fluoranthene (**VIII**, 51 mg, 0.071 mmol), dioxane (2.0 mL, 23 mmol), and water (0.79 mL, 44 mmol) were added in a 50-mL round bottom flask. The resulting mixture was heated at 100 °C for one and a half hours, cooled down to room temperature, followed by the addition of equal volume of water, and neutralized using 3 M hydrochloric acid. The precipitate was filtered, washed with water, and dried under reduced pressure. The resulting product was isolated with 27% yield (15 mg) and was used without further purification. HRMS (EI, m/z) calculated for $[C_{19}H_8Br_4+H]^+$: 555.7320, found 555.7321.

5-methylbenzo[*ghi*]fluoranthene ($C_{19}H_{12}$ (X), Scheme S1).

Zinc (0.71 g, 11 mmol), 1,2-dibromo-6-(bromomethyl)benzo[*ghi*]fluoranthene (**IX**, 59 mg, 0.11 mmol), potassium iodide (0.25 g, 1.5 mmol), ethanol (10 mL, 0.18 mol), and 4% hydrochloric acid (0.59 mL, 16 mmol) were added in a 15-mL round bottom flask. The reaction mixture was heated at 100 °C for seven days. Once the reaction mixture cooled to room temperature, solvent was removed under reduced pressure. The crude product was purified by a Soxhlet extraction procedure using dichloromethane as the solvent. The solvent was removed under reduced pressure, and the product was isolated as a yellow solid (**X**, 13 mg, 52 %). Sublimation of **X** in a sealed ampule at 200 °C allowed for the

formation of single crystals. The detailed description for the crystallographic data collection and refinement details are given in Table 2.1. ^{1}H NMR ($CDCl_3$, 400 MHz): δ = 8.14 (1H, d, J = 7.0), 7.99–7.84 (6H, m), 7.71 (1H, t, J = 7.5), 7.48 (1H, d, J = 8.1), 2.97 (3H, s). ^{13}C NMR ($CDCl_3$, 101 MHz): δ = 136.29, 131.37, 128.22, 127.65, 126.78, 126.72, 126.71, 126.61, 126.55, 126.49, 126.45, 126.08, 126.01, 125.99, 125.88, 125.14, 124.24, 125.05, and 19.91 (Figure 2.23). HRMS (EI, m/z) calculated for $[C_{19}H_{12}+H]^+$: 240.0939, found 240.0942.

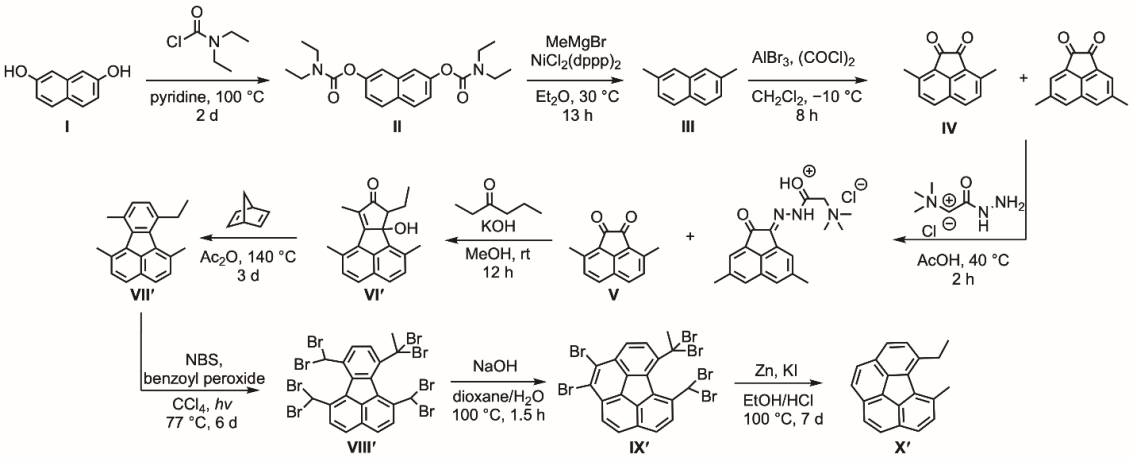

Scheme 2.3. Synthesis of 5-ethyl-6-methylbenzo[*ghi*]fluoranthene (**X′**).

7-ethyl-6b-hydroxy-1,6,9-trimethyl-6b,7-dihydro-8*H*-cyclopenta[*a*]tetraanion-ene-8-one ($C_{20}H_{20}O_2$ (VI′), Scheme 2.3).

Potassium hydroxide (0.35 g, 6.2 mmol) was dissolved in dry methanol (0.64 mL, 16 mmol) in a 5-mL Schlenk flask purged with nitrogen. Then, 3-hexanone (0.24 mL, 2.5 mmol) and 3,8-dimethylacenaphthylene-1,2-dione (**V**, 0.054 g, 0.26 mmol) were added to the flask under a nitrogen flow. After that, the resulting mixture was stirred for 12 hours at room temperature. Then, the mixture was diluted with an equal volume of water and the

desired compound was extracted from the aqueous layer using dichloromethane (3 × 10 mL). The combined organic layers were neutralized with hydrochloric acid (1 mL, 3 M), washed with water (3 × 10 mL), dried using magnesium sulfate, and dichloromethane was removed under reduced pressure, resulting in a brown oil (0.051 g), which was used without further purification.

7-ethyl-1,6,10-trimethylfluoranthene ($C_{21}H_{20}$ (VII′), Scheme 2.3).

Norbornadiene (0.18 mL, 1.8 mmol), 7-ethyl-6b-hydroxy-1,6,9-trimethyl-6b,7-dihydro-8*H*-cyclopenta[*a*]tetraanion-ene-8-one (**VI′**, 0.075 g, 0.26 mmol), and acetic anhydride (2.2 mL, 23 mmol) were added in a 5-mL round bottom flask. The resulting mixture was heated at 140 °C for three days, cooled down to room temperature, and a sodium hydroxide solution (2.2 mL, 10 wt%) was added to quench excess of acetic anhydride. The desired compound was extracted from the aqueous layer with dichloromethane (3 × 10 mL), washed with water (3 × 10 mL), and dried using magnesium sulfate. Dichloromethane was removed under reduced pressure. The resulting crude product was purified by column chromatography using cyclohexane to give 7-ethyl-1,6,10-trimethylfluoranthene (**VII′**, 57 mg, 81%) as a yellow powder. Single crystals of **VII′** were obtained by slow evaporation of a saturated cyclohexane solution at room temperature. The detailed description for the crystallographic data collection and refinement details are given in Table 2.1. ^{1}H NMR ($CDCl_3$, 300 MHz): δ = 7.68 (2H, d, J = 8.3), 7.37 (2H, dd, J = 8.3, 2.7), 7.19 (2H, sext, J = 6.3), 3.13 (2H, q, J = 7.5), 2.84 (3H, s), 2.81 (3H, s), 2.75 (3H, s), and 1.31 (3H, t, J = 7.5) ppm. ^{13}C NMR ($CDCl_3$, 101 MHz): δ = 139.89, 138.98, 136.45, 134.90, 134.83, 133.54, 131.97, 131.74, 131.69, 130.75, 129.51, 128.26, 126.51, 126.32,

126.02, 125.91, 28.46, 24.95, 24.63, 24.16, and 15.63 ppm (Figure 2.22). HRMS (EI, m/z): calculated for $[C_{21}H_{20}]^+$ 272.1565, found 272.1567.

7-(1,1-dibromoethyl)-1,6,10-tris(dibromomethyl)fluoranthene ($C_{21}H_{12}Br_8$ (VIII′), Scheme 2.3).

Benzoyl peroxide (0.35 mg, 0.0015 mmol), 7-ethyl-1,6,10-trimethylfluoranthene (**VII′**) (0.040 g, 0.15 mmol), *N*-bromosuccinimide (0.26 g, 2.1 mmol), and carbon tetrachloride (3.0 mL, 31 mmol) were added to a 5-mL Schlenk flask purged with nitrogen. The reaction mixture was heated at 77 °C while irradiated with a 300 W lamp for six days. After that, the solvent was removed under reduced pressure, and the solid was purified by a Soxhlet extraction procedure using ethanol as the solvent resulting in a brown powder (70 mg, 52%), which was used without further purification.

1,2-dibromo-5-(1,1-dibromoethyl)-6-(dibromomethyl)benzo[*ghi*]fluoranthene ($C_{21}H_{10}Br_6$ (IX′), Scheme 2.3).

Sodium hydroxide (0.12 g, 3.0 mmol), 7-(1,1-dibromoethyl)-1,6,10-tris(dibromomethyl)fluoranthene (**VIII′**, 0.025 g, 0.030 mmol), dioxane (3 mL, 35 mmol), and water (1 mL, 56 mmol) were added in a 10-mL round bottom flask. The reaction mixture was heated at 100 °C for one and a half hours, cooled down to room temperature, followed by the addition of water (4 mL), and neutralized using 3 M hydrochloric acid. The obtained precipitate was filtered, washed with water, and dried under reduced pressure. The resulting product (17 mg, 82%) was then used without further purification.

5-ethyl-6-methylbenzo[*ghi*]fluoranthene ($C_{21}H_{16}$ (X′), Scheme 2.3).

Zinc powder (0.36 g, 5.5 mmol), 1,2-dibromo-6-(bromomethyl)benzo[*ghi*]fluoranthene (**IX′**, 0.040 g, 0.053 mmol), potassium iodide (0.13 g, 0.78 mmol), ethanol (5.0 mL, 0.090 mol), and 4% hydrochloric acid (0.29 mL, 8.0 mmol) were added in a 10-mL round bottom flask. The reaction mixture was heated at 100 °C for seven days, cooled down to room temperature, and the solvent was removed under reduced pressure. The crude product was purified by a Soxhlet extraction procedure using dichloromethane as the solvent. The solvent was removed under reduced pressure and the product was isolated as a yellow powder (6.7 mg, 47 %). ^{1}H NMR ($CDCl_3$, 400 MHz): δ = 7.86 (1H, d, J = 8.6), 7.78-7.68 (5H, m), 7.65 (1H, d, J = 8.5), 7.49 (1H, d, J = 7.8), 2.78 (3H, s), 2.48 (2H, q, J = 7.4), and 0.98 (3H, t, J = 7.4) ppm. ^{13}C NMR ($CDCl_3$, 101 MHz): δ = 136.80, 135.96, 135.91, 135.69, 135.59, 134.76, 131.50, 130.95, 130.88, 130.52, 130.40, 127.06, 127.05, 126.99, 126.86, 126.69, 126.61, 125.74, 30.31, 27.48, and 18.82 ppm (Figure 2.24). HRMS (EI, m/z): calculated for $[C_{21}H_{16}]^+$ 268.1252, found 268.1249. **$C_{20}H_{10}$·$C_{20}H_{14}$·$C_{12}H_4N_4$ ($C_{52}H_{28}N_4$, 1)**.

A mixture of corannulene ($C_{20}H_{10}$, 15 mg, 0.060 mmol), 7,7,8,8-tetracyanoquinodimethane (TCNQ, 14 mg, 0.068 mmol), and zinc powder (50 mg, 0.76 mmol) was ground together followed by the addition of 3 μL of 12 M hydrochloric acid. Then, the resulting mixture was placed in a borosilicate glass ampule (diameter = 12.7 mm; length = 130 mm), which was flame-sealed under vacuum (4×10^{-5} mbar). The tube was placed in a sand bath at 200 °C, and the top end of the tube was wrapped with a piece of aluminum foil. After six days, brown rod-like crystals (**1**) formed (conversion yield 18%). Since the reaction is clean and there are only unreacted byproducts (e.g., corannulene), the conversion yield was determined based on the amount of starting material (corannulene)

that was converted to the product (P-$C_{20}H_{14}$). The obtained crystals were suitable for single-crystal X-ray analysis (Figure 2.5 and Table 2.1). Table 2.1 contains crystallographic refinement data for **1**. More detailed description of the crystal structure can be found in the *X-ray Crystal Structure Determination section* (vide infra). The mass spectrometry (MS) data is shown in Figure 2.6. The epifluorescence microscopy image of **1** and an emission spectrum of **1** collected from a single crystal are shown in Figure 2.8. Parent corannulene and TCNQ were also studied using the epifluorescence microscopy and photoluminescence spectroscopy (Figure 2.8).

$(C_{20}H_{10})_2 \cdot C_{12}H_4N_4$ ($C_{52}H_{24}N_4$, (corannulene)$_2$·TCNQ).

A mixture of corannulene (15 mg, 0.060 mmol), and TCNQ (14 mg, 0.068 mmol) was ground together. Then, the resulting mixture was placed in a borosilicate glass ampule (diameter = 12.7 mm; length = 130 mm), which was flame-sealed under vacuum (4×10^{-5} mbar). The tube was placed in a sand bath at 200 °C, and the top end of the tube was wrapped with aluminum foil.

After six days, brown rod-like crystals were formed. The obtained crystals were suitable for single-crystal X-ray analysis and match closely to the reported crystal structure. The MS spectroscopic data are shown in Figure 2.7.

$C_{16}H_{10} \cdot C_{12}H_4N_4 \cdot$($C_{28}H_{14}N_4$, pyr·TCNQ).

The pyrene and TCNQ (pyr·TCNQ) co-crystals were prepared according to a modified literature procedure. Pyrene (0.010 g, 0.050 mmol) and TCNQ (0.010 g, 0.050 mmol) were heated at reflux in a benzene/toluene mixture (1 mL / 1 mL) for two hours in a 5-mL round bottom flask. The reaction mixture was cooled to room temperature and after

one day of slow evaporation of the solvent, black crystals were obtained. The obtained crystals were suitable for single-crystal X-ray analysis (Figure 2.20). Table 2.1 contains crystallographic refinement data for $C_{16}H_{10}{\cdot}C_{12}H_4N_4$. More detailed description of the crystal structure can be found in the *X-ray Crystal Structure Determination section* (vide infra).

$C_{14}H_{10}{\cdot}C_{12}H_4N_4{\cdot}(C_{26}H_{14}N_4$, phenan·TCNQ).

The phenanthrene and TCNQ (phenan·TCNQ) co-crystals were prepared according to a modified literature procedure. Phenanthrene (13 mg, 0.074 mmol) and TCNQ (15 mg, 0.074 mmol) were ground together, and the resulting mixture was placed in a borosilicate glass ampule (diameter = 12.7 mm; length = 130 mm) before flame-sealing under vacuum (4×10^{-5} mbar). The tube was then placed in a sand bath at 200 °C with the top end of the tube wrapped with aluminum foil. After six days, brown rod-like crystals were isolated, and match closely to the reported one and their crystal structure.

Solution reactions.

A series of reactions were investigated in solution in attempts to repeat the results of the reduction reaction that occurred with corannulene in a sealed ampule. Starting with relatively lower boiling point solvents, such as dichloromethane and methanol, the same equivalents of the reagents were used (i.e., corannulene, TCNQ, Zn, and HCl), and heated at reflux in the solvent for six days. No evidence of the planar 5,6-dimethyl-benzo[*ghi*]fluoranthene was found through ^{1}H NMR spectroscopy or mass spectrometry. In order to more closely match the successful high temperature (200 °C) reaction conditions resulting in the formation of **1**, solvents such as ethylene glycol (b.p. = 197 °C) and glycerol

(b.p. = 290 °C) were used. In this case, no evidence of the planar 5,6-dimethyl-benzo[*ghi*]fluoranthene was also found through ^{1}H NMR spectroscopy or mass spectrometry.

In order to investigate if the type of electron shuttle used could make a difference in solution-based reactions, TCNQ, which was used in the formation of **1**, was replaced with methyl viologen, another common electron shuttle. Using the same conditions as above, still no product was observed through ^{1}H NMR spectroscopy and mass spectrometry.

In addition, the reducing agent (zinc) was replaced with sodium dithionite under the aforementioned reaction conditions, and there was no evidence of product formation.

In addition, we explored the Clemmensen reduction since it utilizes similar reagents (zinc and hydrochloric acid) to transform corannulene using a modified literature procedure. As a first step, zinc amalgam was prepared by combining zinc dust (29 mg, 0.44 mmol), mercury(II) chloride (2.5 mg, 9.2 μmol), and 0.13 mL of 3.5% hydrochloric acid in a round-bottom flask and stirred for five minutes. To a 10-mL round bottom flask, corannulene (25 mg, 0.10 mmol), ethanol (3 mL), and the prepared zinc amalgam were added. Finally, concentrated hydrochloric acid (2 mL) was added and the reaction mixture was heated at 80 °C for 3 days. The solvent was removed under reduced pressure and the residue was extracted with ethyl acetate (3 × 10 mL). The combined organic layers were washed with water (3 × 10 mL), dried over sodium sulfate, and then solvent was removed under reduced pressure. The resulting yellow oil was revealed to be corannulene based on ^{1}H NMR spectroscopy and mass spectrometry.

Electrochemical reactions.

An electrochemical Birch reduction was pursued to hydrogenate or cleave a C=C bond based on a literature procedure. To a glass cell vial, corannulene (15 mg, 0.060 mmol), lithium bromide in anhydrous THF (1.5 M, 3 mL), tripyrrolidinophosphine oxide (0.135 mL), 1,3-dimethylurea (5.3 mg, 0.060 mmol), and 1.8 mL of anhydrous THF were added. A magnesium electrode as the anode and stainless steel as the cathode were submerged in the solution and the resulting solution was purged with nitrogen for five minutes. Using Aftermath software, a chronopotentiometry experiment was set up and 10 mA was applied for 24 h (see Physical Measurements for more details). Then the solution was transferred to a round bottom flask and solvent was removed under reduced pressure. Diethyl ether (10 mL) and a saturated solution of sodium tartrate (10 mL) were added to the flask and stirred overnight. The solution was then extracted with diethyl ether (3 × 15 mL), and the combined organic layers were washed with water (3 × 15 mL). The organic layers were dried over magnesium sulfate and solvent was removed under reduced pressure to produce a yellow oil. The oil was analyzed and found only corannulene based on ^{1}H NMR spectroscopy and mass spectrometry.

X-ray Crystal Structure Determination.

Single-Crystal X-ray Structure of $C_{20}H_{10}\cdot C_{20}H_{14}\cdot C_{12}H_4N_4$ ($C_{52}H_{28}N_4$, 1).

X-ray intensity data from a dark brown needle were collected at 100(2) K using a Bruker D8 QUEST diffractometer equipped with a PHOTON-100 CMOS area detector and an Incoatec microfocus source (Mo Kα radiation, λ = 0.71073 Å). All of several crystals screened were found to be twinned by non-merohedry. From the crystal judged to

be the best quality, all reflections from a trial set of 569 could be indexed to two domains using the Cell_Now program. Orientation matrices for the two domains along with the twin law relating the domains were also derived using Cell_Now. The twin law is (-1 0 0.147 / 0 -1 0 / 0 0 1), corresponding to a two-fold rotation around the real-space [001] axis. The raw area detector data frames were reduced, scaled, and corrected for absorption effects using the Bruker APEX3, SAINT+, and TWINABS programs. The reported unit cell parameters were determined by least-squares refinement of 8512 reflections taken from both domains. The structure was solved by direct methods with SHELXT. Subsequent difference Fourier calculations and full-matrix least-squares refinement against F^2 were performed with SHELXL-2014 using OLEX2. The major twin domain volume fraction refined to 0.633(3).

The compound crystallizes in the triclinic system. The space group *P*–1 (No. 2) was confirmed by structure solution. The asymmetric unit consists of one $C_{20}H_{10}$ (corannulene) molecule, one $C_{20}H_{14}$ molecule, and half each of two $C_{12}H_4N_4$ (TCNQ) molecules. Both TCNQ molecules are located on crystallographic inversion centers. The corannulene molecule is disordered and was modeled with two orientations (A/B). The disorder takes the form of a near-180° rotation around an axis perpendicular to the central five-membered ring. Total group occupancy was constrained to sum to unity and refined to A/B = 0.611(5)/0.389(5). Similar sets of bonds between the two components were restrained to have approximately the same distances, using SHELX SADI instructions. These are: the two sets of five bonds each of the central C5 rings (e.g., C1–C2), the two sets of five bonds radiating from each central C5 ring (e.g., C1–C6), the two sets of five bonds outermost in each phenyl ring (e.g., C7–C8), and the remaining two sets of ten phenyl C–C bonds (e.g.,

C6–C7, C8–C9). Some atoms which appear nearly superimposed were assigned equal displacement parameters. In total 367 restraints were used in the disorder modeling. All non-hydrogen atoms were refined with anisotropic displacement parameters. Most hydrogen atoms bonded to carbon, including the methyl hydrogens of the $C_{20}H_{14}$ molecule, were located in Fourier difference maps before being placed in geometrically idealized positions and included as riding atoms (d(C–H) = 0.95 Å and U_{iso}(H) = 1.2U_{eq}I for aromatic hydrogen atoms and d(C–H) = 0.98 Å and U_{iso}(H) = 1.5U_{eq}I for methyl hydrogens). The methyl hydrogens were allowed to rotate as a rigid group to the orientation of maximum observed electron density. Anti-bumping restraints (d(H–H) > 2.0 Å) were applied to two sets of H atoms, H50A–H8B and H50A–H49C. The largest residual electron density peak in the final difference map is 0.43 e/Å^3, located 1.13 Å from H49A. This peak and the next highest peak lie between C49 and C50 and, though small in magnitude, were considered carefully. Ultimately, no reasonable alternative molecular model could be achieved; they most likely arise from a minor whole-molecule disorder component of this species.

Single-Crystal X-ray Structure of 1,6,7-trimethylfluoranthene ($C_{19}H_{16}$, VII).

X-ray intensity data from a colorless needle were collected at 100(2) K using a Bruker D8 QUEST diffractometer equipped with a PHOTON-100 CMOS area detector and an Incoatec microfocus source (Mo Kα radiation, λ = 0.71073 Å). The raw area detector data frames were reduced and corrected for absorption effects using the Bruker APEX3, SAINT+, and SADABS programs. The structure was solved with SHELXT. Subsequent difference Fourier calculations and full-matrix least-squares refinement against F^2 were performed with SHELXL-2018 using OLEX2.

The compound crystallizes in the orthorhombic system. The pattern of systematic absences in the intensity data was uniquely consistent with the space group $P2_12_12_1$, which was confirmed by structure solution. The asymmetric unit consists of one molecule. All non-hydrogen atoms were refined with anisotropic displacement parameters. Hydrogen atoms bonded to carbon were located in difference Fourier maps before being placed in geometrically idealized positions and included as riding atoms with d(C–H) = 0.95 Å and U_{iso}(H) = 1.2U_{eq}I for aromatic hydrogen atoms and d(C–H) = 0.98 Å and U_{iso}(H) = 1.5II for methyl hydrogens. The methyl hydrogens were allowed to rotate as a rigid group to the orientation of maximum observed electron density. The largest residual electron density peak in the final difference map is 0.19 e/Å^3, located 1.11 Å from C3.

Single-Crystal X-ray Structure of 7-ethyl-1,6,10-trimethylfluoranthene ($C_{21}H_{20}$, VII′).

X-ray intensity data from a colorless block were collected at 100(2) K using a Bruker D8 QUEST diffractometer equipped with a PHOTON-100 CMOS area detector and an Incoatec microfocus source (Mo Kα radiation, λ = 0.71073 Å). The raw area detector data frames were reduced and corrected for absorption effects using the Bruker APEX3, SAINT+, and SADABS programs. The structure was solved with SHELXT. Subsequent difference Fourier calculations and full-matrix least-squares refinement against F^2 were performed with SHELXL-2018 using OLEX2.

The compound crystallizes in the orthorhombic system. The pattern of systematic absences in the intensity data was consistent with the space groups *Pnma* and $Pna2_1$. The acentric group $Pna2_1$ was assigned by the solution program XT and was confirmed by structure solution. The asymmetric unit consists of one molecule. All non-hydrogen atoms

were refined with anisotropic displacement parameters. Hydrogen atoms bonded to carbon were located in difference Fourier maps before being placed in geometrically idealized positions and included as riding atoms with d(C–H) = 0.95 Å and U_{iso}(H) = 1.2U_{eq}I for aromatic hydrogen atoms, d(C–H) = 0.99 Å and U_{iso}(H) = 1.2U_{eq}I for methylene hydrogen atoms, and d(C–H) = 0.98 Å and U_{iso}(H) = 1.5U_{eq}I for methyl hydrogens. The methyl hydrogens were allowed to rotate as a rigid group to the orientation of maximum observed electron density. The largest residual electron density peak in the final difference map is 0.56 e/Å^3, located 0.72 Å from H19B. Because of the absence of heavy atoms in the crystal, Friedel opposites were merged during refinement and no attempt was made to determine the absolute structure.

Single-Crystal X-ray Structure of 5-methylbenzo[*ghi*]fluoranthene ($C_{19}H_{12}$, X).

Crystals formed as pale-yellow blocks. During screening, the diffraction patterns of several specimens showed strong low-angle diffraction diminishing rapidly in intensity at higher θ. The observed d_{max} was > 1 Å for all samples surveyed. This is caused by severe whole-molecule disorder within the crystals (see below). X-ray intensity data collected at 100(2) K using a Bruker D8 QUEST diffractometer equipped with a PHOTON-100 CMOS area detector and an Incoatec microfocus source (Mo Kα radiation, λ = 0.71073 Å). The raw area detector data frames were reduced and corrected for absorption effects using the Bruker APEX3, SAINT+ and SADABS programs. An initial structural solution was obtained with SHELXT. Subsequent difference Fourier calculations and full-matrix least-squares refinement against F^2 were performed with SHELXL-2018 using OLEX2.

The compound crystallizes in the monoclinic system. The pattern of systematic absences in the intensity data was uniquely consistent with the space group $P2_1/c$. The

asymmetric unit consists of two molecules. Initial solutions returned two independent regions of planar, nearly circular concentrations of electron density peaks, corresponding to the two molecules. No single, ordered molecule was evident among these nearly featureless disks of disordered peaks. Several disorder models were undertaken, beginning with two orientations of the target molecule per independent molecular site. This proved insufficient to account for the observed electron density and resulted in R_1-values greater than 17.5%. A somewhat improved model incorporated a third molecular orientation per site, though R_1-values are still high (*ca*. 15%). Molecular site occupancies were constrained to sum to one, and refined to: C1–C19(A/B/C) = 0.626(4)/0.310(4)/0.064(4) and C21–C39(A/B/C) = 0.570(4)/0.362(4)/0.068(4). Many restraints were necessary for the disorder modeling (total 1734 from 1918 data and 795 parameters). The C–C distances were restrained values similar to those found in the few planar benzofluoranthene structures reported in the literature. Further distance restraints were necessary to maintain six-membered ring geometries close to hexagonal (all opposite C–C distances per ring were restrained to be similar). Non-hydrogen atoms were refined with anisotropic displacement parameters except for the minor components of each independent molecule (atom label suffixes "C"). These were refined with a common isotropic displacement parameter for each molecule. All displacement parameters were restrained using an enhanced rigid-bond restraint (SHELX RIGU). Some nearly superimposed atoms were given equal anisotropic displacement parameters. Some disorder components were restrained to planarity using SHELX FLAT. Hydrogen atoms bonded to carbon were placed in geometrically idealized positions and included as riding atoms with d(C–H) = 0.95 Å and U_{iso}(H) = 1.2U_{eq}I for aromatic hydrogen atoms and d(C–H) = 0.98 Å and U_{iso}(H) = 1.5U_{eq}I for methyl

hydrogens. The largest residual electron density peak in the final difference map is 0.42 e/Å^3, located 0.46 Å from C12C. The absence of high-angle data due to the weak diffraction coupled with the extensive whole-molecule disorder requiring a large set of parameters results in a poor data-to-parameter ratio and an approximate, heavily restrained structural model.

Single-Crystal X-ray Structure of $C_{16}H_{10}\cdot C_{12}H_4N_4$, ($C_{28}H_{14}N_4$, pyr·TCNQ).

X-ray intensity data from a dark brown plate were collected at 100(2) K using a Bruker D8 QUEST diffractometer equipped with a PHOTON-100 CMOS area detector and an Incoatec microfocus source (Mo Kα radiation, λ = 0.71073 Å). The raw area detector data frames were reduced and corrected for absorption effects using the Bruker APEX3, SAINT+ and SADABS programs. Final unit cell parameters were determined by least-squares refinement of 9208 reflections taken from the data set. The structure was solved with SHELXT. Subsequent difference Fourier calculations and full-matrix least-squares refinement against F^2 were performed with SHELXL-2018 using OLEX2.

The compound crystallizes in the monoclinic system. The pattern of systematic absences in the intensity data was consistent with the space group $P2_1/n$, which was confirmed by structure solution. The asymmetric unit consists of half of one pyrene molecule and half of one TCNQ molecule, both located on crystallographic inversion centers. All non-hydrogen atoms were refined with anisotropic displacement parameters. Hydrogen atoms bonded to carbon were located in Fourier difference maps and refined freely. The largest residual electron density peak in the final difference map is 0.23 e/Å^3, located 0.72 Å from C3.

Table 2.1. X-ray structure refinement data for **1,** pyr·TCNQ, $C_{19}H_{16}$, $C_{21}H_{20}$, and $C_{19}H_{12}$.[a]

compound	**1**	pyr·TCNQ	$C_{19}H_{16}$	$C_{21}H_{20}$	$C_{19}H_{12}$
formula	$C_{52}H_{28}N_4$	$C_{28}H_{14}N_4$	$C_{19}H_{16}$	$C_{21}H_{20}$	$C_{19}H_{12}$
FW	708.78	406.43	244.32	272.37	240.29
T, K	100(2)	100(2)	100(2)	100(2)	100(2)
crystal system	triclinic	monoclinic	orthorhombic	orthorhombic	monoclinic
space group	*P*–1	$P2_1/n$	$P2_12_12_1$	$Pna2_1$	$P2_1/c$
Z	2	2	4	4	8
a, Å	10.5126(12)	6.9885(3)	5.0524(4)	9.8601(4)	18.410(3)
b, Å	13.2993(15)	10.0688(4)	15.7417(11)	9.0281(4)	11.5059(17)
c, Å	13.3298(15)	14.6611(5)	15.7910(11)	16.8983(6)	12.1836(18)
α, °	88.442(3)	90	90	90	90
β, °	84.692(3)	103.5890(10)	90	90	109.148(4)
γ, °	69.641(3)	90	90	90	90
V, Å^3	1739.7(3)	1002.76(7)	1255.91(16)	1504.3(10)	2438.1(6)
d_{calc}, g/cm^3	1.353	1.346	1.292	1.203	1.309
μ, mm^{-1}	0.080	0.082	0.073	0.068	0.074
F(000)	736.0	420.0	520.0	548.0	1008.0
crystal size, mm^3	0.4 × 0.06 × 0.06	0.16 × 0.12 × 0.06	0.22 × 0.06 × 0.04	0.18 × 0.14 × 0.08	0.22 × 0.10 × 0.08
theta range	4.47 to 50.052	4.954 to 55.126	5.16 to 50.088	5.116 to 55.106	4.684 to 37.68
index ranges	−12 ≤ h ≤ 12 −15 ≤ k ≤ 15 0 ≤ l ≤ 15	−9 ≤ h ≤ 8 −13 ≤ k ≤ 13 −19 ≤ l ≤ 18	−6 ≤ h ≤ 6 −17 ≤ k ≤ 18 −18 ≤ l ≤ 18	−12 ≤ h ≤ 12 −11 ≤ k ≤ 11 −21 ≤ l ≤ 21	−16 ≤ h ≤ 16 −10 ≤ k ≤ 10 −11 ≤ l ≤ 11
Refl. Collected	6143	20689	16295	62323	17727
data/restraints/ parameters	6143/367/666	2306/0/174	2212/0/176	3461/1/194	1918/1734/795
GOF on F^2	1.019	1.037	1.065	1.054	2.103
R_1/wR_2, $[I \geq 2\sigma(I)]^b$	0.0622/0.1365	0.0376/0.0856	0.0451/0.0924	0.0490/0.1159	0.1492/0.4106

[a]Mo-K$_\alpha$ (λ= 0.71073Å) radiation

[b]$R_1 = \Sigma||F_o| - |F_c||/ \Sigma |F_o|$, $wR_2 = \{\Sigma [w(F_o^2-F_c^2)^2]/ \Sigma [w(F_o^2)^2]\}^{1/2}$

Physical measurements.

An Edinburgh FS5 fluorescence spectrometer equipped with a 150 W Continuous Wave Xenon Lamp source for excitation was used to acquire steady-state emission spectra. Emission measurements on solutions were measured using a standard cuvette holder (SC-05) and measurements were collected in quartz cuvettes in THF. In addition, emission measurements on single crystals were collected on an Ocean Optics UV-4000 spectrometer connected to an epifluorescence microscope using a 450 μm SMA fiber optic cable. Epifluorescence microscope images were collected on an Olympus BX51 microscope equipped with a 120 W mercury vapor short arc excitation light source. An Ocean Optics JAZ spectrometer was used for diffuse reflectance measurements with an Ocean Optics ISP-REF integrating sphere connected to the spectrometer using a 450 μm SMA fiber optic cable. The samples were placed in a 6.0 mm quartz sample cell with a cover and placed on top of the integrating sphere. An Ocean Optics WS-1 Spectralon® reference standard was placed on the sample cell throughout the measurements. Absorption spectra were collected on a PerkinElmer Lambda 35 UV-vis spectrometer. FTIR spectra were collected on a PerkinElmer Spectrum 100. A WaveDriver 20 Bipotentiostat combined with Aftermath software was employed to carry out bulk electrolysis experiments in anhydrous *N,N*-dimethylformamide as well as chronopotentiometry experiments in anhydrous tetrahydrofuran. NMR spectra were obtained on a Bruker Avance III-HD 300 and Bruker Avance III 400 MHz NMR spectrometers. ^{13}C and ^{1}H NMR spectra were referenced to natural abundance ^{13}C peaks and residual ^{1}H peaks of deuterated solvents, respectively. A VG70S magnetic sector mass spectrometer was used to record the mass spectra of the

prepared compounds. Sample introduction was by direct probe with electron ionization (EI) at 70 eV.

Computational details.

The electronic structure calculations were performed using density functional theory (DFT), specifically the B3LYP functional paired with the 6-31G* basis to optimize the geometry and with 6-311+G** to obtain the excited electronic states, unless otherwise noted. For the latter, the Grimme′s dispersion correction has been invoked and the electronic excitations analysis is based on the time-dependent density functional theory (TDDFT) with the random phase approximation (RPA). The electronic structure method for geometry optimization has been selected after additional calculations, including the ground state geometry optimization of $C_{20}H_{12}$ at the MP2 and CCSD level using 6-31+G* and cc-pVDZ bases, that yielded marginal differences in geometry compared to the DFT results. Selected excited state calculations were performed using the LRC-ωPBEh density functional and, for experimentally relevant molecular models TCNQ and TCNQ/$C_{20}H_{10}$, yielded electronic excitations at slightly higher energies (by about 0.15 eV or 3-5%). All calculations were performed using Spartan16 and Q-Chem 5.2 software.

As the primary driving force of corannulene flattening, we considered corannulene strain energy. Based on an extensive literature analysis, we found a strain energy database for various polycyclic aromatic hydrocarbons (PAHs) among which extended carbon π-bowls were presented. Cheng and coworkers computationally estimated strain energy (*E*s) as a nonplanar distortion (E_{np}), i.e., *E*s = E_{np} Eqn (S1).

$$E_{\mathrm{np}} = \eta \times \Sigma \frac{m}{m+1} \quad \text{(S1)}$$

where η = 418.4 kJ/mol, the sum ($\Sigma \frac{m}{m+1}$) is over vertexes of a PAH, and m can be estimated as:

$$m = \frac{2\sin^2\left(\theta_{\sigma\pi}-\frac{\pi}{2}\right)}{\left(1-3\sin^2\left(\theta_{\sigma\pi}-\frac{\pi}{2}\right)\right.} \quad \text{(S2)}$$

where $\theta_{\sigma\pi}$ = the solid angle made by the π-orbital axis vector (POAV) commonly used as a parameter for estimation of molecule's curvature and it can be directly calculated from the molecule coordinates. According to this equation (Eqn(S1)), strain energy for planar PAH can be estimated as 0 kJ/mol since every vertex possess the parameter $\theta_{\sigma\pi} = \pi/2$, consequently, m = 0 and hence E_{np} and Es are equal to 0 kJ/mol.

The standard enthalpy changes during the C=C breaking process In Eqn (S3):

$$C_{20}H_{10} + 2H_2 \rightarrow C_{20}H_{14} \text{ (S3)}$$

is 49 kJ/mol. The electronic and the zero-point vibrational energies (ZPE) are –239 and 60 kJ/mol, respectively. Additional data on the energies are given in Table 2.2. Therefore, from a thermodynamics point of view, this process is not favorable, and we probed a possible driving force for this process – strain energy. We attempted to estimate how much energy is released due to strain energy during the planarization of corannulene as a result of the C=C bond breaking process (E'). The electronic component of released energy (E') was computed as the energy difference of the π-bowl energy with only the methyl units relaxed, and that of the fully relaxed P-$C_{20}H_{14}$ and was determined to be 202 kJ/mol. Similarly to the calculated strain energy from literature, released energy (E') was also estimated for several PAHs, such as phenanthrene, anthracene, pyrene, and coronene (Table 2.3). Comparison of released energy (E') and strain energy (E_s) calculated based on

Table 2.2. Electronic and zero-point vibrational energies (ZPE), and the total enthalpy at standard temperature and pressure (298 K, 1 atm). All geometries are optimized; the methods are B3LYP/6-31+G* and LRC-ωPBEh/6-31+G*.

Species	B3LYP			LRC- ωPBEh		
	E_{el}, a.u.	ZPE, kJ/mol	H^0, kJ/mol	E_{el}, a.u.	ZPE, kJ/mol	H^0, kJ/mol
$C_{20}H_{10}^{curved}$	–768.1727	608.449	641.206	–767.392	616.387	648.968
H_2	–1.17548	26.660	36.556	–1.1671	26.752	35.430
$C_{20}H_{14}$	–770.6147	721.301	759.701	–769.8266	729.376	769.525
$C_{20}H_{10}^{planar}$	–768.1578	607.550	644.240	–767.3763	615.052	645.905
$\Delta_{rxn} = C_{20}H_{14} – 2H_2 – C_{20}H_{10}^{curved}$; $\Delta_{inv} = C_{20}H_{10}^{planar} – C_{20}H_{10}^{curved}$ (all in kJ/mol)						
Δ_{rxn}	–239.05	59.532	49.383	–263.60	59.485	49.697
Δ_{inv}	38.962	–0.8990	3.0340	41.220	–1.3350	–3.0630

nonplanar distortions of the molecule are described for the aforementioned PAHs, highlighting the unique nature of corannulene. Namely, corannulene has strain and release energies of 101.4 and 202.0 kJ/mol, respectively, that is significantly higher than for the selected PAHs. From another perspective, we have also investigated a family of extended carbon π-bowls such as cyclopenta[*bc*]corannulene ($C_{22}H_{10}$), dicyclopenta[*bc,ef*]corannulene ($C_{24}H_{10}$), tricyclopenta[*bc,ef,kl*]corannulene ($C_{26}H_{10}$), tetracyclopenta[*bc,ef,hi,kl*]corannulene ($C_{28}H_{10}$), and half-buckminsterfullerene ($C_{30}H_{10}$) which also possess the curved geometry as corannulene molecule. Analysis of key factors

such as strain energy and estimated average released energy (Figure 2.13) for the carbon π-bowls revealed that all parameters are higher for the considered π-bowls than for corannulene (Table 2.4 and Scheme 2.4). For instance, half-buckminsterfullerene has a strain energy nearly four-fold higher (402 kJ/mol) than E_s of corannulene (101 kJ/mol, Table 2.4). Hydrogenation of C=C bond is more likely to be observed in the extended carbon π-bowls possessing even larger strain energy and released energy values compared to corannulene (Scheme 2.4). Therefore, the extended carbon π-bowls could be considered a class of compounds that undergo "unzipping" during a hydrogenation reaction due to high strain energy of the curved molecules.

Table 2.3. Strain energy (E_s) and released energy (E') for several polycyclic aromatic hydrocarbons (PAHs). Released energy was calculated using the B3LYP/6-31+G* level of theory.

PAH	E_s, kJ/mol	E', kJ/mol
phenanthrene	0.0	135.7
anthracene	0.0	119.4
pyrene	0.0	129.1
coronene	0.0	123.4
corannulene	101.4	202.0

Table 2.4. Strain energy (E_s) and average released energy (E'_{avg}) for several extended carbon π-bowls. Released energy was calculated using the B3LYP/6-31+G* level of theory.

Extended carbon π-bowl	E_s, kJ/mol	E'_{avg}, kJ/mol
corannulene	101.4	202.0
cyclopenta[*bc*]corannulene	175.3	239.3
dicyclopenta[*bc,ef*]corannulene	238.8	400.0
tricyclopenta[*bc,ef,kl*]corannulene	300.5	419.7
tetracyclopenta[*bc,ef,hi,kl*]corannulene	352.0	537.9
half-buckminsterfullerene	401.6	664.4

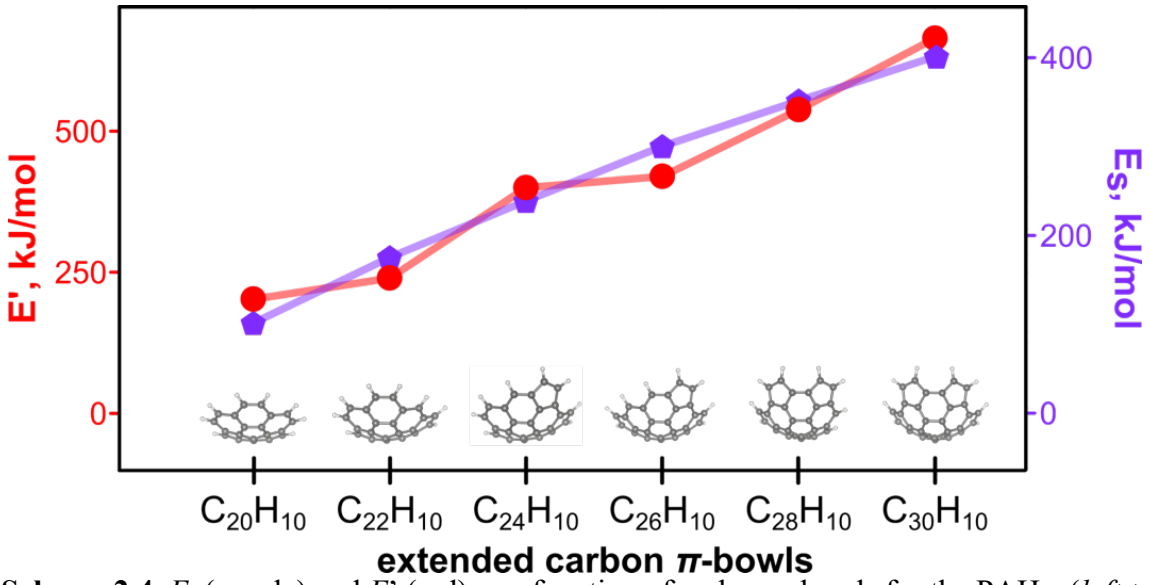

Scheme 2.4. E_s (purple) and E' (red) as a function of carbon π-bowls for the PAHs: (*left to right*) corannulene ($C_{20}H_{10}$), cyclopenta[*bc*]corannulene ($C_{22}H_{10}$), dicyclopenta[*bc*,*ef*]corannulene ($C_{24}H_{10}$), tricyclopenta[*bc*,*ef*,*kl*]corannulene ($C_{26}H_{10}$), tetracyclopenta[*bc*,*ef*,*hi*,*kl*]corannulene ($C_{28}H_{10}$), and half-buckminsterfullerene ($C_{30}H_{10}$).

We have also examined optical excitations of isolated corannulene, "unzipped" corannulene (P-$C_{20}H_{14}$), TCNQ, and the relevant dimers, employing B3LYP-D3/6-311+G** with the dispersion correction in the direct TDDFT calculation. The dispersion correction and a large basis set are employed to produce a more accurate representation of the dimer excitations. The atomic positions for all of the dimers are taken from the

experimental geometry of **1** and (corannulene)$_2$·TCNQ co-crystals. Co-crystals of (corannulene)$_2$·TCNQ consist of two types of columns along the *c*-axis: one with an alternating column with a repeating unit of one corannulene and one TCNQ similar to alternation of P-$C_{20}H_{14}$ and TCNQ molecules in **1**. In the case of TCNQ/$C_{20}H_{10}$ dimer, we examined three mutual orientations of TCNQ and corannulene molecules: TCNQ/$C_{20}H_{10}$/TCNQ, $C_{20}H_{10}$/TCNQ, and TCNQ/$C_{20}H_{10}$ (Figure 2.11). The results from the electronic excitations analysis are in line with the experimentally observed red emission: the TCNQ/P-$C_{20}H_{14}$ "stack" is the only species with excitation energies of appreciable strength around 1.8 eV (690 nm). The lowest excitations for TCNQ, π-bowl, and P-$C_{20}H_{14}$ were estimated to be 3.0, 4.3, and 3.6 eV (413, 288, and 344 nm), respectively (Figure 2.10).

Moreover, the calculated optical band at 1.8 eV corresponding to the TCNQ/P-$C_{20}H_{14}$ "stack" is attributed to the transition between the HOMO-2 and LUMO that are localized mostly on P-$C_{20}H_{14}$ and TCNQ, respectively (Figure 2.3). Such behavior is indicative of charge transfer (CT) between P-$C_{20}H_{14}$ and TCNQ molecules. Moreover, the TCNQ/P-$C_{20}H_{14}$ "stack" exhibits a significant dipole moment of 3.01 D directed towards TCNQ, and an electrostatic charge of −0.134 |e| on TCNQ compared to 1.90 D and −0.070 |e| corresponding to TCNQ/$C_{20}H_{10}$ "stack". Such a result is in line with the experimental evidence. Using the Kistenmacher relationship, the charge on the TCNQ molecules was evaluated based on crystallographic data of **1** and (corannulene)$_2$·TCNQ co-crystals. In the case of **1**, the charge on TCNQ was estimated to be –0.84 and for (corannulene)$_2$·TCNQ co-crystals was found to be –0.20. To understand the effect that a curved molecule can have on charge transfer, we compared electron couplings (that is proportional to CT rate)

of TCNQ/P-$C_{20}H_{14}$ and TCNQ/$C_{20}H_{10}$ "stacks". Following analysis reported by Shustova and co-workers, the electron couplings are estimated, according to the Marcus theory shown in Eqn (S4).

$$k = \frac{2\pi}{\hbar}\frac{|V_c|^2}{\sqrt{4\pi\lambda k_B T}} \cdot \exp\left(-\frac{(\lambda+\Delta G^0)^2}{4\lambda k_B T}\right) \sim |V_c|^2 \qquad \text{(S4)}$$

In Eqn (S4), k is charge transfer rate, λ is the reorganization energy of a system in response to "instantaneous" relocation of an electron from the donor to the acceptor, ΔG° is the difference in the energies of the initial and final states, V_c is the electron coupling constant, and T is the temperature. Eqn (S4) is applicable in the weak initial/final state coupling regime, $V_c << \lambda$. Within the simplest picture, the influence of the molecular environment on the donor and acceptor states is neglected; the initial electronic state is $|i\rangle = |D^-\rangle \times |A\rangle$, the final state is $|f\rangle = |D\rangle \times |A^-\rangle$, and the reorganization energy within the mean-field theory is estimated in Eqn (S5) as:

$$\lambda = E_D^{LUMO} - E_{A^-}^{HOMO} \qquad \text{(S5)}$$

The electron couplings have been estimated using the direct coupling method, defined for Hartree-Fock (HF) theory of the electronic structure. While the accuracy of the HF energies is limited by its mean-field character, the couplings are known to be more sensitive to the quality of the basis set, rather than to the electron correlation. Despite the different mutual orientation of TCNQ and corannulene molecules, electron couplings for TCNQ/P-$C_{20}H_{14}$ "stack" is higher than for TCNQ/$C_{20}H_{10}$ "stack" (Table 2.5 and Figure 2.11). In the case of TCNQ/$C_{20}H_{10}$/TCNQ geometry (Figure 2.11), electron coupling was estimated according to Eqn (S6).

$$V_c = \sqrt{V_c^{(1)} \cdot V_c^{(2)}} \quad \text{(S6)}$$

In Eq. (S5), $V_c^{(1)}$ and $V_c^{(2)}$ are electron couplings for $C_{20}H_{10}$/TCNQ and TCNQ/$C_{20}H_{10}$. Since electron coupling is related to electron transfer rate, we can surmise that there is likely an increased electron transfer rate as well.

Table 2.5. Electron couplings estimated by the direct coupling method for TCNQ/$C_{20}H_{10}$ "stack" with different mutual orientations and TCNQ/ P-$C_{20}H_{14}$ "stack". The theory level is HF/6-31+G*.

electron coupling V_c, eV			
TCNQ/$C_{20}H_{10}$	$C_{20}H_{10}$/TCNQ	TCNQ/$C_{20}H_{10}$/TCNQ	TCNQ/P-$C_{20}H_{14}$
0.0011	0.0899	0.0099	0.1405

Neutral corannulene molecule, $C_{20}H_{10}$, has a bowl depth of 0.87 Å (measured from the plane of the hub carbon atoms to the plane of rim carbon atoms) with an energy barrier for π-bowl inversion through a planar transition state of ~40 kJ/mol. According to the electronic structure calculations, a π-bowl can accommodate up to 4 electrons into its doubly degenerate low-lying LUMO. This analysis is in agreement with experiments on corannulene layered with Li and Li/Cs, forming "sandwiches" of charged π-bowls "sprinkled" with metal ions. Another doubly-degenerate orbital, LUMO+1 of energy –1.8 eV, may also contribute to the charge transfer properties and hydrogenation of the bond cleavage in corannulene. As shown in Table 2.6, addition of a negative charge flattens the π-bowl (measured from the plane of the hub carbon atoms to the plane of rim carbon atoms) and stretches the maximum C–C bond along its rim up to 6%, thus lowering the inversion

barrier to 25.4 kJ/mol for $C_{20}H_{10}^{2-}$. A similar trend of flattening of anionic bowls is reported in literature. For example, in the iconic findings of Petrukhina and co-workers, the bowl depth of the corannulene □etraanion was 0.29 Å compared to 0.88 Å of pristine corannulene. Interestingly, the presence of TCNQ in the reaction mixture also can affect the bowl flattering. For instance, in the alternating TCNQ/corannulene columns, the bowl depth of corannulene is reduced to 0.82 Å in comparison with that of parent corannulene (0.87 Å). The π-orbital axis vector (POAV) pyramidalization angle (another parameter for curvature estimation) was found to be 10% decreased for the alternating TCNQ/corannulene columns. These properties of charged corannulene may contribute to the C–C bond cleavage and formation of P-$C_{20}H_{14}$, characterized by the planar geometry of the structure.

Table 2.6. The bowl depth, bowl-inversion barrier ($E^{\dagger}$), and the maximum and average distance between rim carbons ($d(C_{rim}\text{-}C_{rim})$) for an isolated corannulene molecule computed at B3LYP/6-31+G* level of the electronic structure theory. The electronic energies for optimized molecular geometries are used.

Charge	0	1–	2–
Bowl depth, Å	0.87	0.83	0.78
$E^{\dagger}$, kJ/mol	39.0	30.9	25.4
$d(C_{rim}–C_{rim})_{max}$, Å	1.383	1.426	1.460
$d(C_{rim}–C_{rim})_{avg}$, Å	1.383	1.408	1.425

Furthermore, we proposed that the transformation of a buckybowl, $C_{20}H_{10}$, to a planar moiety, P-$C_{20}H_{14}$, occurs in a series of concomitant reactions that is first initiated by

a sequence of electron and proton transfers (Note that addition of a single electron to the species in Figure 1 creates stable anions). All geometries of intermediates ($C_{20}H_{11}^{\bullet}$, $C_{20}H_{12}$, and $C_{20}H_{13}^{\bullet}$) were optimized at the B3LYP/6-31+G* level of theory (Figures 2.14–2.16). For $C_{20}H_{12}$, three isomers were determined (Figure 2.16) and for one isomer, a C–C bond was cleaved and radicals were delocalized on the carbon atoms of the methyl groups. We estimated that the electronic component for bond dissociation energy ($E_{C–C}$) in $C_{20}H_{12}$ is 115 kJ/mol, that serves as evidence of the weak C–C bond. Moreover, an additional electron reduces $E_{C–C}$ to 9 kJ/mol in $C_{20}H_{12}^{-\bullet}$. For example, in a $RCH_2–CH_2R$ system where R is a pyrene core then the electronic energy of a C–C bond was found to be ~360 kJ/mol (Figure 2.17) or if R belongs to a benzo[*ghi*]fluoranthene core that is present in $C_{20}H_{12}$ or $C_{20}H_{12}^{-\bullet}$ intermediates, $E_{C–C}$ is estimated to be 224 kJ/mol (Figure 2.33). Thus, $C_{20}H_{12}$ and $C_{20}H_{12}^{-\bullet}$ intermediates have weaker C–C bonds that could potentially lead to C–C bond scission. We also probed two key driving forces of the C–C bond cleavage in $C_{20}H_{12}$ and $C_{20}H_{12}^{-\bullet}$: the aromaticity stabilization of formed radicals through delocalization over the conjugated aromatic system and strain energy release. As an analog of $C_{20}H_{12}$ without strain, we chose 1,2-dihydrocoronene ($C_{24}H_{14}$). The rationale of this choice is that $C_{20}H_{12}$ and $C_{24}H_{14}$ are derivatives of corannulene and coronene, respectively, that belong to one class of compounds – circulene. Another factor is that formed biradicals during C–C bond cleavage in both $C_{20}H_{12}$ and $C_{24}H_{14}$ are aromatic according to Hückel's rule (if cyclic hydrocarbons contain $4n+2$ π-electrons, it is aromatic), i.e., they contain 18 and 22 π-electrons, respectively. We estimated $E_{C–C}$ for $C_{20}H_{12}$ and $C_{24}H_{14}$ as well as released energy (Figure 2.18). The bond dissociation energy of a C–C bond in $C_{24}H_{14}$ is 302 kJ/mol (360 kJ/mol for typical C–C bond), which is over 2.5-fold stronger than the C–C bond found in

$C_{20}H_{12}$ suggesting that the driving force of C–C bond scission in $C_{20}H_{12}$ is not aromaticity stabilization. The determined released energy attributed to strain in $C_{24}H_{14}$ is only 10.8 kJ/mol, 15-fold less than the energy released from the partially hydrogenated and significantly strained π-bowl, $C_{20}H_{12}$ (163 kJ/mol). Thus, we argue that the high strain energy as well as high release energy of corannulene is a key factor facilitating the planarization of corannulene.

In relation to the presented experiments, we have examined the optical transitions corresponding to the ground state, the first and the second excited singlet states of **X**, **X′**, and P-$C_{20}H_{14}$ employing the B3LYP-D3/6-31+G* method with the dispersion correction in the direct TDDFT calculation. While the electronic transition of the first excited singlet state for both **X** and **X′** do not differ from the optical transitions corresponding to the ground state (3.53 eV for **X** and 3.43 eV for **X′**), optical transitions for the second excited singlet states were determined to be 3.14 eV and 3.01 eV for **X** and **X′**, respectively (Figures 2.30 and 2.31). A diagram of the electronic transitions pathway, presented in Figure 2.5, is shown for the molecular model of the **X** and **X′** molecules in THF media; S_0 and S_2 refer to the structures optimized in the ground electronic state and S_0' and S_2' refer to the geometry optimized in the second excited singlet state. Absorption is associated with the optical transition from $S_0 \rightarrow S_2$, with the largest contributions coming from the highest occupied natural transition orbital (HONTO) and lowest unoccupied natural transition orbital (LUNTO) of the ground state. Emission involves the $S_2' \rightarrow S_0'$ transition represented primarily by the LUNTO and HONTO of the second excited singlet state at the optimized geometry. Electronic transition analysis for P-$C_{20}H_{14}$ revealed that the optical transitions corresponding to the first and second excited singlet states have close

energies 3.11 and 3.03 eV, respectively (Figure 2.32). That verifies that excited energy levels are more delocalized in P-$C_{20}H_{14}$ compared to corannulene analogs, **X** and **X′**. Overall, electronic transition structures are similar for broken corannulene, P-$C_{20}H_{14}$ (Figure 2.4), and its analogs, **X** and **X′** (Figure 2.5).

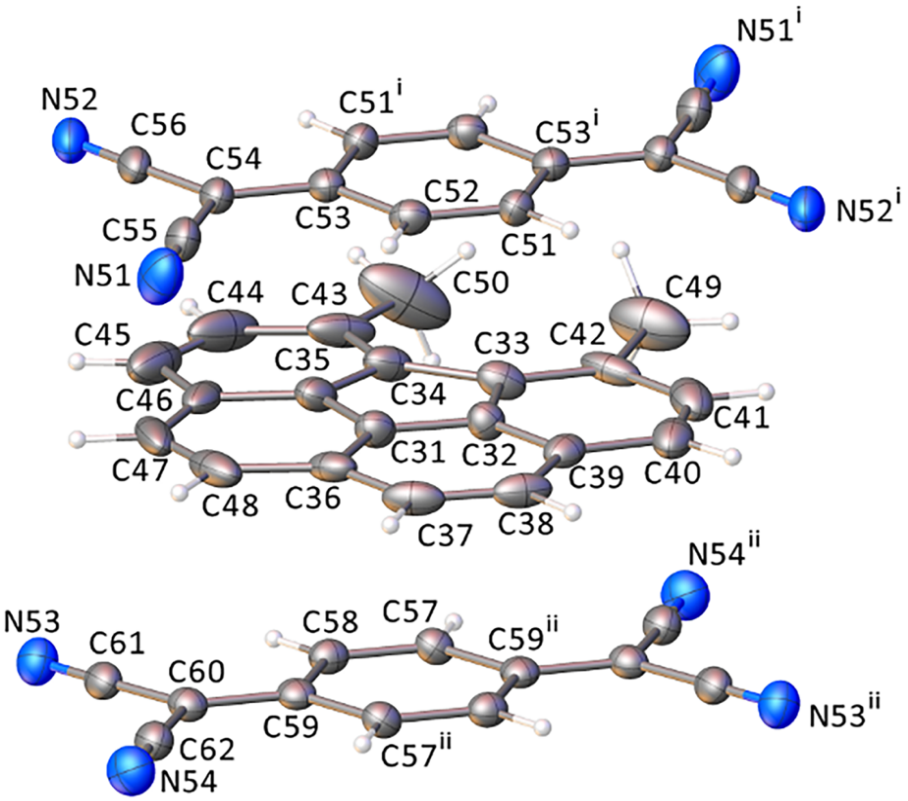

Figure 2.5. Crystal structure of **1**. Displacement ellipsoids drawn at the 40% probability level. Gray, blue, and white spheres correspond to carbon, nitrogen, and hydrogen atoms, respectively.

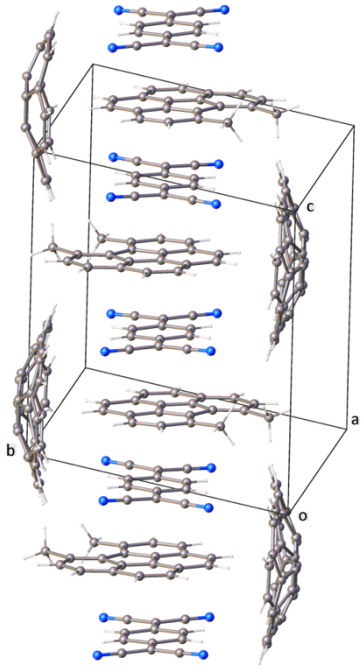

Figure 2.6. Packing of **1** along the *c*-axis. Gray, blue, and white spheres correspond to carbon, nitrogen, and hydrogen atoms, respectively.

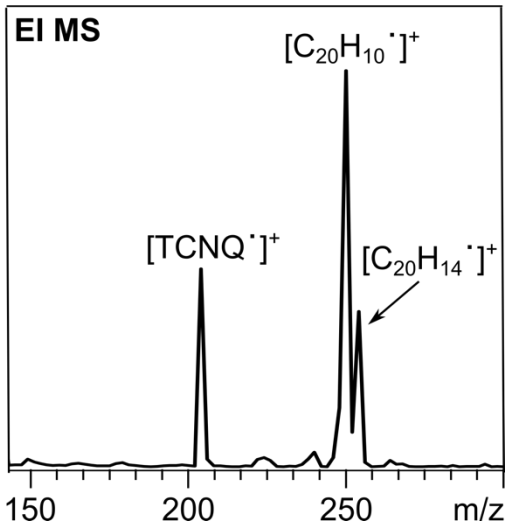

Figure 2.7. Mass spectrum of **1**.

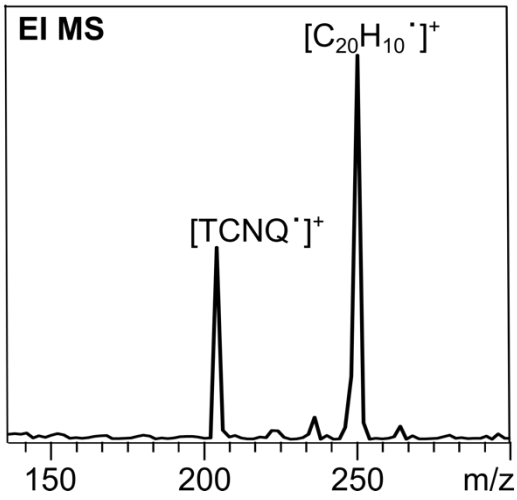

Figure 2.8. Mass spectrum of (corannulene)$_2$·TCNQ.

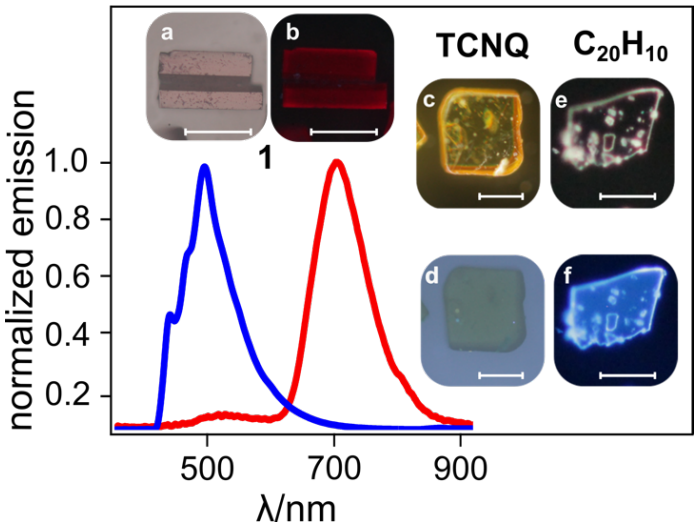

Figure 2.9. Normalized emission spectra of **1** (red) and corannulene ($C_{20}H_{10}$, blue) collected on corresponding single crystals. Epifluorescence images for single crystals of **1** (*a*), TCNQ (*c*), and $C_{20}H_{10}$ (*e*), and after λ_{ex} = 365 nm of **1** (*b*), TCNQ (*d*), and $C_{20}H_{10}$ (*f*). Scale bar represents 100 μm.

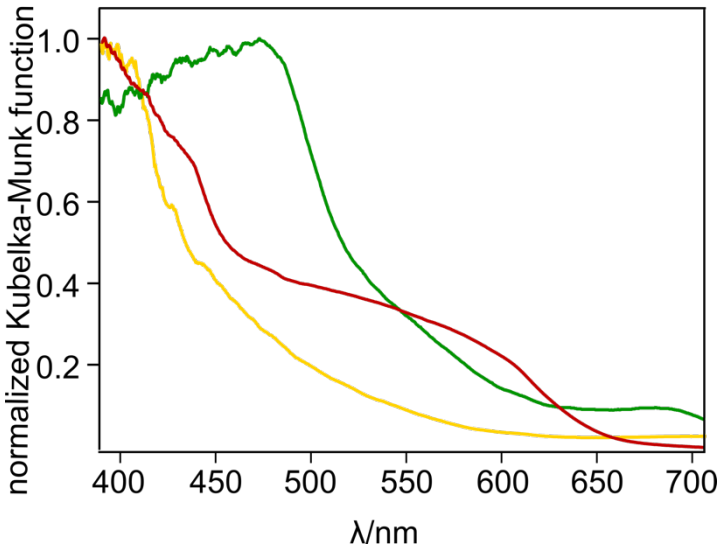

Figure 2.10. Normalized diffuse reflectance spectra of $C_{20}H_{10}$ (yellow), TCNQ (green), and **1** (red).

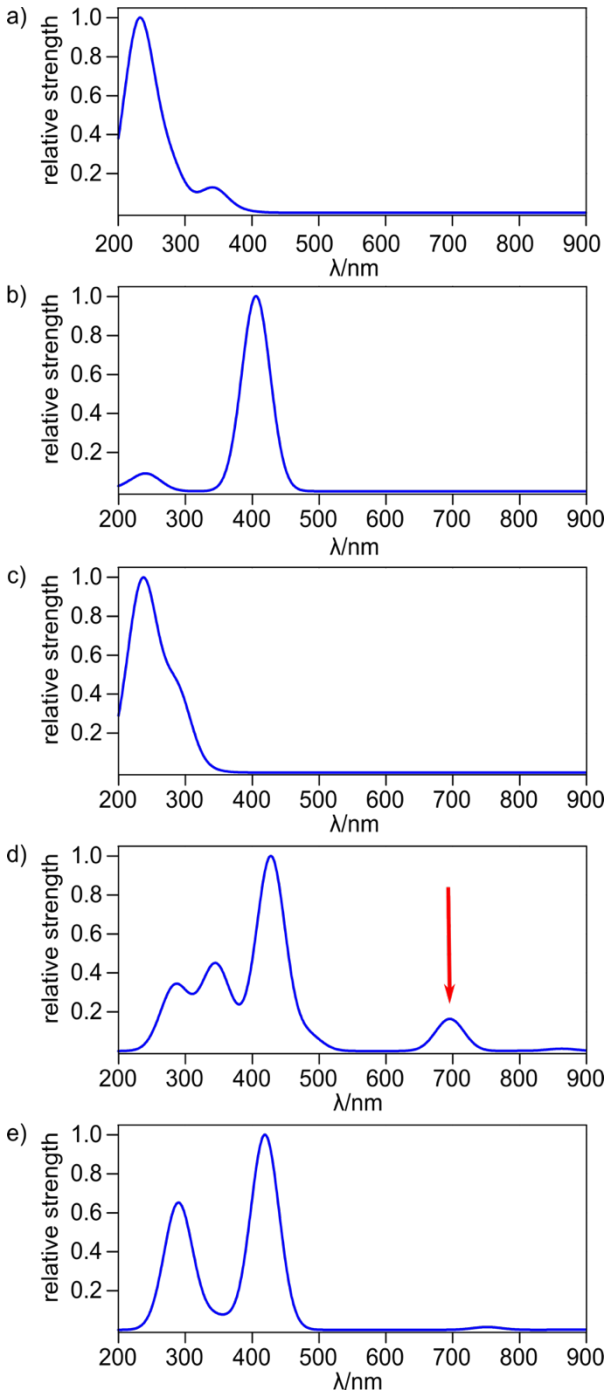

Figure 2.11 Optical transition strengths for the components of (*a*) P-$C_{20}H_{14}$, (*b*) TCNQ, (*c*) $C_{20}H_{10}$, (*d*) TCNQ/P-$C_{20}H_{14}$, (*e*) TCNQ/$C_{20}H_{10}$.

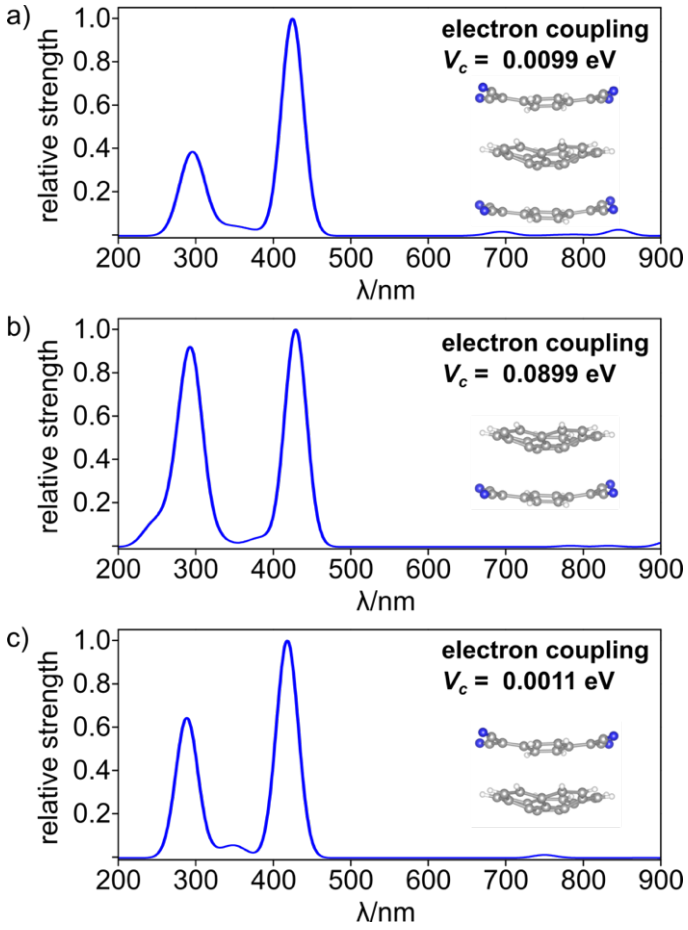

Figure 2.12 Optical transition strengths and the corresponding electron couplings for TCNQ/$C_{20}H_{10}$ "stack" with different mutual orientations: (*a*) TCNQ/$C_{20}H_{10}$/TCNQ, (*b*) $C_{20}H_{10}$/TCNQ, and I TCNQ/$C_{20}H_{10}$.

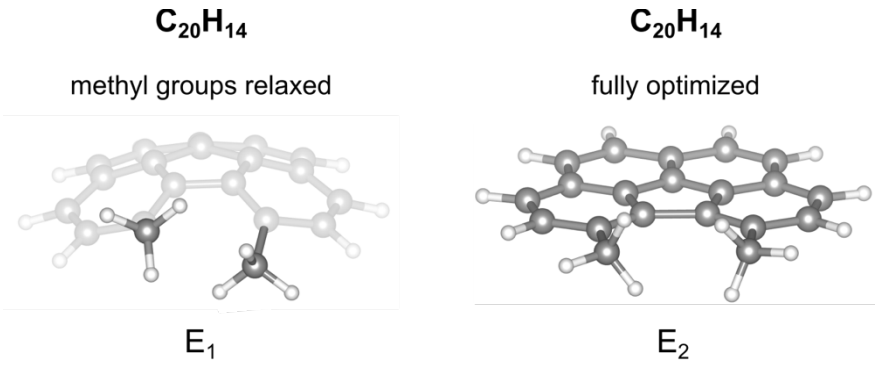

released energy : E' = E_1- E_2

Figure 2.13. Schematic representation of the technique for calculating the electronic component of released energy (*E′*) during planarization of $C_{20}H_{14}$. Highlighted are the atoms which positions were optimized. The theory level is B3LYP/6-31+G* as implemented in Qchem 5.2.

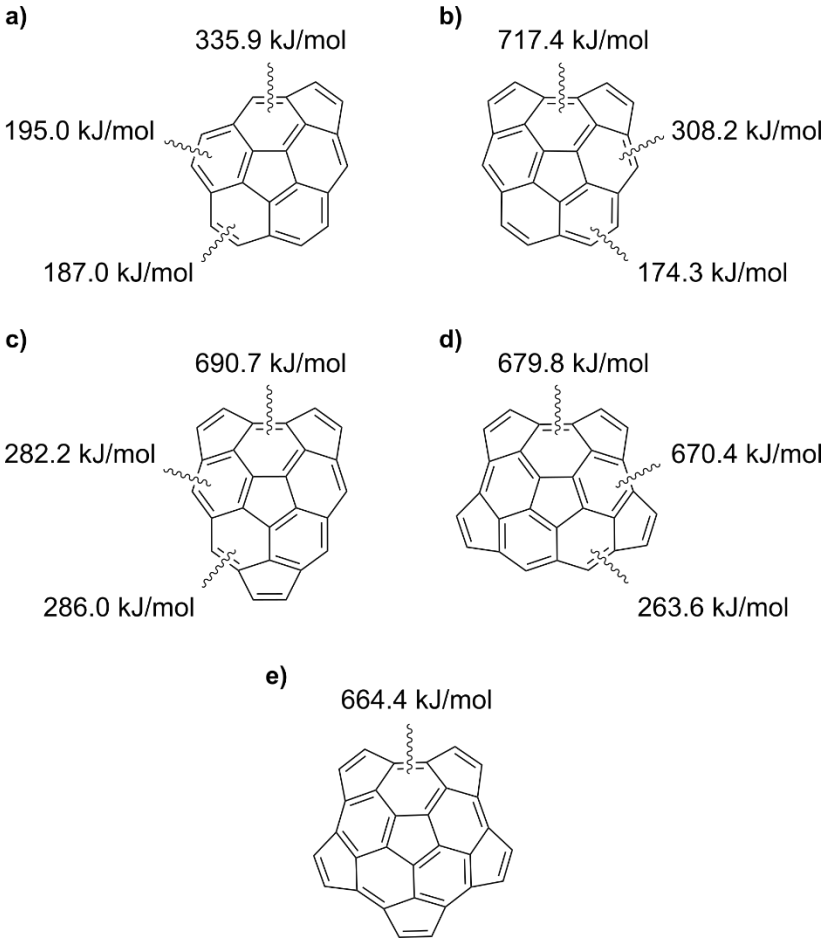

Figure 2.14 Released energy (*E′*) estimated for the cleavage of various C=C bond in: (*a*) cyclopenta[*bc*]corannulene, (*b*) dicyclopenta[*bc,ef*]corannulene, I tricyclopenta[*bc,ef,kl*] corannulene, (*d*) tetracyclopenta[*bc,ef,hi,kl*]corannulene, and (*e*) half-buckminsterfullerene.

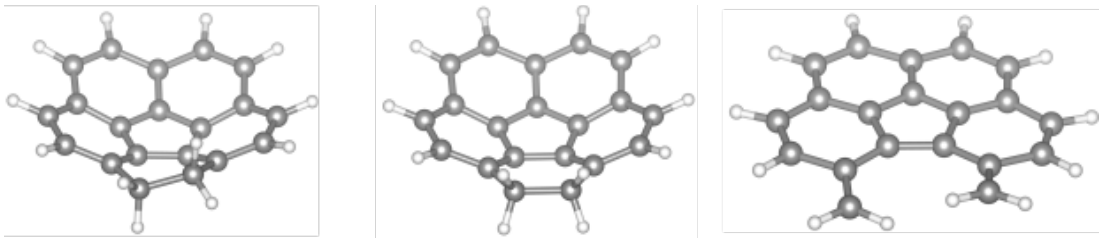

Figure 2.15. (*left to right*) Optimized geometries of three $C_{20}H_{12}$ isomers. The theory level is CCSD/cc-pVDZ.

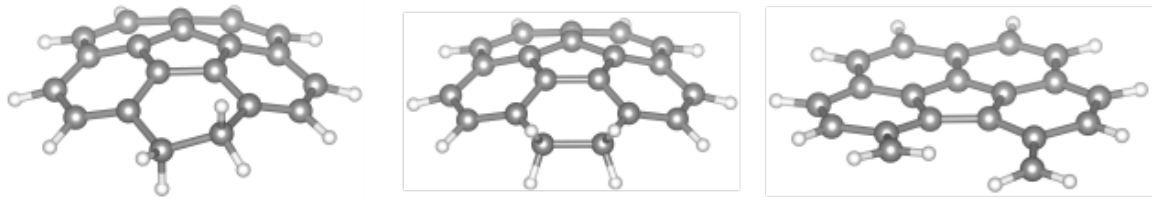

Figure 2.16. (*left to right*) Optimized geometries of three $C_{20}H_{12}^{-\bullet}$ isomers. The theory level is CCSD/cc-pVDZ.

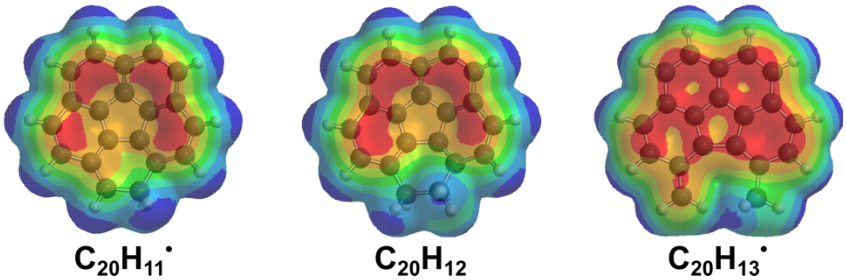

Figure 2.17 (*left to right*) Optimized geometries and molecular electrostatic potential (MEP) maps of $C_{20}H_{11}^{\bullet}$, $C_{20}H_{12}$, and $C_{20}H_{13}^{\bullet}$. The theory level is B3LYP/6-31+G*.

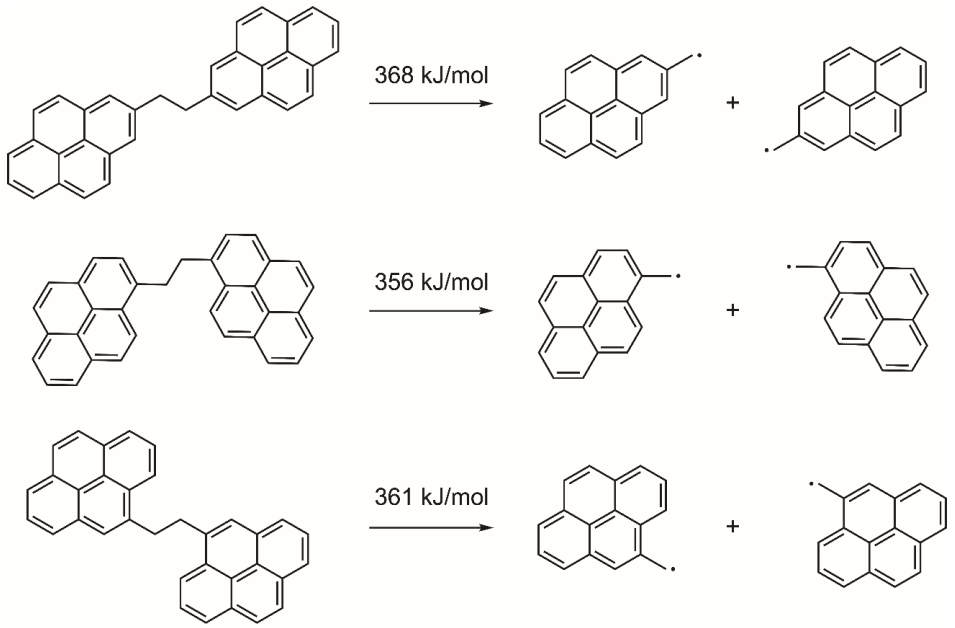

Figure 2.18. Estimation of the electronic component of $E_{C–C}$ in $RCH_2–CH_2R$ with R belonging to a pyrene core. The theory level is B3LYP/6-31+G*.

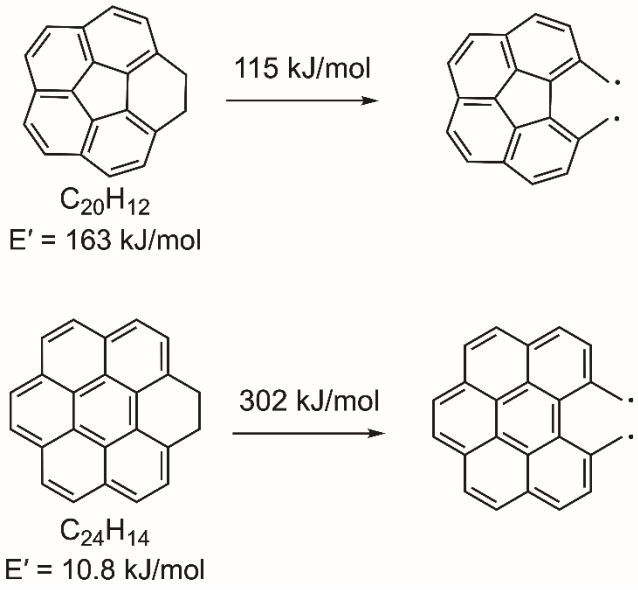

Figure 2.19 Estimation of the electronic component of $E_{C–C}$ and released energy in $C_{20}H_{12}$ and $C_{24}H_{14}$. The theory level is B3LYP/6-31+G*.

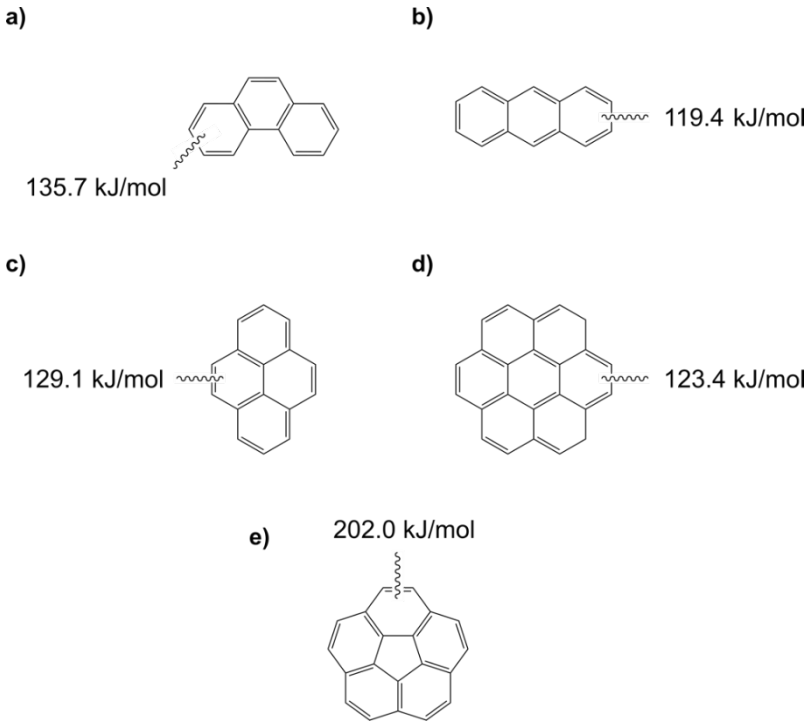

Figure 2.20 Released energy (*E'*) estimated for the cleavage of various C=C bond in: (*a*) phenanthrene, (*b*) anthracene, (*c*) pyrene, (*d*) coronene, and (*e*) corannulene.

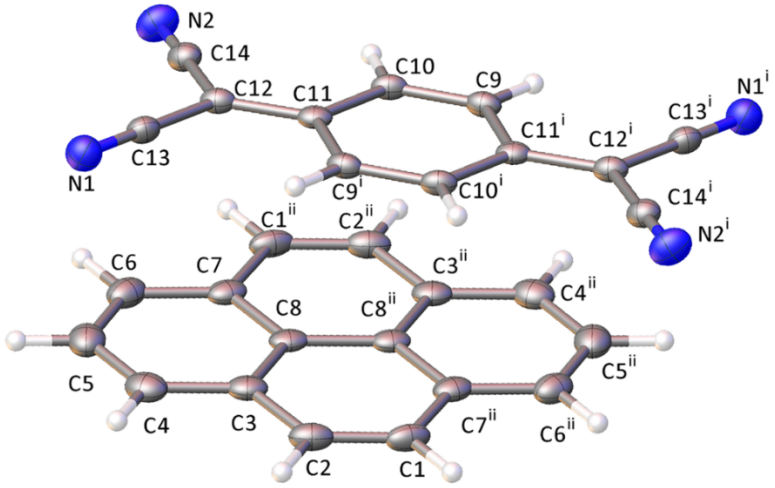

Figure 2.21. Crystal structure of $C_{16}H_{10}{\cdot}C_{12}H_4N_4$ (pyr·TCNQ). Displacement ellipsoids drawn at the 50% probability level. Gray, blue, and white spheres correspond to carbon, nitrogen, and hydrogen atoms, respectively.

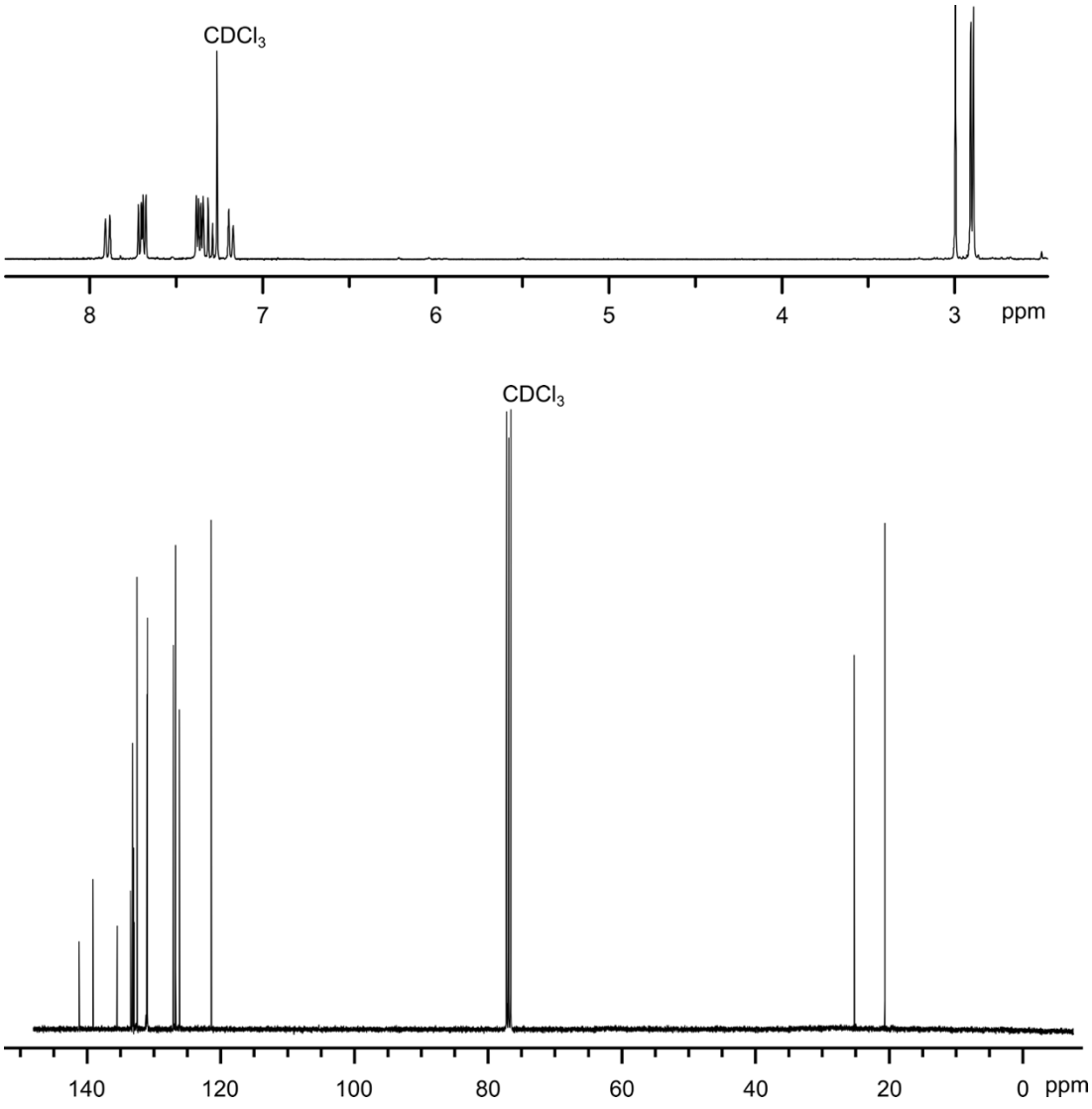

Figure 2.22. ^{1}H NMR and ^{13}C NMR spectra of 1,6,7-trimethylfluoranthene (Scheme 1, compound **VII**).

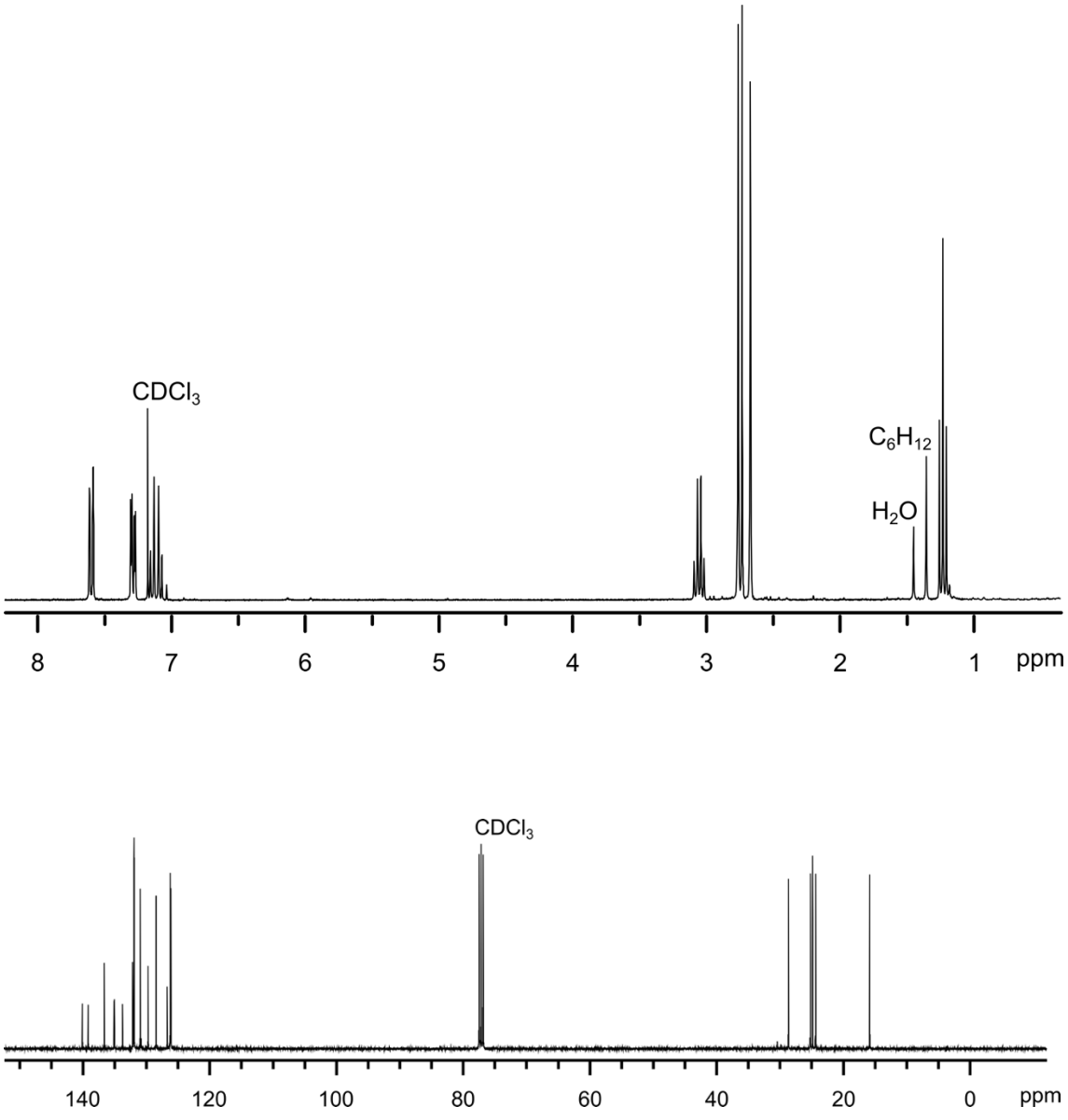

Figure 2.23. ^{1}H NMR and ^{13}C NMR spectra of 7-ethyl-1,6,10-trimethylfluoranthene (Scheme 2, compound **VII′**).

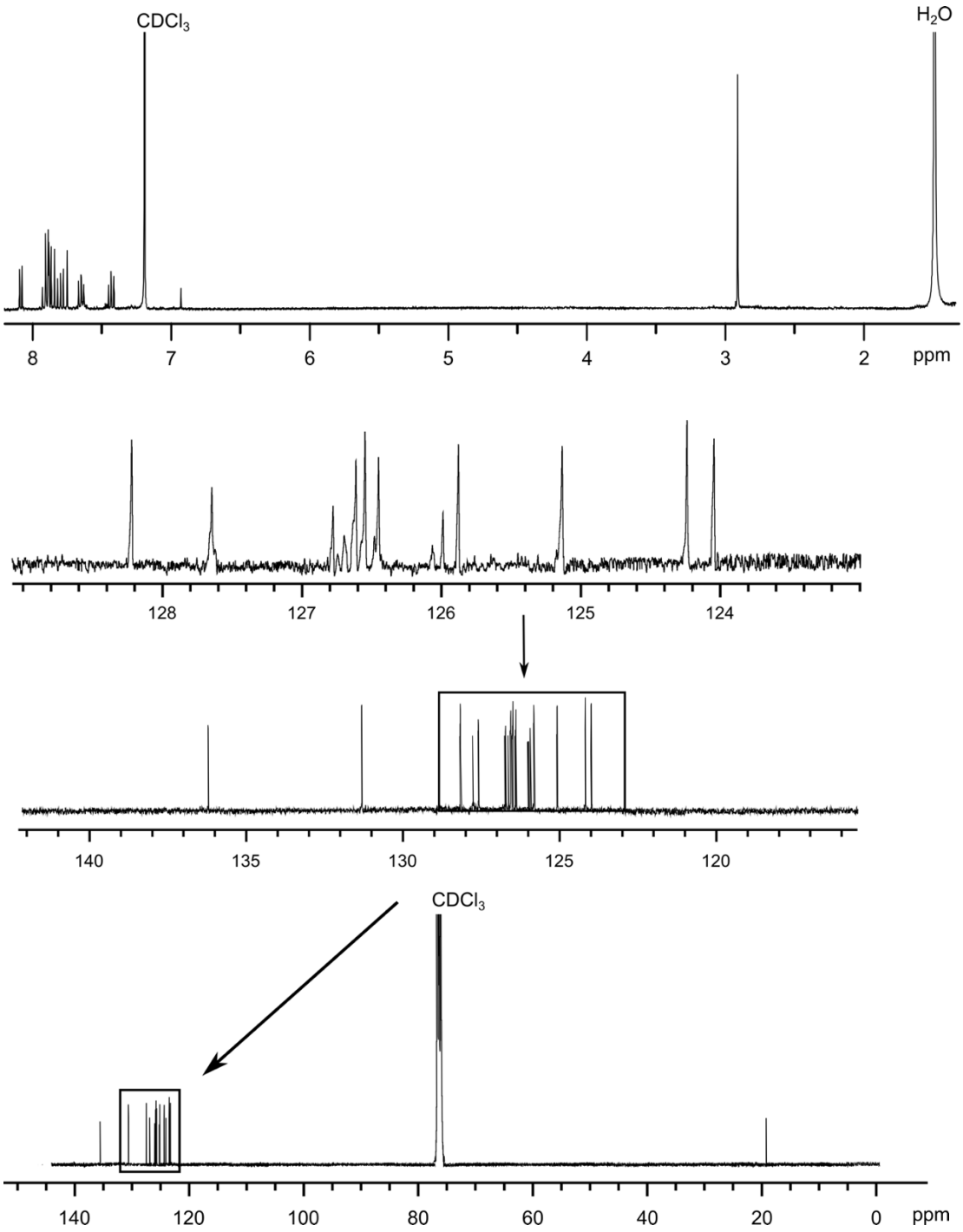

Figure 2.24 ^{1}H NMR and ^{13}C NMR spectra of 5-methylbenzo[*ghi*]fluoranthene (Scheme 1, compound **X**).

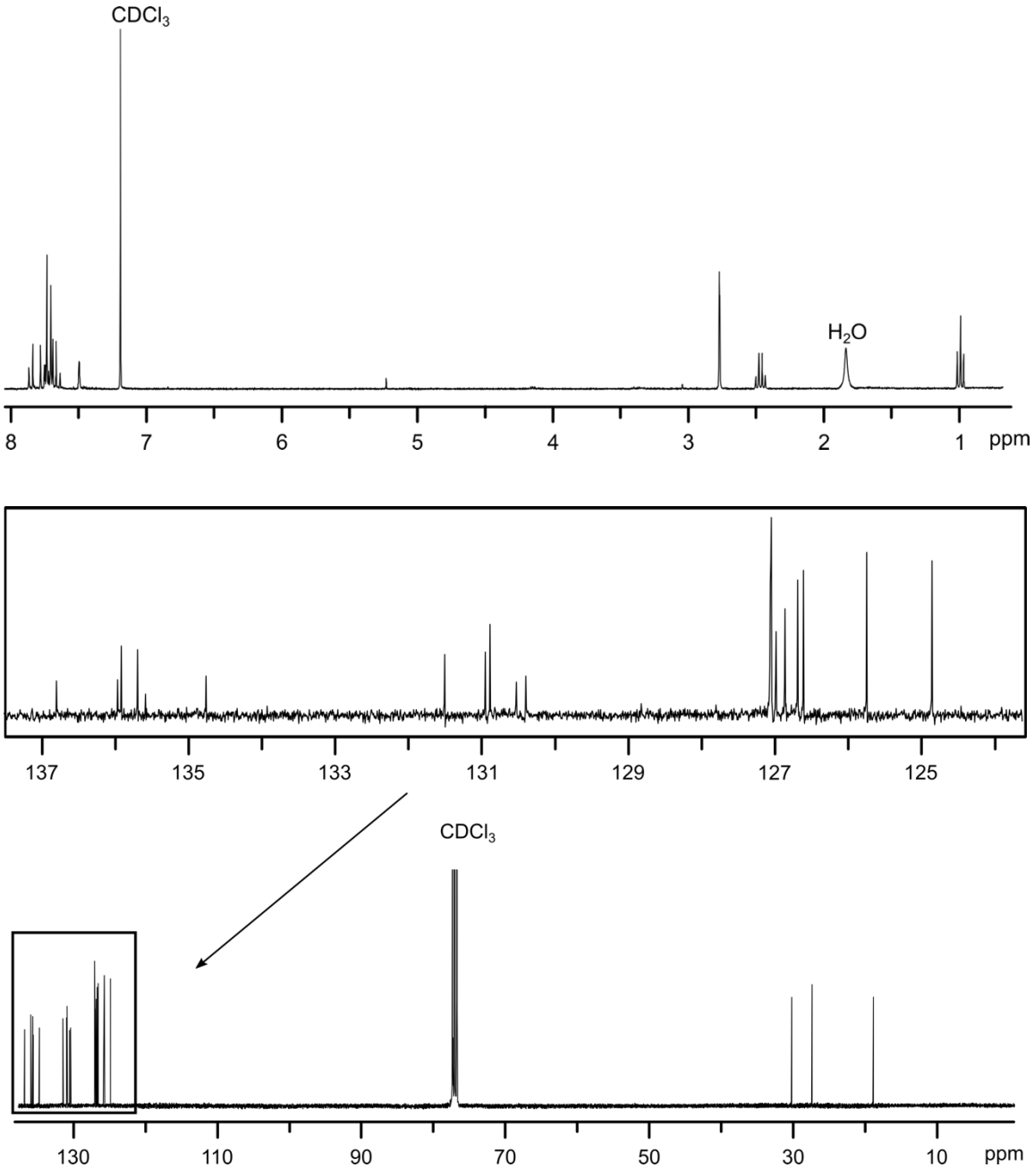

Figure 2.25. ^{1}H NMR and ^{13}C NMR spectra of 5-ethyl-6-methylbenzo[*ghi*]fluoranthene (Scheme 2, compound **X′**).

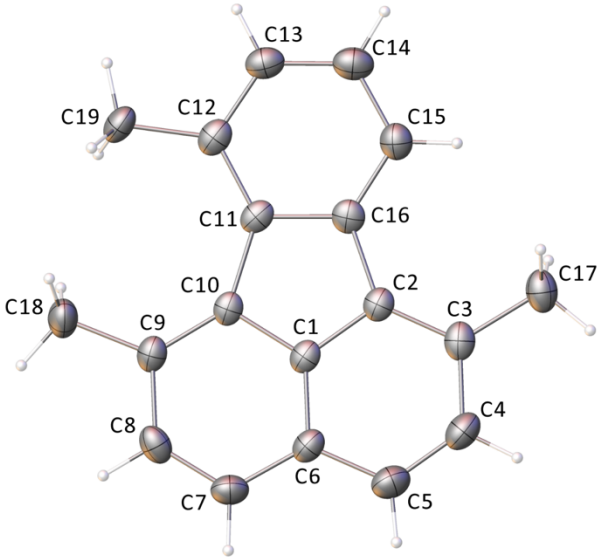

Figure 2.26 Crystal structure of 1,6,7-trimethylfluoranthene ($C_{19}H_{16}$, Scheme 1, compound **VII**). Displacement ellipsoids drawn at the 50% probability level. Gray and white spheres correspond to carbon, and hydrogen atoms, respectively.

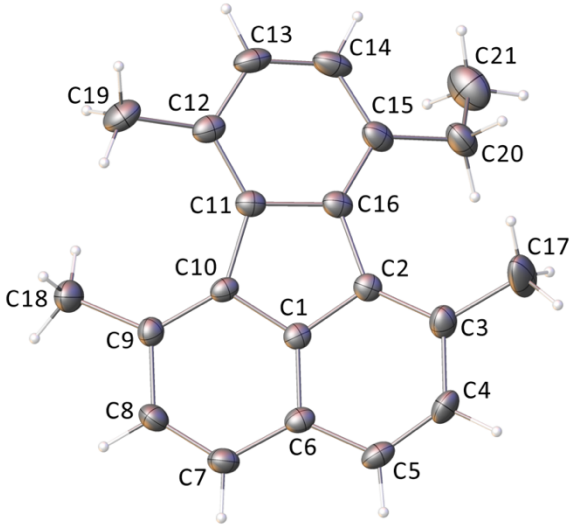

Figure 2.27 Crystal structure of 7-ethyl-1,6,10-trimethylfluoranthene ($C_{21}H_{10}$, Scheme 2, compound **VII′**). Displacement ellipsoids drawn at the 50% probability level. Gray and white spheres correspond to carbon, and hydrogen atoms, respectively.

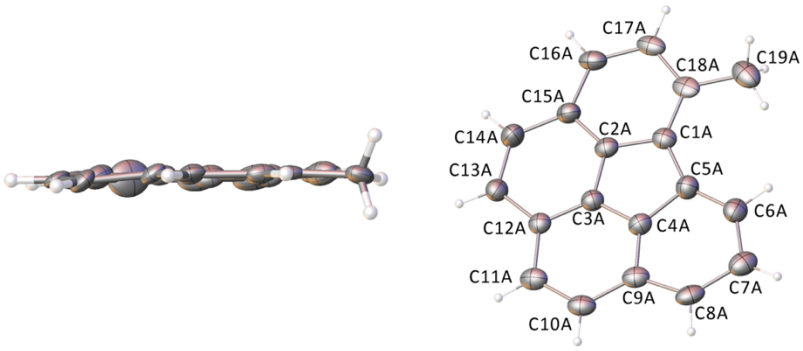

Figure 2.28 Crystal structure of 5-methylbenzo[*ghi*]fluoranthene.

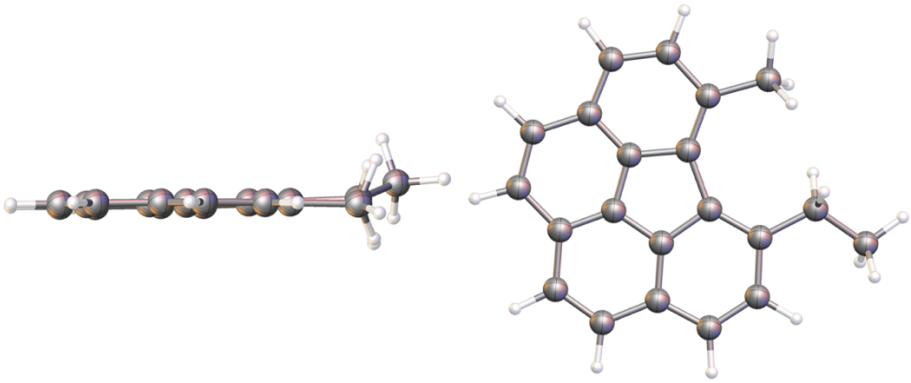

Figure 2.29 Optimized structure of 5-ethyl-6-methylbenzo[*ghi*]fluoranthene.

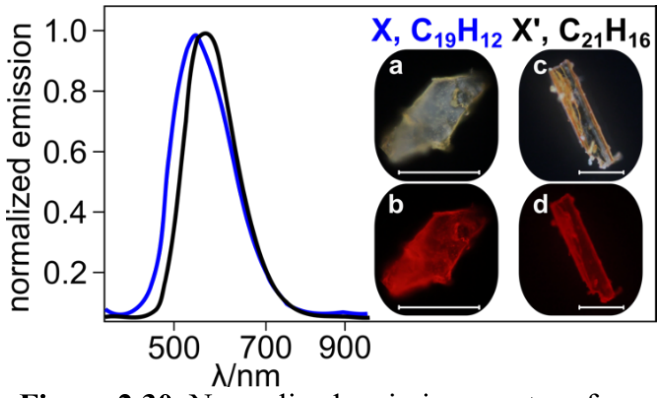

Figure 2.30. Normalized emission spectra of **X** (blue) and **X′** (black) collected on corresponding single crystals. Scale bar represents 50 μm

.

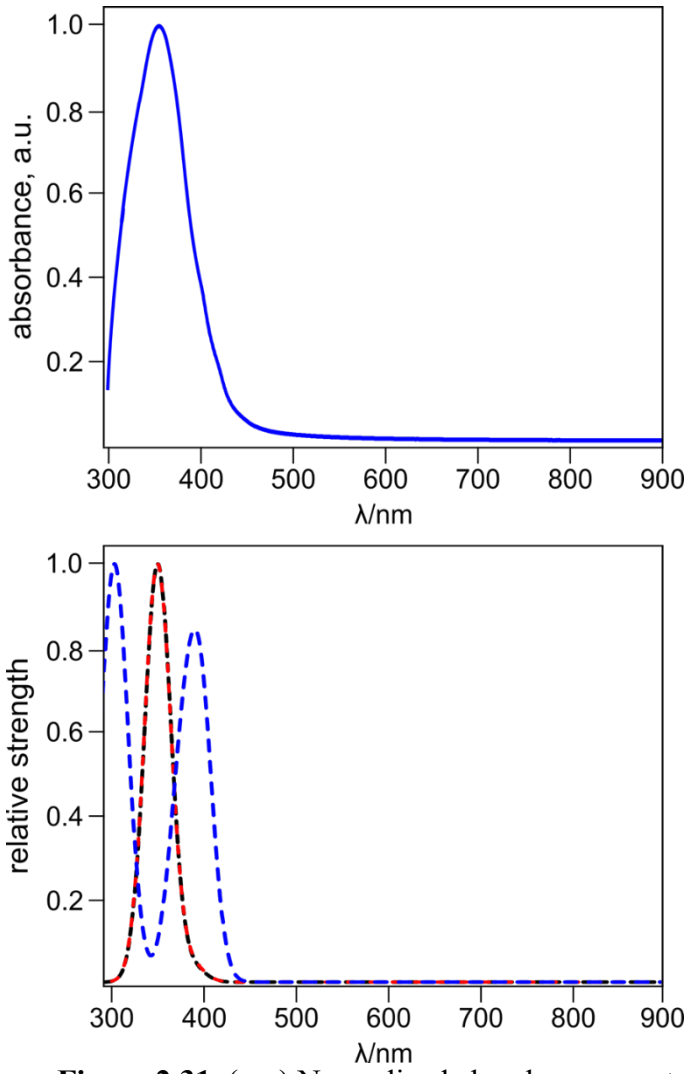

Figure 2.31. (*top*) Normalized absorbance spectrum of 5-methylbenzo[*ghi*]fluoranthene (**X**) in THF. (*bottom*) Optical transition strengths computed at the ground state optimal geometry for **X** in THF (black), at the first excited singlet state optimal geometry for **X** in THF (red), and at the second excited singlet state optimal geometry for **X** in THF (blue).

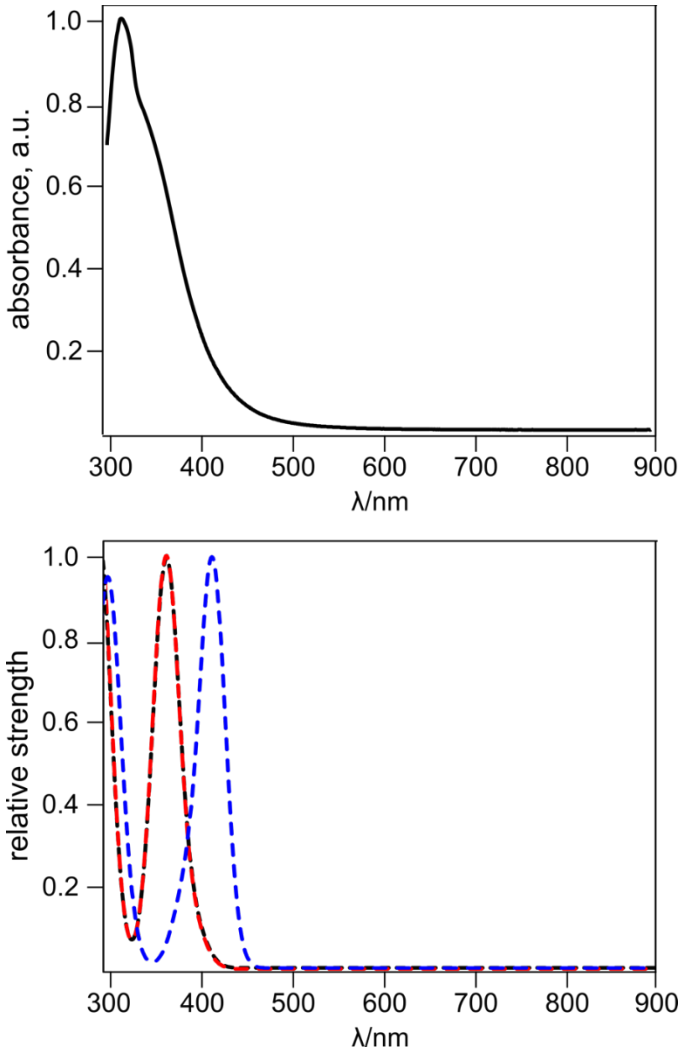

Figure 2.32 (*top*) Normalized absorbance spectrum of 5-ethyl-6-methylbenzo[*ghi*]fluoranthene (**X′**) in THF. (*bottom*) Optical transition strengths computed at the ground state optimal geometry for **X′** in THF (black), at the first excited singlet state optimal geometry for **X′** in THF (red), and at the second excited singlet state optimal geometry for **X′** in THF (blue).

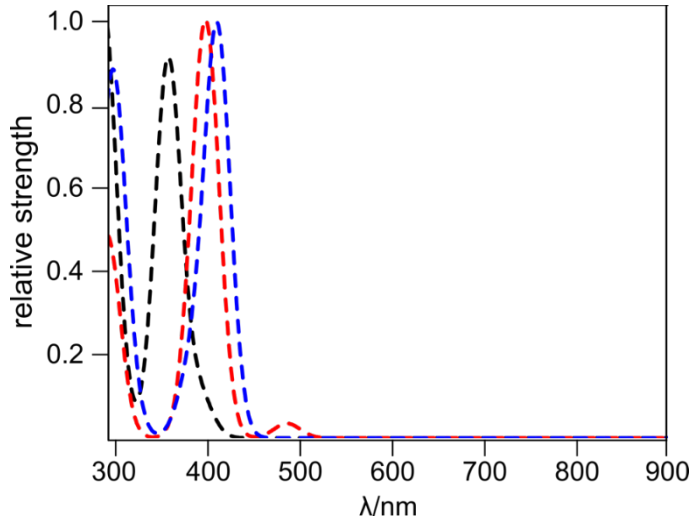

Figure 2.33. Optical transition strengths computed at the ground state optimal geometry for P-$C_{20}H_{14}$ in THF (black), at the first excited singlet state optimal geometry for P-$C_{20}H_{14}$ in THF (red), and at the second excited singlet state optimal geometry for P-$C_{20}H_{14}$ in THF (blue). The theory level is TDDFT/RPA based on B3LYP-D3/6-31+G*.

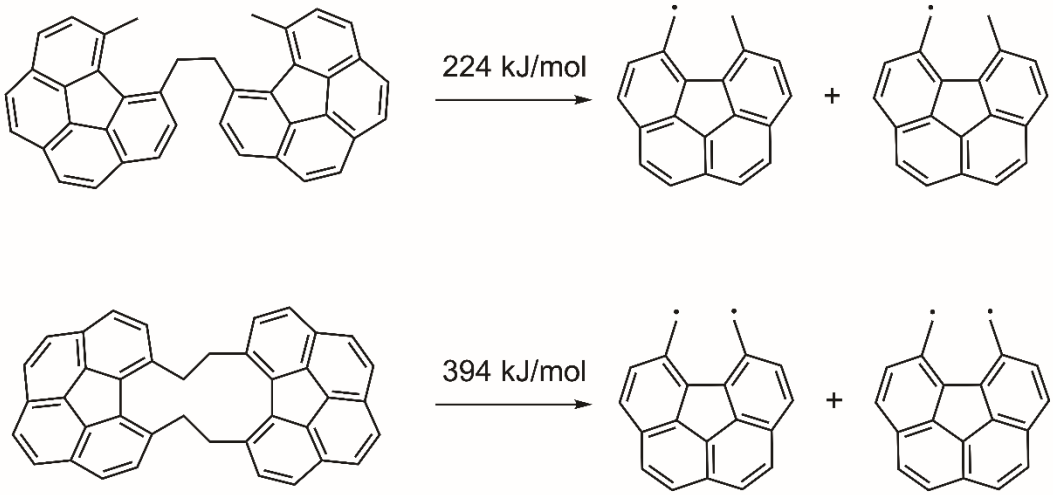

Figure 2.34. Estimation of the electronic component of E_{C-C} in $RCH_2–CH_2R$ with R belonging to a benzo[*ghi*]fluoranthene core. The theory level is B3LYP/6-31+G*.

(127) S. V. Rotkin, I. Zharov and K. Hess, *AIP Conf. Proc.* **2001**, *591*, 454–457.

(128) V. S. Thoi, R. E. Usiskin and S. M. Haile, *Chem. Sci.* **2015**, *6*, 1570–1577.

(129) S.-Y. Zhao, B. Zhang, H. Su, J.-J. Zhang, X.-H. Li, K.-X. Wang, J.-S. Chen, X. Wei and P. Feng, *J. Mater. Chem. A* **2018**, *6*, 4331–4336.

(130) M. K. Smith, K. E. Jensen, P. A. Pivak and K. A. Mirica, *Chem. Mater.* **2016**, *28*, 5264−5268.

(131) Z. Zhang, Y. Che, R. A. Smaldone, M. Xu, B. R. Bunes, J. S. Moore and L. Zang, *J. Am. Chem. Soc.* **2010**, *132*, 14113–14117.

(132) A. Kong, C. Mao, Y. Wang, Q. Lin, X. Bu and P. Feng, *J. Mater. Chem. A* **2016**, *4*, 7305–7312.

(133) A. M. Champsaur, J. Yu, X. Roy, D. W. Paley, M. L. Steigerwald, C. Nuckolls and C. M. Bejger, *ACS Cent. Sci.* **2017**, *3*, 1050–1055.

(134) G. D. Han, A. Maurano, J. G. Weis, V. Bulović and T. M. Swager, *Org. Electron.* **2016**, *31*, 48–55.

(135) O. V Boltalina, A. A. Popov, I. V. Kuvychko, N. B. Shustova and S. H. Strauss, *Chem. Rev.* **2015**, *115*, 1051−1105.

(136) A. Hirsch, *The Chemistry of Fullerenes* John Wiley and Sons, Inc., **2008**.

(137) A. M. Rice, E. A. Dolgopolova and N. B. Shustova, *Chem. Mater.* **2017**, *29*, 7054–7061.

(138) X. Jiang, S. D. Laffoon, D. Chen, S. Pérez-Estrada, A. S. Danis, J. Rodríguez-López, M. A. Garcia-Garibay, J. Zhu and J. S. Moore, *J. Am. Chem. Soc.* **2020**, *142*, 6493–6498.

(139) E. Gonzalez-Rodriguez, M. A. Abdo, G. dos Passos Gomes, S. Ayad, F. D. White, N. P. Tsvetkov, K. Hanson and I. V. Alabugin, *J. Am. Chem. Soc.* **2020**, *142*, 8352–8366.

(140) A. V Zabula, A. S. Filatov, S. N. Spisak, A. Y. Rogachev and M. A. Petrukhina, *Science.* **2011**, *333*, 1008–1011.

(141) C. Dubceac, A. S. Filatov, A. V. Zabula, A. Y. Rogachev and M. A. Petrukhina, *Chem. Eur. J.* **2015**, *21*, 14268–14279.

(142) Z. Zhou, S. N. Spisak, Q. Xu, A. Y. Rogachev, Z. Wei, M. Marcaccio and M. A. Petrukhina, *Chem. Eur. J.* **2018**, *24*, 3455–3463.

(143) A. Béziau, S. A. Baudron, G. Rogez and M. W. Hosseini, *Inorg. Chem.* **2015**, *54*, 2032−2039.

(144) S. A. Baudron and M. W. Hosseini, *Chem. Commun.* **2016**, *52*, 13000–13003.

(145) I. Martin-Fernandez, D. Wang and Y. Zhang, *Nano Lett.* **2012**, *12*, 6175–6179.

(146) M. Terrones, *ACS Nano*, **2010**, *4*, 1775–1781.

(147) B. V. Senkovskiy, M. Pfeiffer, S. K. Alavi, A. Bliesener, J. Zhu, S. Michel, A. V. Fedorov, R. German, D. Hertel, D. Haberer, L. Petaccia, F. R. Fischer, K. Meerholz, P. H. M. Van Loosdrecht, K. Lindfors and A. Grüneis, *Nano Lett.* **2017**, *17*, 4029–4037.

(148) A. Borchardt, A. Fuchicello, K. V Kilway, K. K. Baldridge and J. S. Siegel, *J. Am. Chem. Soc.* **1992**, *114*, 1921–1923.

(149) Z. Chen, J. A. M. Mercer, X. Zhu, J. A. H. Romaniuk, R. Pfattner, L. Cegelski, T. J. Martinez, N. Z. Burns and Y. Xia, *Science* **2017**, *479*, 475–479.

(150) I. V. Alabugin, *Stereoelectronic Effects: A Bridge Between Structure and Reactivity* John Wiley and Sons, Inc., Hoboken, **2016**.

(151) Y.-T. Wu and J. S. Siegel, *Chem. Rev.* **2006**, *106*, 4843–4867.

(152) B. M. Schmidt, B. Topolinski, M. Yamada, S. Higashibayashi, M. Shionoya, H. Sakurai and D. Lentz, *Chem. Eur. J.* **2013**, *19*, 13872–13880.

(153) L. T. Scott, E. A. Jackson, Q. Zhang, B. D. Steinberg, M. Bancu and B. Li, *J. Am. Chem. Soc.* **2012**, *134*, 107–110.

(154) E. Nestoros and M. C. Stuparu, *Chem. Commun.* **2018**, *54*, 6503–6519.

(155) S. Attar, D. M. Forkey, M. M. Olmstead and A. L. Balch, *Chem. Commun.* **1998**, 1255–1256.

(156) T. Hayama, Y. Wu, A. Linden, K. K. Baldridge and J. S. Siegel, *J. Am. Chem. Soc.* **2007**, *129*, 12612–12613.

(157) C. H. Sun, G. Q. Lu and H. M. Cheng, *J. Phys. Chem. B* **2006**, *110*, 4563–4568.

(158) S. Tashiro, M. Yamada and M. Shionoya, *Angew. Chem. Int. Ed.* **2015**, *54*, 5351–5354.

(159) J. C. Fetzer, *Polycycl. Aromat. Compd.* **2007**, *27*, 143–162.

(160) S. Yang and L. M. Stock, *Energy and Fuels* **1996**, *10*, 1181–1186.

(161) M. A. Nkansah, A. A. Christy and T. Barth, *Polycycl. Aromat. Compd.* **2012**, *32*, 408–422.

(162) S. C. Korre, M. T. Klein and R. J. Quann, *Ind. Eng. Chem. Res.* **1997**, *36*, 2041–2050.

(163) X.-M. Yue, X.-Y. Wei, S.-Q. Zhang, F.-J. Liu, Z.-M. Zong and X.-Q. Yang, *Fuel Process. Technol.* **2017**, *161*, 283–288.

(164) M. Murakami and T. Matsuda, *Chem. Commun.* **2011**, *47*, 1100–1105.

(165) R. A. Periana and R. G. Bergman, *J. Am. Chem. Soc.* **1986**, *108*, 7346–7355.

(166) C. T. To, K. S. Choi and K. S. Chan, *J. Am. Chem. Soc.* **2012**, *134*, 11388–11391.

(167) A. Yamaguchi, N. Mimura, M. Shirai and O. Sato, *Sci. Rep.* **2017**, *7*, 46172.

(168) X. Kang, G. Luo, L. Luo, S. Hu, Y. Luo and Z. Hou, *J. Am. Chem. Soc.* **2016**, *138*, 11550–11559.

(169) P. Sivaguru, Z. Wang, G. Zanoni and X. Bi, *Chem. Soc. Rev.* **2019**, *48*, 2615–2656.

(170) Y. Xia and G. Dong, *Nat. Rev. Chem.* **2020**, *4*, 600−614.

(171) Y. Yoshida, K. Isomura, N. Yuto, H. Kishida and G. Saito, *Chem. Lett.* **2015**, *44*, 709–711.

(172) M. Wang, C. Wölfer, L. Otrin, I. Ivanov, T. Vidaković-Koch and K. Sundmacher, *Langmuir* **2018**, *34*, 5435–5443.

(173) F. P. Van der Zee and F. J. Cervantes, *Biotechnol. Adv.* **2009**, *27*, 256–277.

(174) M. D. Peterson, S. C. Jensen, D. J. Weinberg and E. A. Weiss, *ACS Nano* **2014**, *8*, 2826–2837.

(175) L. Striepe and T. Baumgartner, *Chem. Eur. J* **2017**, *23*, 16924–16940.

(176) J. M. Khurana and S. Singh, *J. Indian Chem. Soc.* **1996**, *73*, 487–488.

(177) A. Sygula, R. Sygula, F. R. Fronczek and P. W. Rabideau, *J. Org. Chem.* **2002**, *67*, 6487–6492.

(178) S. N. Spisak, G. C. Hoover, Z. Wei, A. V. Zabula, A. S. Filatov and M. A. Petrukhina, *Acta Crystallogr. Sect. C Struct. Chem.* **2015**, *71*, 690–694.

(179) E. Shabtai, R. E. Hoffman, P. C. Cheng, E. Bayrd, D. V. Preda, L. T. Scott and M. Rabinovitz, *J. Chem. Soc. Perkin Trans.* **2001**, *2*, 129–133.

(180) R. M. Chin, B. Baird, M. Jarosh, S. Rassman, B. Barry and W. D. Jones, *Organometallics* **2003**, *22*, 4829–4832.

(181) R. M. Chin, M. S. Jarosh, J. D. Russell and R. J. Lachicotte, *Organometallics* **2002**, *21*, 2027–2029.

(182) P. W. Rabideau, Z. Marcinow, R. Sygula and A. Sygula, *Tetrahedron Lett.* **1993**, *34*, 6351–6354.

(183) P. Sundararajan, M. Tsuge, M. Baba, H. Sakurai and Y. P. Lee, *J. Chem. Phys.* **2019**, *151*, 044304.

(184) T. Nakabayashi and T. Nakabayashi, *J. Am. Chem. Soc.* **1960**, *82*, 3900–3906.

(185) B. K. Peters, K. X. Rodriguez, S. H. Reisberg, S. B. Beil, D. P. Hickey, Y. Kawamata, M. Collins, J. Starr, L. Chen, S. Udyavara, K. Klunder, T. J. Gorey, S. L. Anderson, M. Neurock, S. D. Minteer and P. S. Baran, *Science* **2019**, *363*, 838–845.

(186) R. D. Adams, J. Kiprotich, D. V Peryshkov and Y. Onn, *Chem. Eur. J* **2016**, *22*, 6501–6504.

(187) R. D. Adams, E. J. Kiprotich and M. D. Smith, *Chem. Commun.* **2018**, *54*, 3464–3467.

(188) R. D. Adams, J. Kiprotich, D. V Peryshkov and Y. O. Wong, *Inorg. Chem.* **2016**, *55*, 8207−8213.

(189) Y. Nagano and M. Nakano, *J. Chem. Thermodyn.* **2003**, *35*, 1403–1412.

(190) M. A. Dobrowolski, G. Garbarino, M. Mezouar, A. Ciesielski and M. K. Cyrański, *CrystEngComm* **2014**, *16*, 415–429.

(191) L. Pauling and L. O. Brockway, *J. Am. Chem. Soc.* **1937**, *59*, 1223–1236.

(192) R. J. Dillon and C. J. Bardeen, *J. Phys. Chem. A* **2012**, *116*, 5145−5150.

(193) H. N. Ghosh, *J. Phys. Chem. B* **1999**, *103*, 10382–10387.

(194) R. A. Marcus, *Rev. Mod. Phys.* **1993**, *65*, 599–610.

(195) T. J. Kistenmacher, T. J. Emge, A. N. Bloch and D. O. Cowan, *Acta Crystallogr. Sect. B Struct. Crystallogr. Cryst. Chem.* **1982**, *38*, 1193–1199.

(196) A. M. Butterfield, B. Gilomen and J. S. Siegel, *Org. Process Res. Dev.* **2012**, *16*, 664–676.

CHAPTER 3

STACK THE BOWLS: TAILORING THE ELECTRONIC STRUCTURE OF CORANNULENE-INTEGRATED CRYSTALLINE MATERIALS

Rice, A. M.; Dolgopolova, E. A.; Yarbrough, B. J.; Leith, G. A.; Martin, C. R.; Stephenson, K. S.; Heugh, R. A.; Brandt, A. M.; Chen, D. A.; Karakalos, S. G.; Smith, M. D.; Hatzell, K. B.; Pellechia, P. J.; Garashchuk, S. and Shustova, N. B. *Angew. Chem. Int. Ed*. **2018**, *57*, 11310–11315.

The unique curvature of π-bowls (πBs) distinguishes them from more traditional flat polycyclic aromatic hydrocarbons (PAHs), and in combination with an unusual electronic structure, results in a number of intriguing properties including, but not limited to, surface charge stabilization, high reversible lithium capacity, bowl-to-bowl inversion, a significant dipole moment, and high charge mobility.[197–204] This combination of material properties can open a pathway for πB utilization in applications ranging from optoelectronic devices or electrodes to thermoresponsive materials.[200,205,206]

Herein, we demonstrated, for the first time, how πB integration (in particular, corannulene (πB-$C_{20}H_{10}$)) inside insulating porous scaffolds could tune electronic properties resulting in ~10000 times conductivity enhancement. Moreover, the porosity of the prepared crystalline (e.g., covalent-organic or metal-organic frameworks (COFs/MOFs)).[207–217] In addition to the first report of azide-alkyne 1,3-cycloaddition utilized for corannulene integration in the solid state, the described corannulene material is the first member in the family of crystalline (purely organic) donor-acceptor (D-A) corannulene-COFs with the highest surface area among corannulene-based extended structures reported to date (Scheme 3.1). In combination with spectroscopic and structural analysis, we employed theoretical calculations, which allowed us to probe charge transfer rates within the Marcus theory as a function of πB mutual orientation for the first time, as well as to shed light on the density of state distribution near the Fermi edge.

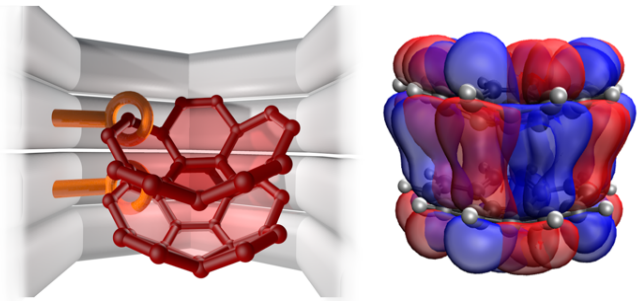

Scheme 3.1. (*left*) Schematic representation of πB organization inside the crystalline framework through 1,3-cyloaddition. (*right*) Delocalization of πB molecular orbitals associated with ground state charge transport.

For engineering corannulene-containing crystalline materials, we considered two methodologies based on the postsynthetic integration of the πB through (i) utilization of azide-alkyne 1,3-cycloaddition as well as (ii) non-coordinative πB inclusion. To accomplish these strategies, the material used for πB integration should satisfy the following criteria: (i) sufficient pore apertures to accommodate πBs (e.g., πB-$C_{20}H_{10}$ diameter is ~6.6 Å), (ii) structural integrity after πB inclusion, and (iii) the presence of functional groups (e.g., –C≡C) for πB integration through covalent bond formation. The covalent-organic scaffolds, **1≡(x%)** (where x = [BPTA]/([BPTA]+[DMTA])×100%; Figure 3.1), made from 2,5-bis(2-propynyloxy) terephthalaldehyde (BPTA), 2,5-dimethoxyterephthalaldehyde (DMTA), and tri-(4-aminophenyl)benzene (TAPB) and **1-Ome** consisting of DMTA and TAPB, were utilized for coordinative and non-coordinative πB integration, respectively (Schemes 3.2–3.6, Figures 3.5–3.23).[218] Both selected frameworks, possessing layered structures with a pore aperture of 33 Å, maintain structural integrity under a wide pH range[218] making it possible to explore a number of synthetic conditions for πB immobilization without material degradation. However, several challenges still had to be addressed for not only reaction condition development, but also

synthesis of corannulene-based building blocks on a gram scale. The latter challenge has been overcome due to recent advances in πB chemistry[199,219–222] allowing for the preparation of azide-containing corannulene (πB-$C_{20}H_9N_3$, Figure 3.1, Scheme 3.6) using a 12-step procedure[222] as well as pristine corannulene (πB-$C_{20}H_{10}$) by a 9-step approach (Scheme 3.6).[221]

A stepwise approach was devised for the investigation of reaction conditions for a copper-catalyzed azide-alkyne cycloaddition (CuAAC), which involved the development of synthetic methodologies using less bulky and more affordable moieties (e.g., 2-azidoethanol, Figure 3.1) before pursuing the reaction with the labor demanding πB-$C_{20}H_9N_3$. Therefore, we started with molecular building blocks, such as 2-azidoethanol and BPTA, in order to observe reaction progress using solution NMR spectroscopy, in contrast to the insoluble COFs (Figures 3.24–3.26).

Based on the spectroscopic data analysis, we have monitored the completion of a CuAAC reaction, and as a result, formation of the desired product, 2,5-bis((1-(2-hydroxyethyl)-1*H*-1,2,3-triazol-4-yl)methoxy)terephthalaldehyde (Figures 3.1 and 3.24–3.26). As a next step, we applied the developed conditions (*N,N*-diisopropylethylamine/CuI/THF/H_2O, 70 °C, 3 d) towards the reaction of 2-azidoethanol with the COF (**1≡(34%)**) instead of BPTA. To monitor the reaction progress, solid-state techniques, including FTIR and solid-state ^{13}C cross-polarization magic angle spinning (CP-MAS) NMR spectroscopies, were employed. In particular, we observed the disappearance of 2120 cm^{-1} (C≡C) and 3300 cm^{-1} (C≡C–H) resonances in the FTIR spectrum, indicative of reaction completion (Figure 3.26).[218] As a control experiment, we treated the COF under the same reaction conditions, but without the presence of the

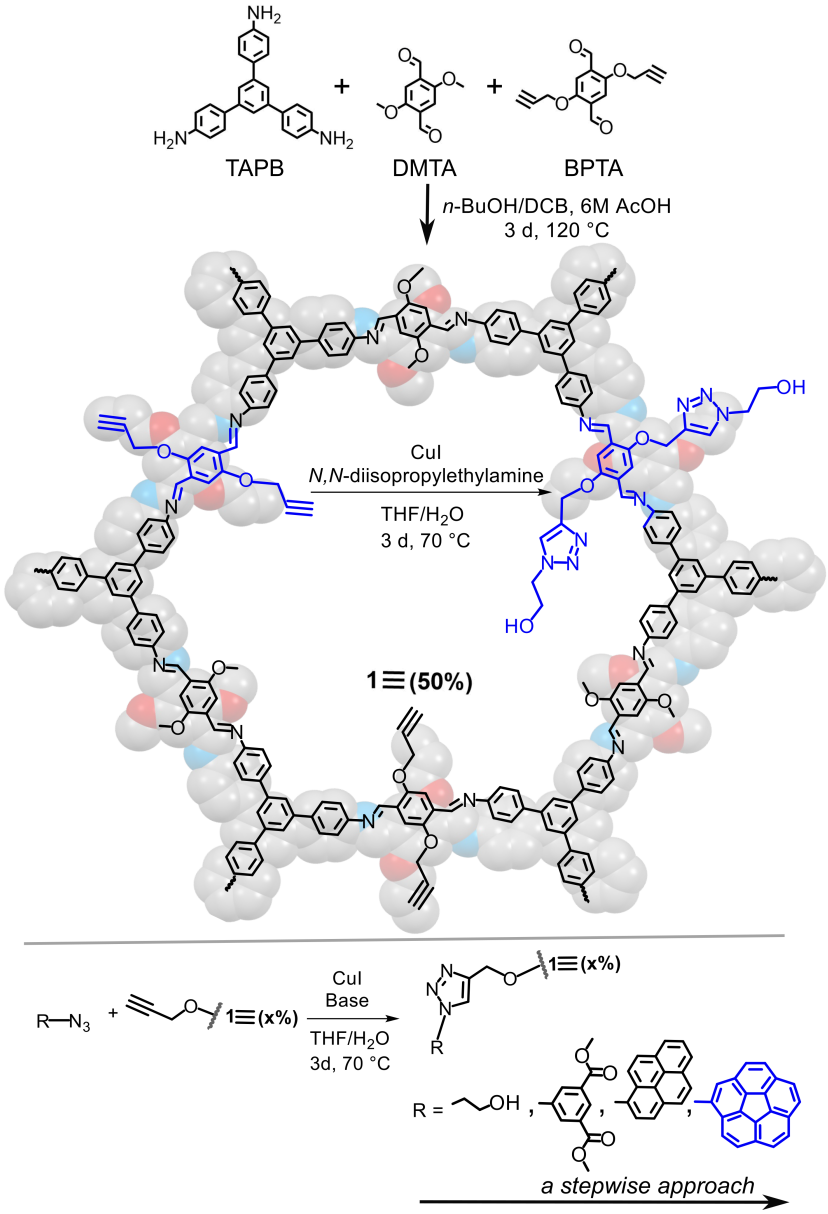

Figure 3.1. (*top*) Synthesis of **1≡(50%)** including the reaction conditions utilized for azide-alkyne cycloaddition reaction in the solid state. Blue color highlights the moieties participating in CuAAC reaction on molecular species. (*bottom*) Building blocks utilized in a stepwise approach for the development of the CuAAC synthetic conditions applicable for the COF.

Azide-containing precursor. As expected, we observed preservation of both 2120 cm^{-1} (C≡C) and 3300 cm^{-1} (H–C≡C) resonances in the FTIR spectrum (Figure 3.32). Interestingly, in the case of the CuAAC reaction with bis(2-azidoethyl) malonate (i.e.,

containing two azide groups, Figure 3.27), the observed disappearance of the stretch at 3300 cm^{-1} (H–C≡C) is evident of the reaction progress, while the persistence of the stretch at 2100 cm^{-1} (N–N=N) is indicative of the preservation of the second azide group.[223]

After 2-azidoethanol and bis(2-azidoethyl) malonate, bulkier precursors such as dimethyl 5-azidoisophthalate and 1-azidopyrene (Figure 3.27) were probed for the CuAAC reaction under the developed experimental conditions. In both cases, the complete disappearance of the resonances at 2120 cm^{-1} and 3300 cm^{-1} was confirmed by FTIR spectroscopy (Figures 3.28 and 3.29). In addition, presence of the characteristic carbonyl stretch at ~1716 cm^{-1} in the case of dimethyl 5-azidoisophthalate after an extensive several-day washing procedure also supports successful reaction completion. After the development of the synthetic methodology for successful solid-state CuAAC reactions, we finally focused on integration of πBs, in particular, an azide-containing building block (πB-$C_{20}H_9N_3$, Figure 3.1). Based on the combination of solid-state ^{13}C CP-MAS NMR and FTIR spectroscopic data, incorporation of the corannulene-based unit led to πB-$C_{20}H_9N_3$[**1≡(50%)**] formation (Figures 3.2, 3.30, and 3.31). Even after πB incorporation, the Brunauer-Emmett-Teller (BET) surface area was found to be 865 m^2/g according to the gas sorption analysis, which is the highest surface area reported for any corannulene-containing structure to date (Figure 3.31). Notably, the observed surface area is in line with corannulene integration since the measured surface area of the parent COF was found to be 1452 m^2/g. The synthesized material also maintains its crystallinity, resulting in the first example of a crystalline, porous corannulene-based COF.

For a comparison, we performed non-coordinative immobilization of the πB inside **1-Ome**. For that, we used a "simpler" 9-step synthetic route required for πB-$C_{20}H_{10}$ preparation rather than the 12-step procedure necessary for πB-$C_{20}H_9N_3$ preparation (Figures 3.33–3.35).[221,222]

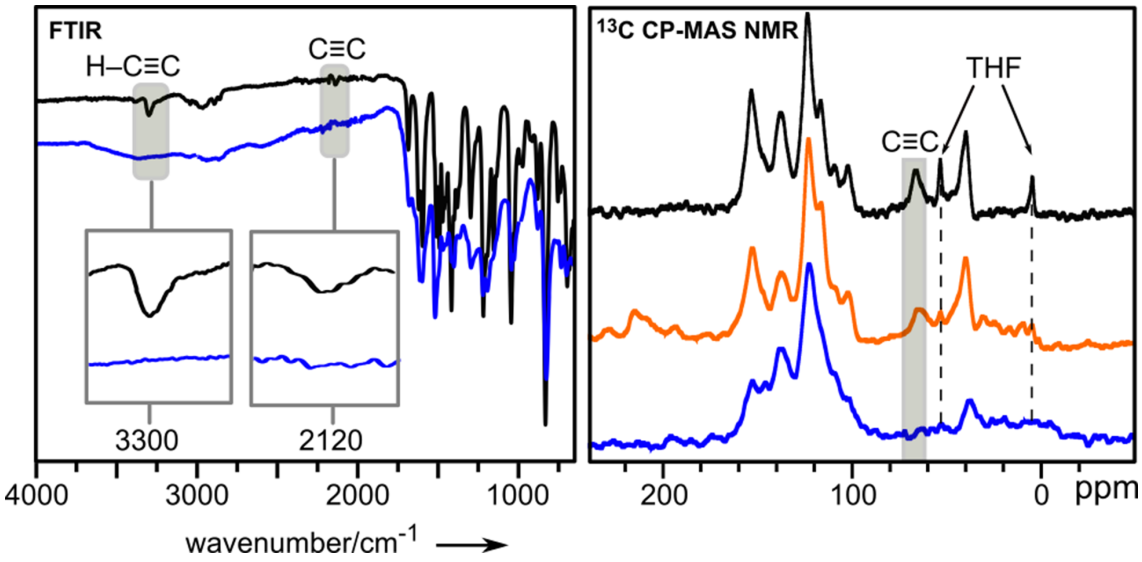

Figure 3.2. (*left*) FTIR spectra of **1≡(50%)** (black) and πB-$C_{20}H_9N_3$[**1≡(50%)**] (blue). Gray areas show H–C≡C and C≡C stretches, present in **1≡(50%)** and absent in πB-$C_{20}H_9N_3$[**1≡(50%)**]. (*right*) ^{13}C CP-MAS NMR spectra of **1≡(50%)** (black), a control experiment with **1≡(50%)** (orange), and πB-$C_{20}H_9N_3$[**1≡(50%)**] (blue).

An additional simplification is also found in πB-$C_{20}H_{10}$@**1-Ome** synthesis. This was achieved through soaking **1-Ome** in a πB-$C_{20}H_{10}$ solution for 5 days, followed by a thorough washing procedure to remove πB-$C_{20}H_{10}$ from the COF surface. Based on ^{1}H NMR spectroscopic analysis of the digested COF, non-coordinative immobilization led to inclusion of one corannulene molecule per six –Ome units. The crystallinity of πB-$C_{20}H_{10}$@**1-Ome** after corannulene incorporation was confirmed by PXRD (Figure 3.34).

The measured BET surface area of πB-$C_{20}H_{10}$@**1-Ome** was found to be 898 m^2/g (Figure 3.35).

To probe the electronic structures of πB-containing materials, we employed diffuse reflectance (DR), steady-state and time-resolved photoluminescence (PL), and X-ray photoelectron (XPS) spectroscopies, conductivity measurements and theoretical calculations. Integration of corannulene moieties inside the COFs through CuAAC or non-coordinative integration resulted in a significant color change from pale-yellow to dark red (Figure 3.3). Indeed, DR spectroscopic analysis revealed that corannulene integration resulted in appearance of an additional absorption band (~550–650 nm) leading to more than a 100-nm bathochromic shift of the absorption profile in comparison with both the pristine COF and corannulene units. Such a drastic change could be attributed to charge transfer (CT) between the covalent-organic host and πB moieties, especially taking into account the electron donating character of the framework functional groups (e.g., –Ome) and electron-accepting behavior of corannulene moieties.[218] This fact is in line with the results observed in the case of naphthalene ($C_{10}H_8$) and pyrene ($C_{16}H_{10}$) integration, both possessing higher lying LUMOs than that of πB-$C_{20}H_{10}$ (-2.27 eV in contrast to -1.20 eV ($C_{10}H_8$)[224] and -1.48 eV ($C_{16}H_{10}$)[225]). Integration of 1,4-dimethoxybenzene and 1,5-dimethoxynaphthalene exhibiting electron-donating behavior also did not result in CT band formation. To further study the behavior of the prepared materials, we employed time-resolved PL spectroscopy. With the assumption that the PL decay rate consisting of radiative, nonradiative, and CT components, analysis should reveal shortening of PL lifetimes of the host due to integration of corannulene moieties.[226,227] Indeed, the estimated amplitude-averaged lifetimes by fitting the time-resolved PL decay curves were found to

be 474 ps (**1-Ome**) while πB-$C_{20}H_{10}$@**1-Ome** and πB-$C_{20}H_9N_3$[**1≡(50%)**] exhibited much shorter lifetimes of 192 ps and 167 ps, respectively, which is in line with the possibility of CT. Similar behavior was previously reported for fullerene-porphyrin dyads where the decrease in lifetime was attributed to an electron transfer from porphyrin moieties (D) to fullerene units (A).[226] Immobilization of planar PAHs (i.e., naphthalene or pyrene) did not result in significant CT, and estimated lifetimes were similar to that of **1-Ome** (Figure 3.3).

As a next step, we employed XPS to probe the electronic structure of the πB-based materials by monitoring the density of states (DOS) near the Fermi level (E_F, binding energy = 0 eV) as a fast and nondestructive pre-screening technique. This capability is especially crucial in the case of the multi-step preparation of corannulene derivatives.[228] The valence band spectrum of πB-$C_{20}H_{10}$ itself exhibits behavior associated with insulating materials, given that there is zero intensity within 3 eV of the Fermi level. The spectrum of **1-Ome** itself also shows nearly zero intensity at 2 eV. In contrast, the XPS valence band spectra for πB-$C_{20}H_{10}$@**1-Ome** and πB-$C_{20}H_9N_3$[**1≡(50%)**] have much higher intensities within ~2 eV of E_F; this indicates a greater DOS near E_F, which is associated with higher conductivity. The DOS curves obtained from the 4-unit computational models are quite similar for the "stack" and "pinwheel" orientations (see below) and show overall agreement with the DOS of pristine corannulene (Figure 3.39). Therefore, we attribute the peaks in the range of 2–3 eV in the spectra of πB-integrated samples to parent **1-Ome** (e.g., modified by interactions with solvent in the pores) and not necessarily to the changes in the corannulene stacking. To further shed light on the changes of electronic structure near E_F, we have performed pressed-pellet conductivity measurements as well as estimated the

optical band gap values based on DR spectroscopic data. The bulk conductivity values for **1-Ome**, πB-$C_{20}H_{10}$@**1-Ome**, and πB-$C_{20}H_9N_3$[**1≡(50%)**] were found to be 2.32×10^{-12},

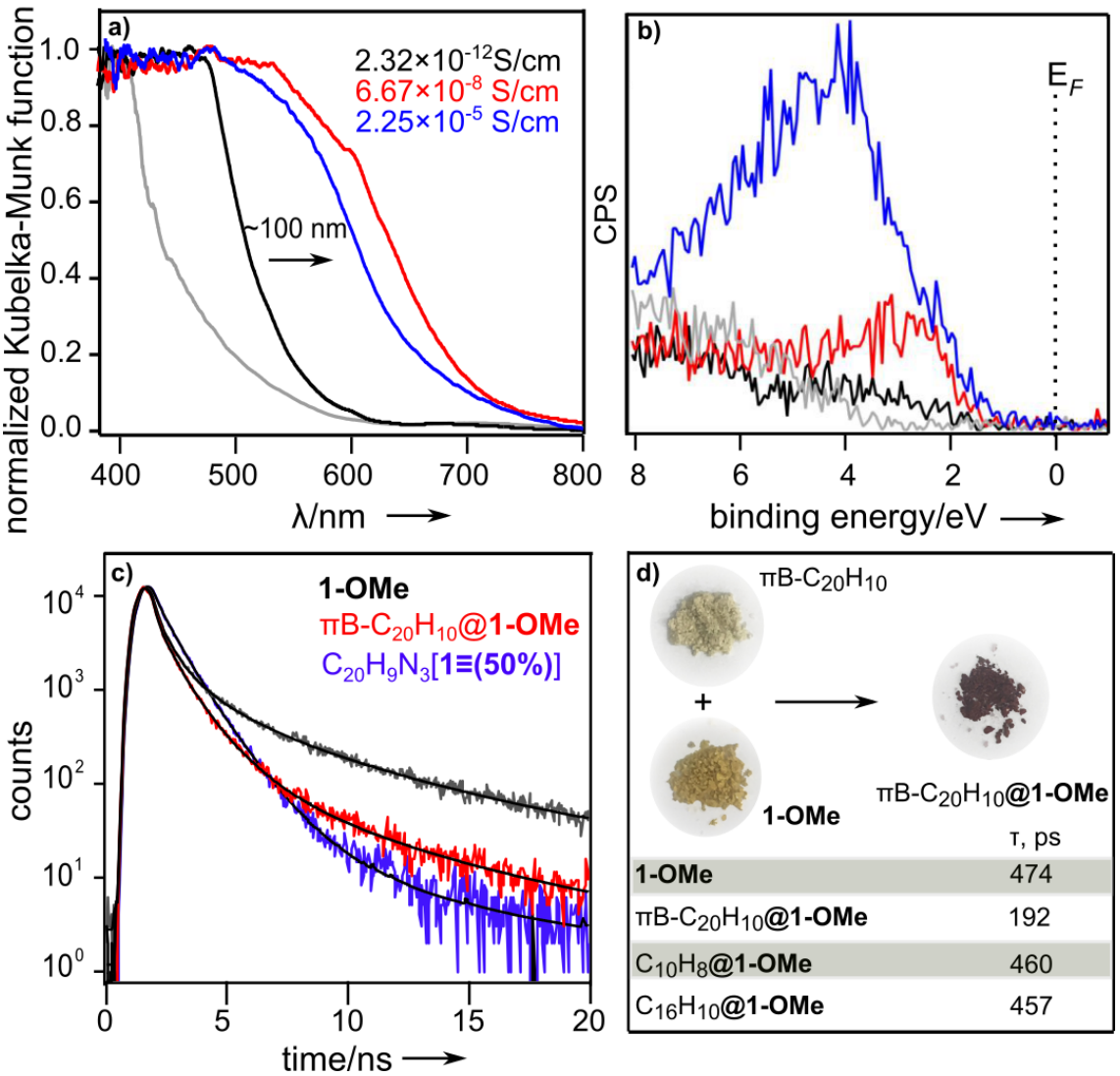

Figure 3.3. (a) Normalized diffuse reflectance spectra of πB-$C_{20}H_{10}$@**1-Ome** (red), **1-Ome** (black), πB-$C_{20}H_9N_3$[**1≡(50%)**] (blue), and πB-$C_{20}H_{10}$ (gray) with corresponding conductivity values. (b) XPS data for the valence band region for πB-$C_{20}H_{10}$@**1-Ome** (red), **1-Ome** (black), πB-$C_{20}H_9N_3$[**1≡(50%)**] (blue), and πB-$C_{20}H_{10}$ (gray). (c) Fluorescent decays of πB-$C_{20}H_{10}$@**1-Ome** (red), πB-$C_{20}H_9N_3$[**1≡(50%)**] (blue), and **1-Ome** (gray). (d) Photographs of **1-Ome**, πB-$C_{20}H_{10}$, and πB-$C_{20}H_{10}$@**1-Ome**. The table shows the amplitude-weighted average lifetimes for **1-Ome**, πB-$C_{20}H_{10}$@**1-Ome**, and PAHs@**1-OMe**.

6.67×10^{-8}, and 2.25×10^{-5} S/cm, respectively, highlighting that conductivity of corannulene-integrated materials is ~10000 times higher in comparison to the parent framework. This

fact is consistent with the appearance of DOS in the XPS spectra as well as the trend observed for the optical band gap values derived from the Tauc plot.[229,230] The estimated band gaps for COF (**1-Ome**), πB-$C_{20}H_{10}$@**1-Ome**, and πB-$C_{20}H_9N_3$[**1≡(50%)**] were found to be 2.24 eV, 1.94 eV, and 1.93 eV, respectively. Thus, πB-incorporation resulted in four orders of magnitude of enhancement of conductivity while preserving material crystallinity and porosity, thus providing a pathway to enhance semiconducting behavior in typically insulating porous COFs. To elucidate how πB packing (in addition to D-A interactions) could potentially promote charge transport, we explored the dependence of electronic properties as a function of possible πB arrangements inside the crystalline host. The πB organization could be defined by the interplay of electrostatic (dipole-dipole attractions, repulsions between electron clouds of π-surfaces, and attractions between the edges and bowl centers), dispersive (surface interactions), and interstack C-H···π interactions with distance between πBs ranging from 3.3 Å to 3.7 Å.[231,232] In addition, the open nature of the one-dimensional COF channels provides a structural basis for accommodation of guest molecules and their efficient confinement and packing. Furthermore, molecular dynamics and intermolecular distances of anchoring corannulene moieties are restricted by the COF interlayer distance of 3.5 Å (Figure 3.4).[218]

We employed theoretical calculations for a series of πB motifs by considering three main packing scenarios: convex-to-concave "stack" (Figure 3.4), concave-to-concave/convex-to-convex "clam", and "pinwheel" observed for the pristine corannulene in the solid state (Figures 3.4 and 3.36).[201,232] We evaluated the ground state CT in the chosen geometrical arrangements assuming a charge hopping mechanism, which involves transfer of charge through its relocation from charged to neutral species.[233–236] The

approach, based on the Hartree-Fock theory paired with 6-31+G* basis, yielded the electronic couplings and the frontier molecular orbitals (Mos) associated with the charge transport (see SI for more details).[237,238] Figure 3.4 illustrates the variation of frontier Mos associated with ground state CT. In the case of convex-to-concave corannulene stacks, frontier Mos form one π-column through all units, suggesting long-range π-interactions promoting charge transport. Our calculations do not show significant orbital delocalization for the cases of corannulene packing with disordered arrangements of units (e.g., "pinwheel", Figures 3.4 and 3.38). The latter fact is in agreement with previous studies that showed a strong correlation of molecular packing with charge transport.[237,239]

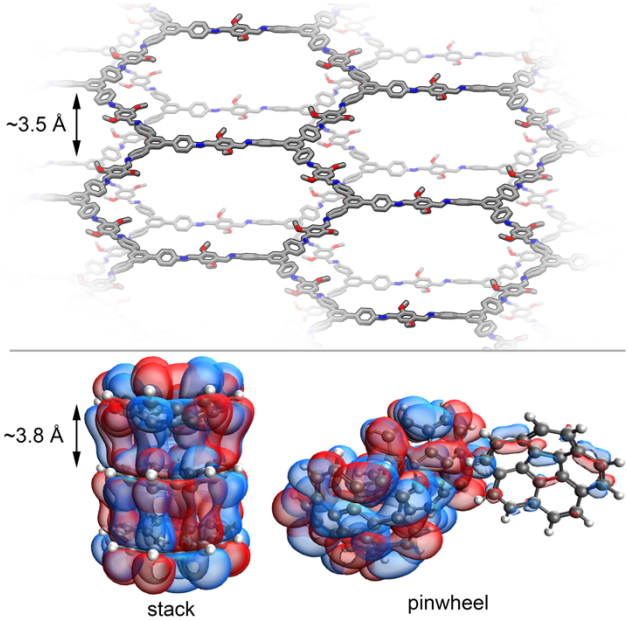

Figure 3.4. (*top*) Interlayer distance in **1-Ome**.[218] (*bottom*) Selected LUMOs, associated with the ground CT for the three πB-$C_{20}H_{10}$ units in "stack" and "pinwheel" orientations. The theory level is LRC-wPBEh/6-31G*.

To apply a more generalized approach and establish the correlation of our suggested model to experimental conductivity data, we estimated CT constants according to the Marcus theory (eq. 1)

$$k = 2\pi/\hbar \cdot |V_c|^2/\sqrt{(4\pi\lambda k_B \mathrm{T})} \cdot \exp\left(-\lambda/(4k_B \mathrm{T})\right) \text{ (eq. 1)}$$

where k – charge transfer rate, V_c – direct effective electron coupling, λ – reorganization energy of the system; see SI for more details.[240,241] By applying the Einstein relation ($\mu = eD/k_BT$, $D = kL^2/2$, where μ – mobility of charge transfer carriers, D – diffusion constant, L – mean length of particle movement) and assumption of the equal number of charge carriers in different packing motifs, we estimated the conductivity value ratio as a ratio of the corresponding k values. Within this model, we found that a shift from noncolumnar organization to a one-dimensional corannulene stack could result in a ~42 times increase in conductivity values (see SI for a detailed description). Therefore, the experimentally observed conductivity enhancement could be attributed not only to the πB integration and/or D-A corannulene-host communication inside the crystalline COF, but also to the mutual orientation of the corannulene moieties as shown in Figure 3.4.

The preceding results describe the properties of the first examples of corannulene-based (purely organic) crystalline and porous scaffolds with embedded πBs. Corannulene integration resulted in significant changes in the valence band structure and, thus, to a four order of magnitude conductivity enhancement. Moreover, 1,3-cyloaddition, utilized for the first time for corannulene integration in the solid state, led to the formation of materials with the highest surface area reported for any corannulene-containing materials to date. Our theoretical analysis paves the way towards simulation of the electronic coupling constants as a function of corannulene mutual orientation. Overall, this work demonstrates high potential of πBs for the development of materials with tunability of electronic structures preserving material porosity and crystallinity; this combination could be crucial

for future technological advances in the fields of optoelectronic devices or highly efficient electrodes.

EXPERIMENTAL

The corannulene-based precursors and 1-azidocorannulene were prepared according to the literature procedures. The COF-based linkers 2,5-dimethoxyterephthalaldehyde (DMTA), 1,3,5-tri-(4-aminophenyl)benzene (TAPB), and 2,5-bis(2-propynyloxy) terephthalaldehyde (BPTA) were synthesized based on modified literature procedures. The **1-Ome** and **1≡(x%)** COFs were synthesized based on a modified literature procedures.

Synthesis.

Tri-(4-aminophenyl)benzene ($C_{24}H_{21}N_3$, TAPB, Scheme 3.2).

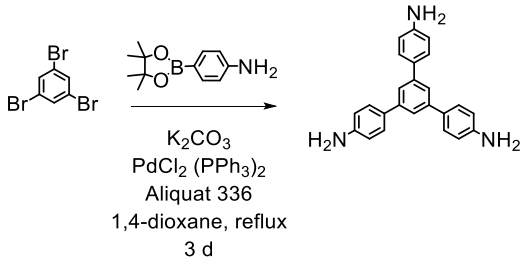

Scheme 3.2. Synthesis of 1,3,5-tri-(4-aminophenyl) benzene (TAPB).

The TAPB linker was prepared according to a modified literature procedure. For that, 1,3,5-tribromobenzene (1.00 g, 3.17 mmol), 4-aminophenyl boronic ester (2.31 g, 13.3 mmol), K_2CO_3 (2 M, 7.50 mL), $PdCl_2(PPh_3)_2$ (68.0 mg, 0.0971 mmol), and Aliquat 336 (100 µL) were heated at reflux in dioxane for 3 d. After cooling to room temperature, the reaction mixture was flushed through a silica plug with ethyl acetate, followed by recrystallization from methanol to afford TAPB in 62% yield. ^{1}H NMR (DMSO-d_6, 300 MHz): δ = 7.48 (6H, s), 7.45 (3H, s), 6.66 (6H, d, J = 8.46), 5.21 (6H, s) ppm (Figure 3.5). ^{13}C NMR (DMSO-d_6, 101 MHz): δ = 148.83, 142.04, 128.49, 127.90, 120.82, and 114.7

ppm (Figure 3.5). IR (neat, cm^{-1}): 668, 706, 822, 871, 951, 1126, 1176, 1279, 1406, 1448, 1513, 1606, 3210, 3355, and 3434 (Figure 3.6). HRMS (ESI, m/z) calculated for $C_{24}H_{21}N_3$ $[M+H]^+$ 352.1808, found 352.1806.

2,5-dimethoxyterephthalaldehyde ($C_{10}H_{10}O_4$, DMTA, Scheme 3.3).

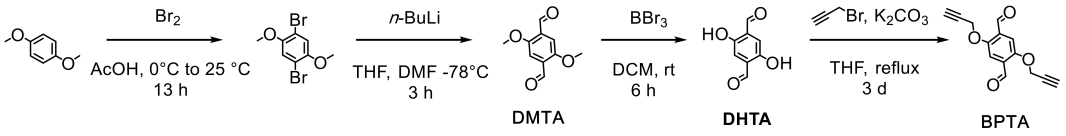

Scheme 3.3. Synthesis of 2,5-dimethoxyterephthalaldehyde (DMTA) and 2,5-bis(2-propynyloxy) terephthalaldehyde (BPTA).[50]

The DMTA linker was prepared according to a modified literature procedure. To a solution of 1,4-dibromo-2,5-dimethoxybenzene (1.00 g, 30.0 mmol) in dry THF (20 mL) at –78 °C under a nitrogen atmosphere, *n*-butyllithium (2.5 M in hexane, 4.80 mL, 12.0 mmol) was added and stirred for 2 h. An additional 20 mL of THF was added along with DMF (3.0 mL, 39.0 mmol) and stirred for 1 h. When 3 M HCl (10 mL) was added, the reaction was warmed to room temperature and the product was filtered. After drying under vacuum, a yellow precipitate was obtained (DMTA) in 61% yield. ^{1}H NMR (DMSO-d_6, 300 MHz): δ = 10.39 (2H, s), 7.44 (2H, s), 3.93 (6H, s) ppm (Figure 3.7). ^{13}C NMR (DMSO-d_6, 101 MHz): δ = 189.44, 155.65, 129.20, 111.73, and 56.88 ppm (Figure 3.8). IR (neat, cm^{-1}): 875, 1018, 1127, 1166, 1210, 1300, 1393, 1408, 1480, 1671, 2869 (Figure 3.11). HRMS (ESI, m/z) calculated for $C_{10}H_{10}O_4$ $[M+H]^+$ 194.0579, found 194.0583.

2,5-bis(2-propynyloxy) terephthalaldehyde ($C_{14}H_{10}O_4$, BPTA, Scheme 3.4).

The BPTA linker was prepared according to a modified literature procedure. To a solution of DMTA (0.200 g, 1.30 mmol) in dry dichloromethane (20 mL), BBr_3 (1 M in DCM, 2.30 mL, 2.30 mmol) was added dropwise at 0 °C under a nitrogen atmosphere.

After stirring for 3 h at room temperature, the reaction mixture was cooled to 0 °C and water (20 mL) was added to quench excess BBr_3. The organic layer was separated, while the aqueous layer was extracted with dichloromethane (3 × 25 mL) and dried over anhydrous Na_2SO_4, and after that the solvent was removed under reduced pressure. The crude material was recrystallized from acetone to yield the precursor, 2,5-dihydroxyterephthalaldehyde (DHTA) in 89% yield. To make desired BPTA, DHTA (150 mg, 0.900 mmol), and K_2CO_3 (624 mg, 4.51 mmol) were heated at reflux in THF for 30 min. Upon cooling to room temperature, propargyl bromide (0.408 mL) was added, and the reaction mixture was heated to reflux for 3 d. The reaction mixture was cooled to room temperature, followed by the addition of the equal volume of water, extracted with $CHCl_3$ (3 × 25 mL), washed with 5% NaOH (2 × 25 mL), washed with brine (25 mL), dried over Na_2SO_4, filtered, and the $CHCl_3$ was removed under reduced pressure to yield BPTA in 71% yield. ^{1}H NMR (DMSO-d_6, 300 MHz): δ = 10.79 (2H, s), 8.01(2H, s), 5.45 (4H, d, J = 2.13), 4.10 (2H, t, J = 2.16) ppm (Figure 3.9). ^{13}C NMR (DMSO-d_6, 101 MHz): δ = 189.16, 154.12, 129.93, 113.90, 79.91, 78.95, and 57.65 ppm (Figure 3.10). IR (neat, cm^{-1}): 705, 761, 800, 878, 931, 1012, 1097, 1139, 1163, 1202, 1260, 1295, 1359, 1403, 1423, 1449, 1480, 1682, 2121, 2881, 2963, 3282 (Figure 3.12). HRMS (ESI, m/z) calculated for $C_{14}H_{10}O_4$ $[M+H]^+$ 242.0579, found 242.0584. BPTA was recrystallized from a saturated dichloromethane solution. Single-crystal X-ray data for BPTA are shown in Table 3.1 and Figure 3.13.

Development of Synthetic Reaction Conditions for COF Preparation. To develop reaction conditions, we initially perform the condensation reactions in solution using the

molecular precursors as shown below, which allowed us to characterize the products by ^{1}H NMR spectroscopy.

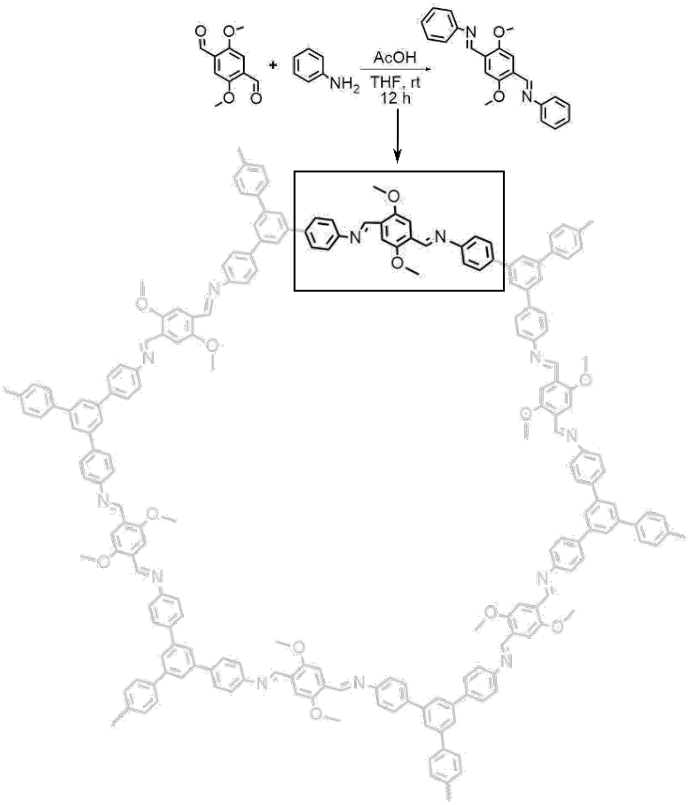

Scheme 3.4. Synthesis of (1*E*,1'*E*)-1,1'-(2,5-dimethoxy -1,4-phenylene)bis(*N*-phenylmethanimine), $C_{22}H_{20}O_2N_2$. This reaction was performed to develop the methodology for **1-Ome** framework.

In a 50 mL round bottom flask, DMTA (100 mg, 0.515 mmol) was dissolved in THF (2.0 mL) and aniline (118 µL, 1.29 mmol) was added to the mixture in the presence of 6M acetic acid catalyst (0.2 mL). After stirring overnight at room temperature, the solvent was removed under reduced pressure to afford a solid in a quantitative yield. ^{1}H NMR (DMSO-d_6, 300 MHz): 8.87 (2H, s), 7.73 (2H, s), 7.44 (4H, m), 7.28 (6H, m), 3.94 (6H, s) ppm (Figure 3.14).

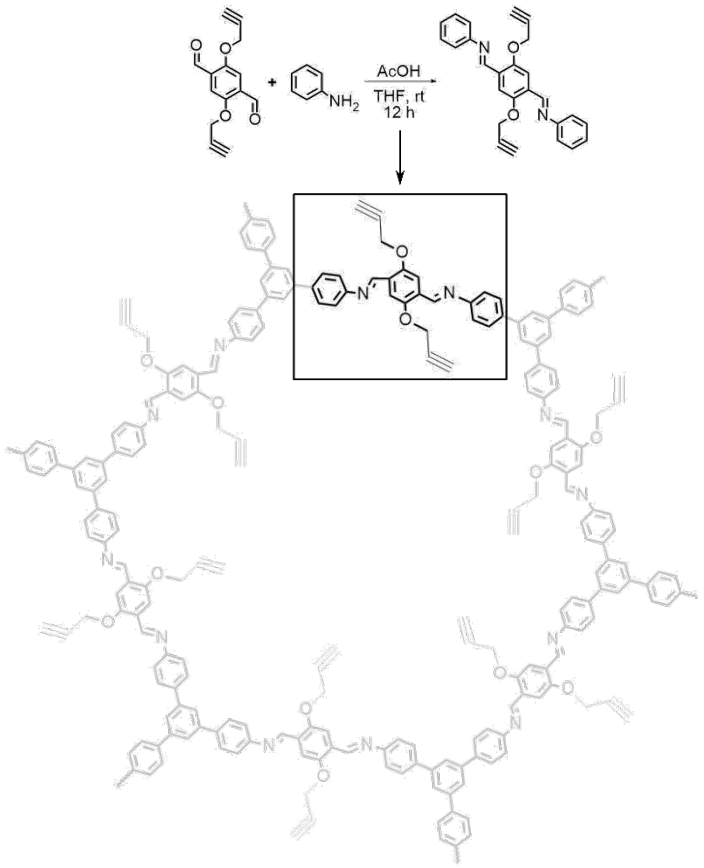

Scheme 3.5. Synthesis of (1*E*,1'*E*)-1,1'-(2,5-bis(prop-2-yn -1-yloxy)-1,4-phenylene)bis(*N*-phenylmethanimine), $C_{26}H_{20}O_2N_2$. This reaction was performed to develop the methodology for 1≡(x%) framework preparation.

In a 50 mL round bottom flask, BPTA (100 mg, 0.413 mmol) was dissolved in THF (2.0 mL) and aniline (94 μL, 1.03 mmol) was added to the mixture in the presence of 6M acetic acid catalyst (0.2 mL). After stirring overnight at room temperature, the solvent was removed under reduced pressure to afford a yellow solid in a quantitative yield. ^{1}H NMR (DMSO-d_6, 300 MHz): 8.39 (2H, s), 7.88 (2H, s), 7.45 (4H, m), 7.29 (6H, m), 5.00 (4H, d, J = 1.95), 3.66 (2H, t, J = 2.19) ppm (Figure 3.15).

Synthesis of 1-Ome. The **1-Ome** framework was prepared according to a modified literature procedure. In a pressure tube (10 mL), a mixture of TAPB (28.0 mg, 0.0800 mmol) and DMTA (23.3 mg, 0.120 mmol) in *o*-dichlorobenzene (*o*-DCB)/*n*-butanol (*n*-

BuOH) (1.00 mL/1.00 mL) mixture were heated at 120 °C for 3 d in the presence of acetic acid (6 M, 0.100 mL). Upon cooling to room temperature, the precipitate was collected, washed three times with THF (50 mL), and subjected to Soxhlet extraction (with THF as a solvent) to remove any unreacted precursors. The obtained powder was collected, dried at 120 °C under vacuum overnight to produce **1-Ome** in 80% yield. IR (neat, cm^{-1}): 2948, 1680, 1589, 1468, 1456, 1407, 1290, 1209, 1145, 1036, 972, 875, 827, 746, 691, and 659. Fitting the N_2 adsorption isotherm to the Brunauer-Emmett-Teller (BET) equation resulted in surface area of 1452 m^2/g. The PXRD pattern, FTIR spectrum, thermogravimetric, and gas sorption analysis are shown in Figures 3.16, 3.17, 3.18, and 3.19, respectively.

Synthesis of 1≡(50%). The **1≡(50%)** framework was prepared according to a modified literature procedure. In a glass tube (10 mL), a mixture of TAPB (28.0 mg, 0.080 mmol) and DMTA/BPTA (a total of 0.120 mmol) at a molar ratio of 50% in *o*-DCB/ *n*-BuOH (1 mL/1 mL) were held at room temperature for 3 d in the presence of an acetic acid (6 M, 0.100 mL). The precipitate was collected, washed three times with THF (50 mL) and subjected to the Soxhlet extraction procedure using THF as a solvent to remove any unreacted precursors. The powder was collected, dried at 120 °C under vacuum overnight to produce **1≡(50%)** in 78% yield. IR (neat, cm^{-1}): 3285, 2940, 1680, 1589, 1486, 1465, 1407, 1290, 1209, 1145, 1036, 972, 875, 827, 746, and 691. Fitting the N_2 adsorption isotherm to the BET equation resulted in surface area of 925 m^2/g. The PXRD pattern, FTIR spectrum, thermogravimetric, gas sorption analysis plots, and ^{13}C CP-MAS NMR data are shown in Figures 3.20, 3.21, 3.22, and 3.2, respectively.

Synthesis of 1≡(34%). The **1≡(34%)** framework was prepared according to a modified literature procedure. In a glass tube (10 mL), a mixture of TAPB (28.0 mg, 0.080 mmol)

and DMTA/BPTA (a total of 0.120 mmol) at a molar ratio of 34% in *o*-DCB/*n*-BuOH (1 mL/1 mL) were held at room temperature for 3 d in the presence of an acetic acid catalyst (6 M, 0.100 mL). The precipitate was collected, washed three times with THF (50 mL) and subjected to Soxhlet extraction with THF to remove unreacted precursors. The powder was collected, dried at 120 °C under vacuum overnight to produce **1≡(34%)** in 78% yield. IR (neat, cm^{-1}): 3285, 2940, 1680, 1589, 1486, 1465, 1407, 1290, 1209, 1145, 1036, 972, 875, 827, 746, and 691 (Figure 3.23).

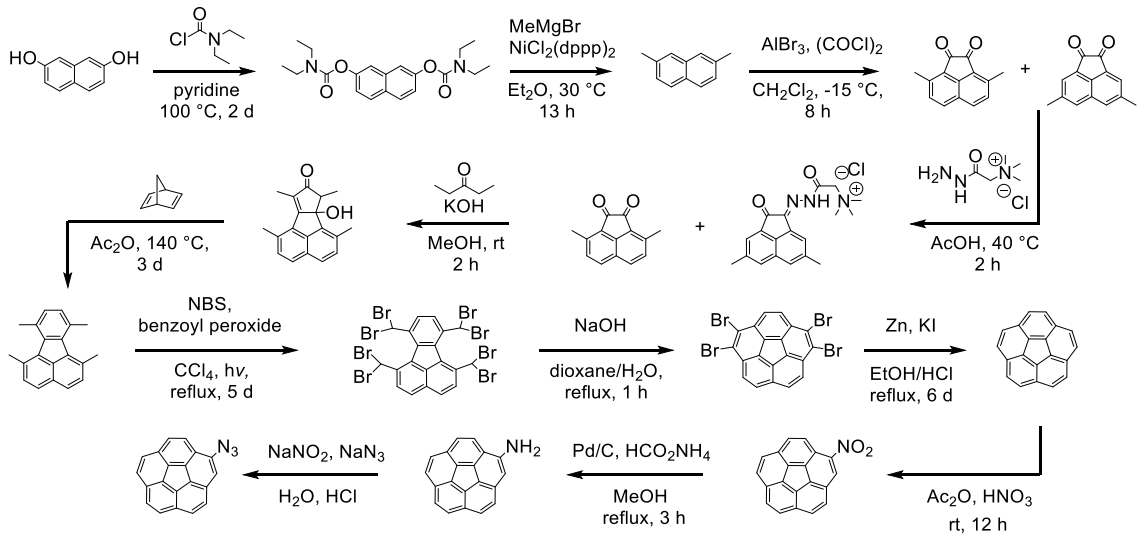

Scheme 3.6. Synthesis of πB-$C_{20}H_9N_3$.

Development of the Synthetic Conditions for CuAAC Reactions. For investigation of reaction conditions necessary to perform CuAAC using πB-$C_{20}H_9N_3$ with the extended insoluble structure **1≡(50%)**, we devised a stepwise approach starting at the molecular level, which includes development of the synthetic methodologies using less bulky and more affordable units (e.g., 2-azidoethanol) before pursuing the reaction with πB-$C_{20}H_9N_3$.

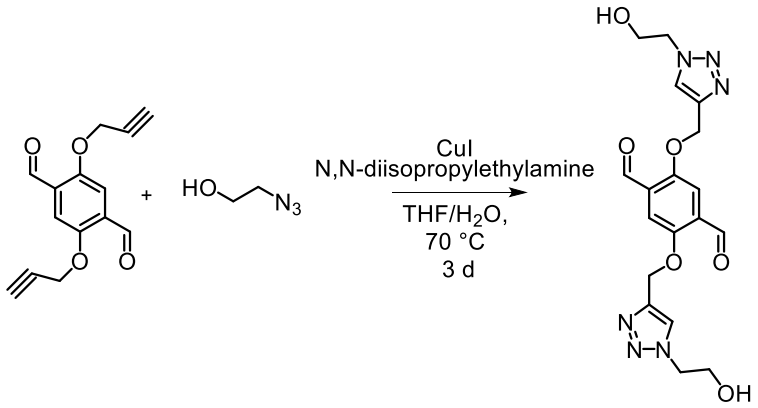

Scheme 3.7. Synthesis of 2,5-bis((1-(2-hydroxyethyl)-1*H*-1,2,3-triazol-4-yl)methoxy)terephthalaldehyde, $C_{18}H_{20}O_6N_6$.

Initially, we coupled just molecular species, such as 2-azidoethanol and BPTA, using THF/H_2O as a medium, which also provided us an access for monitoring the reaction progress by NMR spectroscopy.

In a 25-mL Schlenk tube, BPTA (10.0 mg, 41.0 μmol) and 2-azidoethanol (7.50 mg, 87.0 μmol) were dissolved with THF (0.320 mL) and water (0.110 mL). Next, CuI (2.99 mg, 10.0 μmol) and *N,N*-diisopropylethylamine (THF solution, 1 M, 33 μL) were added. Following degassing with three freeze-pump-thaw cycles, the mixture was reacted at 70 °C for 3 d. After removal of solvent under reduced pressure, the solids were stirred in water overnight, filtered, and dried under vacuum to afford a beige solid isolated in a quantitative yield. ^{1}H NMR (DMSO-d_6, 300 MHz): 10.36 (2H, s), 8.24 (2H, s), 7.68 (2H, s), 5.36 (4H, s), 5.03 (2H, t, J = 5.31), 4.41 (4H, t, J = 5.39), 3.78 (4H, q, J = 5.34) ppm

(Figure 3.24). FTIR (neat, cm^{-1}): 3359 (broad), 2965, 1583, 1381, 1259, 1208, 1154, 1020, and 797 (Figure 3.25). The FTIR data highlights the disappearance of the alkyne triple bond stretches as shown in Figure 3.25. HRMS (ESI, m/z) calculated for $C_{18}H_{20}O_6N_6$ $[M+H]^+$ 417.1444, found 417.1438.

*Stepwise approach for CuAAC reactions with **1≡(x%)***

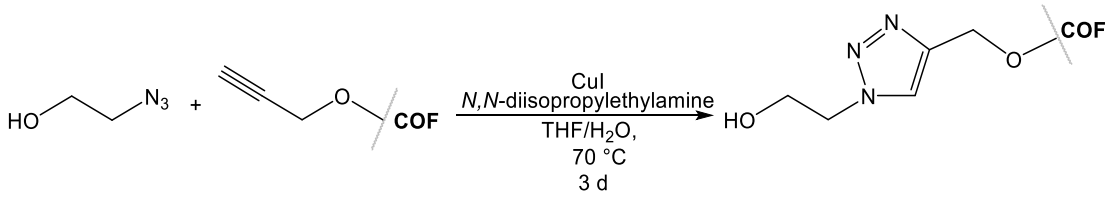

Scheme 3.8. Synthesis of 2-azidoethanol[**1≡(34%)**].

In a 25-mL Schlenk tube, CuI (1.50 mg, 7.50 μmol) and 1≡(34%) (15.0 mg) were added to a mixture of THF/water (2.00 mL/0.75 mL). To the resulting mixture, N,N-diisopropylethylamine (1 M, 75 μL) and 2-azidoethanol (4.40 mg, 50.0 μmol) were added. The flask was degassed through three freeze-pump-thaw cycles, and the reaction mixture was stirred at 70 °C for 3 d. Upon cooling to room temperature, the precipitate was collected, washed with THF/ACN, and dried under vacuum overnight to give a brown solid in a quantitative yield. IR (neat, cm-1) 2926, 1591, 1505, 1465, 1412, 1293, 1209, 1034, 823, and 697 (Figure 3.26). The FTIR data highlights the disappearance of the alkyne triple bond stretches as shown in Figure 3.26.

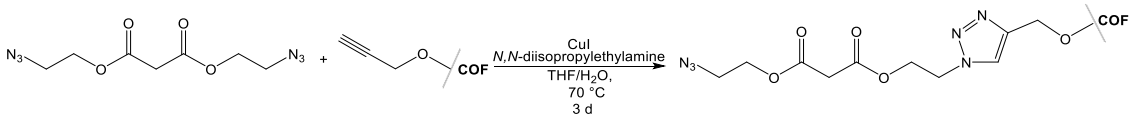

Scheme 3.9. Synthesis of bis(2-azidoethyl) malonate[**1≡(34%)**].

In a 25-mL Schlenk tube, CuI (1.50 mg, 7.50 μmol) and **1≡(34%)** (15.0 mg) were added to a mixture of THF/water (2.00 mL/0.750 mL). To the resulting mixture, *N,N*-

diisopropylethylamine (1 M, 75 μL) and bis(2-azidoethyl) malonate (10.0 mg, 50.0 μmol) were added. The flask was degassed through three freeze-pump-thaw cycles and the mixture was stirred at 70 °C for 3 d. Upon cooling to room temperature, the precipitate was collected, washed with THF/ACN, and dried under vacuum overnight to give a brown solid in a quantitative yield. IR (neat, cm^{-1}): 2100, 1738, 1595, 1504, 1488, 1412, 1287, 1211, 1147, 1036, 829, 732, 698 (Figure 3.27). The FTIR data are shown in Figure 3.27, which highlights the disappearance of –C≡C– and –C≡C–H stretches.

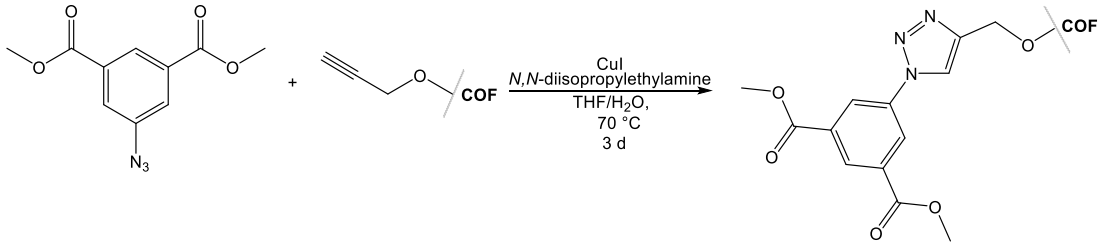

Scheme 3.10. Synthesis of dimethyl 5-azidoisophthalate[**1≡(50%)**].

In a 25-mL Schlenk tube, CuI (6.00 mg, 0.0315 mmol) and **1≡(50%)** (10.0 mg) were added to a mixture of THF/water (0.323 mL/ 0.107 mL). To this mixture, *N,N*-diisopropylethylamine (1 M, 17 μL) and dimethyl 5-azidoisophthalate (1 M, 25 μL) were added. The flask was degassed through three freeze-pump-thaw cycles, and the mixture was stirred at 70 °C for 3 d. Upon cooling to room temperature, the precipitate was collected, washed with THF/ACN and dried under vacuum overnight to give a brown solid in a quantitative yield. FTIR (neat, cm^{-1}): 1730, 1599, 1506, 1411, 1249, 1211, 1039, 879, 827, and 758 (Figure 3.28). The disappearance of –C≡C– and –C≡C–H stretches were observed.

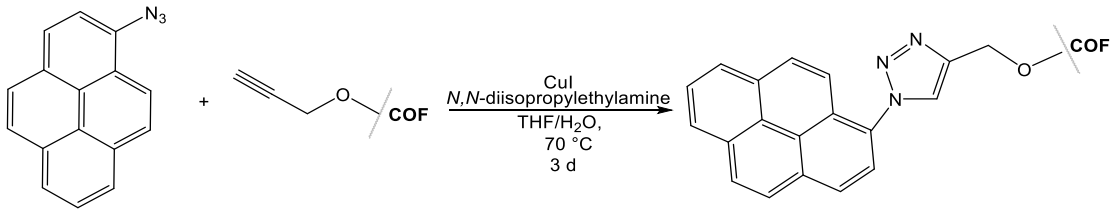

Scheme 3.11. Synthesis of 1-azidopyrene[**1≡(50%)**].

In a 25-mL Schlenk tube, CuI (6.00 mg, 0.0315 mmol) and **1≡(50%)** (10.0 mg) were added to a mixture of THF/H_2O (0.323 mL/0.107 mL). To resulting mixture, *N,N*-diisopropylethylamine (1 M, 17 µL) and 1-azopyrene (1 M, 25 µL) were also added. The flask was degassed through three freeze-pump-thaw cycles, and the mixture was stirred at 70 °C for 3 d. Upon cooling to room temperature, the precipitate was collected, washed with THF/ACN, and dried under vacuum overnight to give a brown solid in a quantitative yield. IR (neat, cm^{-1}): 1682, 1593, 1506, 1488, 1464, 1409, 1289, 1210, 1183, 1143, 1038, 880, 828, and 694. (Figure 3.29). The FTIR data highlight the disappearance of the alkyne triple bond stretches as shown in Figure 3.29.

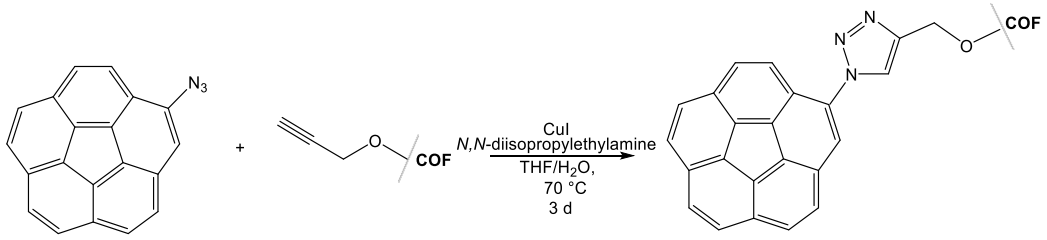

Scheme 3.12. Synthesis of πB-$C_{20}H_9N_3$[**1≡(50%)**].

In a 25-mL Schlenk tube, CuI (6.00 mg, 0.0315 mmol) and **1≡(50%)** (10.0 mg) were added to a mixture of THF/H_2O (0.323 mL/0.107 mL). To the resulting mixture, *N,N*-diisopropylethylamine (1 M, 17 µL) and 1-azidocorannulene (1 M, 18 µL) were added. The flask was degassed through three freeze-pump-thaw cycles, and the mixture was stirred at 70 °C for 3 d. Upon cooling to room temperature, the precipitate was collected, washed

with THF/ACN, and dried under vacuum overnight to give a brown solid in a quantitative yield. FTIR (neat, cm^{-1}): 1673, 1596, 1510, 1458, 1394, 1284, 1210, 1185, 1029, 879, 824, 732, and 695. (Figure 3.2). Fitting the N_2 adsorption isotherm to the BET equation resulted in surface area of 865 m^2/g (Figure 3.31). The PXRD pattern, gas sorption analysis plot, and FTIR spectrum are shown in Figures 3.30, 3.31, and 3.2, respectively. ^{13}C CP-MAS NMR and FTIR data reveal disappearance of the alkyne resonances as shown in Figure 3.2.

A control experiment involving 1≡(50%).

As a control experiment, we treated **1≡(50%)** under the same reaction conditions but without presence of the azide-containing precursor. As expected, we observed preservation of both 2120 cm^{-1} (C≡C) and 3300 cm^{-1} (H–C≡C) resonances in the FTIR spectrum (Figure 3.32).

In a 25-mL Schlenk tube, CuI (10 mg, 0.053 mmol) and **1≡(50%)** were added to a mixture of THF/H_2O (0.32 mL/0.11 mL). To the reaction mixture, *N,N*-diisopropylethylamine (1 M, 17 μL) was added. The flask was degassed through three freeze-pump-thaw cycles and the mixture was stirred at 70 °C for 3 d. Upon cooling to room temperature, the precipitate was collected, washed with THF/ACN, and dried under vacuum overnight to give a brown solid in a quantitative yield. IR (neat, cm^{-1}): 3300, 2120, 1673, 1596, 1510, 1458, 1394, 1284, 1210, 1185, 1029, 879, 824, 732, and 695 (Figure 3.32). ^{13}C CP-MAS NMR data highlight the preservation of 2120 (C≡C) and 3300 cm^{-1} (H–C≡C) resonances as shown in Figure 3.2.

Preparation of πB-$C_{20}H_{10}$@1-OMe.

In a 0.5 dram vial, **1-Ome** (5.0 mg) was added to 0.20 mL THF followed by the addition of πB-$C_{20}H_{10}$ (5.0 mg, 0.020 mmol) in THF (45 μL). After 5 d, THF was used to

remove any excess of corannulene. As a result, a red powder was obtained in a quantitative yield. ^{1}H NMR spectroscopic studies of a digested sample confirmed the presence of corannulene in **1-Ome** after washing, and it was found out presence of one corannulene molecule per six –Ome units (Figure 3.33). FTIR (neat, cm^{-1}): 660, 760, 865, 1064, 1093, 1256, 1388, 1408, 1440, 1496, 1597, and 1657. The PXRD pattern is shown in Figure 3.34. Fitting the N_2 adsorption isotherm to the BET equation resulted in surface area of 898 m^2/g (Figure 3.35).

Digestion Procedure for πB-$C_{20}H_{10}$@1-OMe.

To study the amount of πB-$C_{20}H_{10}$ in πB-$C_{20}H_{10}$@**1-OMe**, a solution of 500 μL DMSO and 10 μL of concentrated HCl was added to ~5 mg of πB-$C_{20}H_{10}$@**1-OMe**, followed by heating at 100 °C for 3 d. Based on ^{1}H NMR spectroscopic analysis of the digested COF, non-coordinative immobilization led to inclusion of one corannulene molecule per six –Ome units (Figure 3.33)

Preparation of $C_{16}H_{10}$@1-OMe.

In a 0.5 dram vial, **1-Ome** (5.00 mg) was added to 0.20 mL THF followed by the addition of pyrene (5.0 mg, 0.024 mmol) in THF (45 μL). After 5 d, solvent was replaced with fresh THF until the solution was clear to remove any excess of pyrene. As a result, an orange powder was obtained in a quantitative yield. Based on ^{1}H NMR spectroscopic analysis of the digested COF, non-coordinative immobilization led to inclusion of four pyrene molecule per six –Ome units.

Preparation of $C_{10}H_8$@1-OMe.

In a 0.5 dram vial, **1-Ome** (5.0 mg) was added to 0.20 mL THF followed by the addition of naphthalene (5.0 mg, 0.039 mmol) in THF (45 μL). After 5 d, the sample was

thoroughly washed with THF to remove any excess of naphthalene. As a result, a yellow powder was obtained in a quantitative yield. Based on ^{1}H NMR spectroscopic analysis of the digested COF, non-coordinative immobilization led to inclusion of three naphthalene molecules per six –Ome units.

X-ray crystal structure determination, BPTA ($C_{14}H_{10}O_4$).

X-ray intensity data from a yellow rectangular plate were collected at 100(2) K using a Bruker D8 QUEST diffractometer equipped with a PHOTON-100 CMOS area detector and an Incoatec microfocus source (Mo K_α radiation, λ = 0.71073 Å). The raw area detector data frames were reduced and corrected for absorption effects using the Bruker APEX3, SAINT+ and SADABS programs. Final unit cell parameters were determined by least-squares refinement of 5779 reflections taken from the data set. The structure was solved with SHELXT. Subsequent difference Fourier calculations and full-matrix least-squares refinement against F^2 were performed with SHELXL-2018 using OLEX2.

The compound crystallizes in the monoclinic system. The pattern of systematic absences in the intensity data was consistent with the space group $P2_1/c$, which was confirmed by the structure solution. The asymmetric unit consists of half of one molecule, which is located on a crystallographic inversion center. All non-hydrogen atoms were refined with anisotropic displacement parameters. Hydrogen atoms bonded to carbon were located in Fourier difference maps and refined freely. The largest residual electron density peak in the final difference map is 0.27 e/Å^3, located 0.69 Å from C3.

Table 3.1. X-ray structure refinement data for BPTA.[a]

compound	**BPTA**
formula	$C_{14}H_{10}O_4$
FW	242.22
T, K	100(2)
crystal system	monoclinic
space group	$P2_1/c$
Z	2
a, Å	9.8628(5)
b, Å	4.5525(2)
c, Å	12.7876(6)
α, °	90
β, °	100.550(2)
γ, °	90
V, Å^3	564.46(5)
d_{calc}, g/cm^3	1.425
μ, mm^{-1}	0.105
F(000)	252.0
crystal size, mm^3	0.26 × 0.2 × 0.09
theta range	6.482 to 56.924
index ranges	$-13 \leq h \leq 13$ $-6 \leq k \leq 6$ $-17 \leq l \leq 17$
refl. Collected	17034
data/restraints/parameters	1419/0/102
GOF on F^2	1.048
R_1/wR_2, $[I \geq 2\sigma(I)]^b$	0.0371/0.0833

Fluorescence spectroscopy.

An Edinburgh FS5 fluorescence spectrometer equipped with a 150 W Continuous Wave Xenon Lamp source for excitation was used to acquire steady-state emission spectra. Emission measurements on solid samples were collected on powders of the desired

materials placed inside a 0.5 mm quartz sample holder using the front-facing module. Fluorescence lifetimes were measured using a Mini-τ lifetime spectrometer from Edinburgh Instruments equipped with a 365-nm picosecond-pulsed-light-emitting diode (EPLED 365).

Fitting of fluorescence decays.

The fluorescence decays for **1-Ome**, $C_{20}H_{10}$πB@**1-OMe**, $C_{16}H_{10}$@**1-OMe**, $C_{10}H_8$@**1-OMe**, and πB-$C_{20}H_9N_3$[**1≡(50%)**] were fit with the triexponential function:

$$\mathrm{I}(t) = \int_{-\infty}^{\mathrm{t}} \mathrm{IRF}(t') \sum_{\mathrm{i}=1}^{\mathrm{n}} B_{\mathrm{i}} \mathrm{e}^{\left[-\frac{t-t'}{\tau_i}\right]}\, dt' \qquad \text{(eq. 4.1)}$$

where τ and B are lifetime and amplitude, respectively.

The amplitude-weighted average fluorescence lifetimes were calculated based on the following equation:

$$\langle \tau_{\mathrm{av}} \rangle = \frac{B_1\tau_1 + B_2\tau_2 + B_3\tau_3}{B_1 + B_2 + B_3} \qquad \text{(eq. 4.2)}$$

Other Physical Measurements.

NMR spectra were obtained on a Bruker Avance III-HD 300 and Bruker Avance III 400 MHz NMR spectrometers. ^{13}C and ^{1}H NMR spectra were referenced to natural abundance ^{13}C peaks and residual ^{1}H peaks of deuterated solvents, respectively. FTIR spectra were collected on a Perkin-Elmer Spectrum 100. Powder X-ray diffraction patterns were recorded from a Rigaku Miniflex II diffractometer with an accelerating voltage and current of 30 kV and 15 mA, respectively. Thermogravimetric analysis was performed on an SDT Q600 Thermogravimetric Analyzer using an alumina boat as the sample holder.

Diffuse reflectance spectra were collected on a PerkinElmer Lambda 45 UV-vis spectrometer referenced to Spectralon®. The BET specific surface area was determined by measuring N_2 adsorption at 75.6 K using a Micromeritics ASAP 2020. Prior to measurement, the samples were heated in vacuum (1.0×10^{-7} Torr) with a heating rate of 1 °C/min up to 60 °C, held for 3 h and subsequently heated to 80 °C at 10 °C/min and then held at this temperature for 9 h.

A two point method was employed to measure conductance σ (S/cm) of pressed pellets according to following equation:

$$\sigma = Il/VA,$$

where I – current, l – thickness of the pellets, V – voltage, A – surface area of the prepared pellets.

The electrical conductance in the prepared materials follows Ohm's law and was measured by fitting a linear current (I)-voltage (V) curve obtained by using a source meter (Keithley Instruments GmbH, Germering, Germany, model 263) and an electrometer (Keithley Instruments GmbH, Germering, Germany, model 617). All samples were prepared consistently by using the same amounts of materials and the same pressing technique (30 mg of material, dried at 120°C for 3 days, were pressed under 4000 psi at room temperature for 5 minutes with an International Crystal Laboratory 20 Ton E-Z Hydraulic Laboratory Press™), which relives the issue of deviations from the ideal configuration. The home-built setup was used to perform 2-contact probe conductivity measurements on the pressed pellets: the pellet was placed between two brass plates with attached contacts. A layer of double sided carbon tape (Electron Microscopy Sciences) was added between a pellet and plates to improve contact.

Solid-state NMR spectra (^{13}C CP-MAS) were collected on a Bruker Avance III-HD 500 MHz spectrometer fitted with a 1.9 mm MAS probe. $^{13}C\{^{1}H\}$ CP-MAS NMR spectra (125.79 MHz) were collected at ambient temperature with a sample rotation rate of 20 kHz. For cross polarization, 2.0 ms contact time with linear ramping on the ^{1}H channel and 62.5 kHz field on the ^{13}C channel were used. ^{1}H dipolar decoupling was performed with SPINAL64 modulation and 147 kHz field strength. Free induction decays (2048–5000 transients) were collected with a 27 ms acquisition time over a 400 ppm spectra width with a relaxation delay of 2.0 s. All XPS experiments were carried out with a Kratos AXIS Ultra DLD system, which was equipped with a monochromatic AlKα source, a hemispherical analyzer, a charge neutralizer for studying insulating samples, and a load lock chamber for rapid introduction of samples into the vacuum chamber. This system has been described in more detail elsewhere. Dwell times were 1000 ms and 600 ms for the valence band and C(1s) regions, respectively, and the step size for both regions was 0.06 eV. Absolute binding energies were set by fixing the C(1s) signal at 284.8 eV, which is the position for adventious carbon, but also has contribution from carbons in πB-$C_{20}H_{10}$ and **1-Ome**. Valence band intensities were not normalized since the C(1s) intensities were comparable for both of the **1-Ome**-corannulene containing samples (see Figure 3.41). Furthermore, normalizing the intensities of the valence band spectra to the total carbon signal does not change the fact that the πB-$C_{20}H_{10}$ and **1-Ome** alone have very little intensity at the valence band edge compared to πB-$C_{20}H_{10}$@**1-Ome** and πB-$C_{20}H_9N_3$[**1≡(50%)**]. **1-Ome** only had a C(1s) intensity that was slightly higher, which means that a normalized valence band spectrum would have even less relative intensity at E_F. Although the corannulene C(1s) intensity was significantly lower than the other three samples, there is zero intensity between 0 and 3 eV.

Computational Details.

Molecular model. In theoretical analysis several arrangements of πB-$C_{20}H_{10}$ units are considered: convex-to-concave bowl orientation ("stack", Figure 3.36), concave-to-concave/convex-to-convex orientation ("clam", Figure 3.36) and the arrangement of pristine corannulene observed in the solid state ("pinwheel", Figure 3.36). The geometries have been taken from Ref. [16,17]. The nearest intramolecular carbon-to-carbon and unit center-to-center distances are listed in Table 3.2.

The ground state electron transfer properties are modeled assuming the hopping mechanism, i.e., an electron moves from a molecule to a molecule via a sequence of independent hops. For the stack geometry all hops are equivalent. For the "clam" geometry, there are two types of hops: concave-to-concave (unit A to unit B) and convex-to-convex (unit B to unit C) as shown in the central panel of Figure 3.36. To move the charge through the material, these two hops take place sequentially. In the case of the "pinwheel" structure, the charge transfer also involves two steps: a hop from unit *1* to *3* followed by a hop from to either unit *2* or to unit *4* (Figure 3.36, right). Therefore, to compare the charge transfer properties of different geometries, for the two-hop processes the geometric mean of single-hop rates is used.

The electronic couplings. To evaluate the electronic coupling, we employ a conventional two-state approach, which is termed "1+1" in Q-Chem. The electron transfer from a donor molecule, *D*, to an acceptor molecule, *A*, ($D^-A \rightarrow DA^-$) is described in the basis of two electronic wavefunctions, representing the initial state *i* (D^-A) and the final state *f* (DA^-) of the electron donor-acceptor system. Minimization of the total energy in this basis is equivalent to the generalized eigenvalue problem,

$$H = ES. \quad (1)$$

In Eq. (1), $\boldsymbol{H}$ is the Hamiltonian matrix and $\boldsymbol{S}$ is the overlap matrix,

$$\boldsymbol{H} = \begin{pmatrix} H_{ii} & H_{if} \\ H_{if} & H_{ff} \end{pmatrix}, \boldsymbol{S} = \begin{pmatrix} S_{ii} & S_{if} \\ S_{if} & S_{ff} \end{pmatrix}. \quad (2)$$

The coupling V_c is determined as the off-diagonal element of $\boldsymbol{H}$ transformed into the orthogonal electronic basis, $\boldsymbol{H}^{eff} = \boldsymbol{S}^{-1/2}\boldsymbol{H}\,\boldsymbol{S}^{-1/2}$. If the electronic eigenstates are normalized to 1, then the coupling is expressed as,

$$V_c = H_{if}^{eff} = \frac{H_{if} - S_{if}(H_{ii}+H_{ff})/2}{1-S_{if}^2}. \quad (3)$$

The matrix elements in Eq. (4.2) are evaluated *directly* using the charge-localized determinants. The charge-localized initial/final states are generated by using the fragment molecular orbitals with appropriate charges, i.e. D^-A as the initial state and DA^- as the final state. The direct coupling method is well-defined for the Hartree-Fock (HF) theory of the electronic structure. While the accuracy of the HF energies is limited by its mean-field character, the couplings are known to be more sensitive to the quality of the basis set, rather than to the electron correlation. Since the system has an overall negative charge, we use basis set 6-31+G* containing diffuse functions without relaxation of the fragment molecular orbitals. The couplings for all relative geometries of two πB-$C_{20}H_{10}$ molecules relevant to "stack", "clam" and "pinwheel" arrangements are listed in Table 3.2. The largest (by at least a factor of four) coupling is obtained for the stacked geometry. This trend is consistent with the LUMO character of the three-unit clusters shown in Figure 3.37 and 3.38: the LUMOs for the stack geometry are delocalized over all three units forming a "π-column"; for the clam geometry, LUMO is localized on two out of three fragments,

while the LUMOs for the three units from the pinwheel geometry (Figure 3.38(d)) can be seen as an intermediate case.

Table 3.2. Analysis of the ground state electron transfer within the two-state direct coupling method (ES method is HF/6-31+G*).

"stack"		**"clam"**		**"pinwheel"**					
		A→B	*B→C*	*1→2*	*1→3*	*1→4*	*2→3*	*2→4*	*3→4*
R_{cntr}, Å	3.80	8.59	5.14	8.45	3.89	11.60	7.16	8.55	10.61
R_{min}, Å	3.46	4.68	3.38	5.22	3.39	3.84	3.52	4.03	3.80
V_c, eV	0.2188	-0.0103	-0.0162	0.0002	0.0294	-0.0203	0.0549	-0.0043	0.0391

The electronic couplings obtained with the direct coupling method should be viewed as rough estimates: besides the limitations of the HF method, the electronic state overlaps are very sensitive (exponential dependence) on the separation between the units as illustrated in Figure 3.37 for the "stack" geometry. Additional estimates can be made from the LUMO gap of two equivalent molecules, such as the neutral dimer of corannulene molecules in the "stack" geometry. Based on Koopmans' theorem, for two equivalent molecules the frontier orbitals of the anionic dimer are the LUMO and LUMO+1 of the neutral system, and their splitting is related to the coupling between the equivalent initial and final states ($D^{-1}A$ and DA^{-1}),

$$E_{LUMO+1} - E_{LUMO} \approx 2V_c.$$

Since the diffuse functions tend to fill up the frontier orbitals, this coupling estimate is made using the valence basis 6-31G*. For the stack geometry the coupling is −0.217 eV (splitting between the two nearly degenerate pairs of LUMOs; for the *BC* and *AB* dimers, the couplings are −0.076 eV (LUMO and LUMO+1) and −0.0133 eV (nearly triply degenerate LUMO, LUMO+1, LUMO+2 vs LUMO+3). Given the simplicity of the energy

gap method, getting the same magnitude for the couplings as with the direct coupling method, gives some support to our computational model.

Rate and diffusion constants, electron mobility.

According to the Marcus theory, the electronic transfer rate for a nonadiabatic process is

$$k = \frac{2\pi}{\hbar}\frac{|V_c|^2}{\sqrt{4\pi\lambda k_B T}}\exp\left(-\frac{\left(\lambda+\Delta G^0\right)^2}{4\lambda k_B T}\right). \quad (4)$$

In Eq. (4) λ - the reorganization energy of the system in response to "instantaneous" relocation of an electron from the donor to acceptor, ΔG° is the difference in the energies of the initial and final states, and T is the temperature. Eq. (4) is applicable in the weak initial/final state coupling regime, $V_c << \lambda$. In the simplest picture, i.e. the influence of the molecular environment on the donor and acceptor states is neglected, the initial electronic state is $|i\rangle = |D^-\rangle \times |A\rangle$, and the final state is $|f\rangle = |D\rangle \times |A^-\rangle$. The energy of the initial state is

$$E_i = E_{D^-} + E_A \quad (5)$$

After the instantaneous electron "hop", i.e. the vertical electronic excitation, the energy of the initial state becomes

$$E_i^* = E_i - E_{D^-}^{HOMO} + E_A^{LUMO} \quad (6)$$

Upon relaxation, the system arrives at its final state of energy

$$E_f = E_D + E_{A^-} \quad (7)$$

Thus, the electronic reorganization energy is

$$\lambda = E_A^{LUMO} - E_{D^-}^{HOMO}, \quad (8)$$

while the total energy change is

$$\Delta E = E_i - E_f + \lambda = \Delta G_0 + \lambda. \quad (9)$$

For the identical donor and acceptor molecules $\Delta G^{\circ} = 0$. Within the theory used in direct coupling calculation (HF/6-31+G*), the reorganization energy of electron transfer between two corannulene molecules is $\lambda = 0.89$ eV. This estimate is the same for all arrangements of the corannulene molecules and is at least 3.3 times larger than the computed couplings.

For closer connection of theory and experiment we examine the ratios of conductivity values (σ) for different geometries. The conductivity is related to the charge transfer rates through the charge carrier mobility, μ

$$\sigma = n\mu e. \tag{10}$$

The latter is related to the charge transfer rates through the diffusion constant D and the mean length of the particle transfer

$$\mu = \frac{eD}{k_B T}, \; D = \frac{kL^2}{2}, \tag{11}$$

Thus, assuming equal number of charge carriers in all packing motifs,

$$\frac{\sigma_i}{\sigma_j} = \frac{\mu_i}{\mu_j} = \frac{D_i}{D_j} = \frac{k_i L_i^2}{k_j L_j^2} \tag{12}$$

The shortest distance between carbon atoms of different πB-$C_{20}H_{10}$ units is used in Eq. (11), $L=R_{min}$ given in Table 3.2. The ratios of the rate and diffusion constants are given in Table 3.3 with respect to those of the most conducting "stack" geometry (k_o and D_o). According to these estimates the charge mobility for the stack geometry there is nearly 40 times larger than for the clam geometry and close to 300 times larger than for the "pinwheel" geometry. These results qualitatively agree with the conductivity measurements implying significant (10000) increase in charge mobility in corannulene integrated into COF compared to that of pristine corannulene. Overall, we argue that in the

COF the corannulene molecules form conductive stack-like columns rather than maintaining "pinwheel" orientation associated with the pristine corannulene material.

Table 3.3. The ratios of the charge transfer rates and diffusion constants for different geometrical arrangements.

Ratio[a, b]	k_{132}/k_o	k_{134}/k_o	k_{clam}/k_o	k_o/k_{132}	k_o/k_{134}	k_o/k_{clam}	D_o/D_{132}	D_o/D_{134}	D_o/D_{clam}
	0.0337	0.0241	0.0035	29.63	41.56	286.6	29.68	38.57	216.9

[a]The coupling constants are given in eV.

[b]Geometric averages are taken for couplings and distances for the two-step transfer in "clam" and "pinwheel" orientation of corannulene units.

The valence band density of states. In conjunction with the XPS results, we have generated the Density of States (DOS) for the valence band as a function of binding energy (Figure 3.39). The DOS was constructed from the energies of occupied molecular orbitals obtained with the Long-Range Corrected (LRC) ωPBEh density functional method for the 4-unit "stack" and "pinwheel" orientations. The chosen electronic structure method, i.e. LRC-ωPBEh/6-31G* has been shown to perform well for the ground and excited state properties including the charge-transfer states. The DOS is simulated by summing the Gaussian functions centered at the energies of 260 occupied MOs. The standard deviation of the Gaussian function is 0.85 eV. On the plot the curves are shifted to have zero binding energy at the Fermi level. The two solid curves are shifted in accord with experimental calibration: the zero of energy is set to the center of the computed carbon gap of 5.87 eV (experimental value for the half-gap is 2.85 eV). The dashed curves are shifted according to the respective computed HOMO-LUMO gaps, which are 7.17 and 7.46 eV for the stack and pinwheel orientations. The simulated DOSs for the two geometries are quite similar to

each other: the main difference is 0.3 eV (0.15 eV for the MO gap) peak shift. The shift is small, but it is in the direction of the XPS results for the pristine rather than COF-integrated corannulene. The overall shape is close to that of the pristine corannulene sample. Therefore, we attribute the lowest energy peak near 2.5 eV in the corannulene-COF samples to the COF states, modified by the interaction with guest molecules. This claim is supported by the fact that XPS of empty COF has significant DOS in this energy region. Extended molecular models for the pristine and COF-integrated corannulene are needed for a more definitive DOS analysis.

Excitation energies and LUMOs. To estimate the band gap in the corannulene-containing materials we have analyzed the excitation energies for the "cluster" models of corannulene materials, consisting of 3 and corannulene molecules for "stack", "clam", and "pinwheel" geometries as well as for the "stack", *AB* and *BC* corannulene dimers (Figure 3.36). The excitation energies are computed within the TDDFT formalism as implemented in Q-Chem. The long-range-corrected density functional with empirical GRIMME correction and diffuse basis (LRC-ωPBEh-D3/6-31+G*) is selected to better capture the intramolecular interactions. As seen from Table 3.4, the lowest excitation energies for both, triplet and singlet states computed for the 3- and 4-unit models are in close agreement. The difference for the "stack" geometry is less than 0.5%; the difference with the dimer is on the order of 3%. Thus, within our computational method, the 4-unit cluster is a reasonable molecular model for the analysis of electronic excitations and band gaps. Our estimates for the band gaps are 2.95/2.87 eV (for the "stack"/"pinwheel" geometry, respectively) for the triplet state excitation, and 3.86/3.81 eV for the singlet state excitation. The computed values for the "stack"/"pinwheel", are higher than the experimentally assessed values of

2.24 and 1.94 eV for the COF-integrated and pristine corannulene, respectively, which is typical for the cluster model calculations. Inclusion of more corannulene molecules is expected to reduce the energy gap. Nevertheless, even within our minimalistic 4-unit model, we see the experimentally observed trend of the stacked geometry having larger band gap compared to the material.

Table 3.4. The lowest excitation energies: method LRC-wPBEh/6-31+G*/EMPIRICAL- GRIMME3 (dispersion correction) in eV.

Units/geometry		**Triplet**	**Singlet**
2	stack	2.9868 (2.9990)	3.9323 (3.9788)
	A→B	3.0188 (3.0256)	4.0116 (4.0480)
	B→C	2.9981 (3.0045)	3.9587 3.9980)
3	"stack"	2.9609	3.8841
	"clam"	2.9967	3.9565
	1→3→2	2.8778	3.8210
	1→3→4	2.8727	3.8159
4	"stack"	2.9507	3.8644
	"clam"	2.9955	3.9543
	"pinwheel"	2.8740	3.8149

The character of the lowest singlet states for the 4-unit geometry is illustrated in Figure 3.40. Two most contributing virtual orbitals are shown for the three geometries. For the "stack" configuration four lowest virtual orbitals nearly equally contribute to a delocalized excited singlet. V2 and V4 (transition originates with HOMO) are shown. For the clam

shell the main contribution comes from LUMO to HOMO (transitions HOMO→V1 and HOMO-1 → V6, V1 and V6 are shown). For the pinwheel the main transitions are HOMO → V2 and HOMO → V5 which correspond to *1→3→4* charge transfer pathway of the direct coupling method. These excited states and the LUMOs from our charge transfer calculations (Figure 3.38) clearly show the same overall features (delocalization for the stack, localization on the *BC* pair for the clam and intermediate delocalization for the pinwheel geometries) supporting our attribution of high conductivity in corannulene-in-COF to the stacking of πB-$C_{20}H_{10}$ units. We expect increased excited state electron and energy transfer for corannulene-in-COF compared to the pristine material as well.

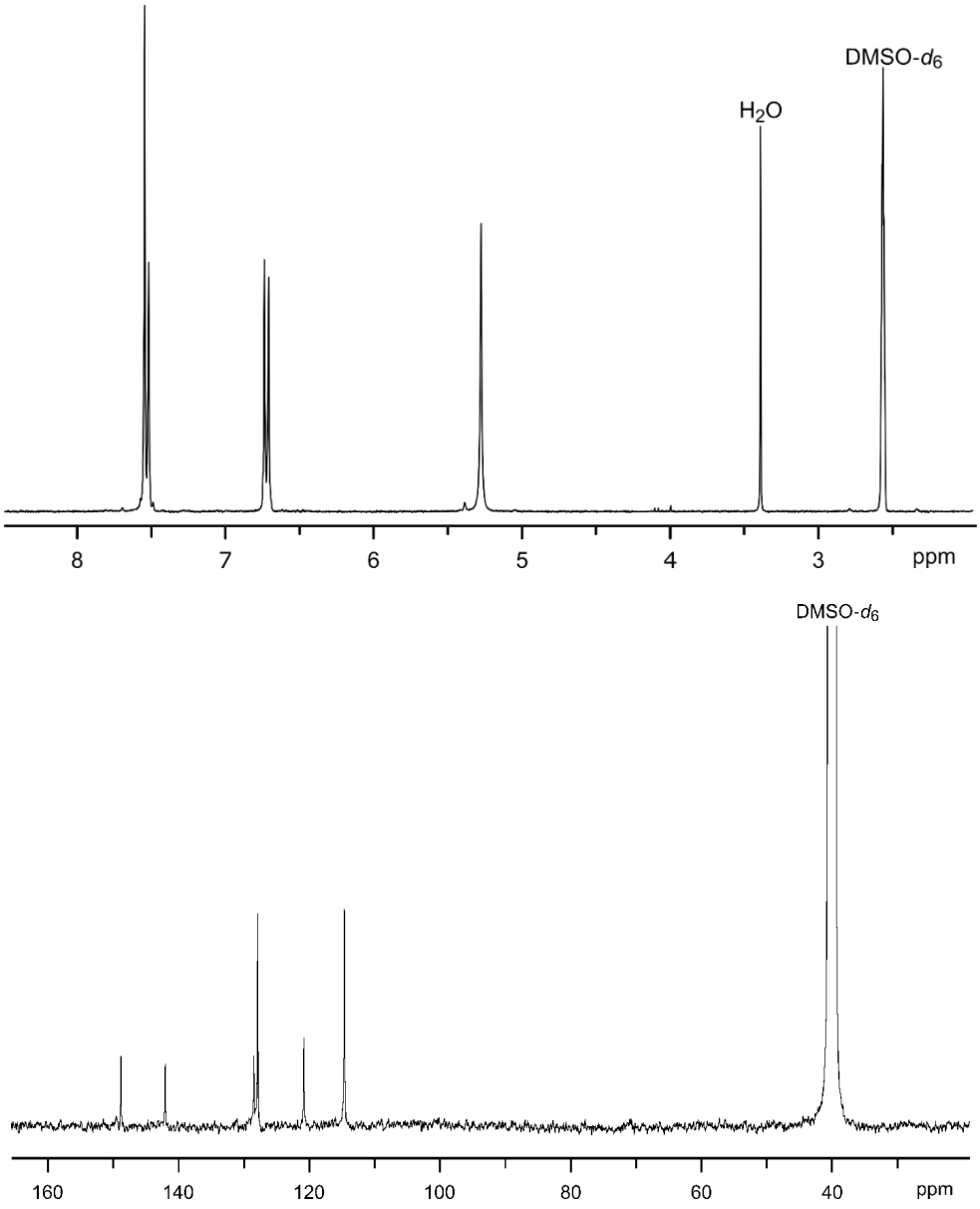

Figure 3.5. ^{1}H NMR (top) and ^{13}C NMR (bottom) spectra of TAPB in DMSO-d_6.

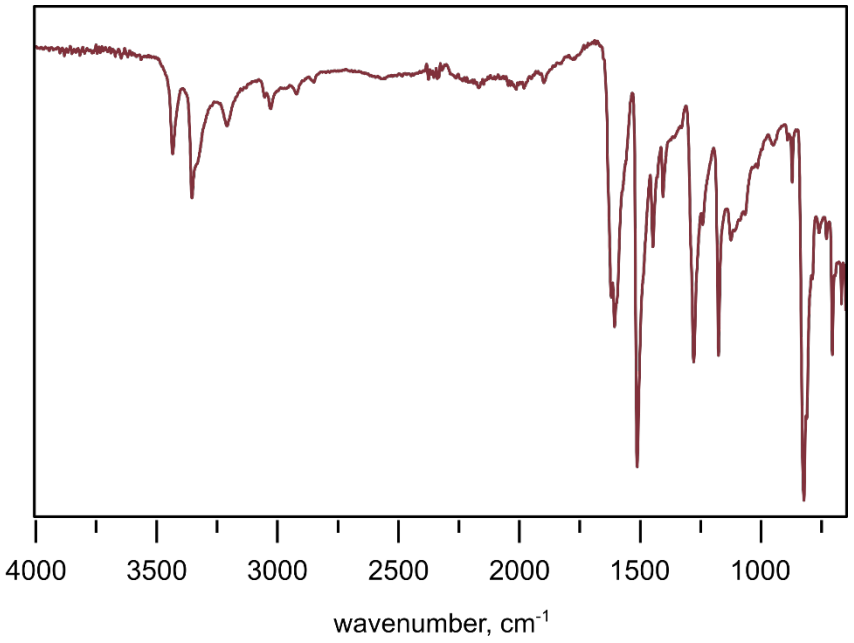

Figure 3.6. FTIR spectrum of TAPB.

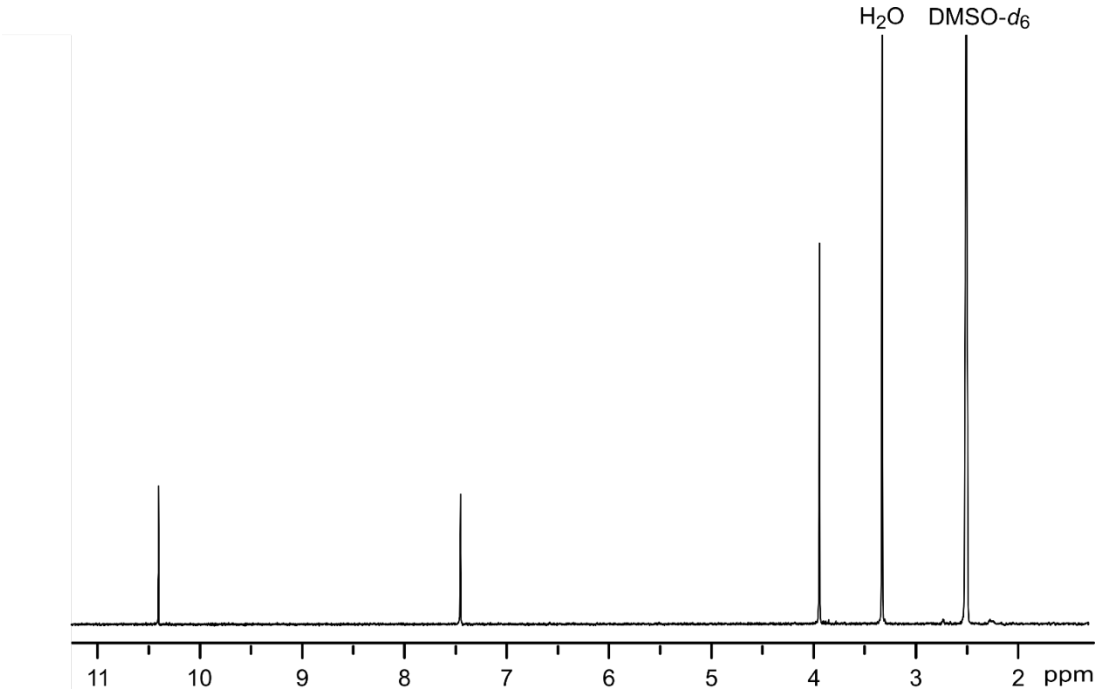

Figure 3.7. ^{1}H NMR spectrum of DMTA in DMSO-d_6.

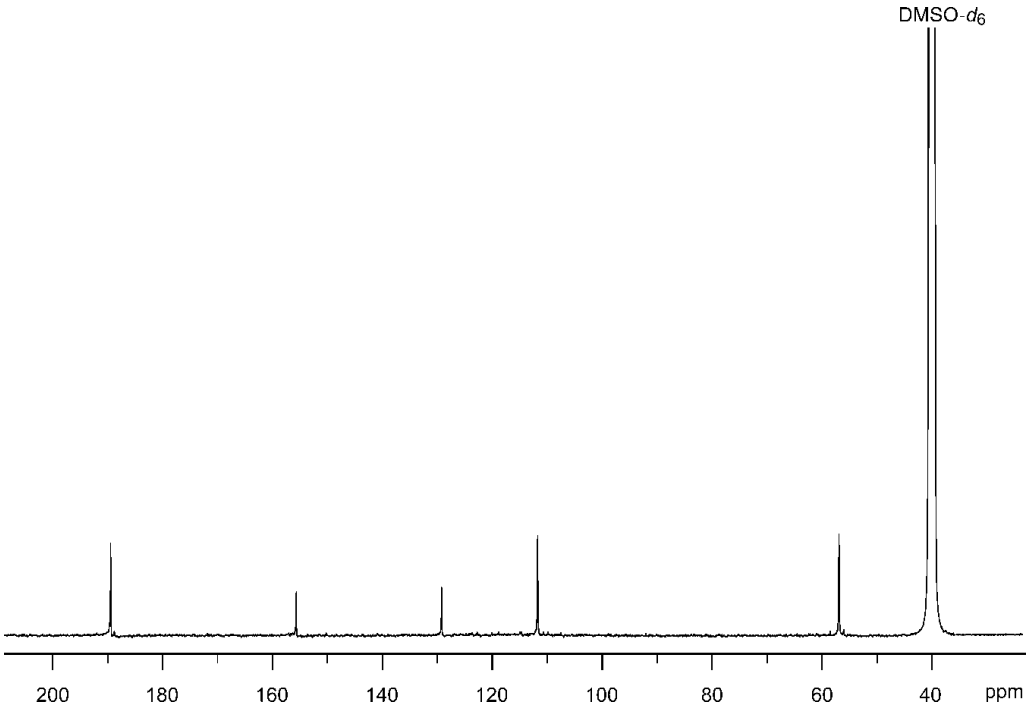

Figure 3.8. ^{13}C NMR spectrum of DMTA in DMSO-d_6.

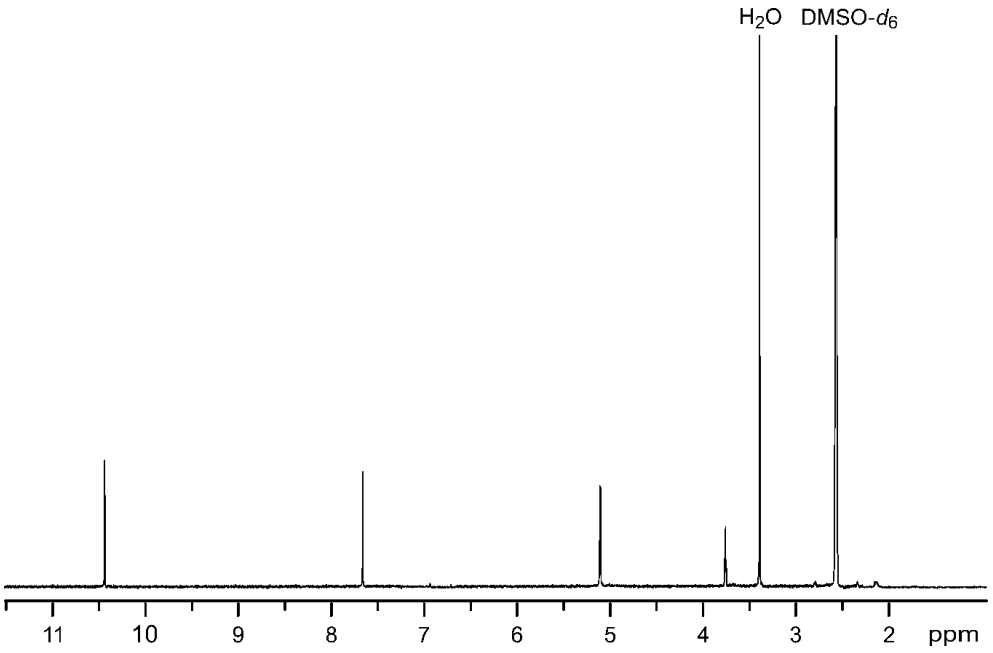

Figure 3.9. ^{1}H NMR spectrum of BPTA in DMSO-d_6.

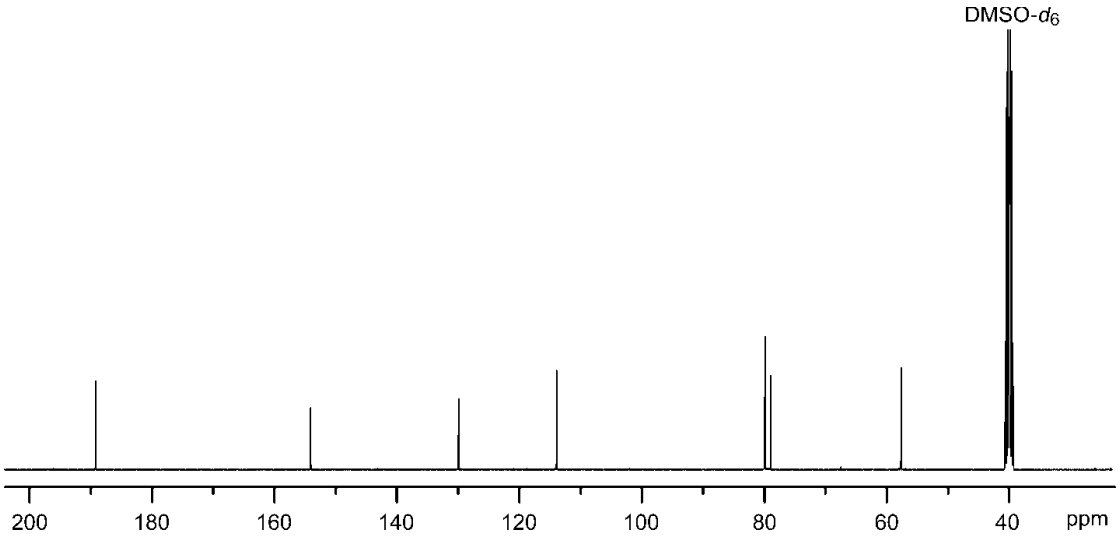

Figure 3.10. ^{13}C NMR spectrum of BPTA in DMSO-d_6.

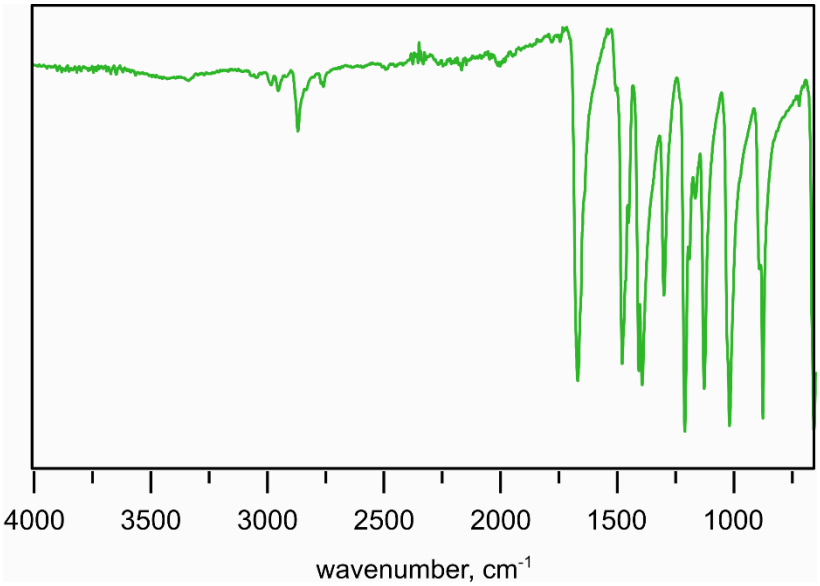

Figure 3.11. FTIR spectrum of DMTA.

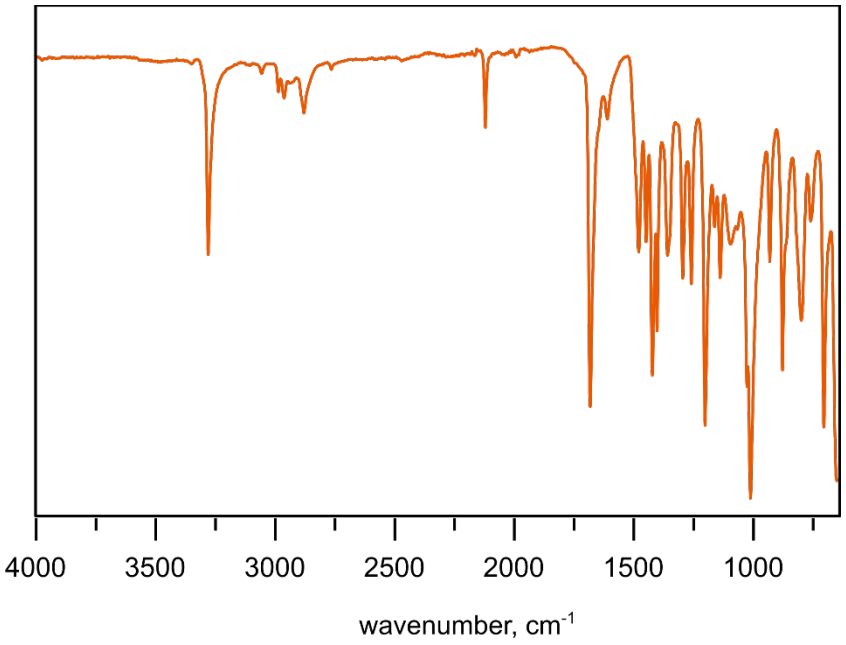

Figure 3.12. FTIR spectrum of BPTA.

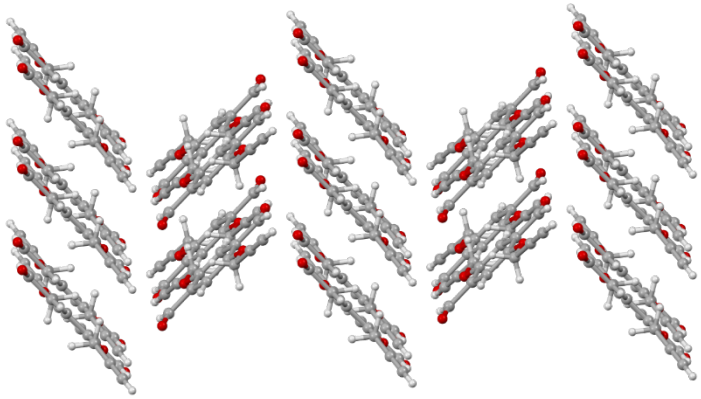

Figure 3.13. Crystal structure of BPTA and packing. Displacement ellipsoids are drawn at the 60% probability level. Red, gray, and white spheres correspond to oxygen, carbon, and hydrogen, respectively.

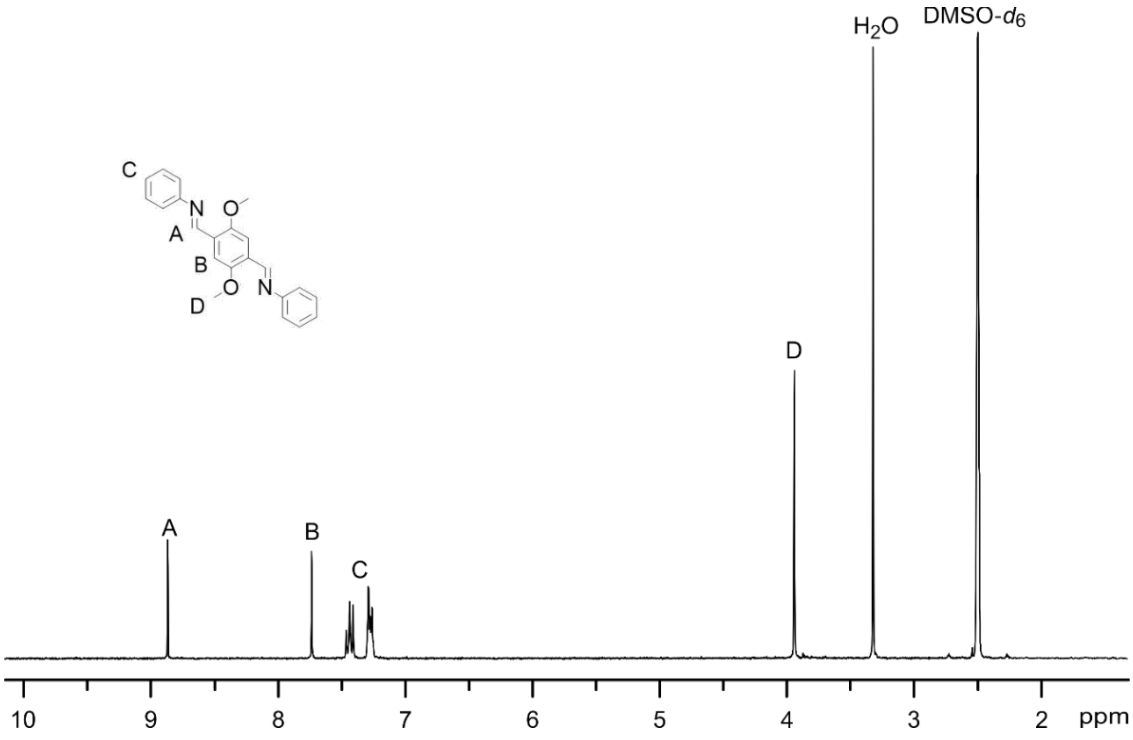

Figure 3.14. ^{1}H NMR spectrum of (1*E*,1'*E*)-1,1'-(2,5-dimethoxy-1,4-phenylene)bis(*N*-phenylmethanimine), $C_{22}H_{20}O_2N_2$.

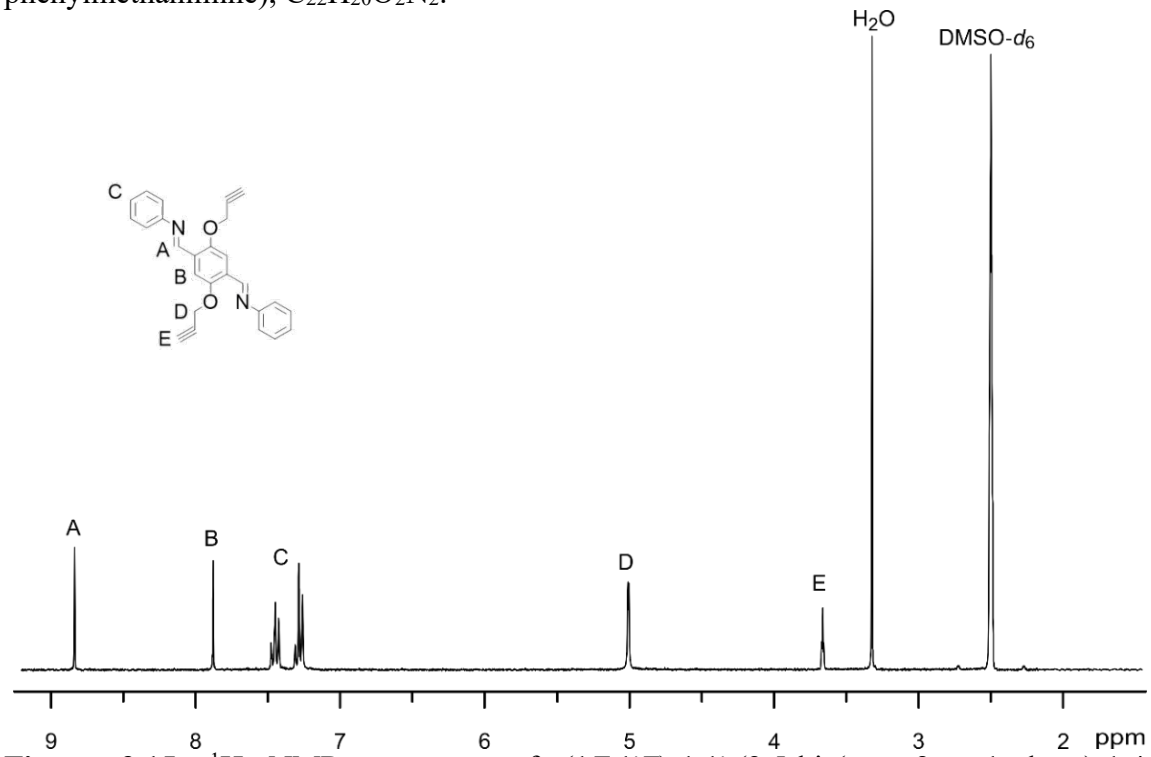

Figure 3.15. ^{1}H NMR spectrum of (1*E*,1'*E*)-1,1'-(2,5-bis(prop-2-yn-1-yloxy)-1,4-phenylene)bis(*N*-phenylmethanimine), $C_{26}H_{20}O_2N_2$.

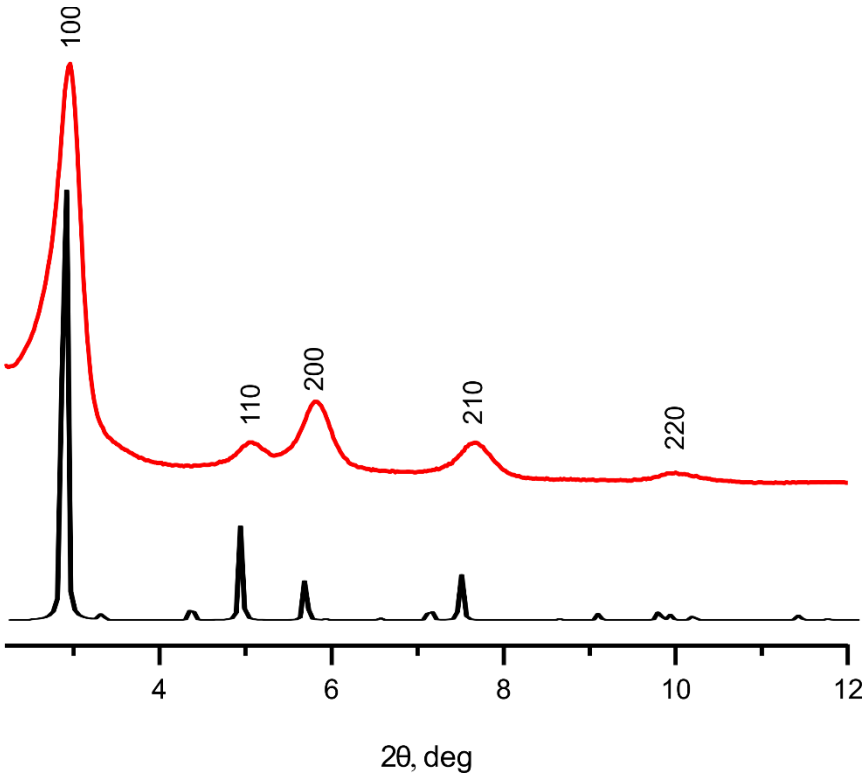

Figure 3.16. PXRD patterns of **1-OMe**: simulated (black) and experimental (red).

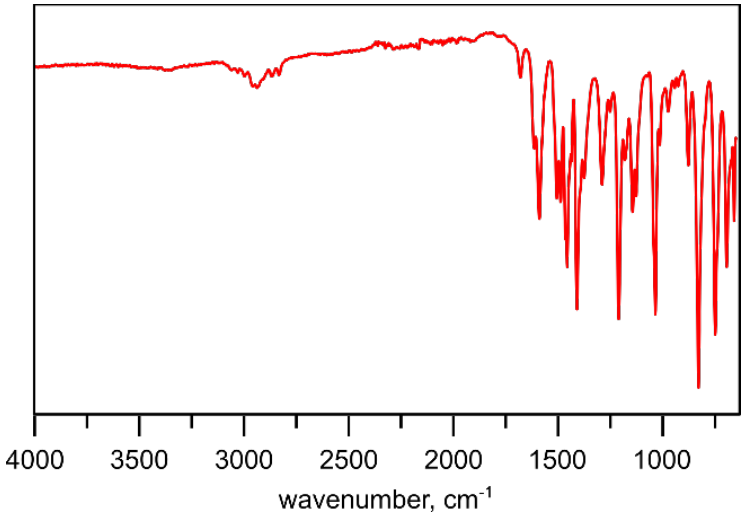

Figure 3.17. FTIR spectrum of **1-OMe**.

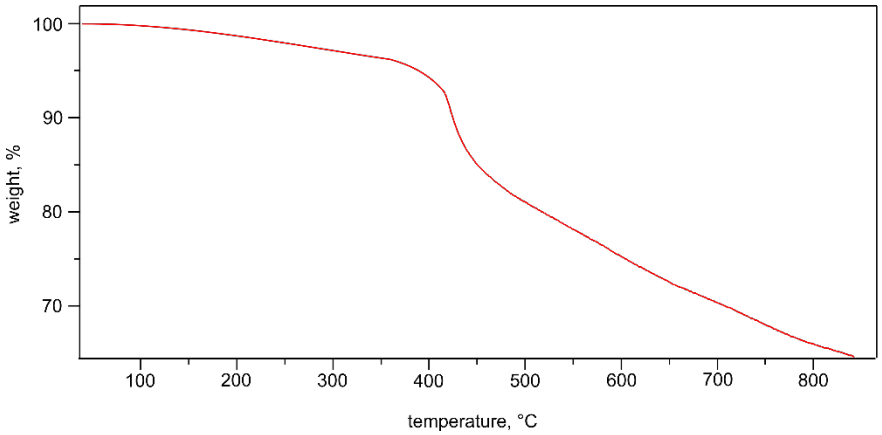

Figure 3.18. Thermogravimetric analysis plot of **1-OMe**.

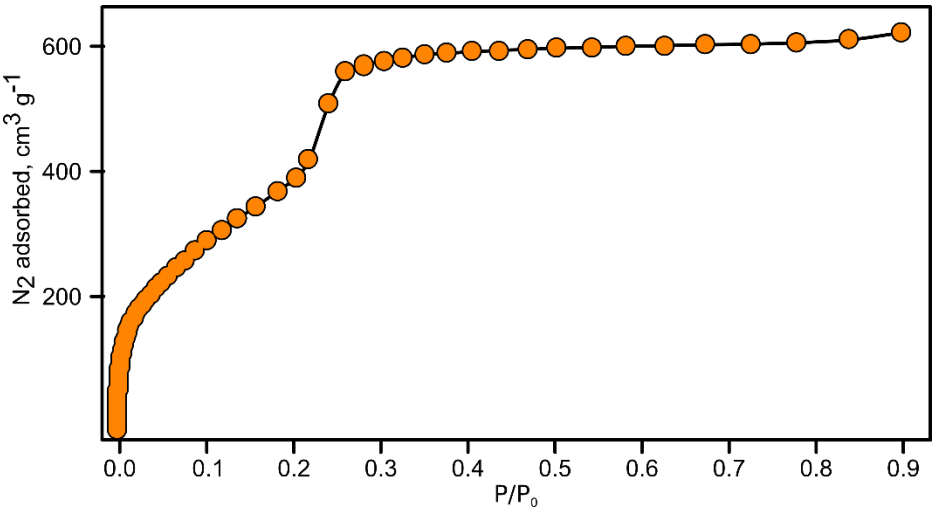

Figure 3.19. N_2 adsorption isotherm of **1-OMe**.

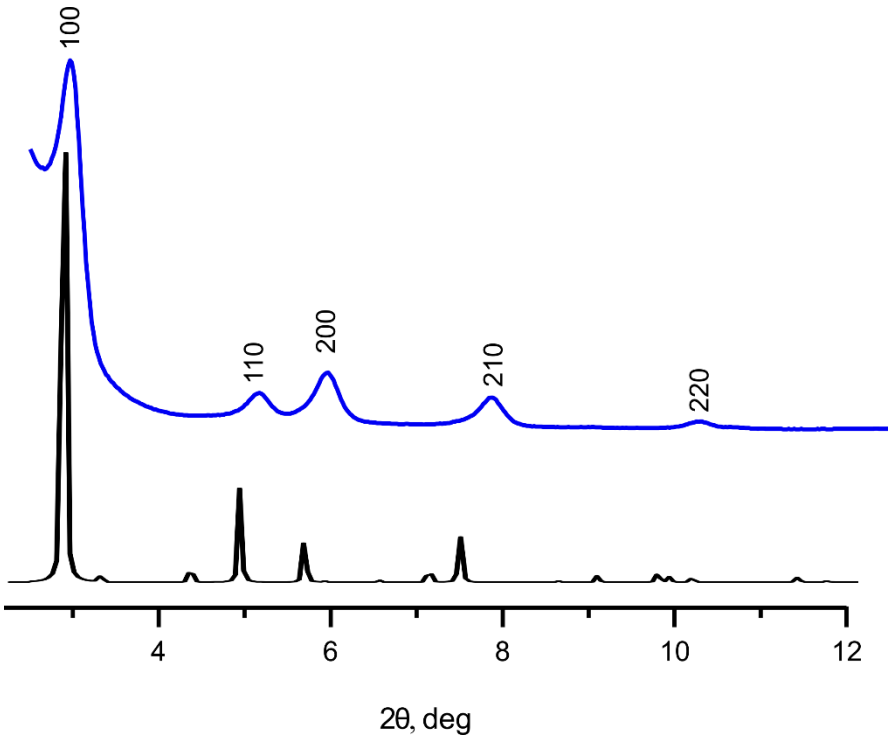

Figure 3.20. PXRD patterns of **1≡(50%)**: simulated (black) and experimental (blue).

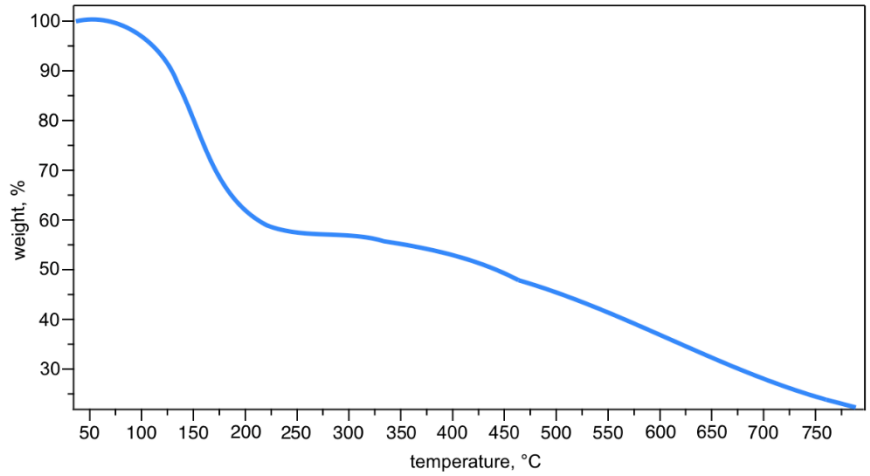

Figure 3.21. Thermogravimetric analysis plot of **1≡(50%)**.

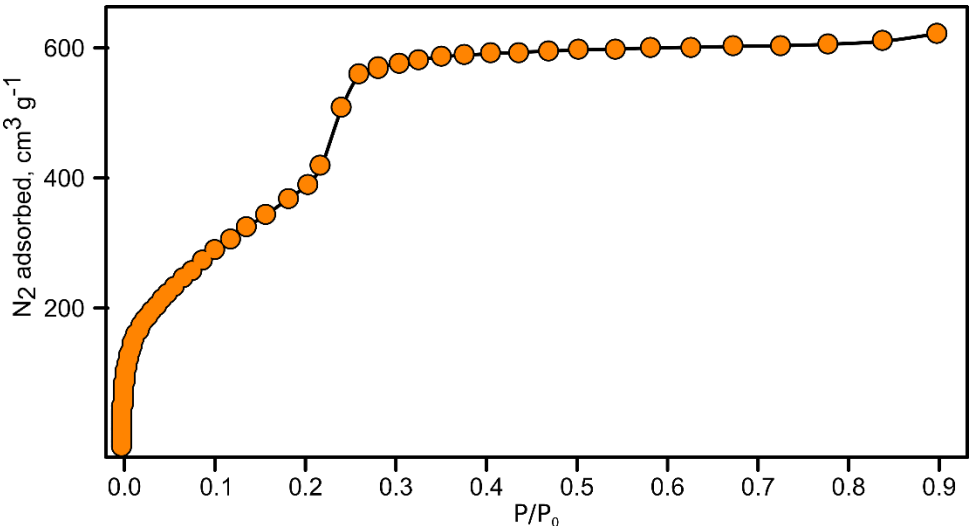

Figure 3.22. N_2 adsorption isotherm of **1≡(50%)**.

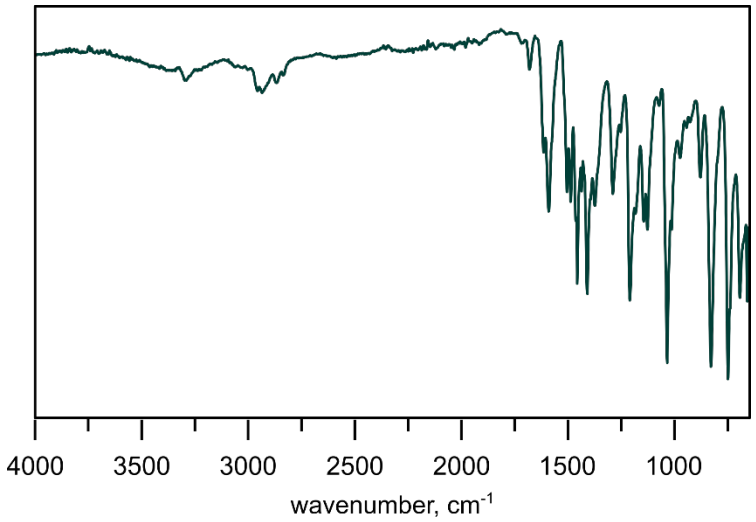

Figure 3.23. FTIR spectrum of **1≡(34%)**.

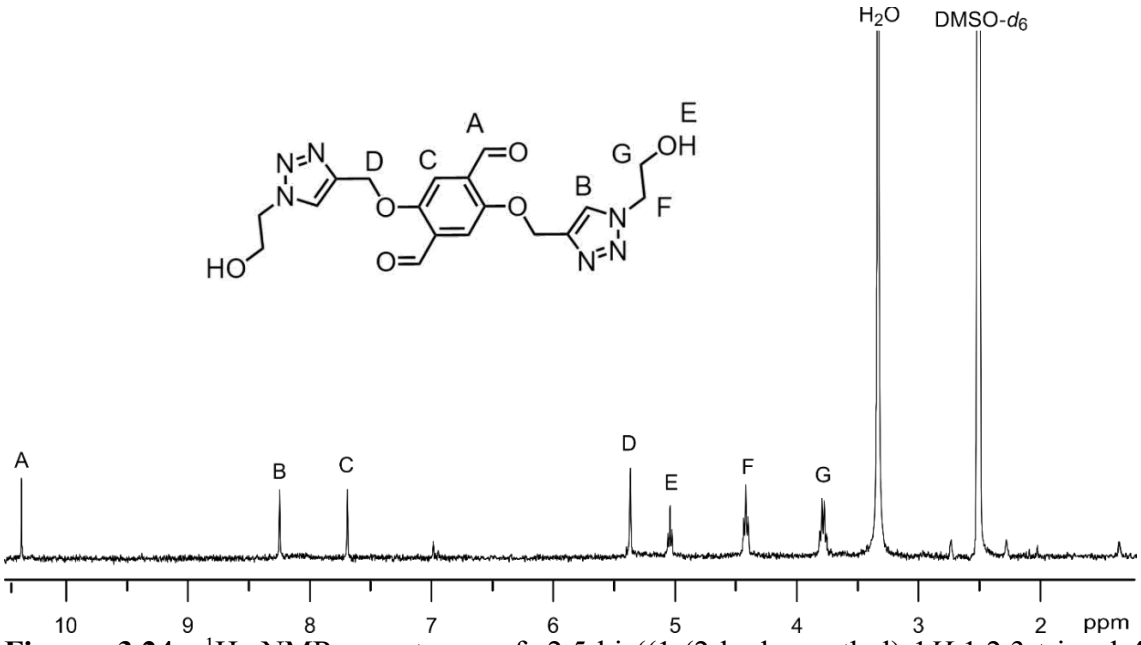

Figure 3.24. ^{1}H NMR spectrum of 2,5-bis((1-(2-hydroxyethyl)-1*H*-1,2,3-triazol-4-yl)methoxy)terephthalaldehyde, $C_{18}H_{20}O_6N_6$.

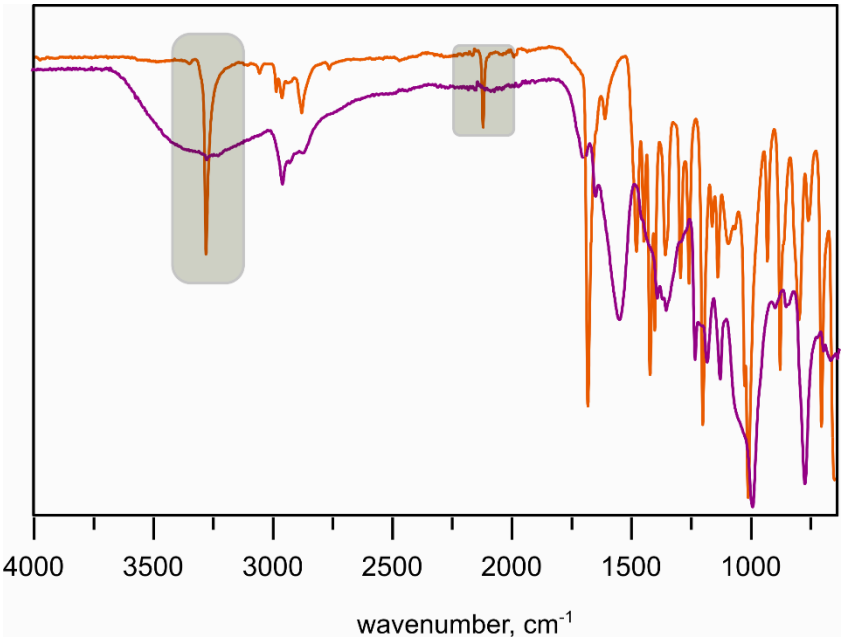

Figure 3.25. FTIR spectra of BPTA (orange) and 2,5-bis((1-(2-hydroxyethyl)-1*H*-1,2,3-triazol-4-yl)methoxy)terephthalaldehyde, $C_{18}H_{20}O_6N_6$ (purple).

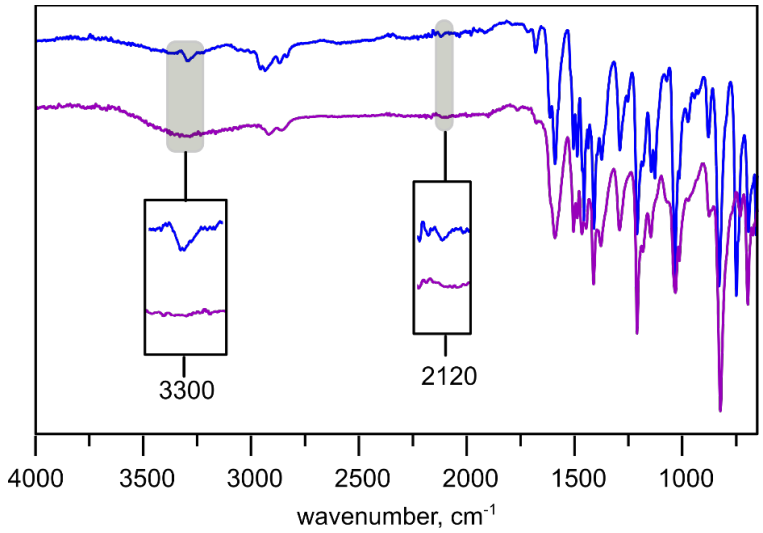

Figure 3.26. FTIR spectra of **1≡(34%)** (blue) and 2-azidoethanol[**1≡(34%)**] (purple).

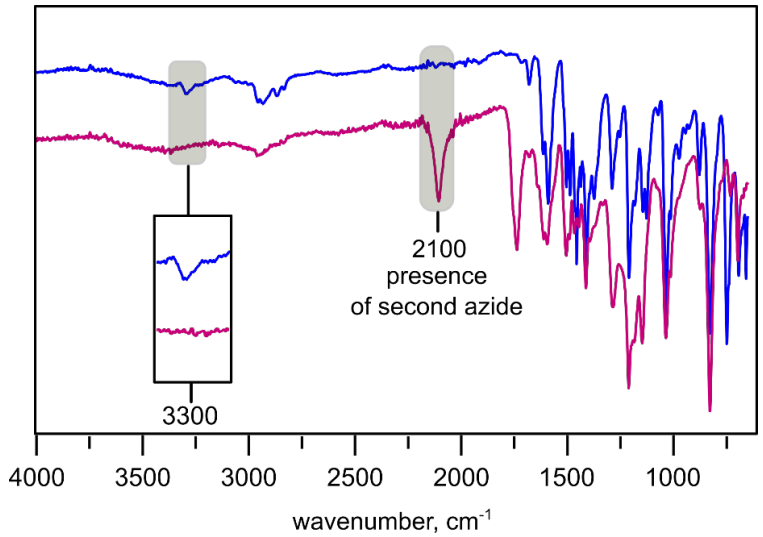

Figure 3.27. FTIR spectra of **1≡(34%)** (blue) and bis(2-azidoethyl) malonate[**1≡(34%)**] (pink).

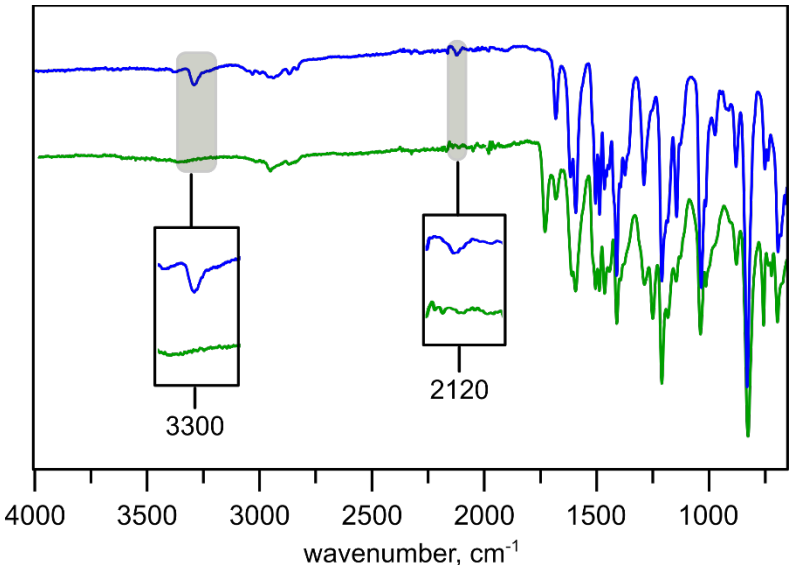

Figure 3.28. FTIR spectra of **1≡(50%)** (blue) and dimethyl 5-azidoisophthalate[**1≡(50%)**] (green).

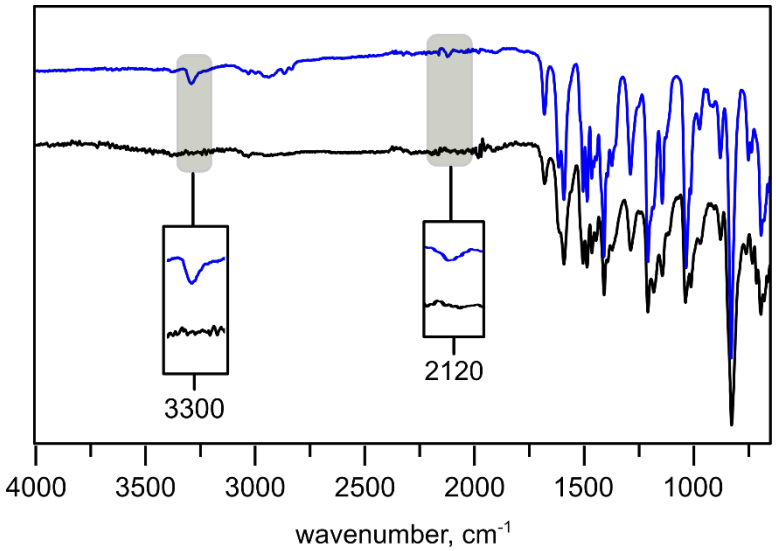

Figure 3.29. FTIR spectra of **1≡(50%)** (blue) and 1-azidopyrene [**1≡(50%)**] (black).

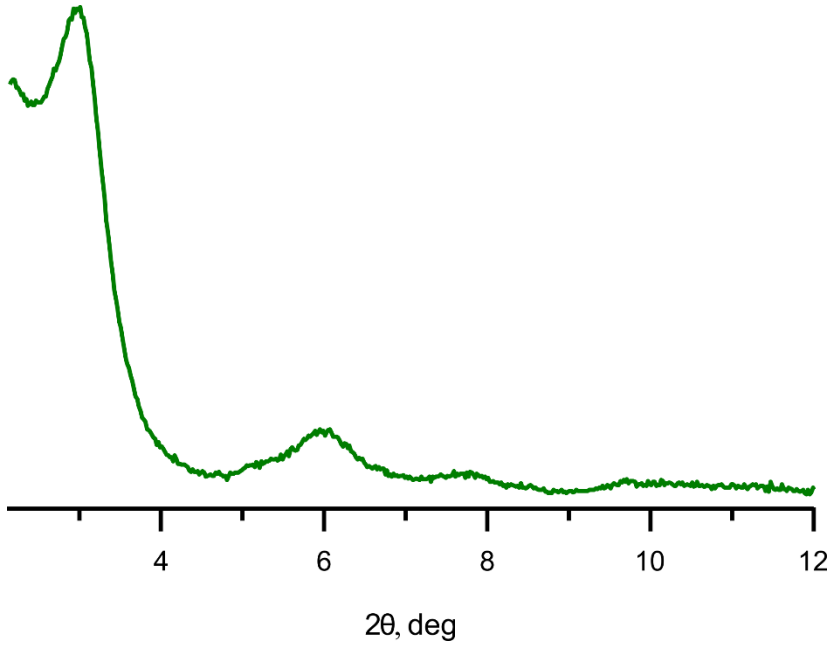

Figure 3.30. PXRD pattern of πB-$C_{20}H_9N_3$[**1≡(50%)**].

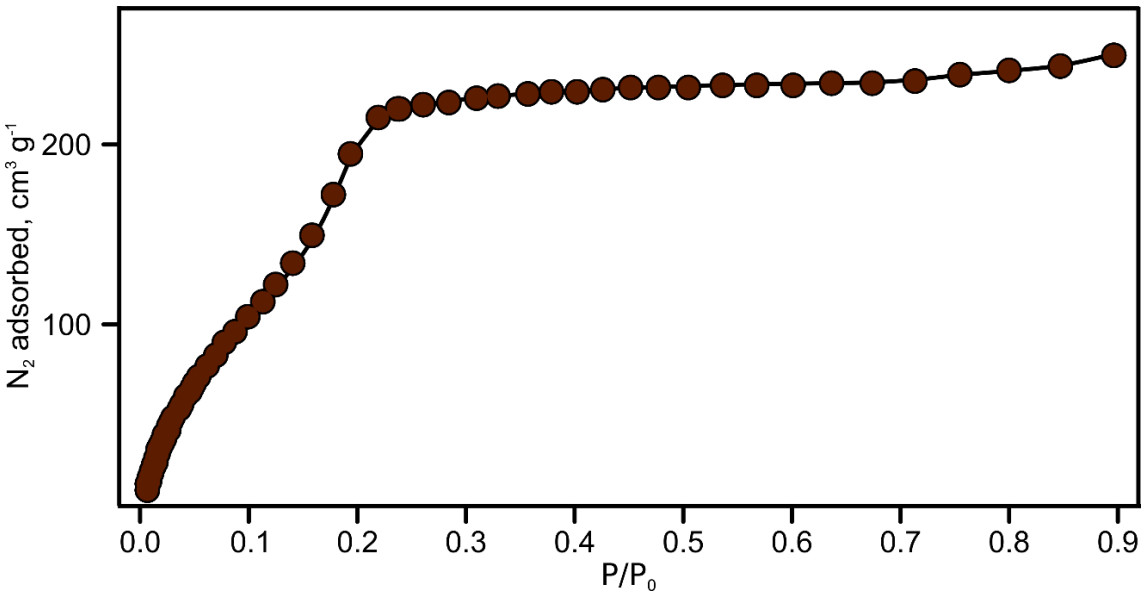

Figure 3.31. N_2 adsorption isotherm of πB-$C_{20}H_9N_3$[**1≡(50%)**].

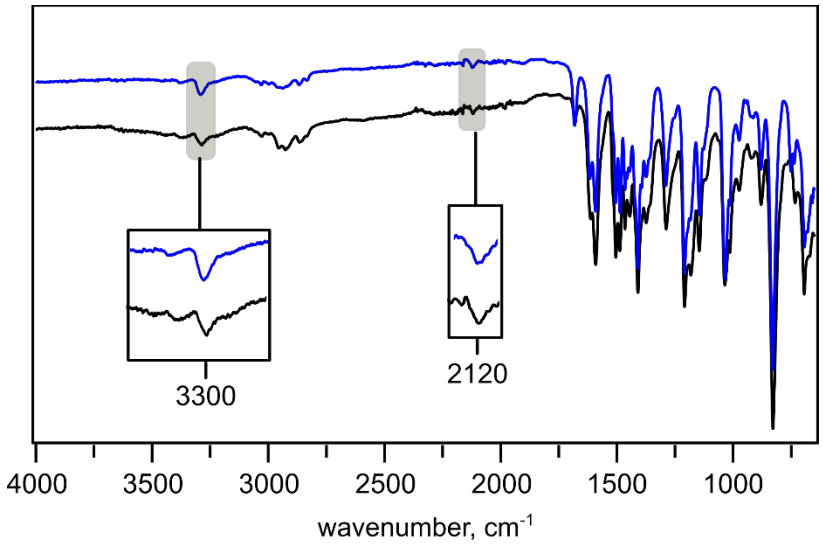

Figure 3.32. FTIR spectra of **1≡(50%)** (blue) and a control experiment involving **1≡(50%)** (black).

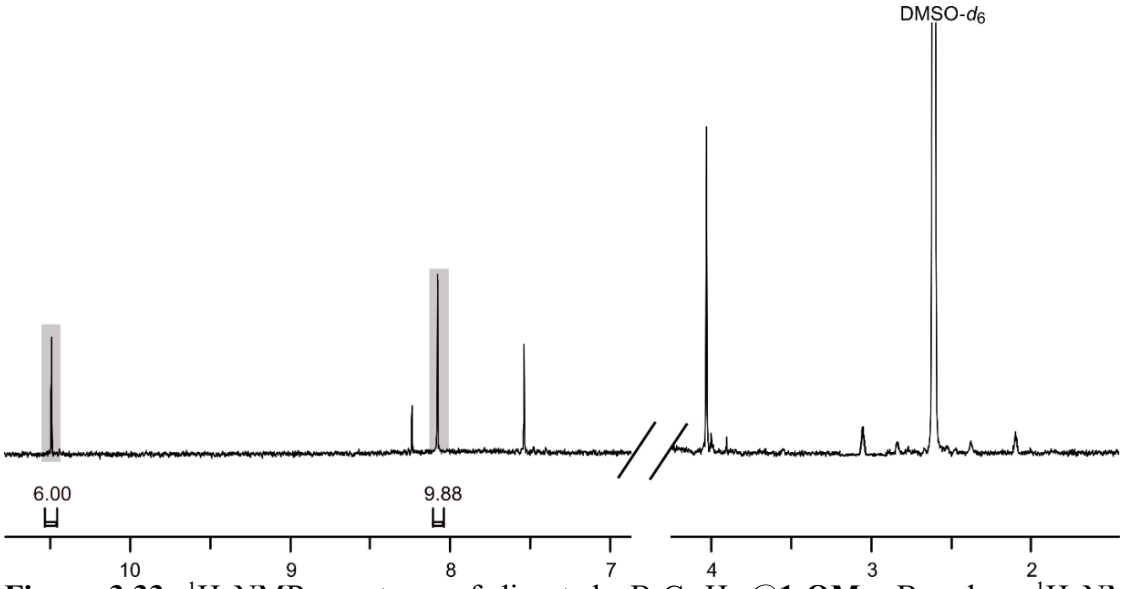

Figure 3.33. ^{1}H NMR spectrum of digested πB-$C_{20}H_{10}$@**1-OMe**. Based on ^{1}H NMR spectroscopic analysis of the digested COF, non-coordinative immobilization led to inclusion of one corannulene molecule per six –OMe units (gray).

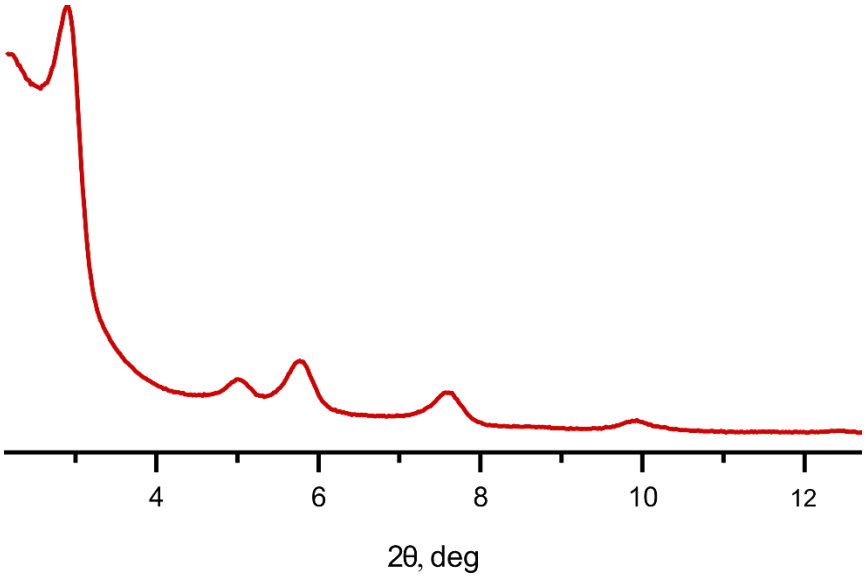

Figure 3.34. PXRD pattern of πB-$C_{20}H_{10}$@**1-OMe**.

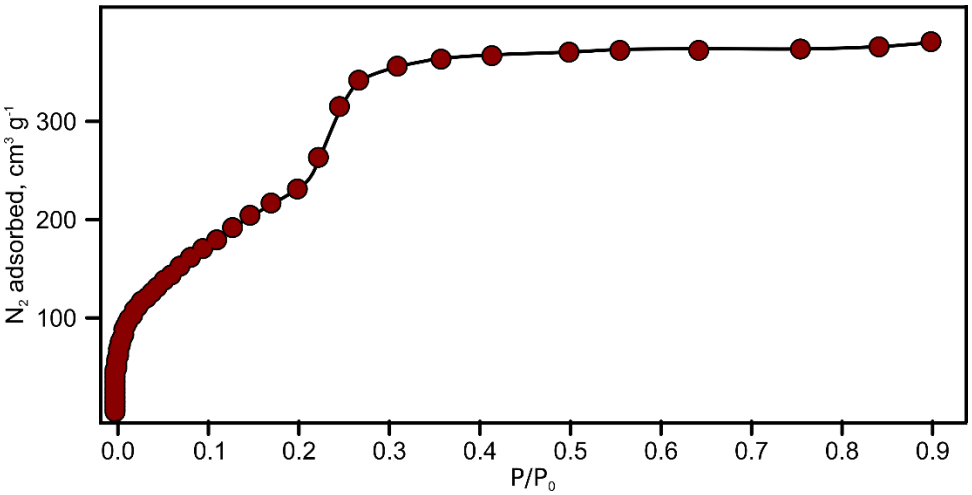

Figure 3.35. N_2 adsorption isotherm of πB-$C_{20}H_{10}$@**1-OMe**.

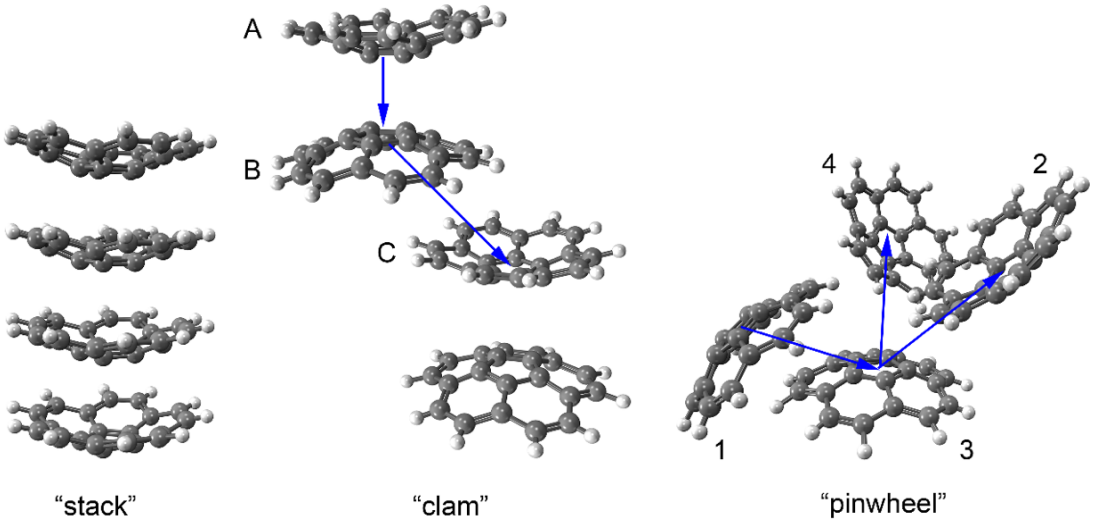

Figure 3.36. Molecular arrangements of πB-$C_{20}H_{10}$. Blue arrows represent possible electron hops during the charge transfer through the material. For the stack geometry all hops are equivalent. For the "clam" geometry charge transfer described through two sequential hops *A*→*B*→*C*. For "pinwheel" geometry charge transfer involves two steps *1*→*3* followed by a hop either to the unit *2* or to the unit *4*.

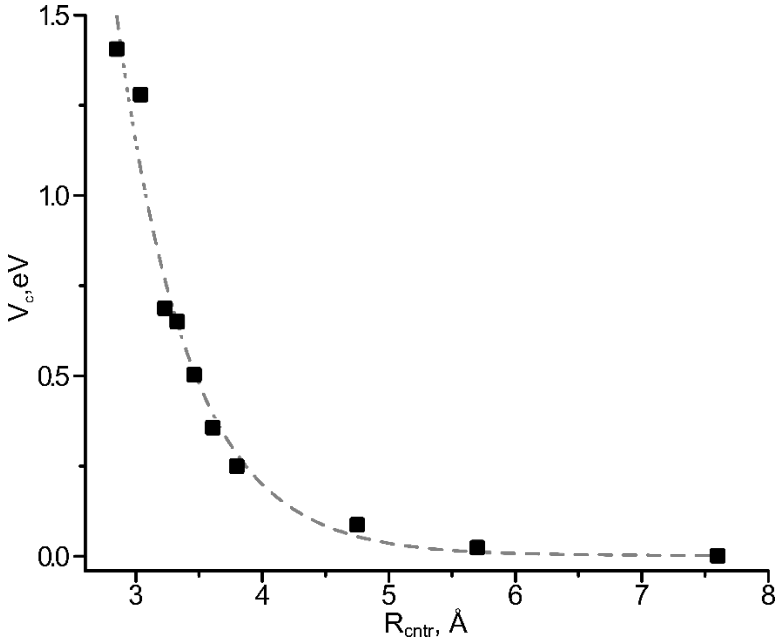

Figure 3.37. Dependence of coupling constants from the distance between πB-$C_{20}H_{10}$ units in the "stack" arrangement.

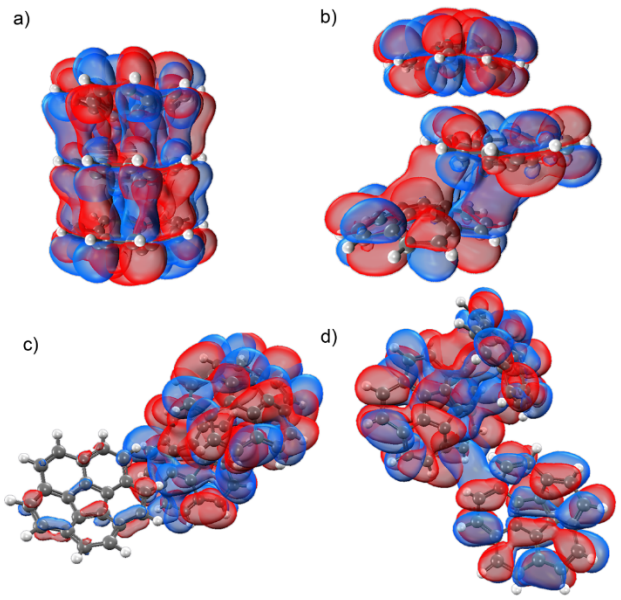

Figure 3.38. Selected LUMOs, associated with the ground state electron transport, for the three-unit πB-$C_{20}H_{10}$: a) "stack", b) "clam", c) "pinwheel"$_{1\rightarrow3\rightarrow2}$, and d) "pinwheel"$_{1\rightarrow3\rightarrow4}$. The theory level LRC-wPBEh/6-31G*. *1→3→2* and *1→3→4* represent the most probable charge transfer pathways in "pinwheel" geometry.

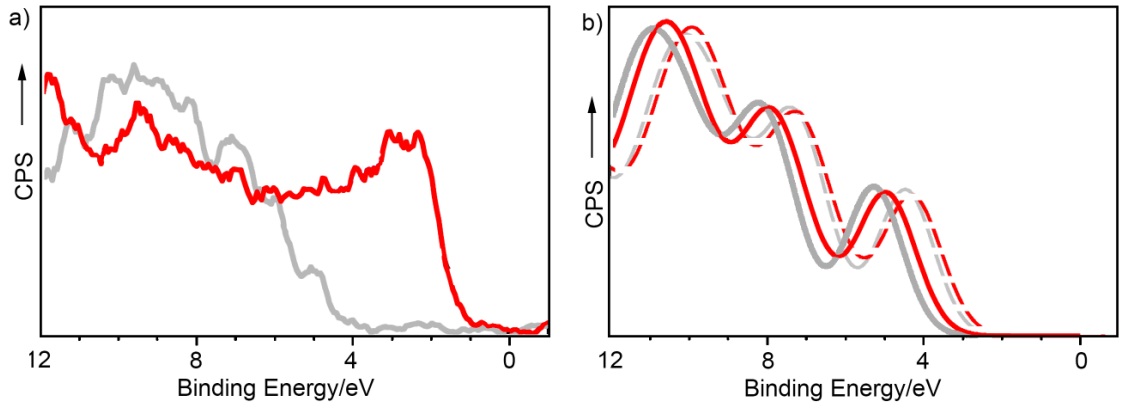

Figure 3.39. (a) XPS data for the valence band region for πB-$C_{20}H_{10}$ (gray) and πB-$C_{20}H_9N_3$[**1≡(50%)**] (red). (b) Simulated density of states for the valence band for the "stack" (red) and "pinwheel" (gray) orientation of four πB-$C_{20}H_{10}$ units with LRC-wPBEh/6-31G* method. The zero energy of energy is set to the center of the respective HOMO-LUMO gaps (dashed lines) and carbon gap (solid line).

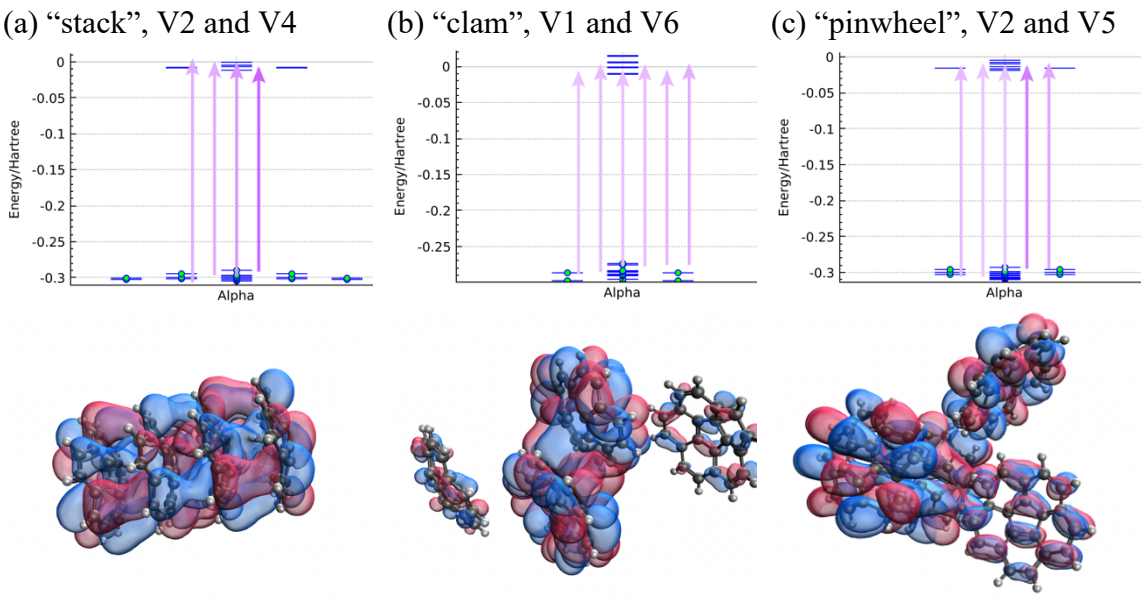

Figure 3.40. Decomposition of the lowest excited singlet state for the 4-unit geometry. Amplitudes of occupied to virtual (labeled V) MO transitions are shown in the middle, while two most contributing virtual orbitals are shown on the top.

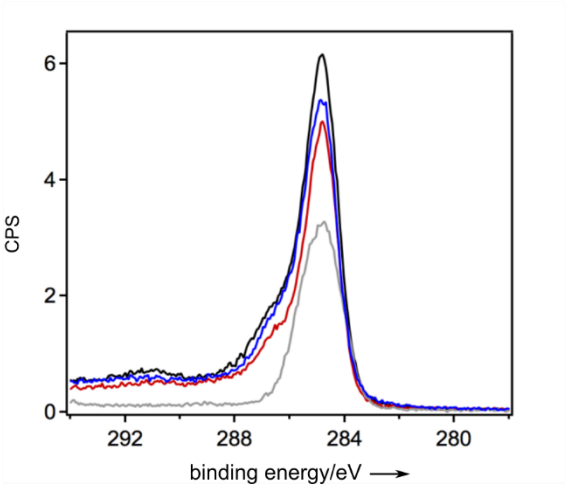

Figure 3.41. X-ray photoelectron spectroscopy data for the C(1s) region for: πB-$C_{20}H_{10}$@**1-OMe** (red); **1-OMe** (black); πB-$C_{20}H_9N_3$[**1≡(50%)**] (blue); and πB-$C_{20}H_{10}$ (gray).

REFERENCES

(197) A. V Zabula, A. S. Filatov, S. N. Spisak, A. Y. Rogachev, M. A. Petrukhina, *Science* **2011**, *333*, 1008–1011.

(198) C. Dubceac, A. S. Filatov, A. V. Zabula, A. Y. Rogachev, M. A. Petrukhina, *Chem. Eur. J.* **2015**, *21*, 14268–14279.

(199) Z. Zhou, S. N. Spisak, Q. Xu, A. Y. Rogachev, Z. Wei, M. Marcaccio, M. A. Petrukhina, *Chem.-Eur. J.* **2018**, *24*, 3455–3463.

(200) E. Nestoros, M. C. Stuparu, *Chem. Commun*. **2018**, *54*, 6503–6519.

(201) Y. T. Wu, J. S. Siegel, *Chem. Rev.* **2006**, *106*, 4843–4867.

(202) H. Yokoi, Y. Hiraoka, S. Hiroto, D. Sakamaki, S. Seki, H. Shinokubo, *Nat. Commun.* **2015**, *6*, 8215.

(203) A. G. Gagorik, J. W. Mohin, T. Kowalewski, G. R. Hutchison, *Adv. Funct. Mater.* **2015**, *25*, 1996–2003.

(204) L. K. San, T. T. Clikeman, C. Dubceac, A. A. Popov, Y.- S. Chen, M. A. Petrukhina, S. H. Strauss, O. V. Boltalina, *Chem. Eur. J*. **2015**, *21*, 9488–9492.

(205) M. Saito, H. Shinokubo, H. Sakurai, *Mater. Chem. Front*. **2018**, *2*, 635–661.

(206) J. Mack, P. Vogel, D. Jones, N. Kaval, A. Sutton, *Org. Biomol. Chem*. **2007**, *5*, 2448–2452.

(207) H. Wang, X. Dong, J. Lin, S. J. Teat, S. Jensen, J. Cure, E. V Alexandrov, Q. Xia, K. Tan, Q. Wang, D. H. Olson, D. M. Proserpio, Y. J. Chabal, T. Thonhauser, J. Sun, Y. Han, J. Li, *Nat. Commun*. **2018**, *9*, 1745.

(208) Q.-G. Zhai, X. Bu, X. Zhao, D.-S. Li, P. Feng, *Acc. Chem. Res*. **2017**, *50*, 407–417.

(209) S.-T. Zheng, J. T. Bu, Y. Li, T. Wu, F. Zuo, P. Feng, X. Bu, *J. Am. Chem. Soc*. **2010**, *132*, 17062–17064.

(210) A. J. Howarth, A. W. Peters, N. A. Vermeulen, T. C. Wang, J. T. Hupp, O. K. Farha, *Chem. Mater.* **2017**, *29*, 26–39.

(211) S. M. Cohen*, J. Am. Chem. Soc*. **2017**, *139*, 2855–2863.

(212) M. K. Smith, K. A. Mirica, *J. Am. Chem. Soc.* **2017**, *139*, 16759–16767.

(213) C. R. DeBlase, W. R. Dichtel, *Macromolecules* **2016**, *49*, 5297–5305.

(214) M. Matsumoto, R. R. Dasari, W. Ji, C. H. Feriante, T. C. Parker, S. R. Marder, W. R. Dichtel, *J. Am. Chem. Soc*. **2017**, *139*, 4999–5002.

(215) C. H. Hendon, A. J. Rieth, M. D. Korzyński, M. Dincă, *ACS Cent. Sci.* **2017**, *3*, 554–563.

(216) A. Béziau, S. A. Baudron, G. Rogez, M. W. Hosseini, *Inorg. Chem.* **2015**, *54*, 2032–2039.

(217) M. W. Logan, J. D. Adamson, D. Le, F. J. Uribe-Romo, *ACS Appl. Mater. Interfaces* **2017**, *9*, 44529–44533.

(218) H. Xu, J. Gao, D. Jiang, *Nat. Chem*. **2015**, *7*, 905–912.

(219) A. M. Rice, E. A. Dolgopolova, N. B. Shustova, *Chem. Mater.* **2017**, *29*, 7054–7061.

(220) A. A. K. Karunathilake, C. M. Thompson, S. Perananthan, J. P. Ferraris, R. A. Smaldone, *Chem. Commun*. **2016**, *52*, 12881–12884.

(221) A. M. Butterfield, B. Gilomen, J. S. Siegel, *Org. Process Res. Dev*. **2012**, *16*, 664–676.

(222) N. Niamnont, N. Kimpitak, K. Wongravee, P. Rashatasakhon, K. K. Baldridge, J. S. Siegel, M. Sukwattanasinitt, *Chem. Commun*. **2013**, *49*, 780–782.

(223) A. Nagai, Z. Guo, X. Feng, S. Jin, X. Chen, X. Ding, D. Jiang, *Nat. Commun*. **2011**, *2*, 536.

(224) J. C. Bachman, R. Kavian, D. J. Graham, D. Y. Kim, S. Noda, D. G. Nocera, Y. Shao-Horn, S. W. Lee, *Nat. Commun*. **2015**, *6*, 7040.

(225) V. Rajeshkumar, M. Courte, D. Fichou, M. C. Stuparu, *Eur. J. Org. Chem*. **2016**, *2016*, 6010–6014.

(226) F. D'Souza, O. Ito, *Coord. Chem. Rev.* **2005**, *249*, 1410–1422.

(227) D. E. Williams, E. A. Dolgopolova, D. C. Godfrey, E. D. Ermolaeva, P. J. Pellechia, A. B. Greytak, M. D. Smith, S. M. Avdoshenko, A. A. Popov, N. B. Shustova, *Angew. Chem. Int. Ed.* **2016**, *55*, 9070–9074.

(228) E. A. Dolgopolova, A. J. Brandt, O. A. Ejegbavwo, A. S. Duke, T. D. Maddumapatabandi, R. P. Galhenage, B. W. Larson, O. G. Reid, S. C. Ammal, A. Heyden, M. Chandrashekhar, V. Stavila, D. A. Chen, N. B. Shustova *J. Am. Chem. Soc.* **2017**, *139*, 5201–5209.

(229) R. López, R. Gómez, J. *Sol-Gel Sci. Technol*. **2012**, *61*, 1–7.

(230) M. Usman, S. Mendiratta, S. Batjargal, G. Haider, M. Hayashi, N. R. Gade, J.-W. Chen, Y.-F. Chen, K.-L. Lu, *ACS Appl. Mater. Interfaces* **2015**, *7*, 22767–22774.

(231) A. Sygula, S. Saebø, *Int. J. Quantum Chem*. **2009**, *109*, 65–72.

(232) A. S. Filatov, L. T. Scott, M. A. Petrukhina, *Cryst. Growth Des.* **2010**, *10*, 4607–4621.

(233) K. Ohta, G. L. Closs, K. Morokuma, N. J. Green*, J. Am. Chem. Soc.* **1986**, *108*, 1319–1320.

(234) A. Farazdel, M. Dupuis, E. Clementi, A. Aviram, *J. Am. Chem. Soc.* **1990**, *112*, 4206–4214.

(235) M. D. Newton, *Chem. Rev*. **1991**, *91*, 767–792.

(236) L. Y. Zhang, R. A. Friesner, R. B. Murphy, *J. Chem. Phys*. **1997**, *107*, 450–459.

(237) S. Sanyal, A. K. Manna, S. K. Pati, *ChemPhysChem* **2014**, *15*, 885–893.

(238) J. Luo, Z. Q. Xue, W. M. Liu, J. L. Wu, Z. Q. Yang, *J. Phys. Chem. A* **2006**, *110*, 12005–12009.

(239) B. -T. Wang, M. A. Petrukhina, E. R. Margine, *Carbon* **2015**, *94*, 174–180.

(240) Y.-Z. Liu, K. Yuan, Z. Yuan, Y.-C. Zhu, S.-D. Zhao, L.-L. Lv, *RSC Adv*. **2017**, *7*, 27960–27968.

(241) K. M. Pelzer, Á. Vázquez-Mayagoitia, L. E. Ratcliff, S. Tretiak, R. A. Bair, S. K. Gray, T. Van Voorhis, R. E. Larsen, S. B. Darling, *Chem. Sci*. **2017**, *8*, 2597–2609.

CHAPTER 4

A DUAL THREAT: REDOX-ACTIVITY AND ELECTRONIC STRUCTURES OF WELL-DEFINED DONOR-ACCEPTOR FULLERETIC COVALENT-ORGANIC MATERIALS

Leith, G. A.; Rice, A. M.; Yarbrough, B. J.; Berseneva, A. A.; Ly, R. T.; Buck, C. N. III; Chusov, D.; Brandt, A. J.; Chen, D. A.; Lamm, B. W.; Stefik, M.; Stephenson, K. S.; Smith, M. D.; Vannucci, A. K.; Pellechia, P. J.; Garashchuk, S. and Shustova, N. B. *Angew. Chem. Int. Ed.* **2020**, *59*, 6000–6006.

Merging the properties of three-dimensional buckyballs (or buckybowls) and covalent-organic frameworks (COFs) provides access to a novel class of materials combining ultrafast energy/electron transport characteristic of three-dimensional (3D) fulleretic linkers with high modularity, crystallinity, and surface area, which are intrinsic properties of COFs.[242-254] The precise donor-acceptor alignment achieved in the materials is imposed by the rigid COF scaffold and is crucial for efficient energy or charge transfer as it can influence the distance of exciton diffusion, π-π stacking, or Förster radius, and as a result, can enhance device performance.[255–261]

Herein, we demonstrate that the donor-acceptor alignment in well-defined frameworks could drastically affect the materials' electronic properties resulting in *ca* 100,000,000-fold conductivity enhancement, one of the largest increases reported for COFs (Scheme 4.1).[262–271] We probed charge transfer rates within the Marcus theory as a function of acceptor stacking. In addition, we estimated redox behavior using cyclic voltammetry of *pure organic* crystalline porous scaffolds containing covalently decorated pores with strong electron accepting bound tetracyanoquinodimethane (TCNQ) and fullerene (C_{60}) moieties,[272–274] which are the first studies of this kind reported for any buckyball- or TCNQ-integrated COFs to date. We demonstrate that the concept of fluorophore tag integration could be an effective avenue to monitor reaction progress inside of a COF. To achieve that, the COF interior for the first time was harnessed for performance of Sonogashira cross-coupling and [2+2] cycloaddition reactions, followed by ring opening of a strained cyclobutene intermediate in the case of the latter. In addition to donor (COF)-acceptor (fullerene or TCNQ) alignment responsible for "static" changes in the materials' electronic structure, we also test the hypothesis that an excitation wavelength could be used

for dynamic control of electronic properties in COFs infiltrated with photoresponsive units as a function of an external stimulus for the first time.[275–277]

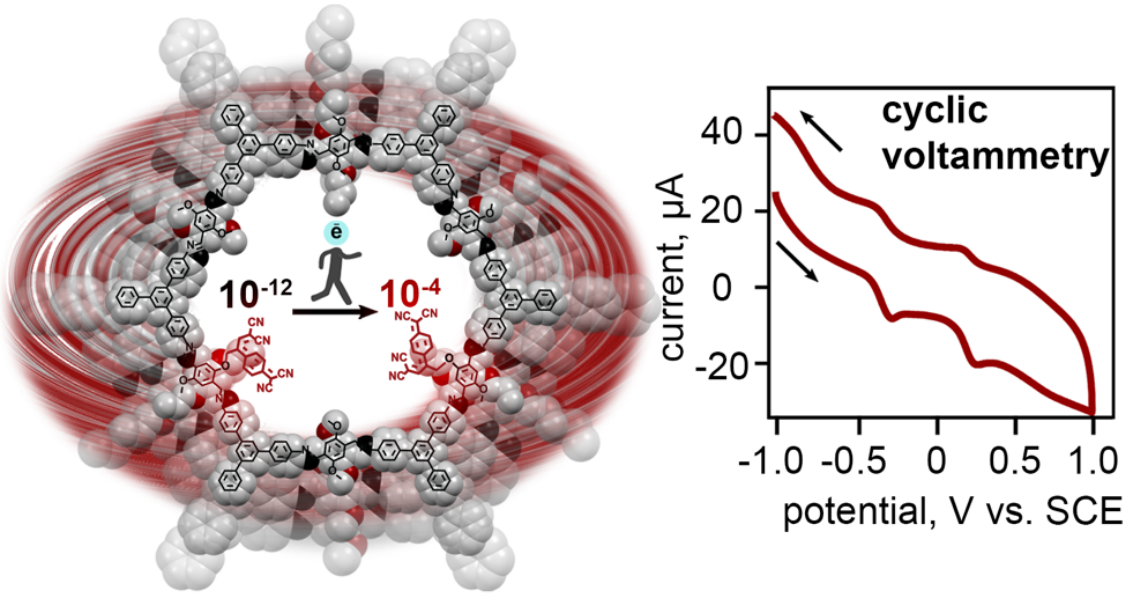

Scheme 4.1. (*left*) Donor-acceptor alignment inside of a porous well-defined organic framework resulting in conductivity enhancement. (*right*) The cyclic voltammetry curve of crystalline porous material with embedded electron-accepting moieties (TCNQ[**1≡(34%)**]; DMF solution containing 0.1 M tetrabutylammonium hexafluorophosphate, TCNQ[**1≡(34%)**] (40 wt.%), carbon black (60 wt.%), and 0.1 mL of Nafion; saturated calomel reference, platinum wire counter, and gold working electrodes). could be used for dynamic control of electronic properties in COFs infiltrated with photoresponsive units as a function of an external stimulus for the first time.[275–277]

For integration of three-dimensional (3D) acceptors such as buckyballs, choice of the host matrix (COF) should satisfy the following criteria: (i) sufficient pore aperture for accommodation of bulky electron acceptors (e.g., C_{60} diameter ~7 Å;), (ii) presence of reactive functional groups promoting cycloaddition or coupling reactions, and (iii) maintenance of structural integrity after derivatization. The first two strategies (1,3- and [2+2] cycloaddition followed by ring opening of a strained intermediate) were utilized to integrate 3D and planar electron acceptors while the third strategy (Sonogashira cross-coupling) was employed to embed fluorophore tags (vide infra). The COF, **1≡(x%)** (where

x = 34 = [BPTA]/([BPTA]+[DMTA]) × 100%; Figure 4.1), prepared from 2,5-bis(2-propynyloxy) terephthalaldehyde (BPTA), 2,5-dimethoxyterephthalaldehyde (DMTA), and tri-(4-aminophenyl)benzene (TAPB), satisfies the mentioned criteria. This COF (i) possesses 30 Å-channels, (ii) contains alkyne groups available for postsynthetic derivatization (see the Supporting Information for synthetic details), and (iii) maintains structural integrity over a wide pH range.[278]

Prior to investigations with bulky and relatively expensive fullerene-containing derivatives, we systematically studied the reaction conditions suitable for 1,3-cycloaddition starting with less bulky and more affordable azide-based derivatives, e.g., 2-azidoethanol and 2-azidoethyl ethyl malonate. Only after such control experiments, where the reaction conditions which were developed for cycloaddition of the small azide-based derivatives, applied for integration of 2-azidoethyl ethyl malonate (NEM) inside the of the COF (**1≡(34%)**, see the Supporting Information). As a result, the methodology for development of donor-acceptor materials includes two-steps: (i) several-day pre-soaking of, for instance, C_{60} derivatives inside the large COF channels promoting acceptor diffusion and (ii) addition of the reagents required for a 1,3-cycloaddition reaction (Figure 4.1) followed by heating. Synthesis of the C_{60} derivative, 2-azidoethyl-(ethyl)-3'*H*-cyclopropa-[1,2](C_{60})[5,6]fullerene-3',3'-dicarboxylate (NEM-C_{60}, Figure 4.1), suitable for the cycloaddition reaction and accessible on a gram-scale without the use of labor-demanding high-pressure liquid chromatography (HPLC) was performed using a 3-step procedure.[279]

Spectroscopic techniques including Fourier-transform infrared (FTIR) and solid-state ^{13}C cross-polarization magic-angle spinning (CP-MAS) nuclear magnetic resonance (NMR) spectroscopies, as well as fluorophore tag integration discussed below, were used

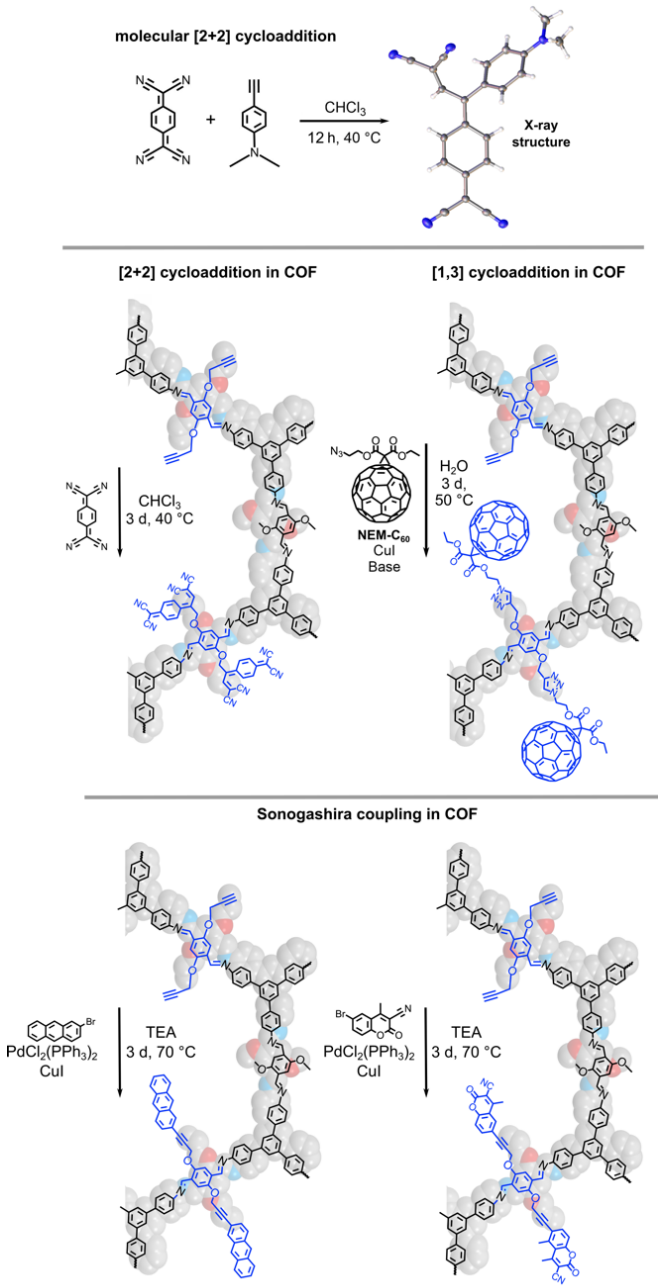

Figure 4.1. (*top*) Development of reaction conditions utilizing molecular TCNQ moieties for the [2+2] cycloaddition reaction, followed by ring opening of a strained cyclobutene intermediate. (*middle*) The 1,3-cycloaddition and [2+2] cycloaddition reactions, followed by ring opening of a strained cyclobutene intermediate in the case of the latter, for integration of fullerene and TCNQ moieties, respectively, are shown. (*bottom*) Integration of a fluorescent tag using Sonogashira cross-coupling reaction.

to monitor reaction progress in the solid state. Control experiments, in which the COF was subjected to the same reaction conditions but without the addition of the azide-containing precursor, were also carried out. In the case of FTIR spectroscopic studies, we monitored the disappearance of 2120 cm^{-1} (C≡C) and 3300 cm^{-1} (C≡C–H) bands (Figures 4.2 and 4.3) in the spectra of products in contrast to the control experiment where both bands were preserved (Figure 4.14). For instance, in the case of NEM-C_{60}[**1≡(34%)**], FTIR spectroscopic studies confirmed disappearance of the C≡C resonance as well as appearance of the carbonyl stretch (1716 cm^{-1}) of the diethyl malonate moiety (Figure 4.2). The ^{13}C CP-MAS spectroscopic studies of NEM-C_{60}[**1≡(34%)**] demonstrated disappearance of the C≡C resonances in contrast to the control experiment (without presence of the azide precursor under the same reaction conditions, Figure 4.2). Moreover, the substantial decrease of Brunauer-Emmett-Teller (BET) surface area from 1253 m^2g^{-1} (**1≡(34%)**, Figure 4.18) to 229 m^2g^{-1} (NEM-C_{60}[**1≡(34%)**], Figure 4.19) also supports incorporation of bulky C_{60} derivatives inside of the porous scaffold. Although the surface area for a covalently linked C_{60}-metalloporphyrin COF was slightly higher (393 m^2/g),[280] we report the highest surface area determined for a purely organic COF with covalently bound C_{60} acceptors to date. The steady-state and time-resolved spectroscopic studies are also in line with integration of electro accepting units inside of the electron donating host (vide infra). Crystallinity of the synthesized material was preserved even after multiple cycles of the 1,3-cycloaddition reaction necessary for maximization of C_{60} content as evident through wide-angle X-ray scattering (WAXS, Figure 4.12) studies; resulting in the first example of a crystalline, porous, and fully organic covalently-linked C_{60}-based COF. [280–283]

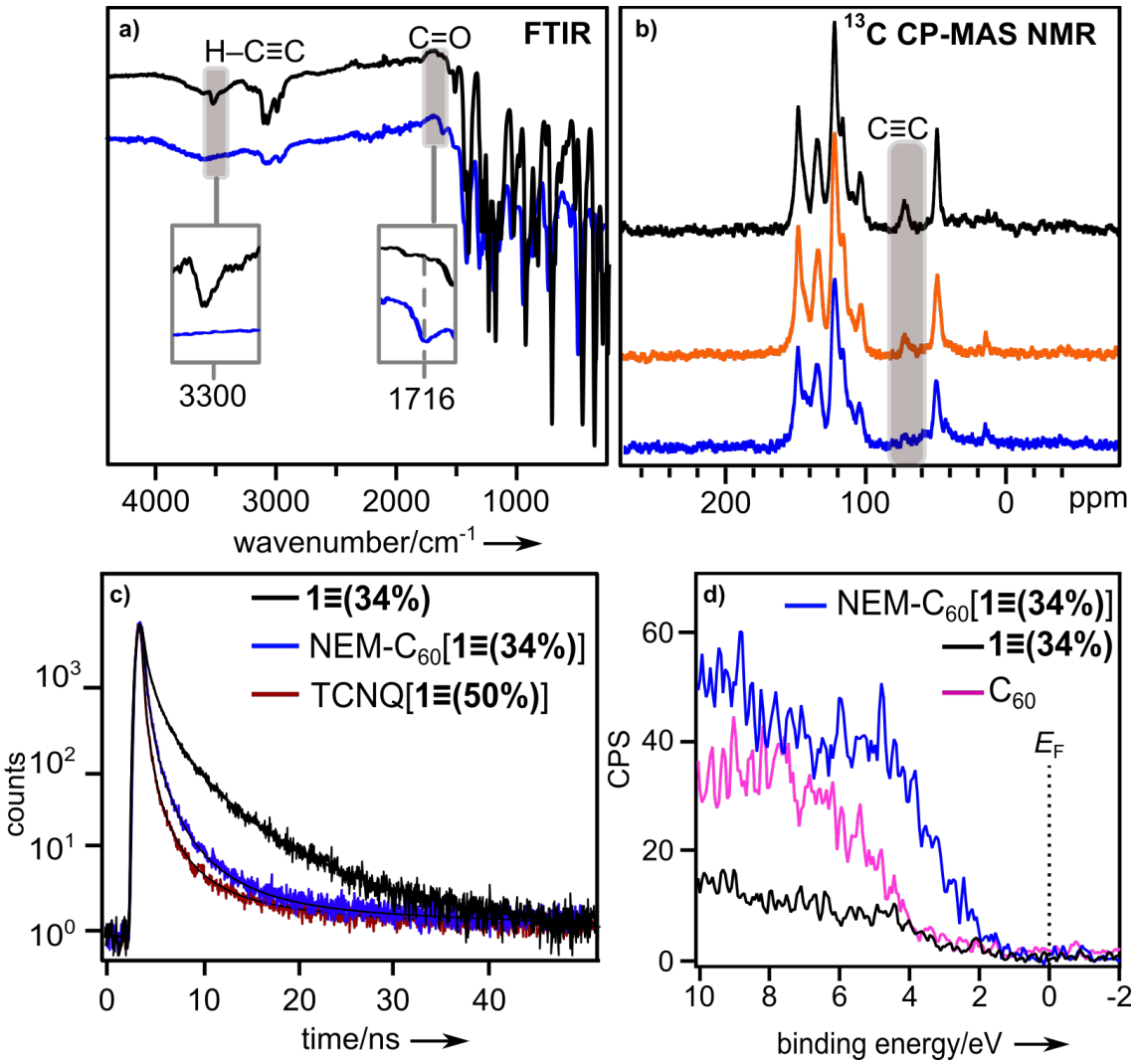

Figure 4.2. (a) FTIR spectra of **1≡(34%)** (black) and NEM-C_{60}[**1≡(34%)**] (blue). Grey areas show H–C≡C present in **1≡(34%)** and absent in NEM-C_{60}[**1≡ (34%)**] and the appearance of the C=O stretch in NEM-C_{60}[**1≡ (34%)**]. (b) ^{13}C CP-MAS NMR spectra of **1≡(34%)** (black), a control experiment with **1≡(34%)** (orange), and NEM-C_{60}[**1≡(34%)**] (blue). (c) Fluorescent decays of **1≡(34%)** (black), NEM-C_{60}[**1≡(34%)**] (blue), and TCNQ[**1≡ (50%)**] (red). (d) XPS data for the valence band region for **1≡(34%)** (black), C_{60} (pink), and NEM-C_{60}[**1≡ (34%)**] (blue).

While C_{60} possesses a unique spherical structure allowing for stabilization of up to six electrons, the LUMO of C_{60} (–4.50 eV) is comparable with a planar acceptor, TCNQ (–4.23 eV).[284,285] TCNQ derivatives usually do not require the labor-intensive HPLC procedure for their isolation, in contrast to C_{60} compounds with a large number of active

centers and possible isomers,[255] making it possible to compare the properties of prepared NEM-C_{60}[**1≡(34%)**] with TCNQ-covalently-linked analogs. To develop suitable reaction conditions to perform a [2+2] cycloaddition reaction followed by ring opening of an intermediate cyclobutene necessary to attach TCNQ through a covalent bond to the COF interior and to monitor reaction progress using "conventional" solution NMR spectroscopy, we started with the molecular building blocks, TCNQ and 4-ethynyl-*N,N*-dimethylaniline (Figure 4.1). In addition to spectroscopic studies, formation of the desired product, 2-(4-(4,4-dicyano-2-(4-(dimethylamino)phenyl)butylidene)cyclohexa-2,5-dien-1-ylidene)malononitrile, was confirmed by single-crystal X-ray crystallography (Figures 4.1 and 4.15). As a next step, the developed conditions were applied toward the reaction of TCNQ with the COF (**1≡(x%)**). For comprehensive characterization of the prepared TCNQ[**1≡(x%)**], we used the same set of techniques as in the case of NEM-C_{60}[**1≡(34%)**]. For instance, we observed disappearance of 2120 cm^{-1} (C≡C) and 3300 cm^{-1} (C≡C–H) bands in the FTIR spectrum, while appearance of the nitrile stretch at 2100 cm^{-1} (C≡N) persisted even after a 24-hour Soxhlet washing procedure, highlighting the presence of TCNQ covalently bound to the COF (Figure 4.3). Due to the smaller size of TCNQ versus the relatively bulky NEM-C_{60}, the measured BET surface area even after TCNQ integration was found to be 812 m^2g^{-1} (Figure 4.20). The determined surface area is the highest for a TCNQ-covalently-linked COF to date in comparison with previous reports that mainly focused on infiltration of TCNQ molecules as guests.[264]

In addition to spectroscopic methods and gas sorption analysis, fluorescent labeling was utilized to address the question about residual unreacted alkyne sites. Two chromophores, 6-bromo-3-cyano-4-methylcoumarin and 2-bromoanthracene, were

selected to perform a Sonogashira cross-coupling reaction within the functionalized COF (Figure 4.1). As a control experiment, we integrated coumarin and anthracene moieties inside **1≡(50%)**. We observed a strong fluorescent signal for both anthracene[**1≡(50%)**] and 4-methyl-2-oxo-2*H*-chromene-3-carbonitrile[**1≡(50%)**] (Figures 4.25 and 4.26). We applied the developed strategy towards detection of residual alkyne moieties in TCNQ[**1≡(50%)**]. In contrast to the reaction with **1≡(50%)**, there was no emission detected for TCNQ[**1≡(50%)**] after the treatment with both fluorescent tags (Figures 4.27 and 4.28). These findings are in line with the spectroscopic evidence and confirm the lack of unreacted alkyne sites concluding reaction completion.

To study the electronic and photophysical properties of the prepared donor-acceptor materials, comprehensive analysis including diffuse reflectance (DR), steady-state and time-resolved photoluminescence (PL), and X-ray photoelectron (XPS) spectroscopies, cyclic voltammetry (CV), and conductivity measurements were employed.

Integration of electron acceptors (TCNQ or C_{60}-derivative) inside the COF was accompanied by a drastic color change from pale yellow to dark red or brown, respectively (Figure 4.3). DR spectroscopic studies confirm that acceptor integration resulted in the appearance of an additional absorption band leading to a bathochromic shift of the absorption profile in comparison with the parent COF, C_{60}, and TCNQ, which is typically associated with charge transfer (CT).[272,286] To further study the observed behavior of both C_{60} and TCNQ-modified COFs, we utilized time-resolved PL spectroscopy. With the assumption that the PL decay rate consists of radiative, nonradiative, and CT components, analysis should reveal shortening of PL lifetimes of the host owing to integration of strong acceptor moieties (i.e., fullerene-based derivative or TCNQ).[287] The amplitude-averaged

lifetime estimated by fitting the time-resolved PL decay curves were 474 ps for **1≡(34%)** while NEM-C_{60}[**1≡(34%)**] and TCNQ[**1≡(50%)**] exhibited much shorter lifetimes of 32 ps and 103 ps, respectively. This is indicative of the potential for CT in the system (Figure 4.2). Similar behavior was previously reported in literature for C_{60} inclusion as guest molecules.[282] In addition, the emission response of the COF itself was quenched when either TCNQ or NEM-C_{60} was covalently bound to the COF walls (Figure 4.30).

As a fast and nondestructive pre-screening technique, XPS was used to probe the electronic structure of the C_{60}-based COF by monitoring the density of states (DOS) near the Fermi level (E_F, binding energy = 0 eV). For **1≡(34%)** itself, the valence band spectrum exhibits behavior associated with insulating materials, given that there is near zero intensity within 3 eV of the Fermi level (E_F = 0 eV binding energy). The spectrum of C_{60} also shows zero intensity at 3 eV. In contrast, the XPS valence band spectrum for NEM-C_{60}[**1≡(34%)**] exhibits higher intensity at 3 eV from E_F. This indicates a greater DOS near E_F, which would be consistent with a more conductive material.

To further elaborate on the observed changes in the XPS spectra, we performed conductivity measurements demonstrating that, for instance, the conductivity of NEM-C_{60}[**1≡(34%)**] was found to be 1.97×10^{-6} S/cm in comparison with the parent COF (2.32×10^{-12} S/cm).[272] Our observations that conductivity increases with promotion of donor-acceptor alignments are in line with literature reports.[273] On the example of TCNQ-integrated materials, we also studied changes in electronic properties as a function of the degree of acceptor integration. Conductivity measurements demonstrate an order-of-magnitude difference for TCNQ[**1≡(34%)**] (1.67×10^{-7} S/cm) versus TCNQ[**1≡(100%)**] (2.12×10^{-6} S/cm) resulting in a six-orders-of-magnitude increase in comparison to the

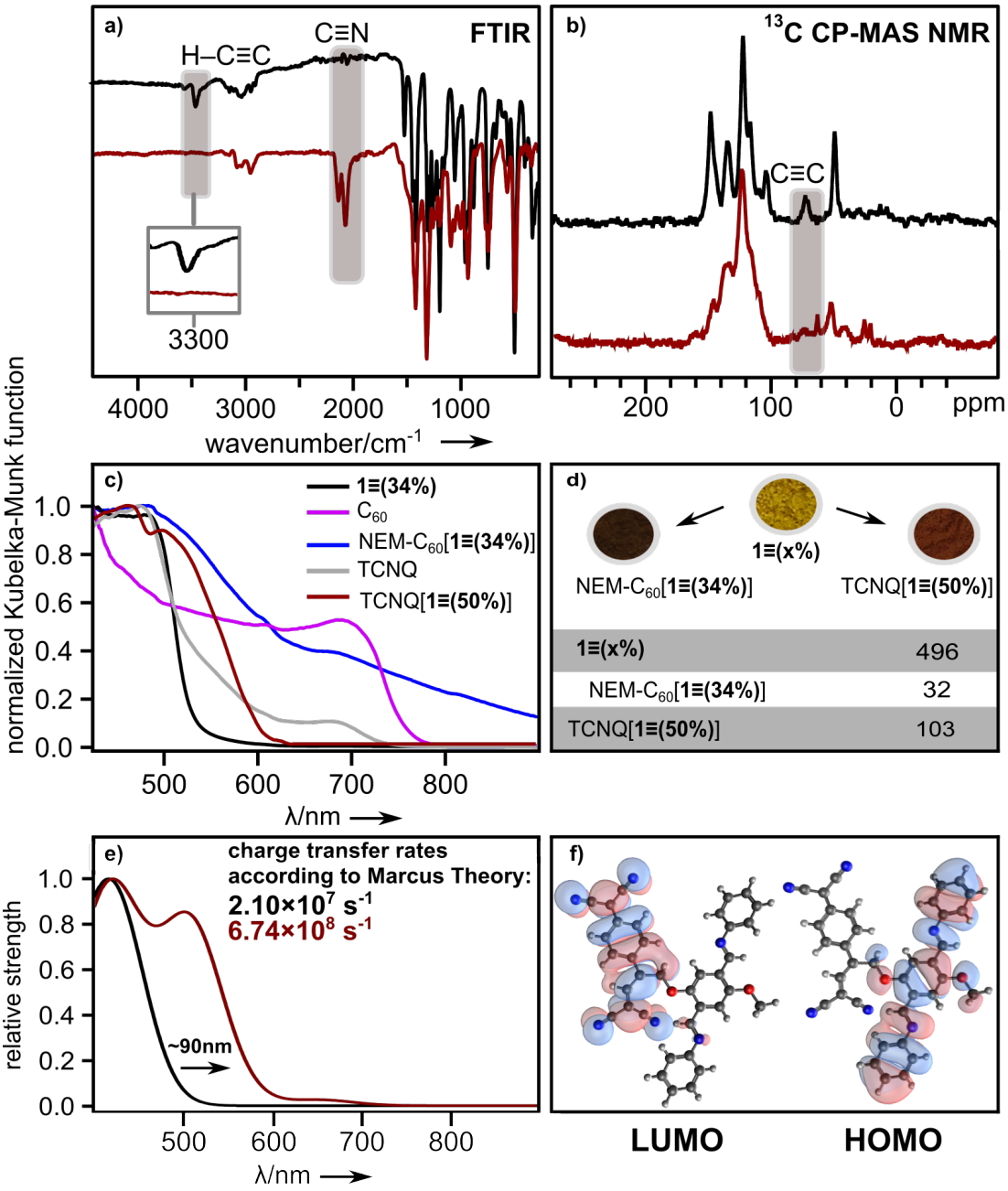

Figure 4.3. (a) FTIR spectra of **1≡(34%)** (black) and TCNQ[**1≡(50%)**] (red). (b) ^{13}C CP-MAS NMR spectra of **1≡(34%)** (black) and TCNQ[**1≡(50%)**] (red). (c) Normalized diffuse reflectance spectra of **1≡(34%)** (black), C_{60} (pink), NEM-C_{60}[**1≡(34%)**] (blue), TCNQ (grey), and TCNQ[**1≡(50%)**] (red). (d) Photographs of **1≡(x%)**, NEM-C_{60}[**1≡(34%)**], and TCNQ[**1≡(50%)**]. The table shows the amplitude-weighted average lifetimes for **1≡(34%)**, NEM-C_{60}[**1≡ (34%)**], and TCNQ[**1≡(50%)**]. (e) The optical transition strength calculated for the COF-fragment (black) and TCNQ**[COF]**-fragment (red) and the corresponding electron transfer rates. The theory level is RPA TDDFT based on B3LYP-D3/6-31+G**. (f) Schematic representation of the frontier orbitals for the truncated molecular model comprised of the TCNQ**[COF]**-fragment.

eV, 1.81 eV, and 2.04 eV, respectively, and they are in line with the conductivity measurements (Figures 4.37 and 4.38).[288,289] Further tuning of electronic properties was achieved through iodine doping, resulting in further increases of conductivity in the range of two- to four-orders-of-magnitude with values of 5.06×10^{-8} S/cm, 1.08×10^{-5} S/cm, and 1.41×10^{-4} for COF, TCNQ[**1≡(50%)**], and TCNQ[**1≡(100%)**], respectively. The conductivity of NEM-C_{60}[**1≡(34%)**] increased to 3.63×10^{-5} S/cm when the material was doped with iodine. The detailed procedure of iodine doping can be found in the Supporting Information. The values obtained herein are among some of the highest values reported in COFs to date.[262–268] In addition, these conductivity studies are the first reports for COFs with covalently bound TCNQ moieties.

To shed light on how acceptor modulation and stacking (e.g., TCNQ moieties) could potentially affect COF properties, electronic structure calculations and electron transfer rates were estimated according to the Marcus theory[290] (Eq. 1).

$$k = 2\pi/\hbar \cdot |V_c|^2/\sqrt{(4\pi\lambda k_B \mathrm{T})} \cdot \exp\left(-\lambda/(4k_B \mathrm{T})\right) \quad (1)$$

where k = charge transfer rate, V_c = electron coupling, and λ = reorganization energy of the system; see the Supporting Information for more details. According to this model, TCNQ stacking inside of the COF could result in a *ca* 32-fold increase in electron transfer rates compared to the parent COF itself (see the Supporting Information for more details). In addition, the electronic structure analysis corroborates donor-acceptor alignment resulting in a bathochromic shift in optical transitions after TCNQ-integration (Figure 4.3) which is in good agreement with the experimental results (Figure 4.3).

In addition to "static" changes through acceptor incorporation inside the electron donating matrix, the electronic properties of COF materials could also be dynamically

controlled through integration of photoresponsive molecules. To investigate this possibility, a spiropyran derivative, 1′,3′-dihydro-1′,3′,3′-trimethyl-6-nitrospiro[2*H*-1-benzopyran-2,2′-(2*H*)-indole] (SP, Figure 4.36), was encapsulated in **1≡(0%)**. In general, SP derivatives isomerize under UV irradiation to the charge-separated merocyanine form which could result in π-electron delocalization and possibly promote conductivity enhancement. Indeed, upon UV irradiation, a drastic color change from light yellow to dark brown was observed for SP@[**1≡(0%)**], indicating the transformation from the closed spiropyran form to the open merocyanine form (Figure 4.36).[291] Based on ^{1}H NMR spectroscopic analysis of the digested SP@**1≡(0%)**, one SP molecule was found per six –OMe units (Figure 4.35). Furthermore, after 30-min-UV irradiation, a 39%-increase in conductivity was observed in comparison with SP@**1≡(0%)** (5.38×10^{-11} S/cm). As a result, these studies could be considered as a blueprint for the development of stimuli-responsive crystalline doped COFs with dynamically controlled electronic behavior.

Due to the presence of redox-active building units, fullerene and TCNQ moieties, we studied the redox behavior of the prepared NEM-C_{60}[**1≡(34%)**] and TCNQ[**1≡(34%)**]. Significant modifications of the commonly used electrochemical setup were employed[292] since cyclic voltammetry studies of COFs are still relatively rare. The redox-active COFs (40 wt.%) were combined with carbon black (60 wt.%) and Nafion, and the obtained slurry was pipetted onto the tip of the electrode and dried under high vacuum. Cyclic voltammetry of TCNQ itself (1.0×10^{-4} M) was performed in a 0.1 M solution of tetrabutylammonium hexafluorophosphate in acetonitrile to afford one quasireversible reduction at E_p = –0.5 V and one oxidation at 0.1 V vs. saturated calomel electrode (SCE) (Figure 4.22). Comparison of the acquired CV data for TCNQ[**1≡(34%)**] to TCNQ itself, shows that both

potentials of TCNQ[**1≡(34%)**] are less negative at E_p = –0.3 V and 0.2 V vs. SCE (Scheme 4.1), which could be evidence of the stronger electron accepting properties of the prepared material. Thus, inclusion of TCNQ in a COF matrix affects the redox potential, which enables this compound to be electrochemically sensed.[293] In comparison with C_{60} itself which exhibits four quasireversible reductions at E_p = –0.3 V, –0.7 V, –1.4 V, and –1.9 V in DMF vs. SCE, the NEM-C_{60} shows similar redox features at E_p = –0.9 V and –1.8 V (Figures 4.21 and 4.22). The reduction waves are more negative than that of pristine C_{60}, which is a known consequence of the saturation of a double bond on the C_{60} sphere.[294] The redox potentials of NEM-C_{60} (E_p = –0.9 V and –1.8 V) and NEM-C_{60}[**1≡(34%)**] (E_p = –1.2 V and –2.1 V vs. SCE) are also similar, with a slight shift in potential (Figures 4.23 and 4.24) supporting integration of NEM-C_{60} and reinforcement of the redox-active nature within the COF. Such electrochemical behavior (i.e., presence of two waves in the cyclic voltammogram) is comparable with C_{60}-based dimers in the literature,[294] with a reduced symmetry comparable to NEM-C_{60}. While CVs with integrated acceptors have been measured for other systems such as molecular rectangles,[293] these are the first studies, to the best of our knowledge, that demonstrate redox-active behavior of TCNQ- and C_{60}-integrated COFs.

The aforementioned results demonstrate preparation of the first family members of purely organic, crystalline, porous scaffolds with covalently bound TCNQ and C_{60} moieties; integration of the latter ones not only resulted in increases in conductivity by eight-orders-of-magnitude, but affect the redox behavior of the material. Moreover, the interior of a COF was harnessed for the first time to perform a Sonogashira cross-coupling and [2+2] cycloaddition reactions, followed by ring opening of a strained intermediate in

the case of the latter. The former reaction was probed for fluorophore tag integration that opens an avenue to control reaction progress inside of the COF. Notably, the reported purely organic covalently-integrated-acceptor scaffolds have the highest surface area and they are the first buckyball- and TCNQ-integrated COFs that exhibit redox behavior to date. Our theoretical analysis probing charge transfer rates within the Marcus theory as a function of TCNQ stacking within COFs showed a 32-fold increase in electron transfer rates compared to the parent COF itself. Despite the theory limitations, it is the first successful attempt to explain charge transfer in COFs using the Marcus theory that paves the way for further simulations of electronic structures and CT studies of hierarchical materials. Shifting from "static" tuning of the electronic structure, dynamic control of electronic properties in COFs as a function of external stimulus was achieved through spiropyran guest infiltration in the porous scaffold. Overall, this work demonstrates the potential for donor-acceptor alignment on the example of buckyball- and TCNQ-electron acceptors and COF-based donors for the development of porous and crystalline materials with tunable electronic structures that could open a new avenue for the rational design of electroactive and conductive multidimensional and multifunctional crystalline porous materials.

EXPERIMENTAL

The covalent-organic framework (COF)-based linkers, 2,5-dimethoxyterephthalaldehyde (DMTA), 1,3,5-tri-(4-aminophenyl)benzene (TAPB), and 2,5-bis(2-propynyloxy) terephthalaldehyde (BPTA), were synthesized based on modified literature procedures. The COFs, **1≡(x%)** (where **x** = [BPTA]/([BPTA] + [DMTA]) × 100%), were also synthesized based on modified literature procedures.

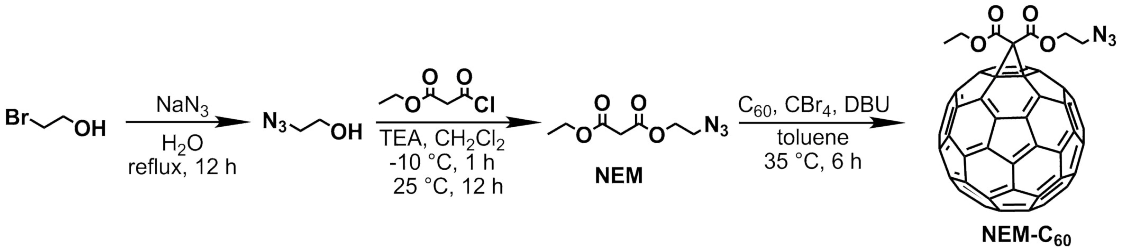

Scheme 4.2. Synthesis of **NEM-C_{60}** (TEA = triethylamine, DBU = 1,8-diazabicyclo[5.4.0]undec-7-ene).

Synthesis of 2-azidoethanol ($C_2H_5ON_3$, Scheme 4.2)

The first intermediate, 2-azidoethanol, was synthesized based on a modified literature procedure. In a 100-mL Schlenk flask under a nitrogen atmosphere, 2-bromoethanol (1.0 g, 8.0 mmol) was added to NaN_3 (0.78 g, 12 mmol), and then the reaction mixture was heated at reflux in water (7.2 mL) for 12 hours. Once cooled to room temperature, NaCl (1.0 g, 17 mmol) was added to the reaction mixture. The desired compound was extracted from the aqueous layer using dichloromethane (3 × 25 mL) and the solvent was removed under reduced pressure to afford yellow oil in 80% yield. ^{1}H NMR (DMSO-d_6, 300 MHz): δ = 5.00 (1H, t, J = 5.04), 3.57 (2H, q, J = 5.04), 3.26 (3H, t, J = 5.04) ppm (Figure 4.4). ^{13}C NMR ($CDCl_3$, 101 MHz): δ = 63.51 and 53.42 ppm (Figure 4.4). FTIR (neat, cm^{-1}): 3353, 2936, 2093, 1635, 1442, 1347, 1284, 1061, 977, 878, and 829 (Figure 4.6).

Synthesis of 2-azidoethyl ethyl malonate ($C_7H_{11}O_4N_3$, NEM, Scheme 2.2)

The second intermediate, NEM, was synthesized based on a modified literature procedure. A 50-mL Schlenk flask was charged with 2-azidoethanol (0.35 g, 4.0 mmol) and anhydrous dichloromethane (20 mL). The solution was cooled to −10 °C using a dry ice/ethylene glycol bath and then triethylamine (0.71 mL) and ethyl malonyl chloride (0.52

mL, 4.1 mmol) were added slowly to the mixture. The solution was kept at –10 °C for one hour, slowly warmed to room temperature, and then stirred overnight. The resulting solution was diluted with water (20 mL) and extracted with dichloromethane (3 × 25 mL). The combined organic layers were washed with water (3 × 25 mL) and the solvent was removed under reduced pressure to afford yellow oil in 93% yield. ^{1}H NMR ($CDCl_3$, 300 MHz): δ = 4.32 (2H, t, J = 5.04), 4.22 (2H, q, J = 7.14), 3.51 (2H, t, J = 5.04), 3.43 (2H, s), 1.29 (3H, t, J = 7.14) ppm (Figure 4.5). ^{13}C NMR ($CDCl_3$, 101 MHz): δ = 166.27, 64.08, 61.83, 48.92, 41.73, 14.06 ppm (Figure 4.5). FTIR (neat, cm^{-1}): 2985, 2105, 1741, 1445, 1369, 1328, 1266, 1144, 1031, 959, 847, and 680 (Figure 4.7). HRMS (ESI, m/z) calculated for $[NEM+H]^+$ 202.0828, found 202.0831.

Development of the Synthetic Conditions for 1,3-Dipolar Cycloaddition Reactions

For investigation of reaction conditions necessary to perform a 1,3-dipolar cycloaddition reaction using NEM-C_{60} with **1≡(34%)**, we devised a stepwise approach starting with azide-containing molecules. We initially chose less bulky and more affordable units such as 2-azidoethanol and NEM for development of synthetic methodologies before pursuing the reaction between NEM-C_{60} and **1≡(34%)**.

Synthesis of 2-azidoethanol[1≡(34%)]

In a 25-mL Schlenk tube, 2-azidoethanol (4.4 mg, 51 μmol), **1≡(34%)** (15 mg), *N,N*-diisopropylethylamine (75 μL of a 1.0 M THF solution), and CuI (1.5 mg, 7.9 μmol) in a mixture of THF/water (2.0 mL/0.75 mL) were added. The reaction mixture was degassed through three freeze-pump-thaw cycles and the mixture was heated at 70 °C for three days. Upon cooling to room temperature, the precipitate was collected via vacuum filtration, washed thoroughly with THF and acetonitrile, and dried under reduced pressure

to give a brown precipitate in quantitative yield. FTIR (neat, cm^{-1}): 2926, 1591, 1505, 1465, 1412, 1293, 1209, 1034, 823, and 697. The FTIR data highlight disappearance of the alkyne bands, ν(C≡C), at 2120 cm^{-1} and ν(H–C≡C) at 3300 cm^{-1} and appearance of the alcohol band ν(OH) at ~2900 cm^{-1} in the spectrum which is indicative of the reaction progress (Figure 4.9).

Synthesis of NEM[1≡(34%)]

In a 25-mL Schlenk tube, COF **1≡(34%)** (15 mg), NEM (6.8 mg, 34 μmol), *N,N*-diisopropylethylamine (75 μL of a 1.0 M THF solution), CuI (1.5 mg, 7.5 μmol), and THF/water (2.0 mL/0.75 mL) were added. The reaction mixture was degassed through three freeze-pump-thaw cycles, and the mixture was heated at 70 °C for three days. Upon cooling to room temperature, the precipitate was collected via vacuum filtration, washed with THF and acetonitrile (3 × 5 mL for each solvent), and dried under reduced pressure to give a brown precipitate in quantitative yield. FTIR (neat, cm^{-1}): 2962, 1737, 1594, 1505, 1412, 1284, 1210, 1035, 828, and 697. The FTIR data highlight disappearance of the alkyne bands, ν(C≡C), at 2120 cm^{-1} and ν(H–C≡C) at 3300 cm^{-1} and appearance of the carbonyl band ν(–C=O) at ~1700 cm^{-1}, which is indicative of the reaction progress. The control experiment was also performed and discussed below.

Control Experiment Involving 1≡(34%)

As a control experiment, we treated **1≡(34%)** under the same reaction conditions developed for the 1,3-dipolar cycloaddition reactions (such as in the synthesis of NEM[**1≡(34%)**]) but without presence of the azide-containing precursor. As expected, we observed preservation of both 2120 cm^{-1}, ν(C≡C), and 3300 cm^{-1}, ν(H–C≡C), bands in the

FTIR spectrum showing that the alkyne moieties within the COF pores were not affected (Figure 4.14).

In a 25-mL Schlenk tube, CuI (1.5 mg, 7.5 μmol) and **1≡(34%)** (15 mg) were added to a mixture of THF/H_2O (2.0 mL/0.75 mL). To the prepared reaction mixture, *N,N*-diisopropylethylamine (75 μL of a 1.0 M THF solution) was added. The reaction mixture was degassed through three freeze-pump-thaw cycles, and the mixture was stirred at 70 °C for three days. Upon cooling to room temperature, the precipitate was collected, washed with THF and acetonitrile (3 × 5 mL for each solvent), and dried under vacuum overnight to give a brown precipitate in quantitative yield. FTIR (neat, cm^{-1}): 3300, 2120, 1673, 1596, 1510, 1458, 1394, 1284, 1210, 1185, 1029, 879, 824, 732, and 695 (Figure 4.14).

Synthesis of NEM-C_{60}[1≡(34%)]

Initially, we prepared (2-azidoethyl)-(ethyl)-3'H-cyclopropa-[1,2](C_{60})[5,6]fullerene-3',3'-dicarboxylate (NEM-C_{60}, Scheme 2.2) according to a literature procedure.[5] In the absence of light, a 100-mL Schlenk flask was charged with C_{60} (50 mg, 69 μmol) and anhydrous toluene (50 mL). Once the C_{60} was fully dissolved, NEM (9.7 mg, 69 μmol), carbon tetrabromide (110 mg, 0.34 mmol), and DBU (21 mg, 0.14 mmol) were added to the solution. The solution was heated at 35 °C for six hours. The crude product was purified via column chromatography (SiO_2, toluene → 1:1 toluene:dichloromethane), and the solvent was removed under reduced pressure to afford dark brown oil in 51% yield. FTIR (neat, cm^{-1}): 2921, 2097, 1742, 1430, 1259, 1015, 795, and 703 (Figure 4.8). HRMS (ESI, m/z) calculated for $[NEM\text{-}C_{60}]^-$ 919.0593, found 919.0595. Cyclic voltammetry was used to study the redox potential of NEM-C_{60} in comparison with C_{60} itself (Figures 4.21 and 4.23, see the Physical Measurements section

for more details). As a next step, isolated NEM-C_{60} was used for integration inside the COF. In order to avoid exposure to light during the reaction, a 25-mL Schlenk tube was wrapped with foil, and then NEM-C_{60} (2.0 mL of a 15 μM toluene solution) was added to **1≡(34%)** (15 mg). The COF was allowed to soak in the NEM-C_{60} solution for one day, and then *N,N*-diisopropylethylamine (75 μL of a 1.0 M THF solution), CuI (0.5 mg, 2.6 μmol), and water (0.75 mL) were added to the reaction mixture. The reaction mixture was degassed through three freeze-pump-thaw cycles, wrapped with aluminum foil to prevent exposure to light, and then heated at 50 °C for three days to perform the 1,3-dipolar cycloaddition reaction. Upon cooling to room temperature, the precipitate was collected via vacuum filtration and washed thoroughly with THF and acetonitrile (3 × 5 mL for each solvent). In order to maximize fullerene content, the material was subjected to multiple cycles of soaking in the NEM-C_{60} solution followed by the 1,3-dipolar cycloaddition reaction. To clarify, the collected precipitates were re-added to a solution of NEM-C_{60} (2.0 mL of a 15 μM toluene solution) in a foil-wrapped 25-mL Schlenk tube and soaked in this solution for one day. Then, the same reaction conditions (*N,N*-diisopropylethylamine/CuI/THF/H_2O, 70 °C, 3 days) were repeated two additional times, until the reaction solution retained color, indicating complete incorporation of NEM-C_{60}. Once complete incorporation of NEM-C_{60} was achieved, the reaction mixture was cooled to room temperature, and the precipitate was collected via vacuum filtration. The precipitate was thoroughly washed with THF and acetonitrile and dried under reduced pressure to give a brown precipitate in quantitative yield. FTIR (neat, cm^{-1}): 2921, 1742, 1683, 1591, 1504, 1409, 1287, 1209, 1037, 879, 827, and 732 (Figure 4.2). The FTIR data highlight disappearance of the alkyne bands, ν(C≡C), at 2120 cm^{-1} and ν(H–C≡C) at 3300

cm^{-1} in the spectra, which is indicative of reaction completion (Figure 4.2). In addition, presence of the characteristic carbonyl band, ν(–C=O), at ~1716 cm^{-1} from NEM-C_{60} in the FTIR spectrum of NEM-C_{60}[**1≡(34%)**] also supports reaction completion. As an additional technique to monitor reaction progress, ^{13}C CP-MAS NMR spectroscopy was used, since the alkyne (C≡C) bond is the reactive species, and is observed in the ^{13}C CP-MAS NMR spectra for **1≡(34%)** (see Figure 4.2). This spectrum highlights disappearance of the alkyne (C≡C) resonance at 80 ppm, indicative of completion of the 1,3-dipolar cycloaddition reaction. In addition, the appearance of resonances at ~15 and 40 ppm may be attributed to the ethyl group of NEM-C_{60} (see ^{13}C NMR spectrum of NEM (Figure 4.7)), further indicating reaction completion. In addition, WAXS data demonstrates that structural integrity of the framework was maintained after undergoing multiple 1,3-dipolar cycloaddition reactions (Figure 4.12) when compared to **1≡(34%)** itself (Figure 4.11). Fitting the N_2 adsorption isotherm to the Brunauer-Emmett-Teller (BET) equation resulted in surface area of 229 m^2/g (Figure 4.19).

To further study the reaction between NEM-C_{60} and the COF, we employed diffuse reflectance (DR), steady-state and time-resolved photoluminescence (PL), and X-ray photoelectron (XPS) spectroscopies, as well as conductivity measurements. Integration of electron-accepting units inside the COF resulted in a significant color change from yellow to brown. A DR spectroscopic analysis revealed that fullerene integration resulted in the appearance of an additional absorption band (Figure 4.3), which can be attributed to charge transfer between COF and fullerene moieties. The analysis of time-resolved PL decay curves revealed an amplitude-averaged lifetime of 32 ps for NEM-C_{60}[**1≡(34%)**] in comparison with 496 ps for the COF itself (Figure 4.2). In addition, the presence of an

electron acceptor, such as NEM-C_{60} in the COF structure, resulted in complete PL quenching (Figure 4.30).

Development of Synthetic Conditions for [2+2] Cycloaddition Reactions.

To demonstrate the ability of TCNQ to participate in [2+2] cycloaddition reactions with alkynes in the COF structure, the reaction was initially performed with molecular species in solution according to a modified literature procedure. In a 50-mL Schlenk flask, 7,7,8,8-tetracyanoquinodimethane (70 mg, 0.34 mmol), 4-ethynyl-*N,N*-dimethylaniline (50 mg, 0.34 mmol), and chloroform (20 mL) were added. The resulting solution was heated at 40 °C for six hours. Once cooled to room temperature, the solvent was removed under reduced pressure, and the crude product was purified via column chromatography (SiO_2, dichloromethane) to afford the product with a 54% yield. ^{1}H NMR (CD_2Cl_2, 300 MHz): δ = 8.18 (1H, s), 7.30 (4H, s), 7.15 (2H, d, J = 9.0), 6.78 (2H, d, J = 9.0), and 3.15 (6H, s) ppm (Figure 4.16). ^{13}C NMR (CD_2Cl_2, 101 MHz): δ = 156.63, 152.95, 152.89, 146.45, 135.74, 134.22, 126.39, 122.72, 114.08, 113.78,112.31, 110.53, 92.58, 76.46, and 40.17 ppm (Figure 4.16). HRMS (ESI, m/z) calculated for $C_{22}H_{15}N_5$ $[M+H]^+$ 350.1406, found 350.1408. The product was recrystallized from a saturated benzene solution. Single-crystal X-ray data are shown in Table 4.1 and Figure 4.15.

Scheme 4.3. Synthesis of TCNQ[**1≡(x%)**], where x = 34, 50, and 100.

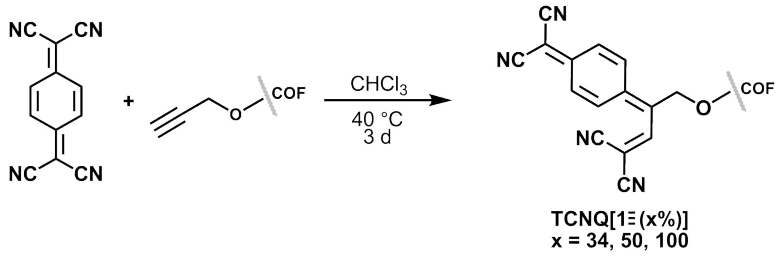

Synthesis of TCNQ[1≡(x%)] (Scheme 4.3).

In a 25-mL Schlenk tube, COF **1≡(x%)** (15 mg, where **x** = 34, 50, or 100%), 7,7,8,8-tetracyanoquinodimethane (varying amounts based on alkyne percent in the pores: 10 mg, 49 μmol for **1≡(34%)**; 15 mg, 75 μmol for **1≡(50%)**; or 30 mg, 150 μmol for **1≡(100%)**), and chloroform (2.0 mL) were added. The reaction mixture was degassed through three freeze-pump-thaw cycles, and the mixture was heated at 40 °C for three days. Upon cooling to room temperature, the precipitate was collected via vacuum filtration, washed with chloroform and acetonitrile (3 × 5 mL for each solvent), and dried under reduced pressure to give a brown precipitate in quantitative yield. FTIR (neat, cm^{-1}): 2962, 2104, 1737, 1594, 1505, 1412, 1284, 1210, 1035, 828, and 697 (Figure 4.3). The FTIR data highlight disappearance of the alkyne bands, ν(C≡C) and ν(H–C≡C), at 2120 cm^{-1} and at 3300 cm^{-1}, respectively, and the appearance of the nitrile band, ν(C≡N), at 2100 cm^{-1}, which is indicative to reaction completion. Notably, preservation of bands corresponding to the TCNQ moiety after an extensive several-day washing procedure also supports successful reaction completion. As an additional technique to monitor reaction progress, ^{13}C CP-MAS NMR spectroscopy was used. In all reactions (except the control experiment) the alkyne resonances, (C≡C), are present in the ^{13}C CP-MAS NMR spectra for every **1≡(x%)** and absent in the spectra after reaction completion (Figure 4.3). Thus, ^{13}C CP-MAS NMR spectra highlight both disappearance of the alkyne (C≡C) resonance at 80 ppm, indicative of completion of the [2+2] cycloaddition reaction, and appearance of resonances at 29 and 44 ppm corresponding to the integrated TCNQ moieties. Fitting the N_2 adsorption isotherm to the BET equation resulted in a surface area of 812 m^2/g for TCNQ[**1≡(50%)**] (Figure 4.20).

To further investigate the TCNQ-integrated COF, we employed diffuse reflectance (DR), steady-state and time-resolved photoluminescence spectroscopies as well as conductivity measurements. Integration of the acceptor units inside the COF resulted in a significant color change of the material from yellow to red. A DR spectroscopic analysis revealed that integration of TCNQ-based electron acceptors resulted in appearance of an additional absorption band (Figure 4.3) which can be attributed to charge transfer between the COF and TCNQ. The analysis of time-resolved PL decay curves revealed an amplitude-averaged lifetime of 103 ps for TCNQ[**1≡(50%)**] in comparison with 496 ps for the COF itself (Figure 4.2). In addition, the presence of an electron acceptor, such as TCNQ derivatives in the COF structure, resulted in complete PL quenching (Figure 4.30).

For additional evidence of complete integration of acceptor-containing materials in the COF (i.e., all –C≡C are occupied with acceptor molecules), we devised a strategy to target any remaining alkyne sites within the COF using a fluorescent tag. In the case of remaining unreacted alkyne sites, the fluorescent tag will bind to the COF which can be easily detected through the appearance of emission. In contrast, if all reactive sites are occupied, then no changes in the emission/absorption profile would be detected. Experimental details are described below.

Development of Synthetic Conditions for Sonogashira Coupling Reactions

To demonstrate the ability of fluorophores to participate in a Sonogashira coupling reaction with alkynes in the COF structure, the reaction was initially performed with a molecular species in solution. In a 50-mL Schlenk flask, 2-bromoanthracene (51 mg, 0.19 mmol), 4-ethynyl-*N,N*-dimethylaniline (42 mg, 0.29 mmol), bistriphenylphosphinepalladium(II) dichloride (14 mg, 19 μmol), and CuI (4.0 mg, 19

μmol) were added. Degassed triethylamine (10 mL) and anhydrous THF (10 mL) were added to the flask, and the mixture was stirred at 80 °C for 3 d. Upon cooling to room temperature, the solvent was evaporated, and the sample was subjected to purification using preparative thin layer chromatography (SiO_2, hexane:DCM (1:1)) and a yield of 62% was obtained. ^{1}H NMR ($CDCl_3$, 300 MHz): δ = 8.38 (2H, s), 8.18 (1H, s), 7.99–7.94 (3H, m), 7.55-7.46 (5H, m), 6.71 (2H, d, J = 8.94), and 3.03 (6H, s) ppm (Figure 4.17). ^{13}C NMR ($CDCl_3$, 101 MHz): δ = 150.19, 132.84, 132.07, 131.95, 131.32, 130.88, 130.53, 128.23, 128.20, 128.09, 127.92, 126.15, 126.02, 125.62, 125.58, 120.93, 111.88, 110.03, 91.75, 88.18, and 40.24 ppm (Figure 4.17). HRMS (ESI, m/z) calculated for $C_{24}H_{19}N$ $[M+H]^+$ 322.1587, found 322.1590.

Development of the Synthetic Conditions for Fluorescent Labeling of Unreacted Active Sites

We tested the concept on the **1≡(50%)** using two fluorophores, 6-bromo-3-cyano-4-methylcoumarin and 2-bromoanthracene, and then re-applied this concept for the compound of interest, TCNQ[**1≡(50%)**]. Thus, we coupled **1≡(50%)** with fluorophores using a modified literature procedure and determined reaction progress by FTIR spectroscopy in order to establish a baseline for fluorescent response (control experiments). The experimental details for the control experiments and reactions with TCNQ[**1≡(50%)**] for the two fluorophores are given below.

Synthesis of anthracene[1≡(50%)]

In a 25-mL three-neck round bottom flask, **1≡(50%)** (32 mg), 2-bromoanthracene (2.0 mg, 78 μmol), bistriphenylphosphinepalladium(II) dichloride (5.0 mg, 7.1 μmol), and CuI (2.0 mg, 11 μmol) were added. Degassed triethylamine (10 mL) was added to the flask,

and the mixture was stirred at 40 °C for 1 d. Upon cooling to room temperature, the precipitate was collected, washed with THF/ACN/DCM (3 × 5 mL for each solvent), and dried under vacuum overnight to afford an orange precipitate in quantitative yield. FTIR (neat, cm^{-1}): 2962, 2149, 1613, 1591, 1505, 1488, 1465, 1443, 1409, 1374, 1289, 1209, 1180, 1147, 1039, 1013, 974, 879, 828, 733, and 693 (Figure 4.32). The FTIR data shown in Figure 4.32 highlight the preservation of the ν(C≡C) band and disappearance of the ν(H–C≡C) band, indicating transformation of terminal alkynes to internal alkynes. The PXRD pattern is shown in Figure 4.31. Coupling of the fluorophore with the COF resulted in a significant color change of the material from yellow to orange. Emission and DR spectra are shown in Figures 4.27 and 4.29, respectively. Non-integrated 2-bromoanthracene is almost non-emissive in the solid state which is in line with literature reports. Integration of an anthracene derivative inside the COF matrix with available alkyne moieties resulted in appearance of a strong emission with λ_{max} = 658 nm (λ_{ex} = 365 nm).

Synthesis of 4-methyl-2-oxo-2*H*-chromene-3-carbonitrile[1≡(50%)]

In a 25-mL three-neck round bottom flask, **1≡(50%)** (32 mg), 6-bromo-3-cyano-4-methylcoumarin (22 mg, 83 μmol), bistriphenylphosphinepalladium(II) dichloride (5.0 mg, 7.1 μmol), and CuI (2.0 mg, 11 μmol) were added. Degassed triethylamine (10 mL) was added to the flask and the mixture was stirred at 40 °C for 1 d. Upon cooling to room temperature, the precipitate was collected, washed with THF/ACN/DCM (3 × 5 mL for each solvent), and dried under vacuum overnight to give a brown precipitate in quantitative yield. FTIR (neat, cm^{-1}): 2960, 2160, 1734, 1591, 1505, 1486, 1465, 1408, 1289, 1208, 1181, 1144, 1080, 1030, 875, 825, and 693 (Figure 4.33). The FTIR data in Figure 4.33 highlight the preservation of the ν(C≡C) band and disappearance of the ν(H–C≡C) band,

indicating transformation of terminal alkynes to internal alkynes. We also observed appearance of the carbonyl band, ν(–C=O), as an additional indication that coumarin was coupled to the framework (Figure 4.33). The PXRD pattern is shown in Figure 4.31. Coupling of the fluorophore with the COF resulted in a significant color change of the material from yellow to brown. For the coumarin-integrated scaffold emission enhancement has been observed. Emission and DR spectra are shown in Figures 4.26 and 4.28, respectively. Non-integrated 6-bromo-3-cyano-4-methylcoumarin is non-emissive in the solid state which is in line with the literature reports. Integration of the coumarin derivative inside the COF matrix resulted in the appearance of a strong emission with λ_{max} = 652 nm (λ_{ex} = 365 nm).

Synthesis of 2-bromoanthracene@TCNQ[1≡(50%)]

In a 25-mL three-neck round bottom flask, TCNQ[**1≡(50%)**] (32 mg), 2-bromoanthracene (2.0 mg, 78 μmol), bistriphenylphosphinepalladium(II) dichloride (5.0 mg, 7.1 μmol), and CuI (2.0 mg, 11 μmol) were added. Degassed triethylamine (10 mL) was added to the flask and the mixture was stirred at 40 °C for 1 d. Upon cooling to room temperature, the precipitate was collected, washed with THF/ACN/DCM (3 × 5 mL for each solvent), and dried under vacuum overnight to give a brown precipitate in quantitative yield. FTIR (neat, cm^{-1}): 2938, 2834, 2180, 2136, 1590, 1505, 1488, 1465, 1444, 1409, 1375, 1290, 1247, 1209, 1175, 1144, 1040, 1012, 976, 925, 876, 827, 732, and 694 (Figure 4.34). The FTIR spectra shown in Figure 4.34 highlight the preservation of nitrile band, ν(C≡N), indicating that TCNQ moieties remained covalently bound to the framework. As expected, there was no appearance of any additional resonances. In addition, no color change (previously observed for anthracene[**1≡(50%)**]) was detected in this case.

Moreover, absence of coupling of the fluorophore with TCNQ[**1≡(50%)**] was confirmed by lack of changes in the emission and absorption profiles (Figure 4.27). In contrast to moderate crystallinity loss observed in the case of anthracene[**1≡(50%)**], the PXRD pattern of TCNQ[**1≡(50%)**] after "treatment" with 2-bromoanthracene still indicates high sample crystallinity (similar to as-synthesized TCNQ[**1≡(50%)**]) which can be used as an additional evidence of absence of reactive alkyne species (Figure 4.27).

Combination of the results observed in the case of the fluorophore tag treatment with solid-state NMR and FTIR spectroscopic data indicate that accessible alkyne sites are occupied in the COF by TCNQ-based moieties (Figure 4.3).

Synthesis of 6-bromo-3-cyano-4-methylcoumarin@TCNQ[1≡(50%)]

In a 25-mL three-neck round bottom flask, TCNQ[**1≡(50%)**] (32 mg), 6-bromo-3-cyano-4-methylcoumarin (22 mg, 83 μmol), bistriphenylphosphinepalladium(II) dichloride (5 mg, 7.1 μmol), and CuI (2 mg, 11 μmol) were added. Degassed triethylamine (10 mL) was added to the flask and the mixture was stirred at 40 °C for 1 d. Upon cooling to room temperature, the precipitate was collected, washed with THF/ACN/DCM (3 × 5 mL for each solvent), and dried under vacuum overnight to give a brown precipitate in a quantitative yield. FTIR (neat, cm^{-1}): 2941, 2163, 2136, 1590, 1506, 1490, 1467, 1444, 1375, 1292, 1211, 1180, 1144, 1041, 1013, 977, 926, 877, 828, 732, and 695. The FTIR data (Figure 4.33) highlight the preservation of ν(C≡N) band indicating that TCNQ moieties remained covalently bound to the framework. As expected, there was no appearance of any additional resonances. In addition, no color change (previously observed for 4-methyl-2-oxo-2*H*-chromene-3-carbonitrile[**1≡(50%)**]) was detected in this case. Moreover, absence of coupling of the fluorophore with TCNQ[**1≡(50%)**] was confirmed

by lack of changes in the emission and absorption profiles (Figure 4.28). In contrast to moderate crystallinity loss observed in the case of 4-methyl-2-oxo-2*H*-chromene-3-carbonitrile[**1≡(50%)**], the PXRD pattern of TCNQ[**1≡(50%)**] after "treatment" with 6-bromo-3-cyano-4-methylcoumarin still indicates high sample crystallinity (similar to as-synthesized TCNQ[**1≡(50%)**]), which can be used as an additional support for the absence of reactive alkyne species (Figure 4.31).

Combination of the results observed in the case of fluorophore tag treatment with solid-state NMR and FTIR spectroscopic data indicate that accessible alkyne sites are occupied by TCNQ-based moieties in the prepared COFs.

Preparation of I_2@[1≡(50%)], I_2@NEM-C_{60}[1≡(34%)], I_2@TCNQ[1≡(50%)], and I_2@TCNQ[1≡(100%)]

Preparation of iodine doped frameworks, I_2@[**1≡(50%)**], I_2@NEM-C_{60}[**1≡(34%)**], I_2@TCNQ[**1≡(50%)**], and I_2@TCNQ[**1≡(100%)**], was performed based on a modified literature procedure. An uncapped 0.5 dram vial containing the COF (15 mg) was placed inside a 20 mL vial charged with iodine (100 mg, 0.39 mmol) and subsequently sealed for three days. The iodine-doped materials were then subjected to pressed-pellet conductivity measurements (see the section *Physical Measurements*).

Preparation of SP@[1≡(0%)]

Preparation of a photochromic responsive framework, SP@[**1≡(0%)**], was performed based on a modified doping procedure. In a 20-mL scintillation vial, [**1≡(0%)**] (20 mg) was added to 0.50 mL of THF followed by the addition of 1′,3′-dihydro-1′,3′,3′-trimethyl-6-nitrospiro[2*H*-1-benzopyran-2,2′-(2*H*)-indole (SP) (5.0 mg, 16 μmol) in THF (50 μL). After 2 days, the precipitate was collected and washed thoroughly with THF (3 ×

15 mL) to remove any excess 1′,3′-dihydro-1′,3′,3′-trimethyl-6-nitrospiro[2*H*-1-benzopyran-2,2′-(2*H*)-indole] from the surface of the COF. As a result, a yellow powder was obtained in quantitative yield. ^{1}H NMR spectroscopic studies of a digested sample confirmed the presence of 1′,3′-dihydro-1′,3′,3′-trimethyl-6-nitrospiro[2*H*-1-benzopyran-2,2′-(2*H*)-indole in **1≡(0%)**] after the washing procedure, and it was determined to have a presence of one 1′,3′-dihydro-1′,3′,3′-trimethyl-6-nitrospiro[2*H*-1-benzopyran-2,2′-(2*H*)-indole molecule per six –OMe units.

Digestion Procedure for 1′,3′-dihydro-1′,3′,3′-trimethyl-6-nitrospiro[2*H*-1-benzopyran-2,2′-(2*H*)-indole]@[1≡(0%)]

To estimate the amount 1′,3′-dihydro-1′,3′,3′-trimethyl-6-nitrospiro[2*H*-1-benzopyran-2,2′-(2*H*)-indole in 1′,3′-dihydro-1′,3′,3′-trimethyl-6-nitrospiro[2*H*-1-benzopyran-2,2′-(2*H*)-indole]@[**1≡(0%)**], a solution of 500 μL DMSO and 5 μL of DCl was added to ~5 mg of 1′,3′-dihydro-1′,3′,3′-trimethyl-6-nitrospiro[2*H*-1-benzopyran-2,2′-(2*H*)-indole]@[**1≡(0%)**], followed by heating at 100 °C for 1 d. Based on ^{1}H NMR spectroscopic analysis of the digested COF, non-coordinative immobilization led to inclusion of one 1′,3′-dihydro-1′,3′,3′-trimethyl-6-nitrospiro[2*H*-1-benzopyran-2,2′-(*2H*)-indole] molecule per six –OMe units (Figure 4.35).

X-ray Crystal Structure Determination, $C_{22}H_{15}N_5$

X-ray intensity data from a black plate were collected at 100(2) K using a Bruker D8 QUEST diffractometer equipped with a PHOTON-100 CMOS area detector and an Incoatec microfocus source (Mo Kα radiation, λ = 0.71073 Å). The raw area detector data frames were reduced and corrected for absorption effects using the Bruker APEX3, SAINT+ and SADABS programs. The structure was solved with SHELXT. Subsequent

difference Fourier calculations and full-matrix least-squares refinement against F^2 were performed with SHELXL-2018 using OLEX2.

The compound crystallizes in the space group *P*-1 (No. 2) of the triclinic system. The asymmetric unit consists of one $C_{22}H_{15}N_5$ molecule and half of one benzene molecule. The benzene is located on a crystallographic inversion center. All non-hydrogen atoms were refined with anisotropic displacement parameters. Hydrogen atoms bonded to carbon were located in difference Fourier maps before being placed in geometrically idealized positions and included as isotropically refined riding atoms with d(C–H) = 0.95 Å for aromatic hydrogen atoms and d(C–H) = 0.98 Å for methyl hydrogens. The methyl hydrogens were allowed to rotate as a rigid group to the orientation of maximum observed electron density. The largest residual electron density peak in the final difference map is 0.46 e/Å^3, located 1.00 Å from C25.

Fluorescence spectroscopy.

An Edinburgh FS5 fluorescence spectrometer equipped with a 150 W Continuous Wave Xenon Lamp source for excitation was used to acquire steady-state emission spectra. Emission measurements on solid samples were collected on powders of the desired materials placed inside a 0.5 mm quartz sample holder using the front-facing module. Fluorescence lifetimes were measured using a Mini-τ lifetime spectrometer from Edinburgh Instruments equipped with a 365-nm picosecond-pulsed-light-emitting diode (EPLED 365).

Table 4.1. X-ray structure refinement data for $C_{22}H_{15}N_5 \cdot (C_6H_6)_{0.5}$.[a]

formula	$C_{25}H_{18}N_5$
FW	388.44
T, K	100(2)
crystal system	triclinic
space group	*P*-1
Z	2
a, Å	7.8843(3)
b, Å	9.0131(3)
c, Å	15.2276(5)
α, °	72.9600(10)
β, °	76.2080(10)
γ, °	81.434(2)
V, Å^3	1001.12(6)
d_{calc}, g/cm^3	1.289
μ, mm^{-1}	0.079
F(000)	406.0
crystal size, mm^3	0.4 × 0.26 × 0.18
2-theta range	4.744 to 60.27
index ranges	$-11 \le h \le 11$ $-12 \le k \le 12$ $-21 \le l \le 21$
refl. collected	74218
data/restraints/ parameters	5887/0/292
GOF on F^2	1.027
R_1/wR_2, $[I>=2\sigma(I)]^b$	0.0416/0.1113

[a] Mo-Kα (λ = 0.71073Å) radiation

[b] $R_1 = \Sigma||F_o| - |F_c||/ \Sigma |F_o|$, $wR_2 = \{\Sigma [w(F_o^2 - F_c^2)^2]/ \Sigma [w(F_o^2)^2]\}^{1/2}$

Fitting of fluorescence decays

The fluorescence decays for **1≡(34%)**, NEM-C_{60}[**1≡(34%)**], and TCNQ[**1≡(50%)**] were fit with the triexponential function:

$$I(t) = \int_{\infty}^{t} IRF(t') \sum_{i=1}^{n} B_i e^{\left[-\frac{t-t'}{\tau_i}\right]} dt' \quad \text{(Eq. S1)}$$

where τ and B are lifetime and amplitude, respectively.

The amplitude-weighted average fluorescence lifetimes were calculated based on the following equation:

$$\langle \tau_{av} \rangle = \frac{B_1\tau_1 + B_2\tau_2 + B_3\tau_3}{B_1 + B_2 + B_3} \quad \text{(Eq. S2)}$$

Physical Measurements.

NMR spectra were obtained on Bruker Avance III-HD 300 and Bruker Avance III 400 MHz NMR spectrometers. ^{13}C and ^{1}H NMR spectra were referenced to natural abundance ^{13}C peaks and residual ^{1}H peaks of deuterated solvents, respectively. FTIR spectra were collected on a Perkin-Elmer Spectrum 100. Powder X-ray diffraction patterns were recorded using a Rigaku Miniflex II diffractometer with an accelerating voltage and current of 30 kV and 15 mA, respectively. Thermogravimetric analysis was performed on an SDT Q600 Thermogravimetric Analyzer using an alumina boat as the sample holder. Diffuse reflectance spectra were collected on a PerkinElmer Lambda 45 UV-vis spectrometer referenced to Spectralon®. The BET specific surface area was determined by measuring N_2 adsorption at 75.6 K using a Micromeritics ASAP 2020. Prior to gas sorption measurement, the NEM-C_{60}[**1≡(34%)**] sample was solvent exchanged with benzene for three days, tetrahydrofuran for one day, then heated in vacuum (1.0×10^{-7} Torr) with a heating rate of 1 °C/min up to 65 °C, held for twelve hours, subsequently heated at 75 °C

at 10 °C/min, and held at this temperature for twelve hours. Prior to gas sorption measurement of **1≡(34%)** and TCNQ[**1≡(50%)**], the samples were solvent exchanged with benzene for one day followed by THF for one day, then heated in vacuum (1.0×10^{-7} Torr) with a heating rate of 1 °C/min up to 60 °C, held for three hours, and subsequently heated at 80 °C at 10 °C/min, and held at this temperature for nine hours. Wide-Angle X-ray Scattering (WAXS) experiments were conducted using a SAXSLab Ganesha at the South Carolina SAXS Collaborative (SCSC). A Xenocs GeniX 3D microfocus source was used with a copper target to produce a monochromatic beam with a 0.154 nm wavelength. The instrument was calibrated just before measurements, using the National Institute of Standards and Technology reference material, 640c silicon powder with the peak position at $2\theta = 28.44°$, where 2θ is the total scattering angle. A Pilatus 300k detector (Dectris) was used to collect the two-dimensional (2D) scattering pattern with nominal pixel dimensions of 172×172 μm^2. The SAXS data were acquired with an X-ray flux of ~4.1 M photon per s incident upon the sample and a detector-to-sample distance of 1040 mm. The transmission SAXS data were measured to observe the purely in-plane morphology. The 2D images were azimuthally integrated to yield the scattering vector and intensity. Peak positions were fitted using custom MATLAB software.

Cyclic voltammetry (CV) measurements were carried out in anhydrous *N,N*-dimethylformamide (DMF) or anhydrous acetonitrile (ACN) solution using a WaveDriver 20 Bipotentiostat combined with the Aftermath software. For measurements of TCNQ, C_{60}, and NEM-C_{60}, all solutions contained 0.1 M tetrabutylammonium hexafluorophosphate and 0.5 mM analyte, and measurements were performed in a glass solution reservoir equipped with saturated calomel electrode (SCE) reference, platinum wire counter, and

glassy carbon or gold working electrodes. In order to perform CV measurements on TCNQ[**1≡(50%)**] and NEM-C_{60}[**1≡(34%)**], modification of the electrochemical setup was necessary. The working electrode was modified with a COF slurry prepared by grinding TCNQ[**1≡(50%)**] or NEM-C_{60}[**1≡(34%)**] (40 wt. %) and carbon black (60 wt. %) with 0.1 mL of Nafion. The slurry was then pipetted onto the tip of the electrode and dried overnight under high vacuum before use.

Cyclic voltammetry of TCNQ itself (1.0×10^{-4} M) in a 0.1 M solution of tetrabutylammonium hexafluorophosphate in acetonitrile afforded one reversible reduction at E_p = –0.5 V and one reversible oxidation at 0.1 V (Figure 4.22). Comparison of the acquired CV data for TCNQ[**1≡(34%)**] to TCNQ itself, shows that potentials of TCNQ[**1≡(34%)**] are less negative at E_p = –0.3 V and 0.2 V vs. SCE (Scheme 4.1). In DMF, C_{60} exhibits four reversible reduction waves at E_p = –0.3 V, –0.7 V, –1.4 V, and –1.9 V vs. SCE (Figure 4.21). In comparison with parent C_{60}, NEM-C_{60} exhibits two quasi-reversible reductions in DMF at E_p = –0.9 V and –1.8 V vs. SCE (Figure 4.23). The redox potentials of NEM-C_{60} and NEM-C_{60}[**1≡(34%)**] (–1.2 V and –2.1 V vs. SCE) are also similar (Figure 4.24), with a slight shift in potential, highlighting the inclusion of NEM-C_{60} and reinforcement of the redox active nature within the COF. As a control experiment, CVs of the COF itself and carbon black were measured in which no redox activity was found.

A two-point method was employed to measure conductance σ (S/cm) of pressed pellets according to following equation:

$$\sigma = Il/VA,$$

where I - current, l - thickness of the pellets, V - voltage, and A - surface area of the prepared pellets.

The electrical conductance in the prepared materials follows Ohm's law and was measured by fitting a linear current (I)-voltage (V) curve obtained by using a source meter (Keithley Instruments GmbH, Germering, Germany, model 263) and an electrometer (Keithley Instruments GmbH, Germering, Germany, model 617). All samples were prepared consistently by using the same amount of materials (30 mg of material, dried overnight on vacuum) and the same pressing technique (material was pressed under 4000 psi at room temperature for five minutes with an International Crystal Laboratory 20 Ton E-Z Hydraulic Laboratory PressTM), which relieves the issue of deviations from the ideal configuration. A home-built setup was used to perform two-contact probe conductivity measurements on the pressed pellets: the pellet was placed between two brass plates with attached contacts. A layer of double-sided carbon tape (Electron Microscopy Sciences) was added between the pellet and plates to improve contact. To measure the conductivity of spiropyran embedded materials before and after irradiation with UV light, each batch was divided into two portions. The first portion of the sample was used for electrical measurements after irradiation with visible light (M590L3, Thorlabs, λ_{ex} = 590 nm, distance = 6 cm, t = 30 min), while the second portion of the sample was measured after irradiation with UV light (M365L2, Thorlabs, λ_{ex} = 365 nm, distance = 6 cm, t = 30 min). The irradiation was performed to ensure the complete photoisomerization of guest molecules prior to beginning measurements. The conductivity measurements for the UV-irradiated sample were performed in the dark under constant UV irradiation to minimize conversion of merocyanine to spiropyran.

Solid-state NMR spectra (^{13}C CP-MAS) were collected on a Bruker Avance III-HD 500 MHz spectrometer fitted with a 1.9 mm MAS probe. $^{13}C\{^{1}H\}$ CP-MAS NMR spectra (125.79 MHz) were collected at ambient temperature with a sample rotation rate of 20 kHz. For cross polarization, 2.0 ms contact time with linear ramping on the ^{1}H channel and 62.5 kHz field on the ^{13}C channel were used. ^{1}H dipolar decoupling was performed with SPINAL64 modulation and 147 kHz field strength. Free induction decays (2048-5000 transients) were collected with a 27 ms acquisition time over a 400 ppm spectra width with a relaxation delay of 2.0 s. All XPS experiments were carried out with a Kratos AXIS Ultra DLD system, which was equipped with a monochromatic AlK_{α} source, a hemispherical analyzer, a charge neutralizer for studying insulating samples, and a load lock chamber for rapid introduction of samples into the vacuum chamber. This system has been described in more detail elsewhere. Dwell times were 1000 ms and 600 ms for the valence band and C(1s) regions, respectively, and the step size for both regions was 0.06 eV. For quantitative XPS analysis, analysis of the spectra were performed using IgorPro software and Origin software, where an Adjacent-Averaging smoothing method was used with the points of window set to five for all spectra.

Computational Details.

Theoretical Analysis. As a starting point for simulations, we consider the A···A stacking **1≡(0%)** model of Jiang[] and co-workers based on the semiempirical density-functional tight-binding (DFTB+) calculations. This model is in good agreement with the experimental data. To optimize the geometry and to study charge transfer and optical transitions in the COF with embedded TCNQ molecules, we have applied *ab initio* electronic structure methods to several truncated COF structures ranging from 370 to 46

atoms shown in Figure 4.39. According to the analysis of the frontier orbitals and UV-vis spectra for these structures, COF-fragment (model **A**) gives a reasonable representation of the structure. The electronic excitations were calculated using the time-dependent density functional theory (TDDFT) for several density functionals, i.e. BLYP, B3LYP, B3LYP-D3, and LRC-ωPBEh, paired with 6-31G, 6-31G**, and 6-31+G** basis sets. The UV-vis spectra computed at the B3LYP-D3/6-31+G** level using the random phase approximation (RPA) gave the best agreement with experimental diffuse reflectance spectra (Figure 4.3). The electronic structure calculations were performed using QChem-5.1 electronic structure package and IQmol visualization software.

We have considered two possible alignments of the donor (COF)-acceptor(TCNQ) fragments referred to as models **A** and **B**. In model **A**, the TCNQ molecules are attached to every COF layer while in model B, they are attached to every other layer as shown in Figure 4.40. Stacks of up to five COF-fragments have been considered. The chosen interlayer distance was 3.50 Å according to Jiang and co-workers; the atoms of the COF skeleton were frozen while the TCNQ moieties were optimized at the B3LYP/631G level. In comparison with model **B**, the alignment in model **A** resulted in a more planar TCNQ geometry and shorter interlayer distances. For example, the calculated dihedral angles for model **A** and model **B** are ~20° and ~50°, respectively, using atoms C_1-C_4 (Scheme 4.4). Interaction between the TCNQ molecules strongly depends on the interlayer distance.

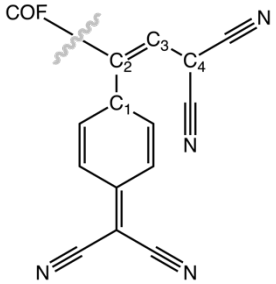

Scheme 4.4. Atomic definition for the TCNQ-[**COF**] fragment.

For models **A** and **B**, the interlayer distance between –CN groups is 3.12 and 3.63 Å, respectively, suggesting that model **A** describes more efficient electron transport within the TCNQ stack. The electronic coupling constants, V_c, obtained from the direct coupling method at the HF/6-31G* level of theory, implemented in QChem support this expectation: the value of V_c for model **A** is 170.58 meV is 200 times larger than that for **B** (0.78 meV). Therefore, given the change in experimental conductivity by six orders of magnitude for TCNQ[**1≡(100%)**] compared to the pristine COF, we hypothesize that the TCNQ molecules in each layer could form a column inside the COF described by model **A**. The geometry of the middle TCNQ molecule aligned in a column within the COF, referred to below as the TCNQ[**COF**]-fragment, is used to estimate the electron transfer rates and optical transitions.

Electron transfer rates. Following analysis reported by Shustova and co-workers, the electron transfer rates are estimated, assuming a charge hopping mechanism, according to the Marcus theory.

$$k = \frac{2\pi}{\hbar}\frac{|V_c|^2}{\sqrt{4\pi\lambda k_B T}}\exp\left(-\frac{(\lambda + \Delta G°)^2}{4\lambda k_B T}\right) \quad \text{(Eq. S3)}$$

In Eq. (S3) λ is the reorganization energy of a system in response to "instantaneous" relocation of an electron from the donor to the acceptor, ΔG° is the difference in the energies of the initial and final states, V_c is the electronic coupling constant, and T is the temperature. Eq. (S3) is applicable in the weak initial/final state coupling regime, $V_c << \lambda$. Within $|i\rangle = |D^-\rangle \times |A\rangle$ the simplest $|f\rangle = |D\rangle \times |A^-\rangle$ picture, the influence of the molecular environment on the donor and acceptor states is neglected; the

initial electronic state is , the final state is and the reorganization energy within the mean-field theory is estimated as,

$$\lambda = E_D^{LUMO} - E_{A^-}^{HOMO} \quad \text{(Eq. S4)}$$

For the identical donor and acceptor molecules, $\Delta G^\circ = 0$. Besides the direct coupling method, the electronic couplings have been estimated using the energy gap method, defined for Hartree-Fock(HF) theory of the electronic structure. While the accuracy of the HF energies is limited by its mean-field character, the couplings are known to be more sensitive to the quality of the basis set, rather than to the electron correlation. To understand the effect of TCNQ stacked along the COF 'wall' on electronic conductivity, we have compared the electronic coupling for TCNQ-, COF- and TCNQ[**COF**]-fragments. Both the direct coupling and the energy gap methods give $|V_c|$~0.20 eV for the TCNQ-fragment and TCNQ[**COF**]-fragments, and $|V_c|$~0.35 eV for the COF-fragment, which is consistent with π-π orbital delocalization between the COF layers (Figure 4.42). For the TCNQ[**COF**]-fragment, the LUMO is localized on the TCNQ moiety, thus TCNQ- and TCNQ[**COF**]-fragments have similar V_c values (Figure 4.42, Table 4.2).

Table 4.2. The Marcus model parameters estimated the direct coupling and energy gap methods.

level of theory	**TCNQ-fragment**	**COF-fragment**	**TCNQ[COF]-fragment**
electronic coupling V_c, eV (direct coupling method)			
HF/631G	-	0.34	0.17
HF/631G*	-	0.36	0.17
electronic coupling V_c, eV (the energy gap method)			
HF/631G	0.20	0.34	0.20
HF/631G*	0.21	0.35	0.21
reorganization energy, eV			
HF/631G	1.25	1.85	1.41
HF/631G*	1.67	1.98	1.84

The reorganization energy of the TCNQ-fragment is ~ 0.16 eV lower than that of the COF-fragment. For the same charge hopping distance, i.e., the interlayer separation (3.50 Å), the ratios of the charge carrier mobilities and diffusion constants are equal to the ratio of the rate constants. Evaluated at T = 298 K, the charge mobility of the TCNQ[**COF**]-fragment is 32 times larger than that of the parent COF-fragment, which is in qualitative agreement with the conductivity measurements showing significant (six orders of magnitude) increase in conductivity upon coordinative integration of TCNQ inside the COF. Thus, our theoretical estimates of the electron transfer rates are consistent with the conductivity enhancement, observed for TCNQ-integrated samples, presumably due to the stacking of TCNQ inside the COF.

Electronic excitations. To assess the effect of the multilayer stacking on the UV-vis spectra, the excitation energies have been computed for the COF- and TCNQ[**COF**]-fragments and for their "dimers." The "dimers" consist of two identical molecules separated by 3.50 Å. As shown in Table 4.3, the lowest excitation energies for a single COF-fragment and its "dimer" differ by a modest 0.11 eV for the three basis sets, while the addition of a TCNQ molecule lowers these energies by 0.51–0.54 eV. The experimental results show a similar trend, i.e., a red shift of excitation energies for TCNQ[**1≡(50%)**] compared to empty COF (Figure 4.3). The band gaps derived from the Tauc analysis of pristine COF, and TCNQ[**1≡(50%)**] samples are found to be 2.32 and 2.04 eV, respectively (Figure 4.38). Moreover, the TCNQ[**COF**]-fragment exhibits an electrostatic charge of –0.20 |e| on TCNQ and a significant dipole moment of 4.13 Debye directed towards TCNQ, while for the empty COF the dipole moment is perpendicular to the COF plane and its magnitude is only 0.52 Debye. Thus, the TCNQ/COF stacks may be considered as the electron acceptor/donor columns within the material, and we hypothesize that the charge separation within the COF basal plane and charge transfer in the vertical direction (between the COF layers) is the possible mechanism of conductivity enhancement in TCNQ[**COF**].

Table 4.3. The lowest optical transition for the COF-fragment, TCNQ[**COF**]-fragment and 2 stacked COF-fragments calculated at different theory levels.

level of theory	**COF-fragment**	**TCNQ[COF]-fragment**	**2 stacked COF-fragments**
B3LYP-D3/6-31G*	3.03 eV	2.49 eV	3.14 eV
B3LYP-D3/6-31G**	3.03 eV	2.49 eV	3.14 eV
B3LYP-D3/6-31+G**	2.95 eV	2.44 eV	3.06 eV

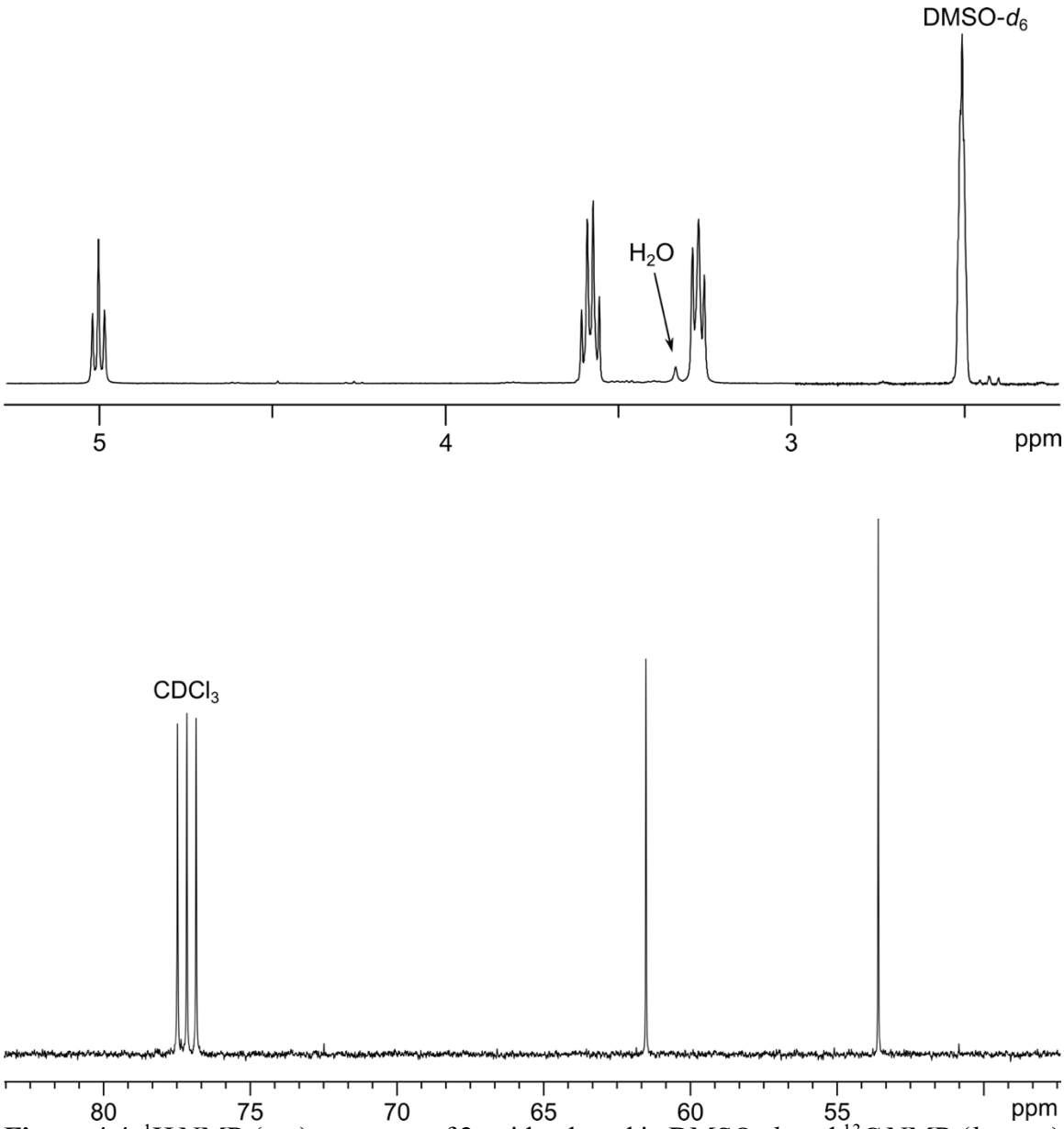

Figure 4.4. ^{1}H NMR (*top*) spectrum of 2-azidoethanol in DMSO-d_6 and ^{13}C NMR (*bottom*) spectrum of 2-azidoethanol in $CDCl_3$.

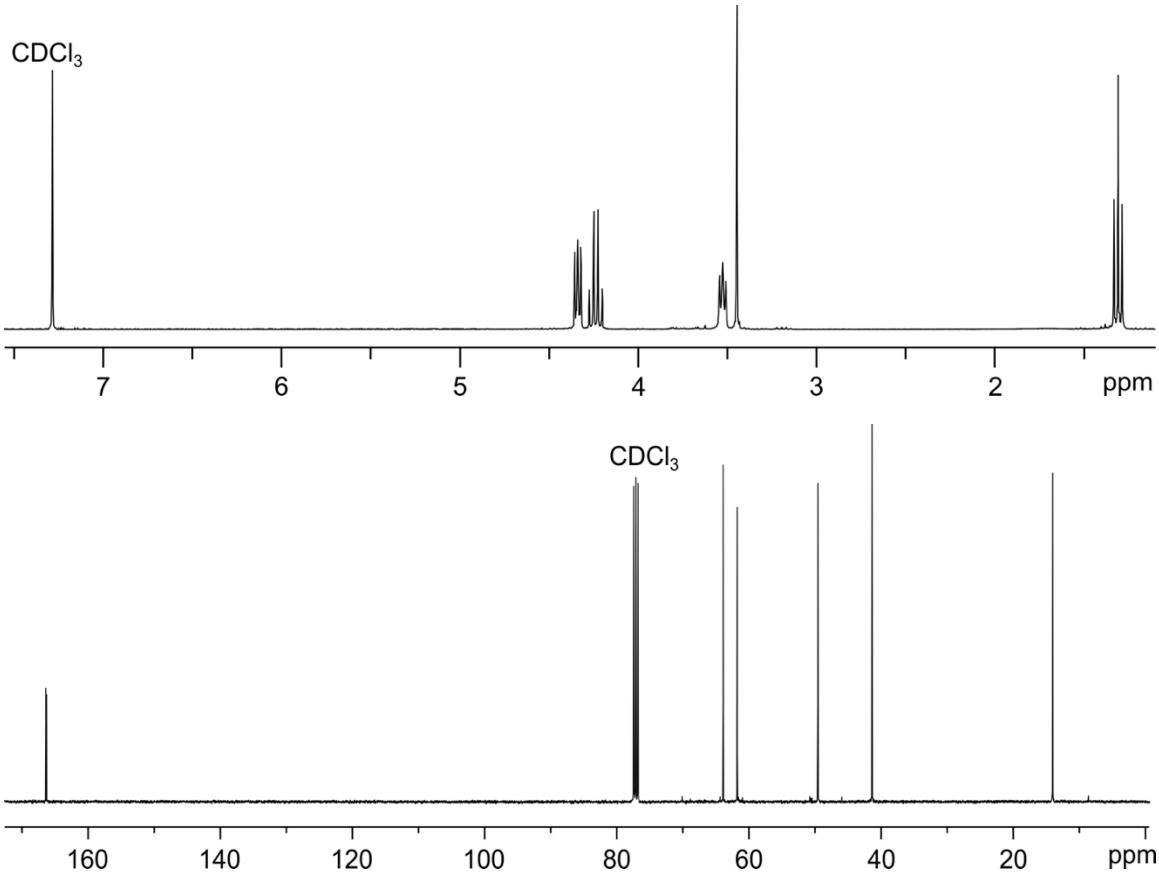

Figure 4.5. ^{1}H NMR (*top*) and ^{13}C NMR (*bottom*) spectra of NEM in $CDCl_3$.

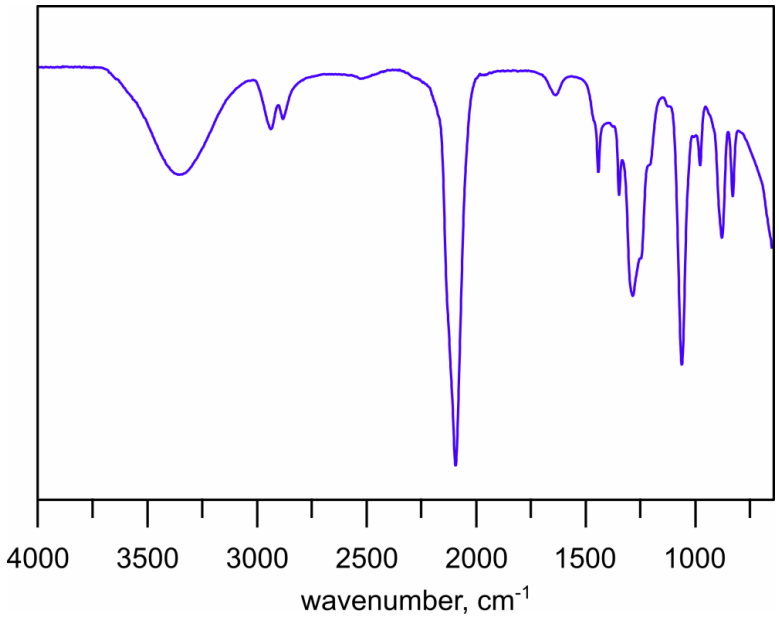

Figure 4.6. FTIR spectrum of 2-azidoethanol.

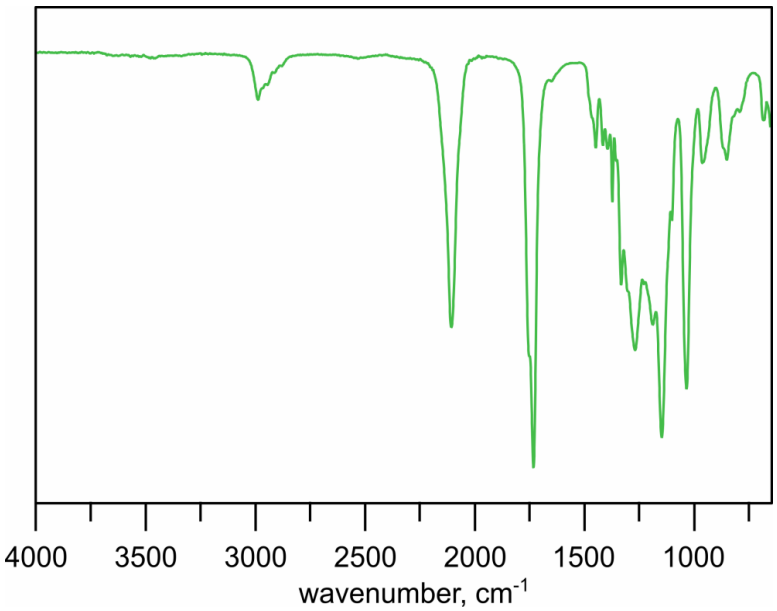

Figure 4.7. FTIR spectrum of NEM.

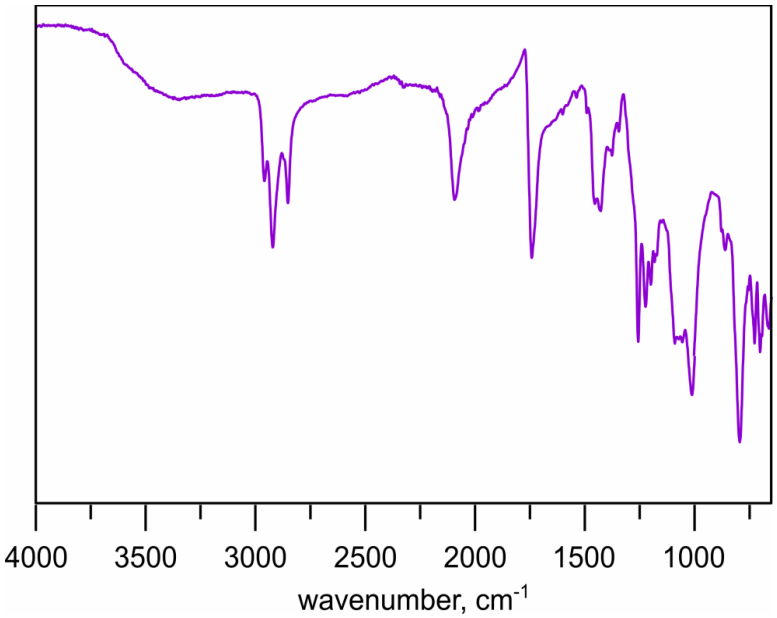

Figure 4.8. FTIR spectrum of NEM-C_{60}.

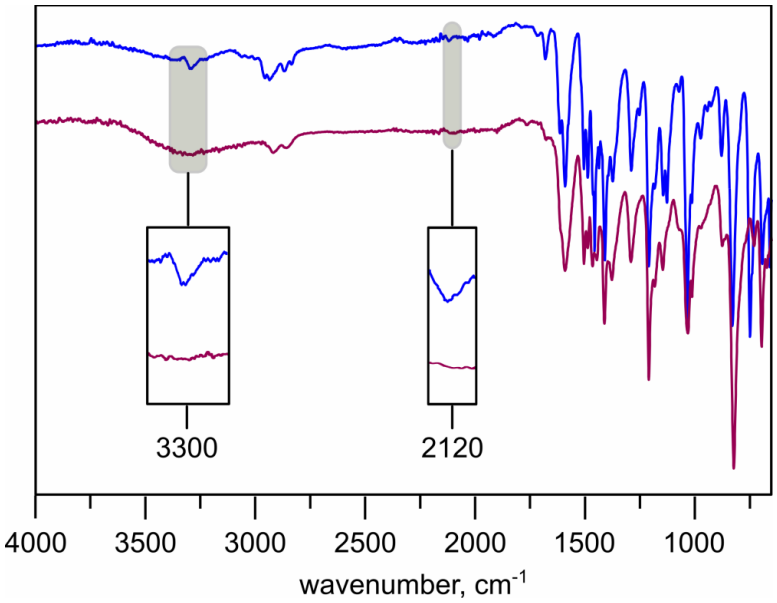

Figure 4.9. FTIR spectra of **1≡(34%)** (blue) and 2-azidoethanol[**1≡(34%)**] (red).

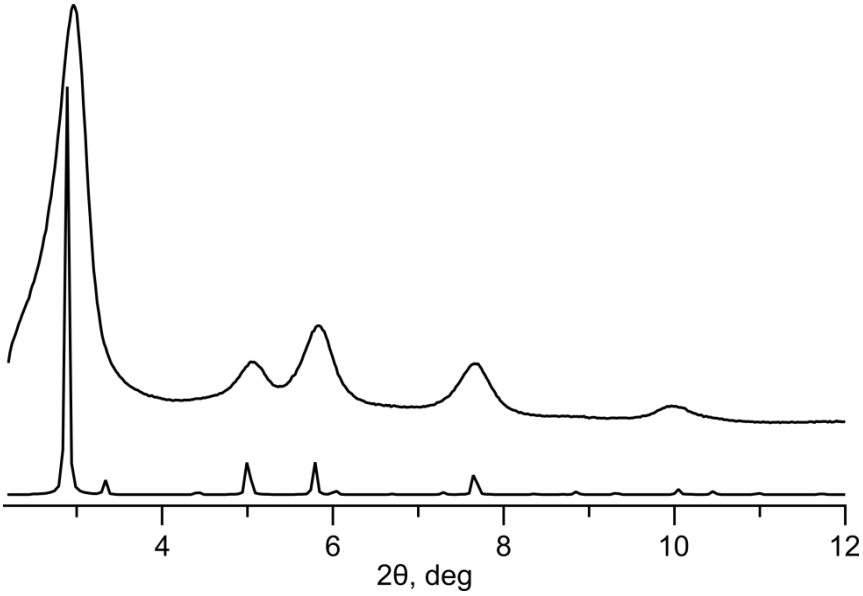

Figure 4.10. PXRD pattern of **1≡(34%)** (*top*) and simulated pattern (*bottom*).

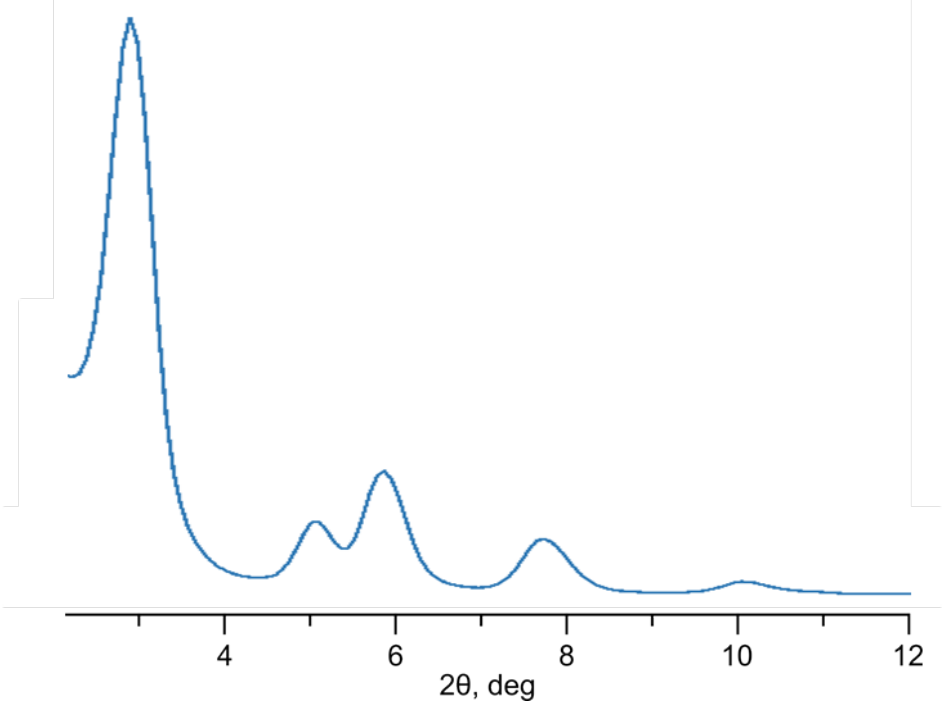

Figure 4.11. WAXS pattern of **1≡(34%)**.

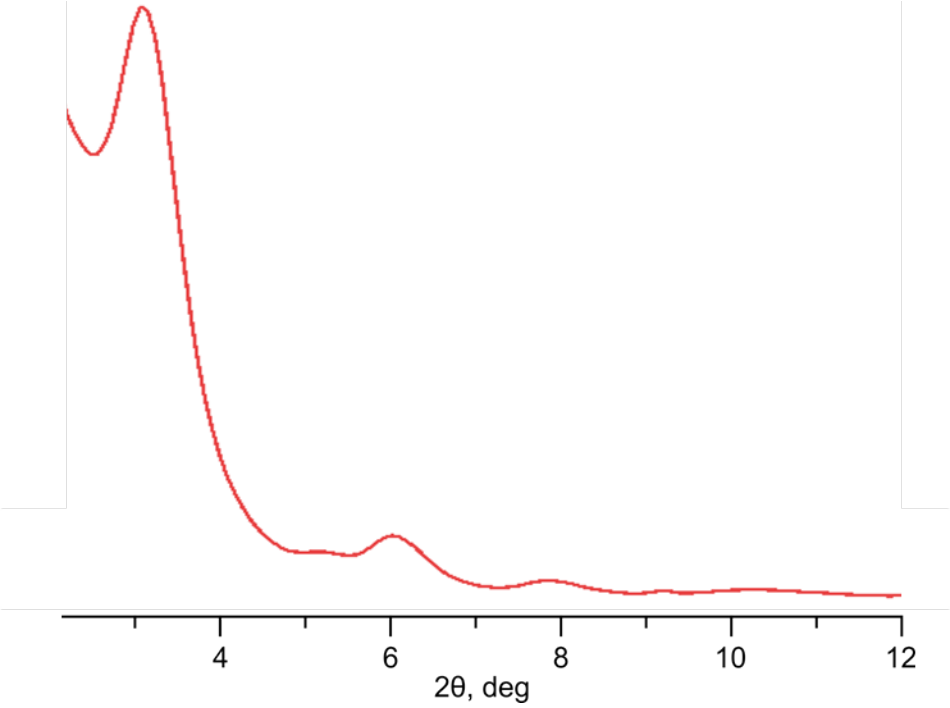

Figure 4.12. WAXS pattern of NEM-C_{60}[**1≡(34%)**].

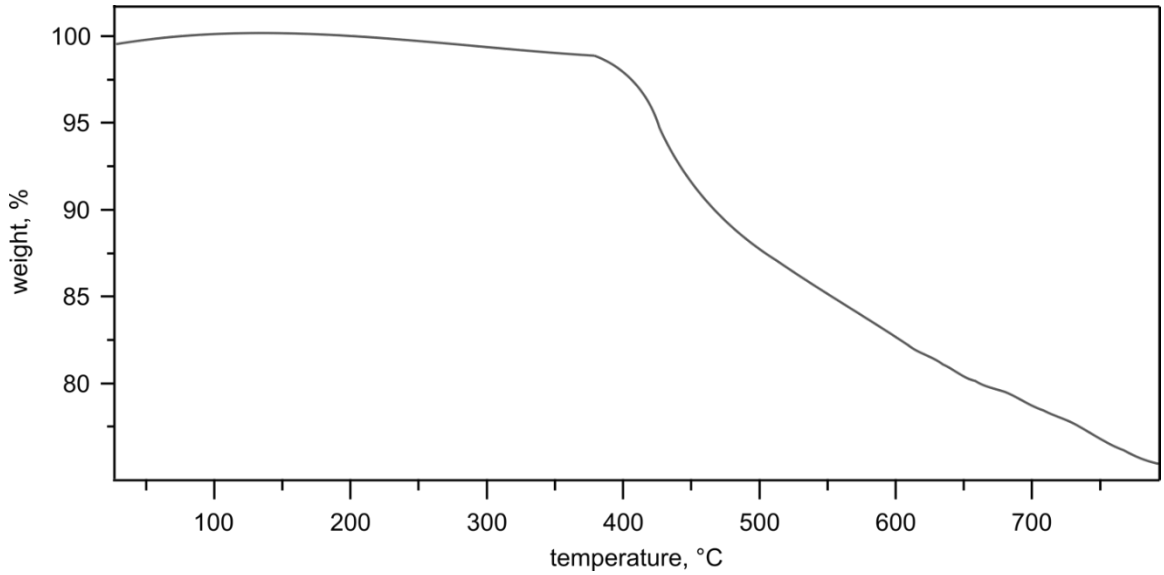

Figure 4.13. Thermogravimetric analysis plot of **1≡(34%)**.

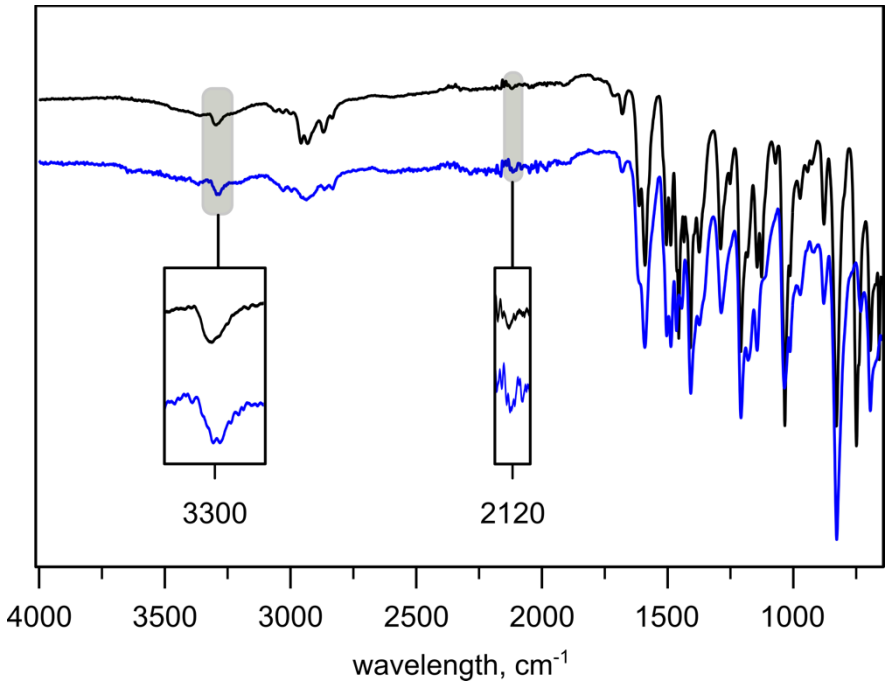

Figure 4.14. FTIR spectra of **1≡(34%)** (black) and a control experiment involving **1≡(34%)** (blue).

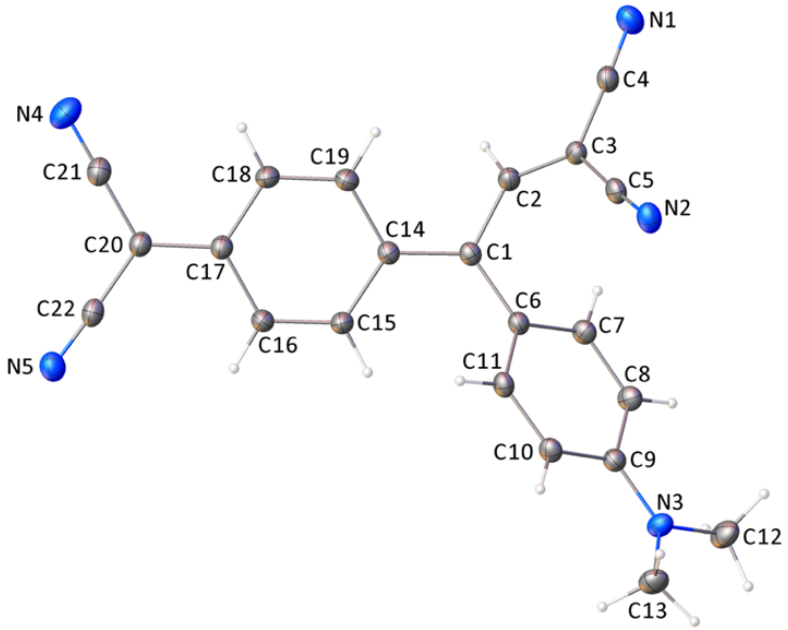

Figure 4.15. X-ray crystal structure of $C_{22}H_{15}N_5$. Thermal displacement ellipsoids are drawn at the 50% probability level. Blue, gray, and white spheres correspond to nitrogen, carbon, and hydrogen atoms, respectively.

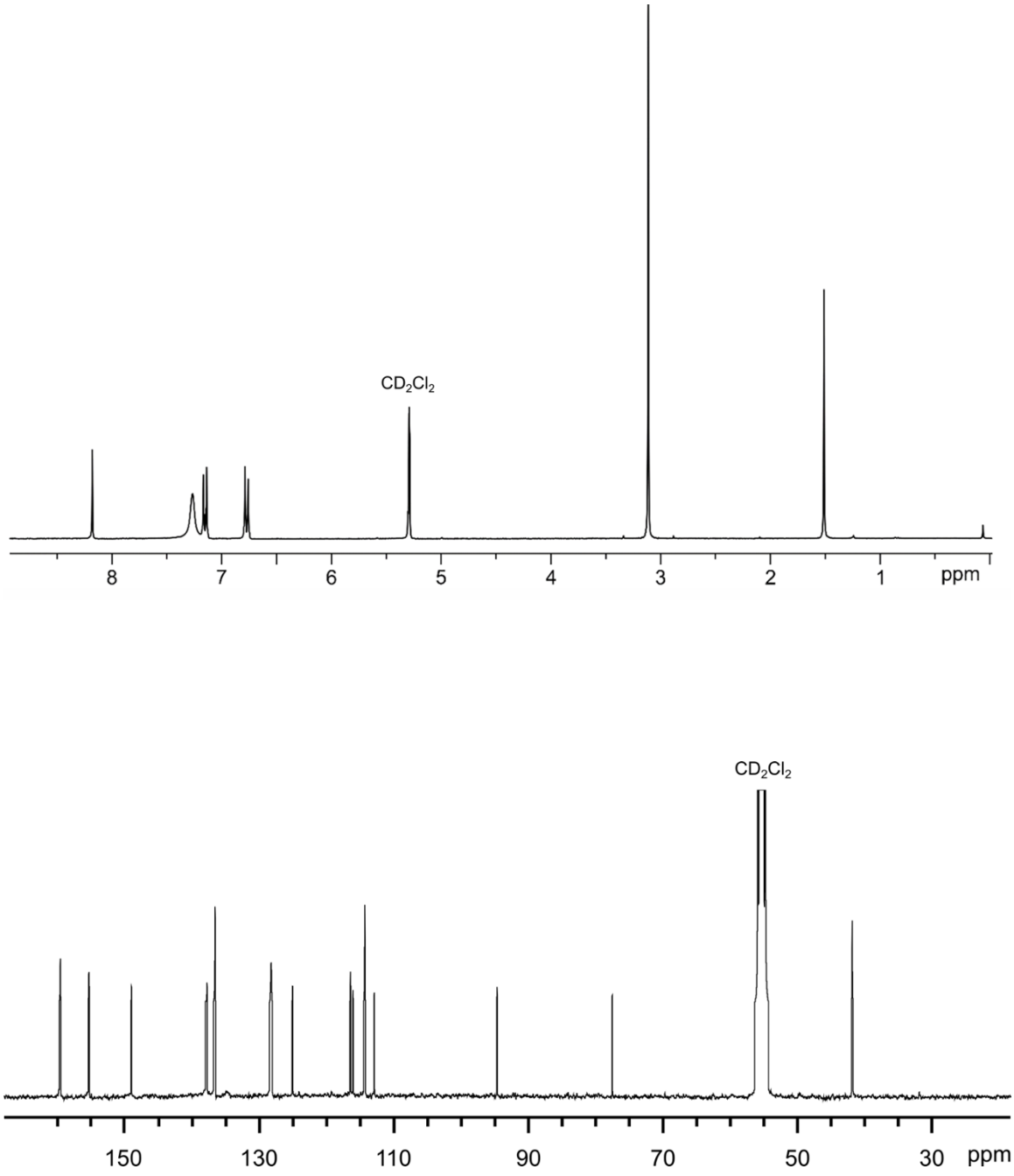

Figure 4.16. ^{1}H NMR (*top*) and ^{13}C NMR (*bottom*) spectra of 2-(4-(4,4-dicyano-2-(4-(dimethylamino)phenyl)butylidene)cyclohexa-2,5-dien-1-ylidene)malononitrile in CD_2Cl_2.

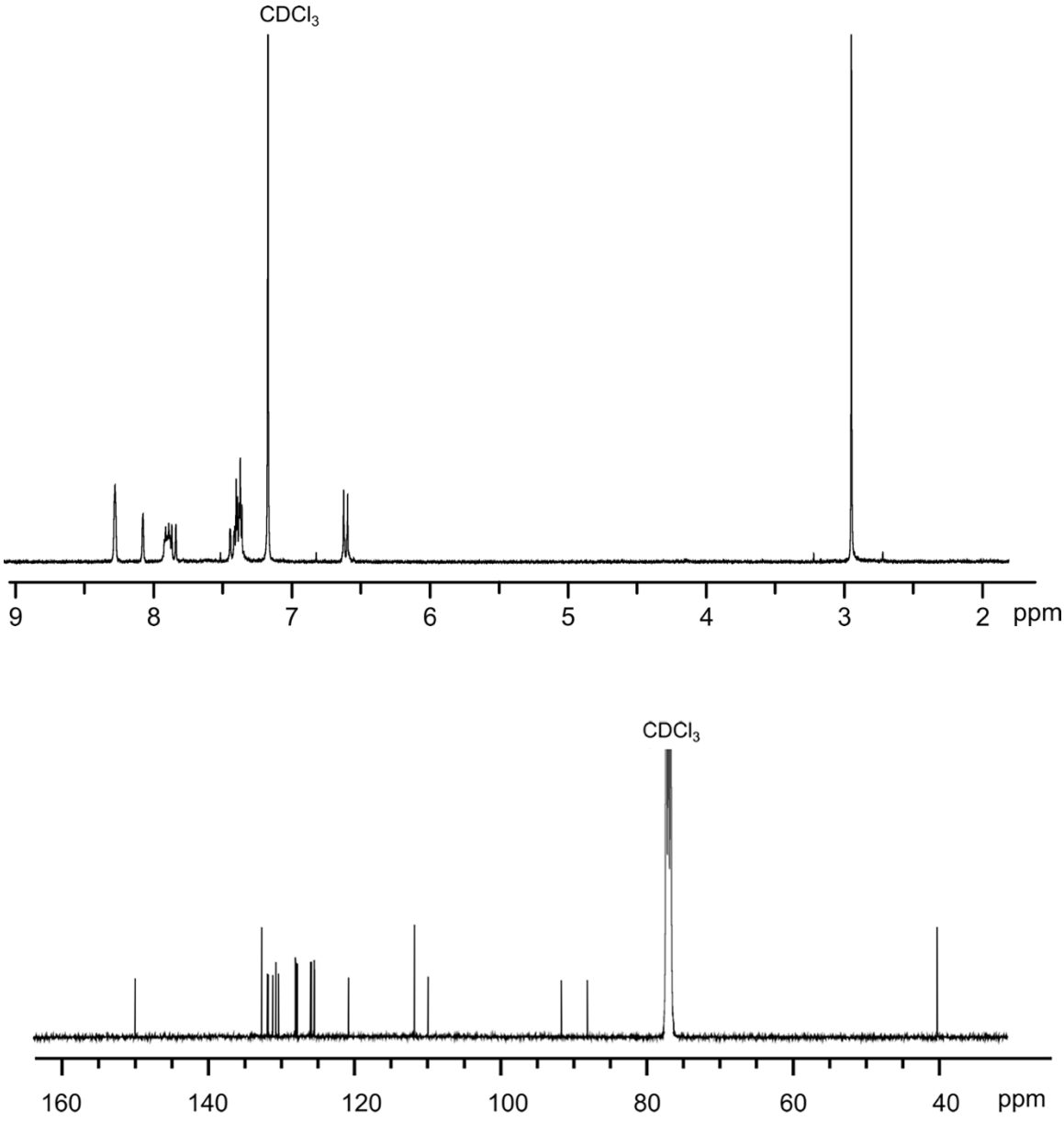

Figure 4.17. ^{1}H NMR (*top*) and ^{13}C NMR (*bottom*) spectra of 4-(anthracen-2-ylethynyl)-*N,N*-dimethylaniline in $CDCl_3$.

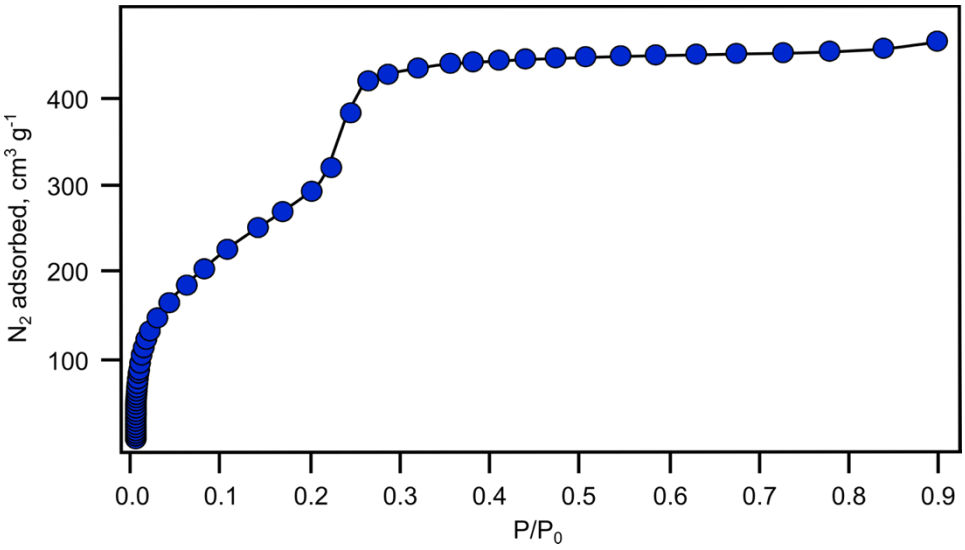

Figure 4.18. N_2 adsorption isotherm of **1≡(34%)**. The surface area was determined to be 1253 m^2/g.

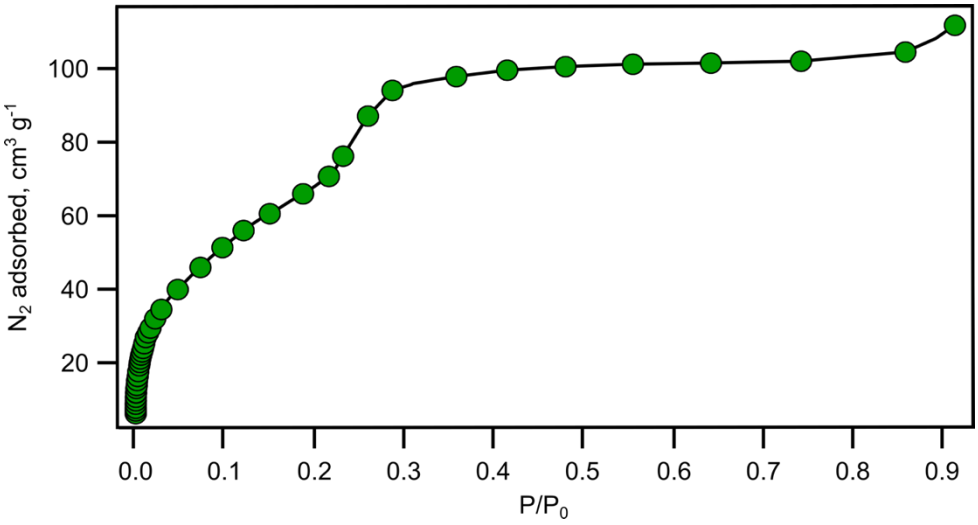

Figure 4.19. N_2 adsorption isotherm of NEM-C_{60}[**1≡(34%)**]. The surface area was determined to be 229 m^2/g.

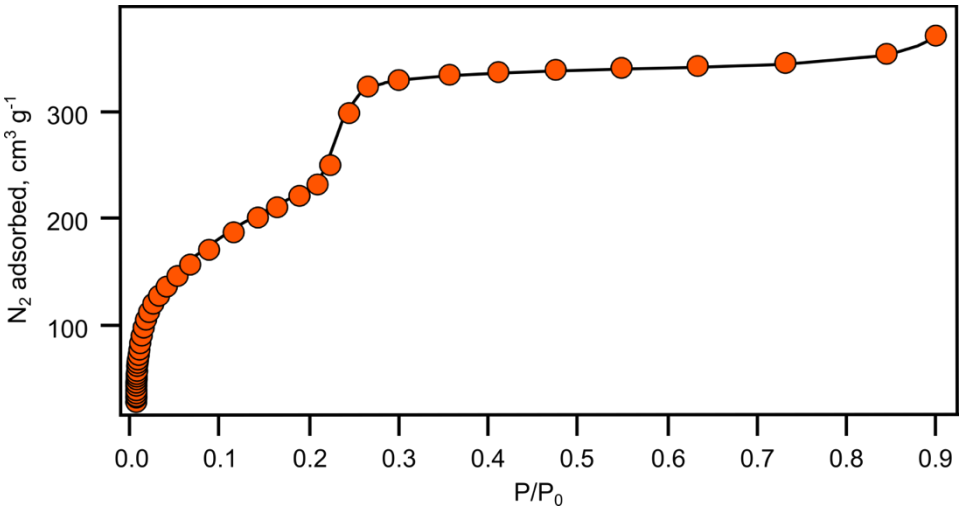

Figure 4.20. N_2 adsorption isotherm of TCNQ[**1≡(50%)**]. The surface area was determined to be 812 m^2/g.

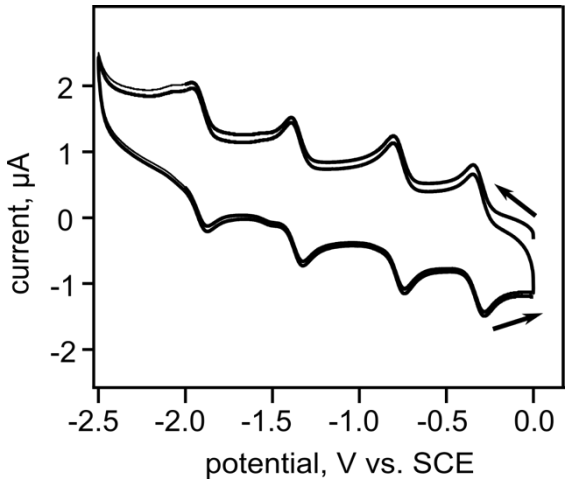

Figure 4.21. Cyclic voltammogram of C_{60} with 0.1 M tetrabutylammonium hexafluorophosphate and 0.5 mM analyte in DMF with a scan rate of 0.1 V. Measurements were performed in a glass solution reservoir equipped with a SCE reference, platinum wire counter, and a glassy carbon working electrode.

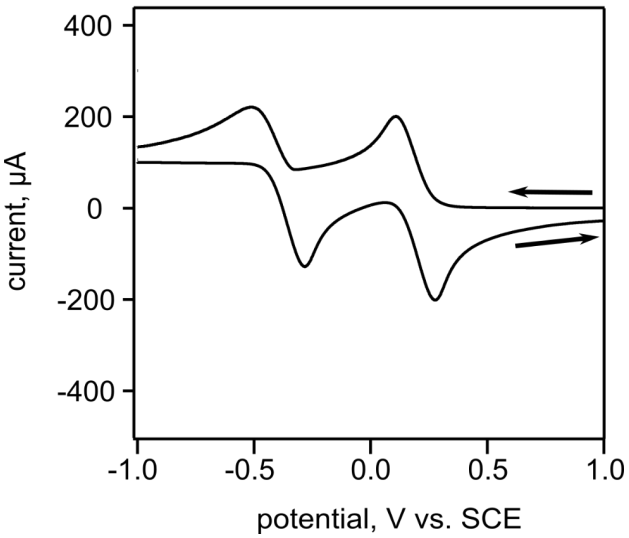

Figure 4.22. Cyclic voltammogram of TCNQ with 0.1 M tetrabutylammonium hexafluorophosphate and 0.5 mM analyte in ACN with a scan rate of 0.1 V. Measurements were performed in a glass solution reservoir equipped with a SCE reference, platinum wire counter, and a glassy carbon working electrode.

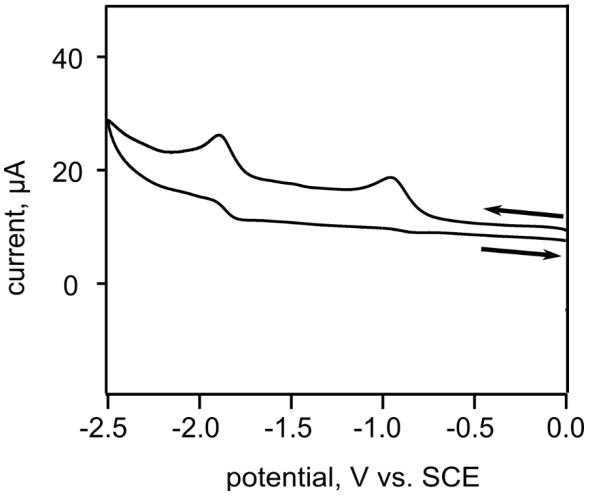

Figure 4.23. Cyclic voltammogram of NEM-C_{60} with 0.1 M tetrabutylammonium hexafluorophosphate and 0.5 mM analyte in DMF with a scan rate of 0.1 V. Measurements were performed in a glass solution reservoir equipped with a SCE reference, platinum wire counter, and a gold working electrode.

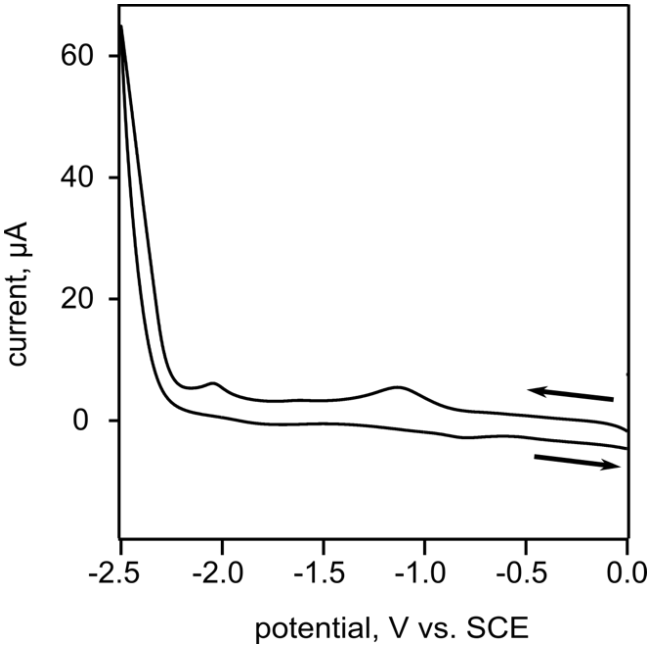

Figure 4.24. Cyclic voltammogram of NEM-C_{60} [**1≡(34%)**] with 0.1 M tetrabutylammonium hexafluorophosphate in DMF with a scan rate of 0.1 V. Measurements were performed in a glass solution reservoir equipped with a SCE reference, platinum wire counter, and a modified gold working electrode. The gold working electrode was modified with a COF slurry prepared by grinding NEM-C_{60}[**1≡(34%)**] (40 wt. %) and carbon black (60 wt. %) with 0.1 mL of Nafion.

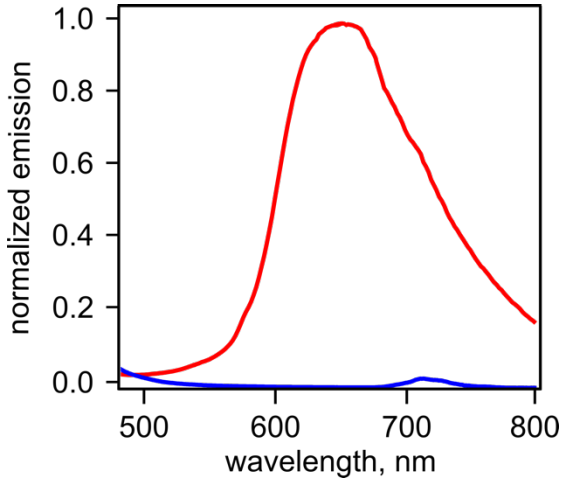

Figure 4.25. Normalized emission spectra of 2-bromoanthracene (–) and anthracene[**1≡(50%)**] (–, λ_{ex}= 365 nm) in the solid state.

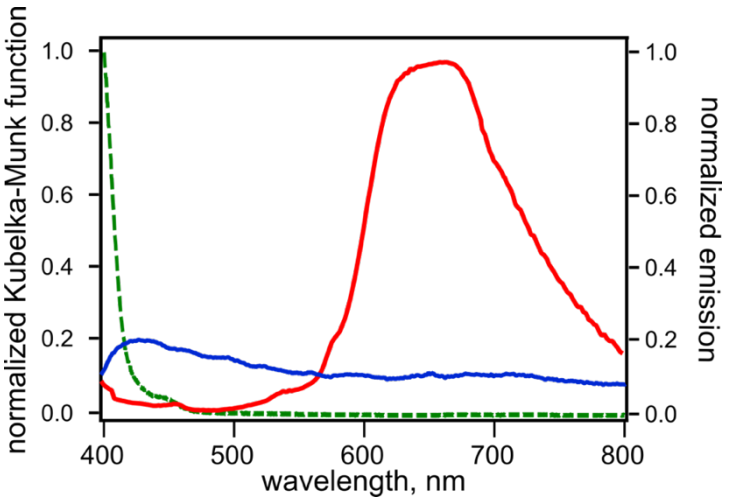

Figure 4.26. Normalized diffuse reflectance (---) and emission (–) spectra of 6-bromo-3-cyano-4-methyl-coumarin, and normalized emission spectrum (–) of 4-methyl-2-oxo-2*H*-chromene-3-carbonitrile[**1≡(50%)**] (λ_{ex}= 365 nm) in the solid state.

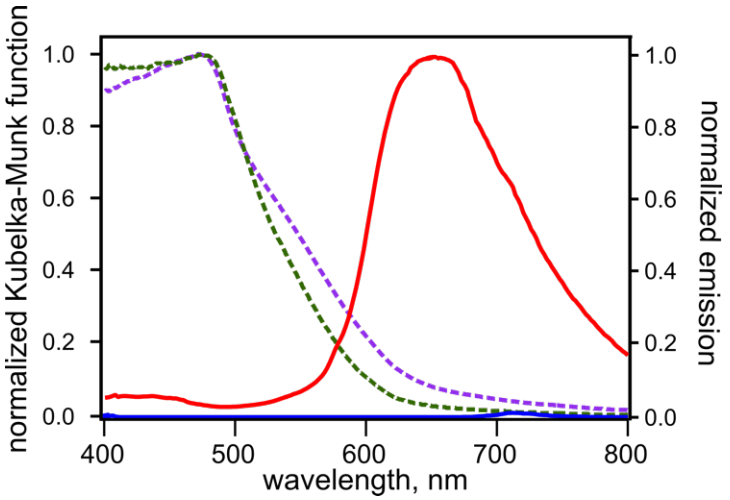

Figure 4.27. Normalized diffuse reflectance (---) and emission (–) spectra of 2-bromoanthracene@TCNQ [**1≡(50%)**], and normalized diffuse reflectance (---) and emission spectra (–) of anthracene[**1≡(50%)**] (λ_{ex}= 365 nm) in the solid state.

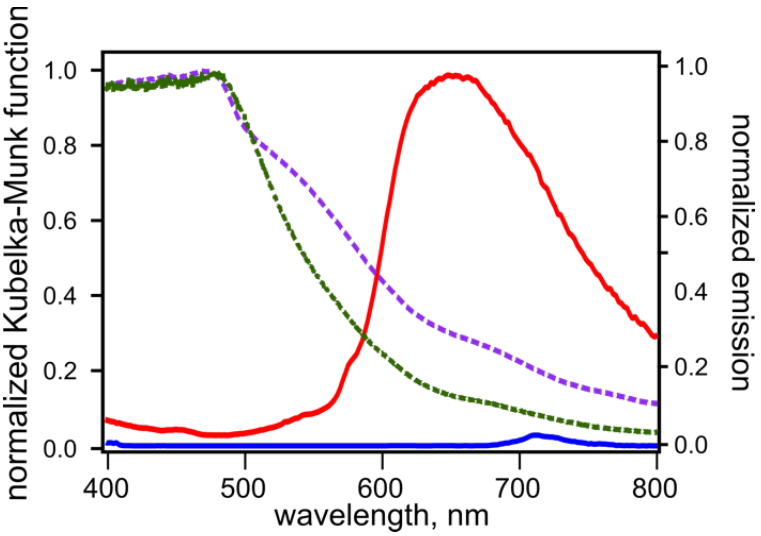

Figure 4.28. Normalized diffuse reflectance (---) and emission (–) spectra of 6-methyl-3-cyano-4-methylcoumarin@TCNQ [**1≡(50%)**] and normalized diffuse reflectance (---) and emission spectra (–) of 4-methyl-2-oxo-2*H*-chromene-3-carbonitrile [**1≡(50%)**] (λ_{ex}= 365 nm) in the solid state.

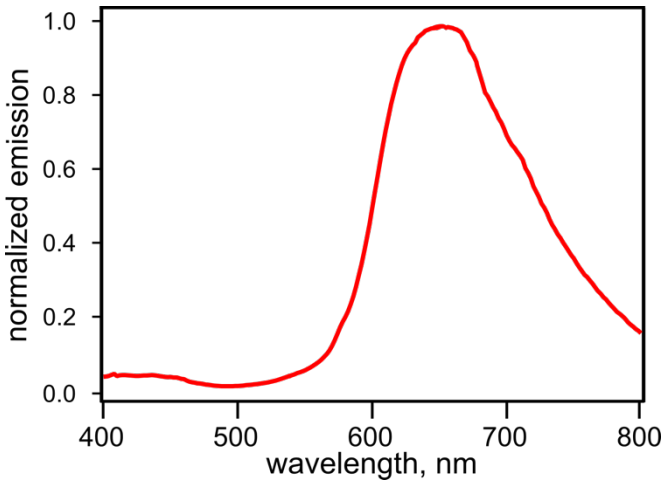

Figure 4.29. Normalized emission spectrum of anthracene[**1≡(50%)**] (λ_{ex}= 365 nm) in the solid state.

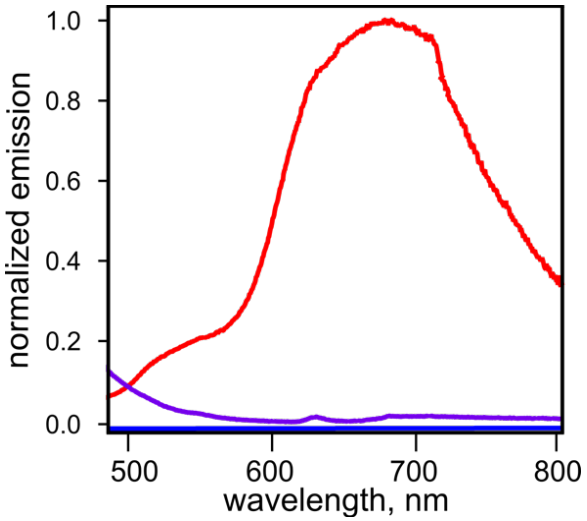

Figure 4.30. Normalized emission spectra of [**1≡(50%)**] (–), TCNQ[**1≡(50%)**] (–), and NEM -C_{60}[**1≡(34%)**](–) (λ_{ex}= 365 nm) in the solid state.

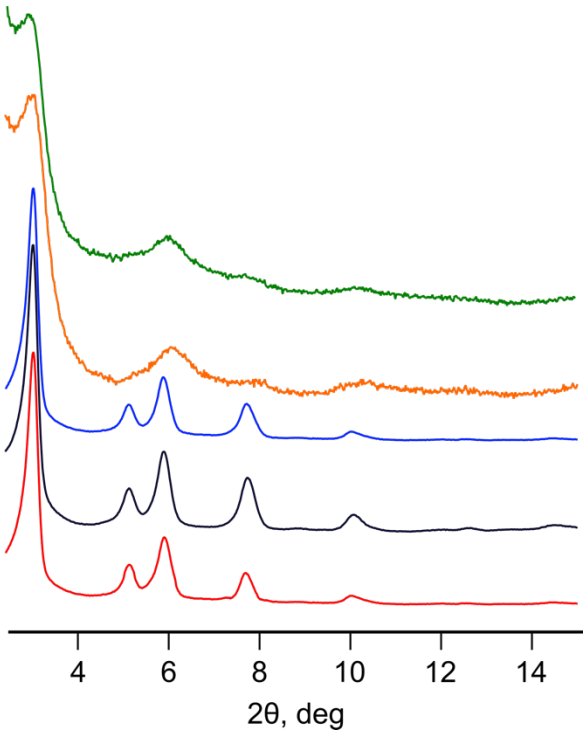

Figure 4.31. PXRD patterns of: 4-methyl-2-oxo-2*H*-chromene-3-carbonitrile[**1≡(50%)**] (green), anthracene[**1≡(50%)**] (orange), 2-bromoanthracene @TCNQ[**1≡(50%)**] (blue), 6-methyl-3-cyano-4-methylcoumarin@TCNQ[**1≡(50%)**] (black), and TCNQ[**1≡(50%)**] (red).

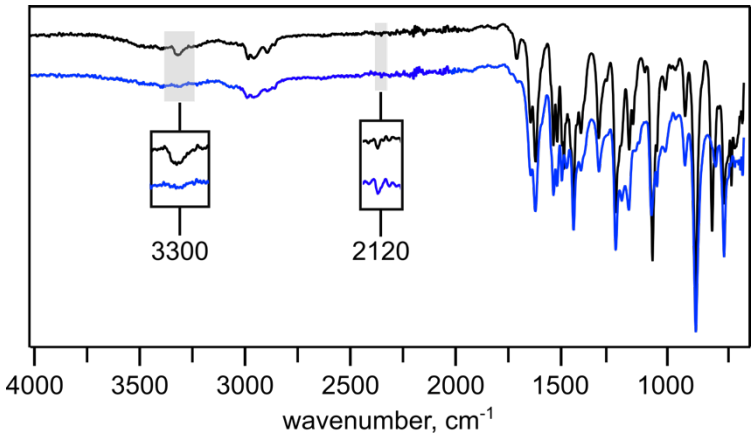

Figure 4.32. FTIR spectra of [**1≡(50%)**] (black) and anthracene[**1≡(50%)**] (blue).

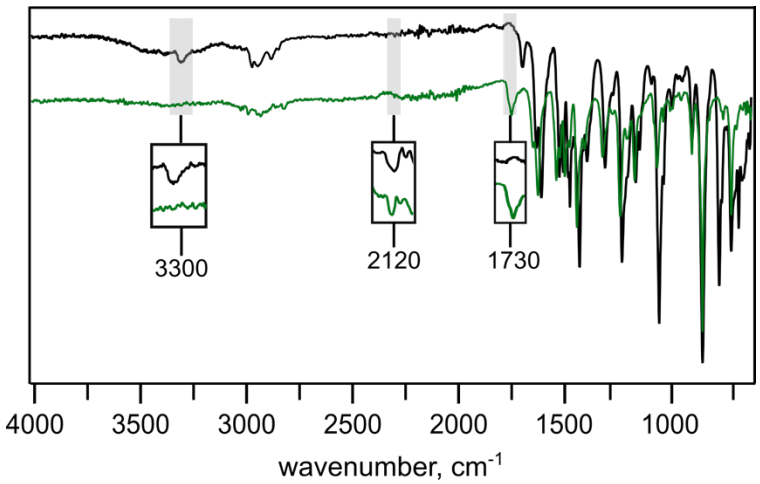

Figure 4.33. FTIR spectra of [**1≡(50%)**] (black) and 4-methyl-2-oxo-2*H*-chromene-3-carbonitrile [**1≡(50%)**] (green).

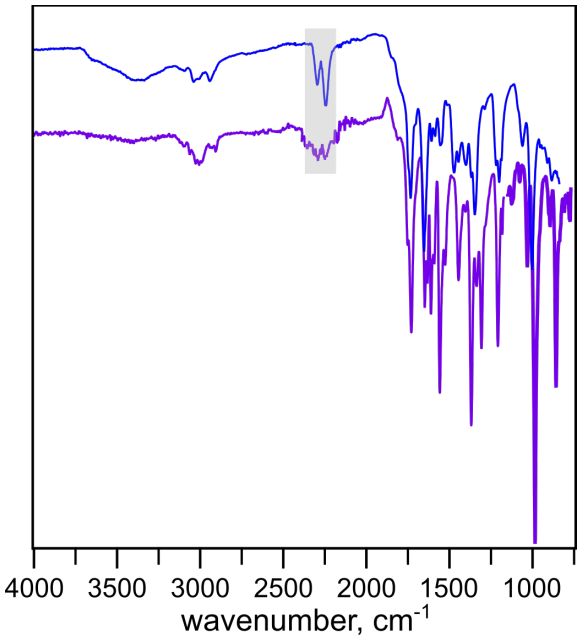

Figure 4.34. FTIR spectra of TCNQ[**1≡(50%)**] (blue) and 2-bromoanthracene@TCNQ[**1≡(50%)**] (purple).

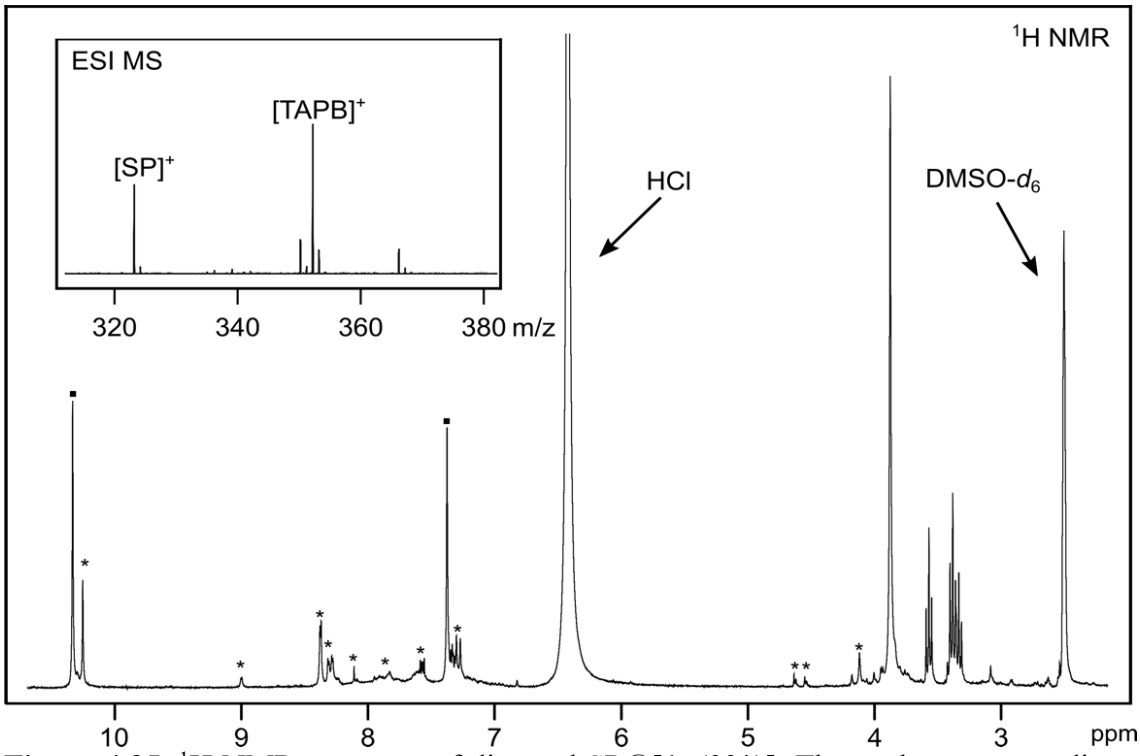

Figure 4.35. ^{1}H NMR spectrum of digested SP@[**1≡(0%)**]. The peaks corresponding to DMTA (▪) and SP (*) are labeled. The inset shows the positive ion electrospray ionization mass-spectrum of digested SP@[**1≡(0%)**].

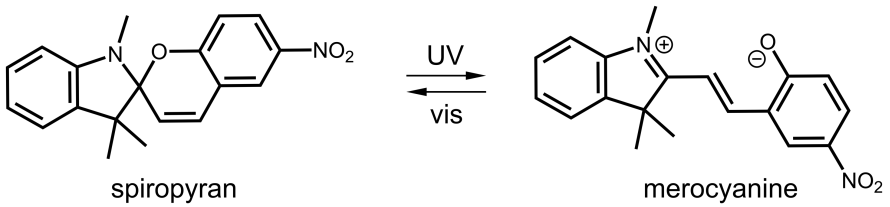

Figure 4.36. Photoisomerization of the spiropyran derivatives.

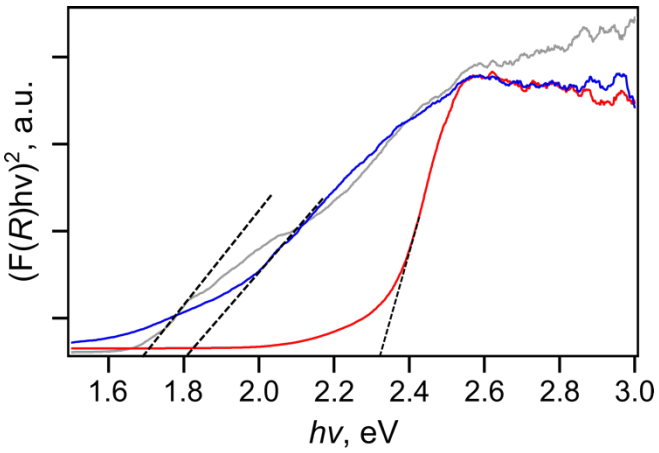

Figure 4.37. Tauc plots for C_{60} (gray), **1≡(34%)** (red), and NEM-C_{60}[**1≡(34%)**] (blue).

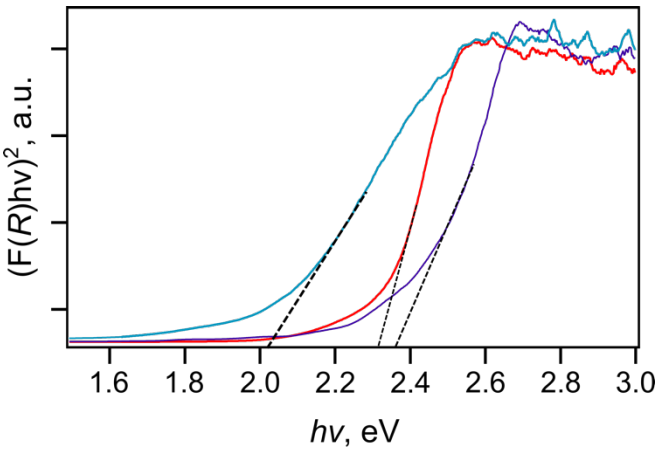

Figure 4.38. Tauc plots for TCNQ (purple), **1≡(34%)** (red), and TCNQ[**1≡(50%)**] (teal).

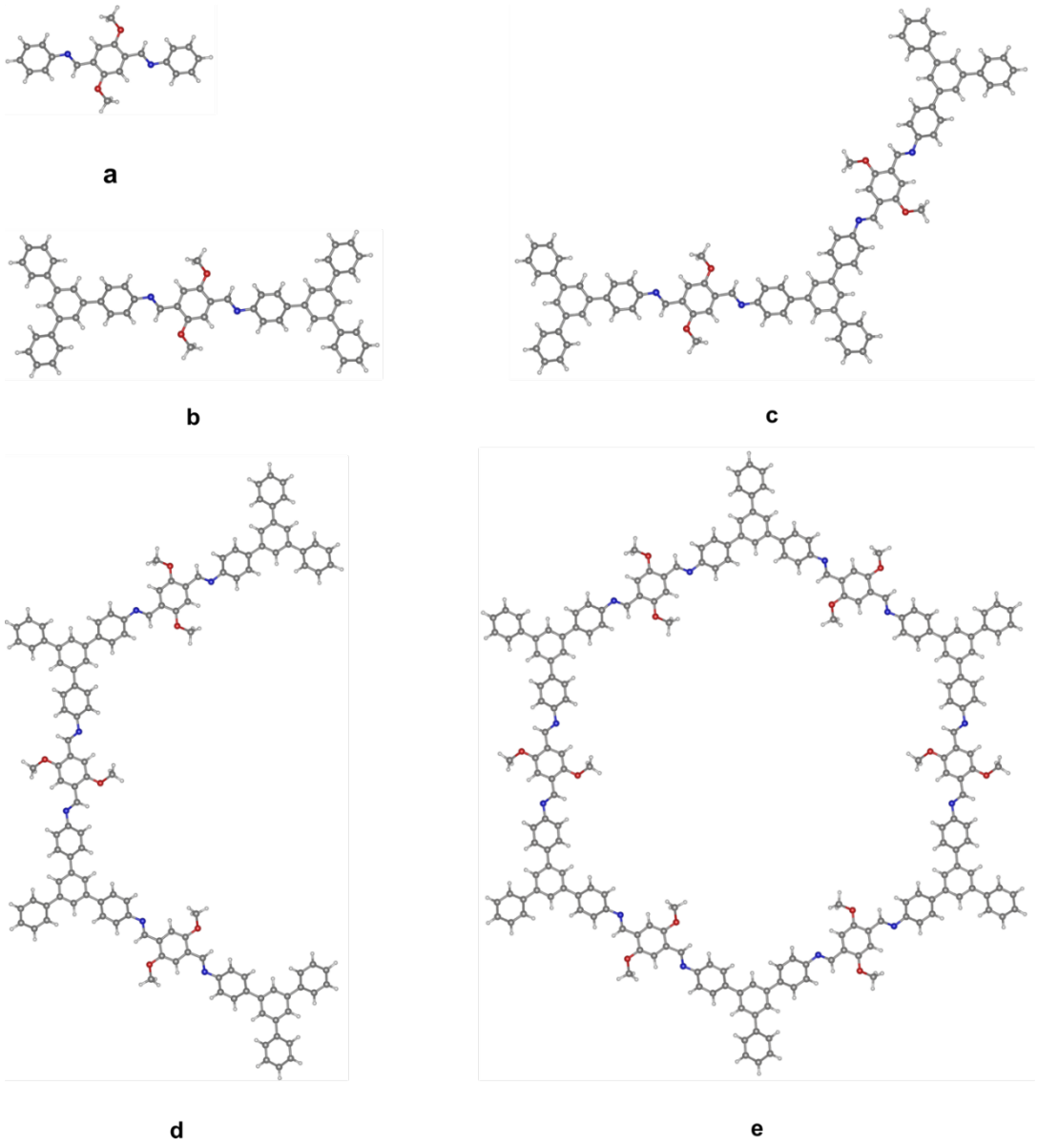

Figure 4.39. Geometries a-e are considered truncated models for the COF theoretical modeling. Simulations using the model a are described above.

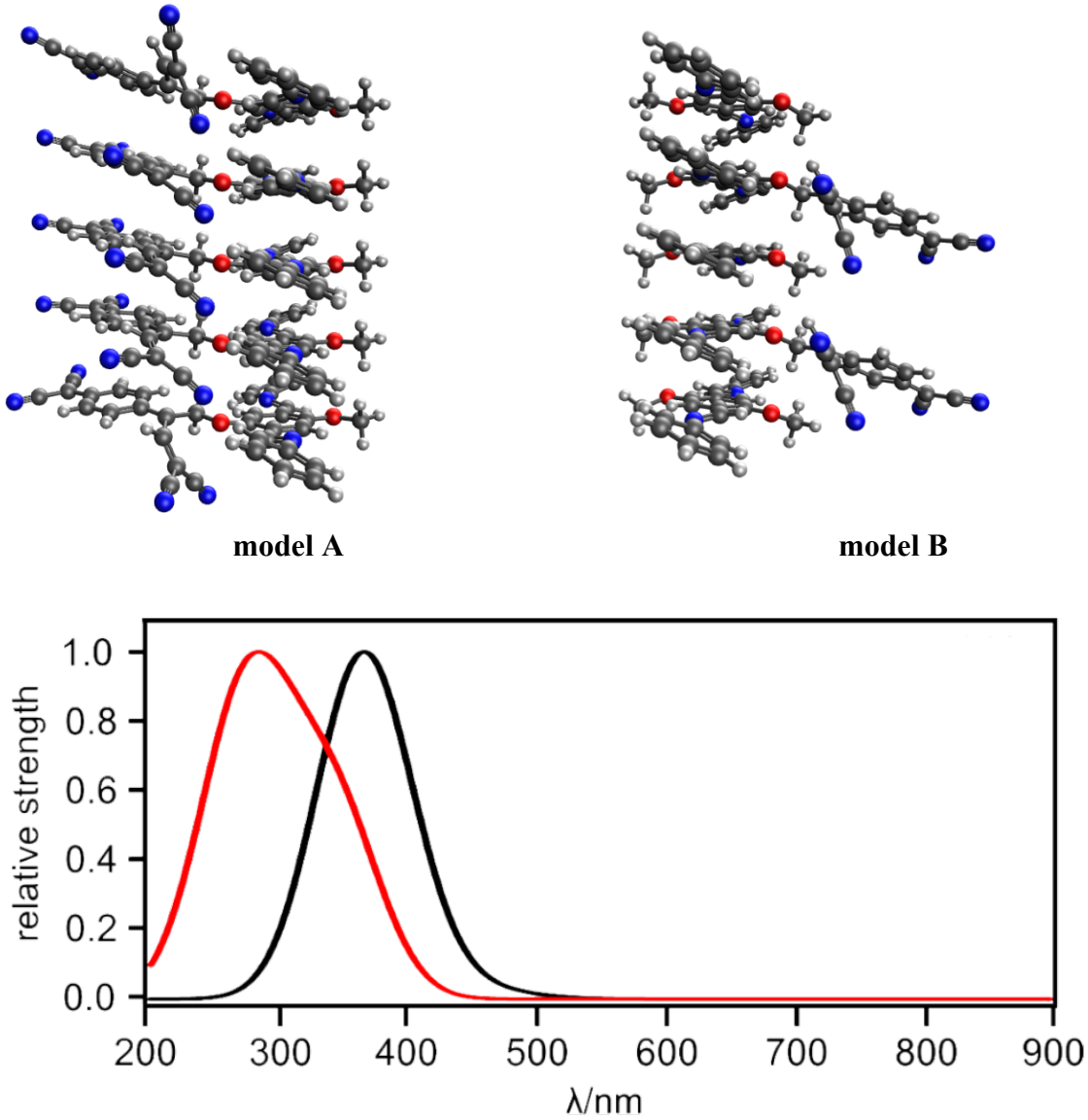

Figure 4.40. Two models for TCNQ bonding within the COF: (*top left*) TCNQ in every layer and (*top right*) TCNQ in every second layer. The geometry of TCNQ fragments is optimized at the B3LYP/6-31G level. (*bottom*) Calculated UV-vis spectra for **A** (black) and **B** (red) models. The theory level is TDDFT based on B3LYP-D3/6-31G.

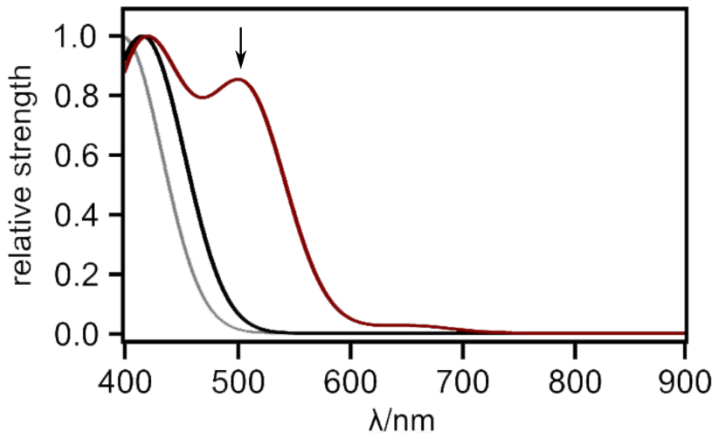

Figure 4.41. Optical transition strengths for TCNQ (gray), COF-fragment (black), and TCNQ[**COF**]-fragment (red).

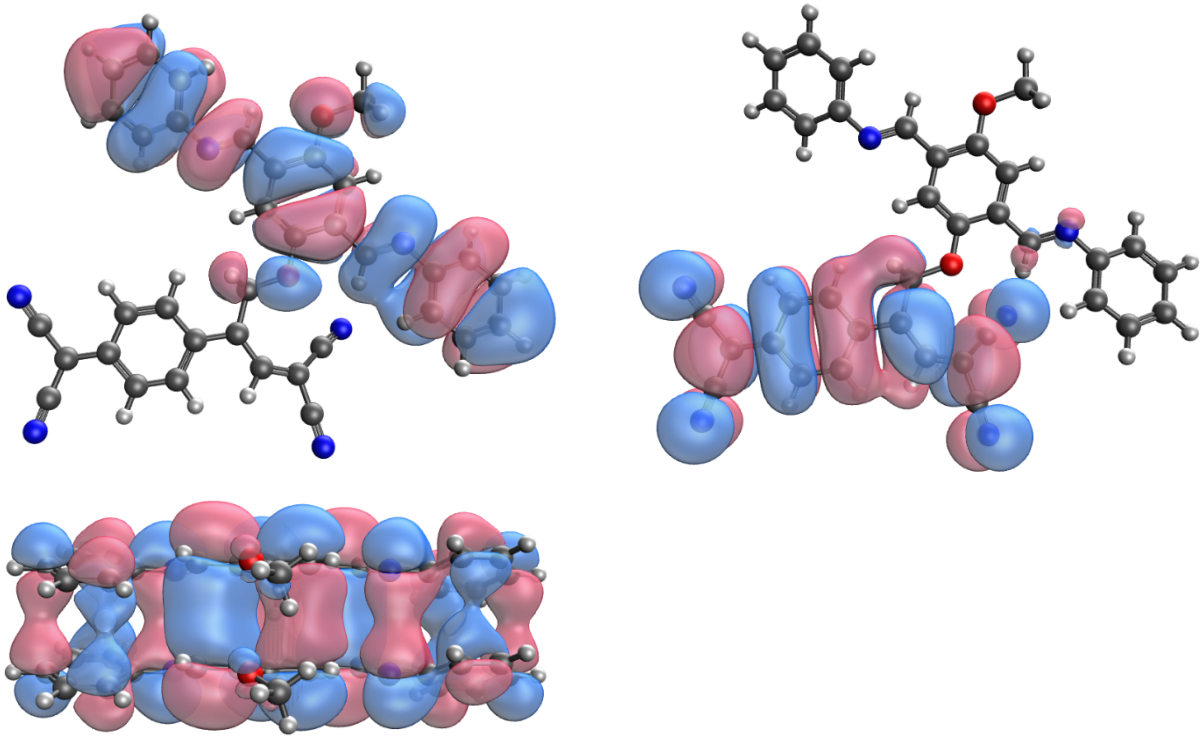

Figure 4.42. (*top left*) HOMO and (*top right*) LUMO orbitals for the TCNQ[**COF**]-fragment. (*bottom*) LUMO orbital for 2 stacked COF-fragments.

(242) M. Matsumoto, R. R. Dasari, W. Ji, C. H. Feriante, T. C. Parker, S. R. Marder, W. R. Dichtel, *J. Am. Chem. Soc.* **2017**, *139*, 4999–5002.

(243) C. R. DeBlase, W. R. Dichtel, *Macromolecules* **2016**, *49*, 5297–5305.

(244) A. J. Howarth, C. T. Buru, Y. Liu, A. M. Ploskonka, K. J. Hartlieb, M. McEntee, J. J. Mahle, J. H. Buchanan, E. M. Durke, S. S. Al-Juaid, J. F. Stoddart, J. B. DeCoste, J. T. Hupp, O. K. Farha, *Chem. Eur. J.* **2017**, *23*, 214–218.

(245) S. B. Alahakoon, C. M. Thompson, G. Occhialini, R. A. Smaldone, *ChemSusChem* **2017**, *10*, 2116–2129.

(246) S. Yang, W. Hu, X. Zhang, P. He, B. Pattengale, C. Liu, M. Cendejas, I. Hermans, X. Zhang, J. Zhang, J. Huang, *J. Am. Chem. Soc.* **2018**, *140*, 14614–14618.

(247) H. Wang, X. Dong, J. Lin, S. J. Teat, S. Jensen, J. Cure, E. V. Alexandrov, Q. Xia, K. Tan, Q. Wang, D. H. Olson, D. M. Proserpio, Y. J. Chabal, T. Thonhauer, J. Sun, Y. Han, J. Li, *Nat. Commun.* **2018**, *9*, 1745.

(248) Y. Wang, X. Zhao, H. Yang, X. Bu, Y. Wang, X. Jia, J. Li, P. Feng, *Angew. Chem. Int. Ed.* **2019**, *58*, 6316–6320.

(249) O. V. Boltalina, A. A. Popov, I. V. Kuvychko, N. B. Shustova, S. H. Strauss, *Chem. Rev.* **2015**, *115*, 1051−1105.

(250) S. A. Baudron, *CrystEngComm* **2016**, *18*, 4671–4680.

(251) A. Schneemann, V. Bon, I. Schwedler, I. Senkovska, S. Kaskel, R. A. Fischer, *Chem. Soc. Rev.* **2014**, *43*, 6062–6096.

(252) M. A. Petrukhina, *Dalton*. *Trans.,* **2019**, *48*, 5125–5130.

(253) J. Kurpiers, T. Ferron, S. Roland, M. Jakoby, T. Thiede, F. Jaiser, S. Albrecht, S. Janietz, B. A. Collins, I. A. Howard, D. Neher, *Nat. Commun.* **2018**, *9*, 2038.

(254) M. Adams, N. Baroni, M. Oldenburg, F. Kraffert, J. Behrends, R. W. MacQueen, R. Haldar, D. Busko, A. Turshatov, G. Emandi, M. O. Senge, C. Wöll, K. Lips, B. S. Richards, I. A. Howard, *Phys. Chem. Chem. Phys.*, **2018**, *20*, 29142–29151.

(255) D. E. Williams, E. A. Dolgopolova, D. C. Godfrey, E. D. Ermolaeva, P. J. Pellechia, A. B. Greytak, M. D. Smith, S. M. Avdoshenko, A. A. Popov, N. B. Shustova, *Angew. Chem. Int. Ed.* **2016**, *55*, 9070–9074.

(256) J. Sukegawa, C. Schubert, X. Zhu, H. Tsuji, D. M. Guldi, E. Nakamura, *Nat. Chem.* **2014**, *6*, 899–905.

(257) C.-Z. Li, H.-L. Yip, A. K.-Y. Jen, *J. Mater. Chem.* **2012**, *22*, 4161–4177.

(258) C. D. Wessendorf, R. Eigler, S. Eigler, J. Hanisch, A. Hirsch, E. Ahlswede, *Sol. Energy Mater. Sol. Cells* **2015**, *132*, 450–454.

(259) A. Hirsch, *The Chemistry of Fullerenes*, John Wiley And Sons, Inc., **2008**.

(260) D. M. Guldi, *Chem. Commun.* **2000**, 321–327.

(261) D. Josa, J. Rodríguez-Otero, E. M. Cabaleiro-Lago, L. A. Santos, T. C. Ramalho, *J. Phys. Chem. A* **2014**, *118*, 9521−9528.

(262) H. Yang, S. Zhang, L. Han, Z. Zhang, Z. Xue, J. Gao, Y. Li, C. Huang, Y. Yi, H. Liu, Y. Li, *ACS Appl. Mater. Interfaces* **2016**, *8*, 5366–5375.

(263) H. S. Sasmal, H. B. Aiyappa, S. N. Bhange, S. Karak, A. Halder, S. Kurungot, R. Banerjee, *Angew. Chem. Int. Ed.* **2018**, *57*, 10894–10898.

(264) S.-L. Cai, Y.-B. Zhang, A. B. Pun, B. He, J. Yang, F. M. Toma, I. D. Sharp, O. M. Yaghi, J. Fan, S.-R. Zheng, W.-G. Zhang, Y. Liu, *Chem. Sci.,* **2014**, *5*, 4693–4700.

(265) S. Duhović, M. Dincă, *Chem. Mater.* **2015**, *27*, 5487–5490.

(266) H. Guo, J. Wang, Q. Fang, Y. Zhao, S. Gu, J. Zheng, Y. Yan, *CrystEngComm*, **2017**, *19*, 4905–4910.

(267) D. A. Vazquez-Molina, G. S. Mohammad-Pour, C. Lee, M. W. Logan, X. Duan, J. K. Harper, F. J. Uribe-Romo, *J. Am. Chem. Soc.* **2016**, *138*, 9767–9770.

(268) E. Jin, M. Asada, Q. Xu, S. Dalapati, M. A. Addicoat, M. A. Brady, H. Xu, T. Nakamura, T. Heine, Q. Chen, D. Jiang, *Science* **2017**, *357*, 673–676.

(269) X. Feng, X. Ding, D. Jiang, *Chem. Soc. Rev.*, **2012**, *41*, 6010–6022.

(270) M. S. Lohse, T. Bein, *Adv. Funct. Mater.* **2018**, *28*, 1705553.

(271) R. P. Bisbey, W. R. Dichtel, *ACS Cent. Sci.* **2017**, *3*, 533–543.

(272) A. M. Rice, E. A. Dolgopolova, B. J. Yarbrough, G. A. Leith, C. R. Martin, K. S. Stephenson, R. A. Heugh, A. J. Brandt, D. A. Chen, S. G. Karakalos, M. D. Smith, K. B. Hatzell, P. J. Pellechia, S. Garashchuk, N. B. Shustova, *Angew. Chem. Int. Ed.* **2018**, *57*, 11310–11315.

(273) S. Goswami, D. Ray, K.-I. Otake, C.-W. Kung, S. J. Garibay, T. Islamoglu, A. Atilgan, Y. Cui, C. J. Cramer, O. K. Farha, J. T. Hupp, *Chem. Sci.*, **2018**, *9*, 4477–4482.

(274) A. A. Talin, A. Centrone, A. C. Ford, M. E. Foster, V. Stavila, P. Haney, R. A. Kinney, V. Szalai, F. El Gabaly, H. P. Yoon, F. Léonard, M. D. Allendorf, *Science.* **2014**, *343*, 66–69.

(275) S. B. Kalidindi, C. Wiktor, A. Ramakrishnan, J. Weßing, A. Schneemann, G. Van Tendeloo, R. A. Fischer, *Chem. Commun.*, **2013**, *49*, 463–465.

(276) J. Zhang, L. Wang, N. Li, J. Liu, W. Zhang, Z. Zhang, N. Zhou, X. Zhu, *CrystEngComm*, **2014**, *16*, 6547–6551.

(277) S. Zhao, B. Dong, R. Ge, C. Wang, X. Song, W. Ma, Y. Wang, C. Hao, X. Guo, Y. Gao, *RSC Adv.*, **2016**, *6*, 38774–38781.

(278) H. Xu, J. Gao, D. Jiang, *Nat. Chem.* **2015**, *7*, 905–912.

(279) A. M. Rice, E. A. Dolgopolova, N. B. Shustova, *Chem. Mater.* **2017**, *29*, 7054–7061.

(280) L. Chen, K. Furukawa, J. Gao, A. Nagai, T. Nakamura, Y. Dong, D. Jiang, *J. Am. Chem. Soc.* **2014**, *136*, 9806–9809.

(281) D. D. Medina, V. Werner, F. Auras, R. Tautz, M. Dogru, J. Schuster, S. Linke, M. Döblinger, J. Feldmann, P. Knochel, T. Bein, *ACS Nano* **2014**, *8*, 4042–4052.

(282) M. Dogru, M. Handloser, F. Auras, T. Kunz, D. Medina, A. Hartschuh, P. Knochel, T. Bein, *Angew. Chem. Int. Ed.* **2013**, *52*, 2920–2924.

(283) J. Guo, Y. Xu, S. Jin, L. Chen, T. Kaji, Y. Honsho, M. A. Addicoat, J. Kim, A. Saeki, H. Ihee, S. Seki, S. Irle, M. Hiramoto, J. Gao, D. Jiang, *Nat. Commun.* **2013**, *4*, 2736.

(284) P. Hu, K. Du, F. Wei, H. Jiang, C. Kloc, *Cryst. Growth Des.* **2016**, *16*, 3019–3027.

(285) K. Kanai, K. Akaike, K. Koyasu, K. Sakai, T. Nishi, Y. Kamizuru, T. Nishi, Y. Ouchi, K. Seki, *Appl. Phys. A* **2009**, *95*, 309–313.

(286) H. Alves, R. M. Pinto, E. S. Maçôas, *Nat. Commun.* **2013**, *4*, 1842.

(287) F. D'Souza, O. Ito, *Coord. Chem. Rev.*, **2005**, *249*, 1410–1422.

(288) M. Usman, S. Mendiratta, S. Batjargal, G. Haider, M. Hayashi, N. Rao Gade, J.-W. Chen, Y.-F. Chen, K.-L. Lu, *ACS Appl. Mater. Interfaces* **2015**, *7*, 22767–22774.

(289) R. López, R. Gómez, *J. Sol-Gel Sci. Technol.* **2012**, *61*, 1–7.

(290) R. A. Marcus, *Rev. Mod. Phys.* **1993**, *65*, 599–610.

(291) A. M. Rice, C. R. Martin, V. A. Galitskiy, A. A. Berseneva, G. A. Leith, N. B. Shustova, *Chem. Rev.* **2019**, DOI: 10.1021/acs.chemrev.9b00350.

(292) C. R. DeBlase, K. E. Silberstein, T.-T. Truong, H. D. Abruña, W. R. Dichtel, *J. Am. Chem. Soc.* **2013**, *135*, 16821–16824.

(293) T. Rajendran, B. Manimaran, R.-T. Liao, Y.-H. Liu, P. Thanasekaran, R.-J. Lin, I.-J. Chang, P.-T. Chou, R. Ramaraj, S. Rajagopal, K.-L. Lu, *Dalton. Trans.*, **2010**, *39*, 2928–2935.

(294) A. Sastre-Santos, C. Parejo, L. Martin-Gomis, K. Ohkubo, F. Fernández-Lázaro, S. Fukuzumi, *J. Mater. Chem.*, **2011**, *21*, 1509–1515.

APPENDIX A: PERMISSION TO REPRINT

Graphitic supramolecular architectures based on corannulene, fullerene, and beyond

G. A. Leith and N. B. Shustova, *Chem. Commun.*, 2021, **57**, 10125 **DOI:** 10.1039/D1CC02896K

To request permission to reproduce material from this article, please go to the Copyright Clearance Center request page.

If you are **an author contributing to an RSC publication, you do not need to request permission** provided correct acknowledgement is given.

If you are **the author of this article, you do not need to request permission to reproduce figures and diagrams** provided correct acknowledgement is given. If you want to reproduce the whole article in a third-party publication (excluding your thesis/dissertation for which permission is not required) please go to the Copyright Clearance Center request page.

Read more about how to correctly acknowledge RSC content.

“Broken-hearted” carbon bowl *via* electron shuttle reaction: energetics and electron coupling

G. A. Leith, A. M. Rice, B. J. Yarbrough, P. Kittikhunnatham, A. Mathur, N. A. Morris, M. J. Francis, A. A. Berseneva, P. Dhull, R. D. Adams, M. V. Bobo, A. A. Vannucci, M. D. Smith, S. Garashchuk and N. B. Shustova, *Chem. Sci.*, 2021, **12**, 6600 **DOI:** 10.1039/D0SC06755E

This article is licensed under a Creative Commons Attribution-NonCommercial 3.0 Unported Licence. **You can use material from this article in other publications, without requesting further permission** from the RSC, provided that the correct acknowledgement is given and it is not used for commercial purposes.

To request permission **to reproduce material from this article in a commercial publication**, please go to the Copyright Clearance Center request page.

If you are **an author contributing to an RSC publication, you do not need to request permission** provided correct acknowledgement is given.

If you are **the author of this article, you do not need to request permission to reproduce figures and diagrams** provided correct acknowledgement is given. If you want to reproduce the whole article in a third-party commercial publication (excluding your thesis/dissertation for which permission is not required) please go to the Copyright Clearance Center request page.

Read more about how to correctly acknowledge RSC content.

JOHN WILEY AND SONS LICENSE
TERMS AND CONDITIONS

Mar 09, 2022

This Agreement between University of South Carolina -- Gabrielle Leith ("You") and John Wiley and Sons ("John Wiley and Sons") consists of your license details and the terms and conditions provided by John Wiley and Sons and Copyright Clearance Center.

License Number	5264980578932
License date	Mar 09, 2022
Licensed Content Publisher	John Wiley and Sons
Licensed Content Publication	Angewandte Chemie International Edition
Licensed Content Title	A Dual Threat: Redox-Activity and Electronic Structures of Well-Defined Donor–Acceptor Fulleretic Covalent-Organic Materials
Licensed Content Author	Gabrielle A. Leith, Allison M. Rice, Brandon J. Yarbrough, et al
Licensed Content Date	Feb 12, 2020
Licensed Content Volume	59
Licensed Content Issue	15